



IMPROVEMENT OF ALGORITHMS FOR THE ASSESSMENT OF AIR QUALITY AND ATMOSPHERIC COMPOSITION FROM OBSERVATION OF SPECTRAL RADIANCES

Ana Filipa Alves Real Domingues

Tese apresentada à Universidade de Évora
para obtenção do Grau de Doutor em Ciências da Terra e do Espaço.
Especialidade: Física da Atmosfera e do Clima.

ORIENTADOR: *Doutor Daniele Bortoli*
CO- ORIENTADORA: *Professora Doutora Ana Maria Almeida e Silva*

ÉVORA, ABRIL 2015



IMPROVEMENT OF ALGORITHMS FOR THE ASSESSMENT OF AIR QUALITY AND ATMOSPHERIC COMPOSITION FROM OBSERVATION OF SPECTRAL RADIANCES

Ana Filipa Alves Real Domingues

Tese apresentada à Universidade de Évora
para obtenção do Grau de Doutor em Ciências da Terra e do Espaço
Especialidade: Física da Atmosfera e do Clima

ORIENTADOR: *Doutor Daniele Bortoli*
CO- ORIENTADORA: *Professora Doutora Ana Maria Almeida e Silva*

ÉVORA, ABRIL 2015



Acknowledgments

I am sincerely grateful to my supervisors Dr. Daniele Bortoli and Prof^a Dr. Ana Maria Silva for their guidance, availability, generosity and friendship through the development of this work. They have accompanied me in every step of this journey and inspired me to move forward.

I am also thankful to Geophysics Centre of Évora and University of Évora for providing all the resources needed for the development of this work. And also for providing the means to extend my education through the participation in complementary courses and workshops and in national and international conferences.

I want to acknowledge to my CGE colleagues (Dr. Dina Santos, Vanda Salgueiro, Marta Melgão, Dr. Sérgio Pereira, Dr. Miguel Potes, Flávio Couto, Prof^a Dr. Maria João Costa, Prof. Dr. Rui Salgado, Dr. Manuel Antón, Dr. Pavan Kulkarni) for the good atmosphere at the office. I am thankful in particular to Prof^a Dr. Maria João Costa for her support and encouragement, to Dr. Manuel Antón for his availability in sharing his knowledge, and to Vanda Salgueiro for her valuable tips in MATLAB.

I also have to acknowledge to Lyzia Bensehil from Laboratoire de Météorologie et Dynamique (LMD), to Dr. Frederick Tack and Dr. Nicolas Theys from Belgian Institute for Space Aeronomy (BIRA-IASB), to Professor Alain Sarkissian and Dr. Florence Goutail from Laboratoire from LATMOS, to Dr. G.S. Meena from the Indian Institute of Tropical Meteorology, to Dr. Andreas Richter and Dr. Alexei Rosanov from Institute of Environmental Physics- University of Bremen (IUP Bremen) and Dr. Janis Pukite from Max Plack INstitute from MAInz (MPI), for articles, data and clarifications. I would like to thanks also Dr. Margherita Premuda, Dr. Samuele Masieri and Dr. Giorgio Giovanelli, researchers of the Institute for Atmospheric Science and Climate/ National Council for the Research (ISAC/CNR) in Bologna-Italy, for their advice in the use of the radiative transfer models.

Fundação para a Ciência e a Tecnologia (FCT) funded this work with the grant FCT-SFRH/BD/44920/2008. This grant was also valuable because supported partially my participation in conferences which were important for the diffusion and improvement of this research.

This work was financed through other projects as well like the FEDER (Programa Operacional Factores de Competitividade – COMPETE) and national funding through FCT in the framework of project FCOMP-01-0124-FEDER-014024 (Ref^a. FCT PTDC/AAC-CLI/114031/2009), PTDC/CTE-ATM/65307/2006, PROPOLAR SPATRAM-MIGE and POCI/AMB/59774/2004.

I also acknowledge for the financial support provided by the French program LABEX that allowed for my participation in the European Research Course on Atmospheres organized by Université Joseph Fourier & CNRS which was a valuable educational experience for the conclusion of this thesis.

I gratefully acknowledge also to scientists that participate in the acquirement and provision of the environmental data and the following institutions:

- NOAA Air Resources Laboratory for the provision of the HYSPLIT data.
- ESA team for the accomplishment of all satellite missions and NO₂ and O₃ total columns data
- SCIAMACHY team and in particular to Dr. Andreas Richter for his availability in the explanation of SCHIAMACHY products
- OMI team for the accomplishment of all satellite missions and for NO₂, O₃ and BrO total columns data
- GOME-2 team for the accomplishment of all satellite missions and for NO₂ and BrO total columns data
- GOME team for the accomplishment of all satellite missions and for O₃ total columns data
- IUP Bremen team lead by Prof. J.P. Burrows for providing the data sets of NO₂ vertical profiles by Dr. Alexei Rosanov
- BIRA- IASB UV-Visible DOAS group for BrO total columns from GOME-2 data by Dr. Nicolas Theys
- MPI, Mainz team for the SCIAMACHY NO₂ vertical profiles by Dr. Janis Pukite

And last (but not the least) my sincere gratitude for the support of my friends Rute Feiteira, João Marques, Raquel Pina, José Garcez, Sofia Pinto, Filomena Mascarenhas and family. My deepest regards to my father Joaquim Domingues, husband Luís Bengala, daughter Joana Bengala and to my dearest mother Digna Domingues for their infinite love, care and patient.

Contents

<i>Contents</i>	<i>i</i>
<i>List of Figures</i>	<i>v</i>
<i>List of Tables</i>	<i>xi</i>
<i>Resumo</i>	<i>xiii</i>
<i>Abstract</i>	<i>xiii</i>
<i>Extended abstract</i>	<i>xv</i>
<i>Acronyms</i>	<i>xvii</i>
<i>List of principal symbols</i>	<i>xix</i>
1. Introduction	1
1.1 State of the art	1
1.2 Motivation.....	3
1.3 Objectives.....	4
1.4 Thesis structure	5
2. Chemistry of atmosphere: the role of ozone and nitrogen dioxide	7
2.1 Introduction	7
2.2 Atmospheric composition and structure	7
2.2.1 Atmospheric composition	7
2.2.2 Atmospheric vertical structure.....	9
2.3 Trace gases in the atmosphere	11
2.3.1.1 Nitrogen oxides - NO _x	14
2.3.1.2 Ozone – O ₃	15
2.3.2 Stratospheric O ₃	18
2.3.3 Stratospheric NO _x	20
2.3.4 Tropospheric ozone and nitrogen dioxide	22
2.3.4.1 Tropospheric NO _x	22
2.3.4.2 Tropospheric ozone.....	25
2.3.4.3 VOC-NO _x –O ₃ system	28
2.4 Bromine Oxide - BrO	29
3. Absorption and scattering of solar radiation in the atmosphere	31
3.1 Interaction processes between electromagnetic radiation and the Earth's atmosphere components.....	31
3.2 Basic principles of Molecular absorption (and emission)	31

3.2.1	Rotational energy levels and transitions.....	33
3.2.2	Vibrational energy levels and transitions.....	34
3.2.3	Electronic transitions and energy.....	35
3.2.4	Molecular transitions in the UV-VIS region.....	36
3.3	Absorption, emission and scattering of solar radiation	36
3.3.1	Absorption in the UV- Visible part of the spectrum.....	37
3.4	Atmospheric radiative transfer	40
3.4.1	Radiative Transfer Equation (Platt & Stutz, 2008; Burrows et al., 2011)	41
4.	Methods and instruments to monitor atmospheric composition with solar radiation	43
4.1	Introduction	43
4.2	PART I - Remote Sensing/sounding techniques	44
4.3	PART II – Instruments	48
4.3.1	The SPATRAM system.....	48
4.3.1.1	VELOD – VERTICAL LOOking Device.....	50
4.3.1.2	MIGE -Multiple Input Geometry Equipment.....	50
4.3.1.3	SPATRAM products.....	51
4.3.2	Satellites data sources.....	52
4.3.2.1	The Ozone Monitoring Instrument	52
4.3.2.2	The SCanning Imaging Absorption spectroMeter for Atmospheric CHartography	53
4.3.2.3	Global Ozone Monitoring Experiment	53
4.3.2.4	Global Ozone Monitoring Experiment 2	53
4.4	Part III – Methods.....	54
4.4.1	DOAS History and background	54
4.4.1.1	Beer-Bouguer Lambert Law.....	55
4.4.1.2	DOAS master equation	57
4.4.2	DOAS applied to SPATRAM spectral data	58
4.4.2.1	Atmospheric Model for Enhancement Factor Computation - AMEFCO	63
4.4.2.2	PROcessing of Multi-Scattered Atmospheric Radiation – PROMSAR	66
4.4.2.3	Multiple AXis Differential Optical Absorption Spectroscopy (MAX-DOAS)	69
4.4.2.4	Reference spectrum	70
4.4.2.5	Error assessment for SCD and VCD calculations	71
4.4.3	Retrieval of atmospheric trace gases profiles	73
4.4.3.1	Retrieval process / theory	73

4.4.3.2	Algorithm to retrieve the NO ₂ stratospheric vertical profiles	73
4.4.3.3	Algorithm to retrieve the NO ₂ tropospheric vertical profiles and tropospheric vertical columns	76
5.	Results	79
5.1	Introduction	79
5.2	Measurement site description.....	79
5.3	Total O ₃ , NO ₂ and BrO variability from ground-based and satellite instruments over South of Portugal	80
5.3.1	O ₃ over Évora station for the period 2007-2011.....	80
5.3.1.1	O ₃ diurnal variation	80
5.3.1.2	O ₃ seasonal variation.....	83
5.3.1.3	Ground based and satellite dataset	84
5.3.1.3.1	O ₃ VCD - SPATRAM vs OMI.....	84
5.3.1.3.2	O ₃ VCD - SPATRAM vs SCIAMACHY	89
5.3.1.3.3	O ₃ VCD - SPATRAM vs GOME	91
5.3.1.3.4	Statistical analysis	93
5.3.2	NO ₂ over Évora station for the period 2007-2011	95
5.3.2.1	NO ₂ diurnal variation.....	95
5.3.2.2	NO ₂ seasonal variation	97
5.3.2.3	Ground based and satellite dataset	99
5.3.2.3.1	NO ₂ VCD - SPATRAM vs SCIAMACHY.....	99
5.3.2.3.2	NO ₂ VCD - SPATRAM vs GOME-2	101
5.3.2.3.3	NO ₂ VCD - SPATRAM vs OMI	103
5.3.3	Case study: BrO VCD retrieval	106
5.3.3.1	BrO – SPATRAM vs OMI.....	107
5.3.3.2	BrO – SPATRAM vs GOME-2.....	111
5.4	NO ₂ Vertical profiles.....	114
5.4.1.1	Retrieval of NO ₂ vertical profiles and tropospheric columns at Évora with the SPATRAM and MIGE instruments	115
5.4.1.2	NO ₂ tropospheric total columns.....	115
5.4.2	NO ₂ vertical profiles in PBL.....	116
5.5	Retrieval of NO ₂ stratospheric vertical profiles.....	119
5.6	Air quality evaluation in the south-western regions of the Iberian Peninsula.....	123
5.6.1	Introduction.....	123
5.6.2	Methodology	125

5.6.3	Results	126
6.	Conclusion and outlook	133
6.1	Conclusion	133
6.2	Future work	135
7.	References	137

List of Figures

Figure 2.1 - Typical vertical distribution of the concentration of chemical atmospheric constituents under about 120 km (from Liou, 2002.)	9
Figure 2.2- Temperature variation in Earth's atmosphere (from Platt & Stutz, 2008).	9
Figure 2.3- Variation of atmospheric pressure in Earth's atmosphere with altitude in the Earth's atmosphere for tropical regions, mid latitudes in summer and winter, and high latitude sub arctic summer and winter (from Burrows et al., 2011).	11
Figure 2.4- Spatial and temporal scales variability of some atmospheric gases (from Platt & Stutz, 2008).	12
Figure 2.5 - Global distribution of Total Ozone (DU) varying with latitude and time of the year (from http://exp-studies.tor.ec.gc.ca/e/ozone/Curr_map.htm).....	17
Figure 2.6 - Arctic total ozone (DU) varying with the time of the year from http://exp-studies.tor.ec.gc.ca/e/ozone/Curr_map.htm	17
Figure 2.7 - Antarctica total ozone (DU) varying with the time of the year from http://exp-studies.tor.ec.gc.ca/e/ozone/Curr_map.htm	18
Figure 2.8 - Sinks of NO _x in troposphere (from Jacob, 1999).	25
Figure 2.9 - Scheme of the reactions involving tropospheric NO _x and O ₃ (from Volz-Thomas et al., 2003).....	27
Figure 2.10 - Typical ozone isopleths generated from initial mixtures of VOC and NO, in air, illustrating the relation between VOC- NO _x -O ₃ in troposphere. The VOC-limited region is found in some highly polluted urban centres while the NO _x , limited region is typical of downwind suburban and rural areas.	28
Figure 3.1- The electromagnetic spectrum and the types of transitions in molecules and atoms provoked by the different wavelengths of radiation (from Burrows et al., 2011).	31
Figure 3.2 - Geometries of important trace gases and dipole moment status (from http://flux.aos.wisc.edu/~adesai/documents/aos640/AtmosRadCh9-10.pdf).	32
Figure 3.3 - Axes in red of rotational freedom for linear diatomic and triatomic and asymmetric top molecules and some examples (from Socolik, 2009). Diatomic molecules show two degrees of rotational freedom and asymmetric top three and respectively the same number of inertia moments.	33
Figure 3.4- Vibrational modes of diatomic and triatomic atmospheric molecules (from http://flux.aos.wisc.edu/~adesai/documents/aos640/AtmosRadCh9-10.pdf).	34
Figure 3.5- Vibrational-rotational transitions for $\Delta v = \pm 1$, $\Delta J = [-1, 0, +1]$ and illustration of the transitions in the spectrum. P and R branches correspond, respectively, to transitions involving $\Delta J = -1$ and $\Delta J = +1$ (from Liou, 2002)	35
Figure 3.6- Scheme for the electronic, vibration and rotation energy levels (from www.google.com/webhp?nord=1#nord=1&q=http%3F%3Fflux.aos.wisc.edu%3F~adesai%3Fdocuments%3Faos640%3FAtmosRadCh9-10.pdf).....	35
Figure 3.7- Potential energy curves for two electronic states of a diatomic molecule. Molecules can be excited into a dissociation level (e.g. transition 1) or into a specific vibrational level of the upper electronic state (e.g. transition 2) (from Liou, 2002).	36

Figure 3.8 - Low resolution solar irradiance at top of atmosphere and at sea level and atmospheric absorption for average atmospheric conditions and an overhead sun (from Palazzi, 2000).....	39
Figure 3.9- Spectral distribution of the absorption cross section of O ₂ and O ₃ adapted (from Haigh, 2007).	40
Figure 4.1-General Plan of Remote Sensing techniques (from Strong,2005)	47
Figure 4.2 - Representation of the main modules of the SPATRAM Instrument.	48
Figure 4.3- a) The location of Évora city in mainland Portugal. b) The container in the Observatory of the Geophysics Centre of Évora in Évora (38.5°N; 7.9 °W, 300 m a.s.l.). c) The SPATRAM instrument installed inside the container.	49
Figure 4.4 – VELOD a) optical layout; b) project design with the vacuum proof box and the optic fibre. The arrows specify the direction of the input and output of the radiation.	50
Figure 4.5- The MIGE platform installed on the roof of the container where the SPATRAM instrument is placed. This platform ensure the possibility to carry out measurements in off-axis configuration along many azimuthally directions since the horizon line is almost completely free (from Domingues, 2011).	51
Figure 4.6- Absorption cross sections in cm ⁻² of some trace gases from (Platt & Stutz, 2008). .	56
Figure 4.7- Intensity of monochromatic radiation that crosses the atmosphere (I_{λ,S_1}) at twilight (AM or PM) versus the intensity of monochromatic radiation at local noon ($I_{\lambda,0}$) obtained with SPATRAM for Ozone measurements.	60
Figure 4.8- Plot of $\ln(I_0(\lambda, \theta_{\min})/I_s(\lambda, \theta))$ versus wavelength for UV spectral range (orange) and the smoothing function (brown).	61
Figure 4.9- “Smoothing” process which consists in filtering the high frequency features in the spectral data series. The presented values are $\ln(I_{\lambda,0}/I_{\lambda,S_1}) - \ln(I_{\lambda,0}/I_{\lambda,S_1})$ versus wavelength (grey) and ozone differential absorption cross section (red).	62
Figure 4.10- Path of radiation (yellow) along the vertical direction for Solar Zenith Angles (SZA) inferior to 90° (upper panel) and superior to 90° (from Bortoli, 2005).	64
Figure 4.11- Illustration of the zenith sky and off-axis viewing geometry. It is possible to see the enhancement of absorption path length in the troposphere due to several off-axis viewing direction near the horizon (adapted from Heckel et al., 2005).	69
Figure 4.12- Ratio of the signal obtained by the spectrometer and its “exposure” time (Flux Index in ms/ digital counting) calculated at the Évora station for a clear sky day and cloudy day.	71
Figure 5.1- (Left Panel) Location of the Évora station in the South Western part of the Iberian Peninsula; (Right Panel) Évora city. SPATRAM + MIGE positioning at the Observatory of the Geophysics Centre of the University of Évora (adapted from Bortoli et al, 2009).	79
Figure 5.2- Time series of the O ₃ Slant Column Density (SCD) in molecules/cm ² obtained with the SPATRAM equipment installed at Évora Observatory for the 19 th January 2007.....	81
Figure 5.3- O ₃ Slant Column Densities (SCD) values and Air Mass Factor (AMF) versus time for the 19 th January 2007 over Évora retrieved from SPATRAM measurements.....	82
Figure 5.4- O ₃ VCD for the 19 th January 2007 over Évora retrieved from SPATRAM measurements.....	82
Figure 5.5- Time series of the O ₃ VCD obtained with the SPATRAM equipment installed at Évora	

Observatory during March 2008 - March 2009 period.....	83
Figure 5.6- Full time series of the O ₃ VCD obtained with the SPATRAM equipment installed at Évora Observatory during 2007-2011, and the O ₃ data from the OMI (TOMS) - OMT03 instrument aboard the NASA EOS- Aura Satellite.....	85
Figure 5.7- a) Filtered time series of the O ₃ VCD obtained with the SPATRAM equipment at Évora during 2007-2010, and the O ₃ data from the OMI (OMI-TOMS) b) Scatter plot of the O ₃ data from the OMI instrument (OMI-TOMS OMT03 product) aboard the NASA EOS – Aura satellite versus O ₃ SPATRAM data retrieved at Évora Observatory during 2007 – 2011 period.....	86
Figure 5.8- Full time series of the O ₃ VCD obtained with the SPATRAM equipment installed at Évora Observatory for the SZA of 87°, during 2007-2011, and the O ₃ data from the OMI (DOAS) instrument aboard the EOS- Aura Satellite.....	87
Figure 5.9- Filtered time series of the O ₃ VCD obtained with the SPATRAM equipment at Évora during 2007-2010, and the O ₃ data from the OMI (OMI-DOAS). b) Scatter plot of the O ₃ data from the OMI instrument (OMI-DOAS OMD0A3 product) aboard the NASA EOS – Aura satellite versus O ₃ SPATRAM data retrieved at Évora Observatory during 2007 – 2011 period.....	88
Figure 5.10- Full time series of the O ₃ VCD obtained with the SPATRAM equipment installed at Évora Observatory during 2007-2010, and the O ₃ data from the SCIAMACHY instrument aboard the ENVISAT satellite.....	90
Figure 5.11- a) Filtered time series of the O ₃ VCD obtained with the SPATRAM equipment at Évora during 2007-2010, and the O ₃ data from the SCIAMACHY. b) Scatter plot of the O ₃ data from the SCIAMACHY instrument (TOSOMI product) aboard the ENVISAT satellite versus O ₃ SPATRAM data retrieved at Évora Observatory during 2007 – 2011 period.....	91
Figure 5.12- Full time series of the O ₃ VCD obtained with the SPATRAM equipment installed at Évora Observatory during 2007-2010, and the O ₃ data from the GOME instrument aboard the ERS-2 satellite.....	92
Figure 5.13- a) Filtered time series of the O ₃ VCD obtained with the SPATRAM equipment at Évora during 2007-2010, and the O ₃ data from the GOME. b) Scatter plot of the O ₃ data from the GOME instrument aboard the ERS-2 satellite versus O ₃ SPATRAM data retrieved at Évora Observatory during 2007 - 2011 period including the regression line (black line).....	93
Figure 5.14 - NO ₂ Slant Column Densities (SCD) and AMF versus SZA obtained with SPATRAM at Évora-Portugal for 24 th April 2010.	96
Figure 5.15- Daily variation of NO ₂ VCD obtained with SPATRAM at Évora-Portugal for 24 th April 2010.....	97
Figure 5.16- Time series of the NO ₂ VCD obtained with the SPATRAM equipment installed at Évora Observatory for the SZA of 90°, during 2007-2011.	98
Figure 5.17 - Time series of the NO ₂ VCD obtained with the SPATRAM equipment installed at Évora Observatory for the SZA of 90°, during 2007-2011, and the NO ₂ total columns acquired from the SCIAMACHY spectrometer aboard ENVISAT.	99
Figure 5.18 - Scatter plot of the NO ₂ data from the SCIAMACHY instrument versus NO ₂ SPATRAM AM (morning) and PM (afternoon) data retrieved at Évora Observatory for the SZA of 90°, during 2007 - 2011 period including the regression lines for each dataset....	100
Figure 5.19 - Time series of the NO ₂ VCD obtained with the SPATRAM equipment installed at Évora Observatory for the SZA of 90°, during 2007-2011, and the NO ₂ total columns acquired from the GOME-2 instrument aboard EUMETSAT.....	102

Figure 5.20 - Correlation of SPATRAM data retrieved at Évora Observatory for the SZA of 90°, during 2007-2011, and the NO ₂ data from the GOME-2 instrument.....	102
Figure 5.21- Time series of the NO ₂ VCD obtained with the SPATRAM equipment installed at Évora Observatory for the SZA of 90°, during 2007-2011, and the filtered NO ₂ total columns acquired from the OMI instrument aboard AURA	103
Figure 5.22- Correlation of SPATRAM data retrieved at Évora Observatory for the SZA of 90°, during 2007-2011, and the NO ₂ data from OMI instrument.	104
Figure 5.23- Correlation of SPATRAM NO ₂ data (average between AM and PM values) retrieved at Évora Observatory for the SZA of 90°, during 2007-2011, and the NO ₂ data from the SCIAMACHY instrument.	104
Figure 5.24- Correlation of SPATRAM NO ₂ data (average between AM and PM values) retrieved at Évora Observatory for the SZA of 90°, during 2007-2011, and the NO ₂ data from the GOME-2 instrument.	105
Figure 5.25- Correlation of SPATRAM NO ₂ data (average between AM and PM values) retrieved at Évora Observatory for the SZA of 90°, during 2007-2011, and the NO ₂ data from the OMI instrument.....	105
Figure 5.26 -Time series of the BrO VCD obtained with the SPATRAM equipment for the SZA of 90°, a) for morning (AM) and afternoon (PM) and averaged values for the period 23 January – 2 August 2008 at Évora Observatory and the polynomial fit.....	106
Figure 5.27- Time series of the BrO VCD obtained with the SPATRAM equipment installed at Évora Observatory for the SZA of 90°, for morning (AM) and afternoon (PM), for the period 23 January – 2 August 2008, and the BrO total columns measured with the OMI equipment.....	107
Figure 5.28- Correlation of SPATRAM BrO data retrieved at Évora Observatory for the SZA of 90°, during 2007-2011, and the BrO data from the OMI instrument... ..	108
Figure 5.29- Time series (all dataset) of the BrO VCD averaged values from morning (AM) and afternoon (PM) obtained with the SPATRAM equipment installed at Évora Observatory for the SZA of 90° for the period 23 January – 2 August 2008, and the BrO total columns measured with the OMI equipment.....	109
Figure 5.30- Correlation of SPATRAM BrO VCD averaged AM and PM datasets retrieved at Évora Observatory for the SZA of 90°, during 2007-2011, and the BrO data from the OMI instrument.....	109
Figure 5.31- Time series (filtered dataset) of the BrO VCD averaged values from morning (AM) and afternoon (PM) obtained with the SPATRAM equipment installed at Évora Observatory for the SZA of 90° for the period 23 January – 2 August 2008, and the BrO total columns measured with the OMI equipment.	110
Figure 5.32- Correlation of SPATRAM BrO VCD averaged AM and PM and filtered datasets retrieved at Évora Observatory for the SZA of 90°, during 2007-2011, and the BrO data from the OMI instrument.....	111
Figure 5.33- Time series of the BrO VCD obtained with the SPATRAM equipment installed at Évora Observatory for the SZA of 90°, for morning (AM) and afternoon (PM), for the period 23 January – 2 August 2008, and the BrO total columns measured with the GOME-2 equipment.....	112
Figure 5.34- Time series (all dataset) of the BrO VCD averaged values from morning (AM) and afternoon (PM) obtained with the SPATRAM equipment installed at Évora Observatory for	

the SZA of 90° for the period 23 January – 2 August 2008, and the BrO total columns measured with the OMI equipment.....	113
Figure 5.35- Correlation of SPATRAM BrO VCD AM and PM datasets retrieved at Évora Observatory for the SZA of 90°, during 23 January – 2 August 2008, and the BrO data from the GOME-2 instrument.....	114
Figure 5.36- Correlation of SPATRAM BrO VCD averaged AM and PM datasets retrieved at Évora Observatory for the SZA of 90°, during 23 January – 2 August 2008, and the BrO data from the GOME-2 instrument.....	114
Figure 5.37- NO ₂ SCDs during 30 th March 2009 for a zenith elevation of 88° along the a) West, b) East, c) North and d) South azimuthal direction.....	115
Figure 5.38- NO ₂ vertical profiles for 8 th April 2009 retrieved a) East b) North azimuthal direction with an horizontal visibility of 30 km.....	117
Figure 5.39- NO ₂ vertical profiles for 9 th April 2009 retrieved a) East b) North azimuthal direction with an horizontal visibility of 30 km.....	118
Figure 5.40- NO ₂ stratospheric vertical profiles for May of 2010 retrieved with SPATRAM at Évora Observatory.....	119
Figure 5.41- NO ₂ stratospheric vertical profiles for June- August of 2010 retrieved with SPATRAM at Évora Observatory.....	120
Figure 5.42- NO ₂ stratospheric vertical profiles for September and October of 2010 retrieved with SPATRAM at Évora Observatory.....	120
Figure 5.43- NO ₂ stratospheric vertical profiles for some days of May 2010, comprising the minimum values, maximum values and the averaged values retrieved with SPATRAM instrument and comparison with SCIAMACHY datasets from Max Plank Institute Mainz (SCIAMACHY MPI) and the Institute of Environmental Physics (IUP/IFE) of University of Bremen (SCIAMACHY Bremen).	122
Figure 5.44- NO ₂ stratospheric vertical profiles for some days of June, July and August 2010, comprising the minimum values, maximum values and the averaged values retrieved with SPATRAM instrument and comparison with SCIAMACHY datasets from Max Plank Institute Mainz (SCIAMACHY MPI) and the Institute of Environmental Physics (IUP/IFE) of University of Bremen (SCIAMACHY Bremen).	122
Figure 5.45- NO ₂ stratospheric vertical profiles for some days of September and October of 2010, comprising the minimum values, maximum values and the averaged values retrieved with SPATRAM instrument and comparison with SCIAMACHY datasets from Max Plank Institute Mainz (SCIAMACHY MPI) and the Institute of Environmental Physics (IUP/IFE) of University of Bremen (SCIAMACHY Bremen).	123
Figure 5.46 a) The NO ₂ Slant Column Densities (SDC) daily variation during 11 th May of 2010 retrieved by SPATRAM at Évora. b) The HYSPLIT back-trajectories for the 11 th May of 2010 at the heights of 1000, 3000 and 5000 m (at http://ready.arl.noaa.gov/hysplit-bin/trajtype.pl?runtype=archive).....	126
Figure 5.47- Location of the potential pollution sources (Setúbal, Barreiro, Seixal, Lisboa, Amadora) detected by the combination of SPATRAM data and HYSPLIT back-trajectories for the 11 th May of 2010 at the heights of 1000, 3000 and 5000 m- at www.maps.google.com	127
Figure 5.48 - Number of pollution events registered at Évora's Observatory in 2010 with the potential sources located in Portugal.	127

Figure 5.49- The NO ₂ Slant column densities (SDC) daily variation during 12 th June of 2010 retrieved by SPATRAM at Évora.....	128
Figure 5.50 - The HYSPLIT back-trajectories for the 12 th June of 2010 (ending at 13 UTC) at the heights of 1000, 3000 and 5000 m (at http://ready.arl.noaa.gov/hysplit- bin/trajtype.pl?runtype=archive).....	128
Figure 5.51- The NO ₂ Slant column densities (SDC) daily variation during the 2 nd of March 2010 retrieved by SPATRAM at Évora.....	129
Figure 5.52- The HYSPLIT back-trajectories for the 2 nd March of 2010 (ending at 17 UTC) at the heights of 10000, 15000 and 25000 m (at http://ready.arl.noaa.gov/hysplit- bin/trajtype.pl?runtype=archive).	129
Figure 5.53- The HYSPLIT back-trajectories for the 2 nd March of 2010 at the heights of 1000, 3000 and 5000 m (at http://ready.arl.noaa.gov/hysplit-bin/trajtype.pl?runtype=archive).	130
Figure 5.54- Number of pollution events registered at Évora’s Observatory in 2010 with the potential sources located in Spain.	130
Figure 5.55- Histogram that illustrated the quantity of NO ₂ detected in Évora in µg/m ³ with the SPATRAM instrument for each pollution event, for the 115 events recorded at Évora Station.	131

List of Tables

Table 2.1 - Permanent gases in atmosphere and their mixing ration volume in dry unpolluted air (adapted from Brasseur et al. 1999).	7
Table 2.2 - Trace gases in atmosphere and their mixing ration volume in dry unpolluted air (adapted from Brasseur et al., 1999).	8
Table 2.3 - Tropospheric major sources, mixing ratios in clean atmosphere, major sinks and atmospheric lifetime of some nitrogen, sulphur, carbon, nitrogen and halogen atmospheric compound species (adapted from Brasseur & Solomon, 2005; Platt & Stutz, 2008).	13
Table 3.1 - Wavelengths of absorption in the UV- Visible range by several atmospheric gases (adapted from Jacobson, 1999).	38
Table 4.1 - Observable species detected with SPATRAM and their respective spectral range and ID and optical	60
Table 5.1- O ₃ total columns maximums and minimums values obtained with SPATRAM \pm 1 standard deviation from OMI- DOAS for the period 2007-2011 over Évora-Portugal.....	88
Table 5.2 - Correlation analysis of SPATRAM, OMI (TOMS), OMI (DOAS), GOME and SCIAMACHY total ozone data for the period of 2007-2011.	94
Table 5.3- NO ₂ total columns maximums and minimums values obtained with SPATRAM \pm 1 standard deviation from SCIAMACHY for the period 2007-2011 over Évora-Portugal.	101
Table 5.4- Correlation analysis of SPATRAM, OMI, GOME-2 and SCIAMACHY total nitrogen dioxide data for the period of 2007-2011.	106
Table 5.5- Correlation analysis of SPATRAM (averages AM and PM values) and OMI total BrO data for the period of 23 January- 2 August 2008 for dataset 1, dataset 2 and dataset 3.....	114

“Aperfeiçoamento de algoritmos para avaliação da qualidade do ar e da composição atmosférica a partir de medidas de radiâncias espectrais”

Resumo

O principal objetivo deste trabalho consiste na aplicação e aperfeiçoamento de algoritmos numéricos para a inversão de medidas espectrais feitas com um instrumento de deteção remota instalado no Observatório do Centro de Geofísica de Évora (38.6ºN, 7.9ºW, 300 a.s.l.). Os algoritmos explorados são os seguintes: i) metodologia DOAS para a determinação da concentração média de compostos atmosféricos ao longo do caminho ótico, ii) duas diferentes abordagens ao algoritmo de inversão de Chahine que consiste num método iterativo para a obtenção dos perfis dos constituintes atmosféricos minoritários usando o output da técnica espectral. Os resultados obtidos permitiram a avaliação dos ciclos diurnos e sazonais e de variações anuais das colunas totais de ozono, dióxido de azoto e de óxido de bromo, dos perfis verticais de dióxido de azoto e informação acerca de massas de ar poluídas no período compreendido entre 2007-2011. As quantidades obtidas são comparadas/validadas com os respectivos resultados obtidos com instrumentos instalados em satélites.

“Improvement of algorithms for the assessment of air quality and atmospheric composition from observations of spectral radiances”

Abstract

The central part of this work is the application and improvement of numerical algorithms for the inversion of spectral measurements carried out with a remote sensing instrument, installed at the Geophysics Centre of Évora’s Observatory (38.6ºN, 7.9ºW, 300 a.s.l.). The exploited algorithms are: i) the Differential Optical Absorption Spectroscopy method, for the determination of the mean concentration of an atmospheric compound along an optical path; ii) two different approaches to the Chahine inversion algorithm that is an iterative method for profile retrieval of atmospheric tracers using the output of the spectroscopic technique. The obtained results allow for the assessment of diurnal cycles, seasonal and inter-annual variations for the total columns of ozone, nitrogen dioxide and bromine oxide, the atmospheric profiles of nitrogen dioxide and information about nitrogenous air masses transported over Évora for the period 2007-2011. In addition, the retrieved quantities are compared/ validated with analogous results obtained with satellite borne instruments.

Extended Abstract

The atmospheric composition and structure play a key role on the climate system. Atmospheric tracers and aerosols affect climate by altering incoming solar radiation and out-going infrared radiation that are part of Earth's energy balance. Since the start of the industrial era, the overall effect of human activities on climate has been a warming influence. The human impact on climate during this era greatly exceeds that due to known changes in natural processes, such as solar changes and volcanic eruptions. In this frame, this PhD work tries to clarify the present atmospheric composition, the modifications occurred in the last centuries in our climate system and the main role played by the gaseous atmospheric tracers (ozone, nitrogen and bromine oxides) with the presentation of their main chemical cycles in the atmosphere. Moreover, the central part of this work is the application and improvement of numerical algorithms for the inversion of spectral measurements carried out with the SPATRAM (SPectrometer for Atmospheric TRacers Monitoring) remote sensing instrument, installed at Geophysics Centre of Évora - University of Évora (CGE-UE) (38.6° N, 7.9 W, 300 a.s.l.) in the south of Portugal since 2004. The exploited algorithms are: i) the DOAS (Differential Optical Absorption Spectroscopy) method, for the determination of the mean concentration of an atmospheric compound along an optical path; ii) two different approaches to the Chahine inversion algorithm that is an iterative method for profile retrieval of atmospheric tracers using the output of the DOAS technique. The obtained results allow for the assessment of diurnal cycles, seasonal and inter-annual variations for the total columns and atmospheric profiles of ozone, nitrogen and bromine oxides. In addition, the retrieved quantities are compared/validated with analogous results obtained with satellite borne instruments. The analysis is performed for the period 2007-2011. This study also provides information about nitrogenous air masses transported over Évora, in 2010. The joint action of the SPATRAM data and HYSPLIT (HYbrid Single-Particle Lagrangian Integrated Trajectory) maps, allowed for the identification of possible sources responsible for the pollution events recorded at the city.

Acronyms

AERONET = AERosol RObotic NETwork
AMEFCO = Atmospheric MOdel for Enhancement Factor COmputation
AMF = Air Mass Factor
APA = Agência Portuguesa do Ambiente
BASCOE = Belgian Assimilation System of Chemical Observations from ENVISAT
BIRA- IASB = Belgian Institute for Space Aeronomy
BL = Boundary Layer
CCD = Charged Coupled Device
CFC = Chlorofluorocarbons
CGE-UE = Geophysics Centre of Évora – University of Évora
DAS = Data Acquisition System
DLR = German Aerospace Centre
DOAS = Differential Optical Absorption Spectroscopy
DSCD = Differential Slant Column Density
DU = Dobson Unit
ECU = Electronic Control Unit
ENEA = Italian National Agency for New Technology, Energy and Environment
ENVISAT = ENVironmental SATellite
EOS = Earth Observing System
ERS-2 = European Remote Sensing 2
EUMETSAT = European Organisation for the Exploitation of Meteorological Satellites
FI = Flux Index
FFT = Fast Fourier Transform
FSSD = Fair Spacing of the Spectral Data
FOP = Free Optical Path
FRESCO = Fast retrieval scheme for clouds from the oxygen A-band
GAW = Global Atmosphere Watch
GOME = Global Ozone MONitoring Experiment
GOME-2 = Global Ozone MONitoring Experiment 2
HYSPLIT = HYbrid Single-Particle Lagrangian Integrated Trajectory
IR = Infrared
INTA = Atmospheric Sounding Station of the Spanish Institute for Aerospace Technology
ISAC-CNR = Institute of Atmospheric Sciences and Climate of the Italian National Research Council
IPMA = Instituto Português do Mar e da Atmosfera
IUP = Institute of Environment Physics
IWOP = Intensity Weighted Optical Path
LIDAR = Light Detection and Ranging
LOS = Line Of Sights
MC = Monte Carlo

METEOP-A= Meteorological operational satellite A
MIGE = Multiple Input Geometry Equipment
MODTRAN = MODerate resolution TRANSmittance
NASA= National Aeronautics and Space Administration's Earth
NH = Northern Hemisphere
NMHC = Non Methan Hydrocarbons
OEM = Optimal Estimation Method
OMs = Ozone Mini-holes
OMI = Ozone Monitoring Instrument
OMU= Optical Mechanical Unit
OPM = Optical Path of Measurements
PAN = Peroxyacetyl Nitrate
PBL= Planetary Boundary Layer
PSC= Polar Stratospheric Clouds
RADAR= RAdio Detection and Ranging
RHS= Reactive Halogen Species
RTM = Radiative Transfer Model
SAGE = Stratospheric Aerosol and Gas Experiments
SCIAMACHY = Scanning Imaging Absorption Spectrometer for Atmospheric Chartography
SPATRAM= SPectrometer for Atmospheric Tracers MOnitoring
SC= Slant Column
SH = Southern Hemisphere
SL = Sea Level
SOS = Sum Of Squares
SPT = Standard Temperature and Pressure
SPE = Solar Proton Events
SST = Total Sum of Squares
SSR = Regression Sum of Squares
SVD = Singular Value Decomposition
SZA = Solar Zenith Angle
TC= Total Column
TOA = Top of the Atmosphere
TOC = Total Ozone Columns
TOMS = Total Ozone Mapping Spectrometer
UV= Ultraviolet
VC= Vertical Column
VCD = Vertical Column Density
VSA = Var Slant Absorber
VOC = Volatile Organic Compound
WMO = World Meteorological Organization
WOUDC = World Ozone and Ultraviolet Radiation Data Centre

List of principal symbols

$\varepsilon_a(\lambda)$	absorption coefficient (m^{-1})
$\varepsilon_s(\lambda)$	scattering coefficient (m^1)
$\sigma_a(\lambda)$	absorption cross section of the absorbing molecule/atom (m^2)
σ_g	absorption cross section of the gas (m^2)
$\sigma_s(\lambda)$	scattering cross section of the molecule/particles (m^2)
σ_R	Rayleigh scattering coefficient (m^2)
χ_λ	mass extinction cross section for radiation of wavelength λ (m^2 / kg)
τ_λ	monochromatic optical thickness (-)
n	number of absorbers (atoms) per unit of volume (m^{-3})
S	scattering function (-)
C	number of molecules by unit volume (<i>molecules</i> / m^3)
θ	solar zenith angle ($^\circ$)
θ_{min}	solar zenith angle reached at the local noon ($^\circ$)
ΔS_{mul}	mean photon path into the l^{th} layer (cm)
ρ	density of the material (kg / m^3)
ρ_g	gas concentration (<i>molecules</i> / cm^3)
ρ_a	density of the air in the i shell (<i>molecules</i> / cm^3)
N	refractive index (-)
I_λ	intensity of the incident radiation ($W.m^{-2}.sr^{-1}.\mu m^{-1}$)
J_λ	monochromatic source function ($W.m^{-2}.sr^{-1}.\mu m^{-1}$)
I_{λ, S_1}	intensity of monochromatic light that crosses the atmospheric path ($W.m^{-2}.sr^{-1}.\mu m^{-1}$)
$I_0(\lambda, \theta_{min})$	reference spectrum obtained at local noon ($W.m^{-2}.sr^{-1}.\mu m^{-1}$)
$I_s(\lambda, \theta)$	spectrum measured for different condition of SZA ($W.m^{-2}.sr^{-1}.\mu m^{-1}$)
$I_0(\lambda)$	intensity of the radiation at TOA ($W.m^{-2}.sr^{-1}.\mu m^{-1}$)
M	air mean molar mass (0.02897 kg/mol)
g	acceleration of gravity (9.8 m/s ²)
E	Energy of a photon (J)

hPlanck's constant ($6.6236176 \times 10^{-34}$ Js)

cvelocity of light in vacuum (2.9979×10^8 m/s²)

λ wavelength (m)

1. Introduction

1.1 State of the art

During the last two centuries the composition of atmosphere has undergone dramatic changes due mainly to the role of human activities (Valks, 2003; IPCC, 2007; WMO, 2003; IPCC, 2013). The main causes for these variations may be identified as the quasi-exponential growth in population that impelled the development of industrialization and energy production, the intensification of both terrestrial and air traffic, the agriculture practices (that include the use of fertilizers and biomass burning) that contribute to the degradation of the air quality on a global scale. The emission of trace gases like nitrogen oxides (NO_x), methane (CH_4), chlorofluorocarbons (CFC's), carbon dioxide (CO_2), carbon monoxide (CO), sulphur dioxide (SO_2) and other hydrocarbons compounds resulted in several environmental changes mediated through the chemistry of the atmosphere. These changes have direct impact on the environment and currently we are facing their consequences. Some of these changes include (IPCC 2007; WMO, 2003; Brasseur et al., 1999):

- the rising in global mean temperature (enhancement of the greenhouse effect) resulting from increasing emissions of CO_2 and other greenhouse gases,
- global increase of atmospheric pollution,
- the increasing of the concentration of tropospheric oxidants and impacts on the biosphere and human health,
- depletion on the stratospheric ozone over Antarctica during austral spring and ozone mini-holes at the mid-latitudes that cause an increase in UV-B radiation and impacts on living species,
- occurrence of acid precipitation and their impact on the biosphere,
- changes in the self-cleaning capability of the atmosphere and in the residence time of anthropogenic trace gases,
- land use and its impact in environment,
- perturbations of the biogeochemical cycles.

By the mid-1990s the attention of the world community has become focused on new range of global environmental problems. Maybe triggered by the discover of "Ozone Hole" in Antarctica

in 1985, the human community in general become more conscious of environmental questions that started to arise like the climate change and (at the time) possible global warming. With the beginning of the twenty-first century the awareness of these problems by the majority of people, leads to the concerning about quality of life. The increasing interest on the study of those problems is related mainly with their adverse effects on health and ecosystems (Zabalza et al., 2007; Zujic et al., 2009).

The rapid acceleration of the concern about those questions led to real advances in related technologies for the acquisition and processing of environmental data in “real or near real-time”, even from remote locations. This progress provides the assessment of data related to the atmosphere and climate, like trace gases and aerosol concentration and clouds, besides the dynamic and meteorological information of the atmosphere (Laj et al. 2009). Nowadays the monitoring of the atmosphere is carried on by means of ‘in-situ’ and Remote Sensing (RS) measurements obtained from ground-based instruments, balloons, airborne or satellite based equipments. The data-sets acquired with all these instruments and sensors enable the monitoring of the atmosphere and can be kept for present and future prospect studies. In a so complex system as the Earth’s Atmosphere compared by Seinfeld et Pandis, 2006 “to an enormous chemical reactor in which a myriad of species are continually being introduced and removed over a vast array of spatial and temporal scales” the need of short and long term observations are evident since atmospheric processes are still far from being entirely understood.

In 1924, Gordon Dobson (25 February 1889 - 11 March 1976) developed the first instrument that allowed for the measurements of atmospheric total ozone: the Dobson Spectrophotometer. Dobson is globally recognized as a great scientist not only for the invention of the equipment with his name, but also for the idea he had to establish a network of these kind of instruments. During the winter of 1925/26 he built the equipment that was installed at the Arosa observatory (Switzerland) known for more than 80 years of continuously measurements. Nowadays a network of about 90 Dobson Spectrometers are spread all over the world taking trust worthy measurements for the WMO's global ozone observing network run as part of the Global Atmosphere Watch (GAW). Currently, other ground based spectrometers fully automatic are operating around the world (Meena, 2009) and the reference instrument for ozone measurements is the Brewer spectrometer that basically is the automated version of the Dobson equipment.

With the development of Dobson’s spectrometer the atmospheric inverse problems emerge consequently. At the beginning, the measurements made by Dobson were based on the absorption of solar UV light and he was able to retrieve O₃ total column contents. Approximately

10 years later, Götz realized that it was possible to obtain the vertical distribution of that gas by measuring the Rayleigh scattered sunlight from the zenith sky with the same spectrometer. It was the first stone on the development of the so-called Umkehr method (from the German reversal method) (Mateer, 1964) for which several scientists contributed for with a huge success. Nevertheless, in the last years, with the appearance of large computers, the launching of earth orbiting satellites observing the atmosphere from outside, the development of new instruments and the improvements of remote sensing techniques the inversion problems received more attention (Twomey, 1996). One of the first efforts to determine the vertical distribution of the temperature in the atmosphere was proposed by Kaplan using satellites as a function of wavelength and later developed by Wark and Yamamoto (Ferral, 2011). In the beginning of atmospheric satellite era the vertical profiles of several gases and aerosols began to be retrieved using the Stratospheric Aerosol and Gas Experiments (SAGE). Several instruments onboard satellites followed such as Global Ozone Monitoring Experiment (GOME), SCanning Imaging Absorption spectroMeter for Atmospheric CHartography (SCIAMACHY) and Ozone Monitoring Instrument (OMI) using inverse methods for the same purpose.

This work is inserted in the thematic of climate change as well as of air quality since through the monitoring of trace constituents in the entire atmospheric column it is possible to infer the temporal series of total columns and vertical profiles of trace gases and their changes for a chosen temporal period.

Trace gases are known for their minor concentrations in the atmosphere, but their major role in it. This work is focused on the monitoring of ozone and nitrogen dioxide, which are key species in both stratospheric and tropospheric chemistry. The observations are performed with a UV-VIS ground based spectrometer known as SPATRAM (SPectrometer for ATmospheric TRAcers Monitoring).

1.2 Motivation

The main motivations for conducting this work were:

- the importance of monitoring the trace compounds in the atmosphere;
- the lack of atmospheric chemistry measurements in the south of Portugal and the need for such measurements taken automatically on a routine basis;
- the inexistence of long term studies of total atmospheric column and vertical profiles of NO_2 and O_3 , using ground based spectrometers in Portugal. There are several studies focusing the air quality monitoring in urban areas conducted by researchers of the University of Aveiro and University of Porto. The published studies are centered in the

in-situ monitoring of trace gases at the surface, such as tropospheric O₃, NO₂, Volatile Organic Compounds (VOCs) and Particulate Matter (PM) (Mendes et al., 2008; Alvim-Ferraz et al., 2005; Monteiro et al., 2007; Evtugina et al., 2006) and in the direct relation with human health impacts (Sousa et al. 2009; Sousa et al., 2008).

- the improvement and use of the SPATRAM equipment. In Portugal there are only available 2 Brewer spectrophotometers installed in Funchal (Madeira Island) and in Angra do Heroísmo (Azores islands) and a Dobson spectrometer which is deactivated at the moment. Their data are available at the World Ozone and Ultraviolet Radiation Data Centre (WOUDC) platform (http://www.woudc.org/data/MetaQuery/metaquery_e.cfm) but just until 2003. The Ozone profiles are only taken by the Instituto Português do Mar e da Atmosfera (IPMA) with balloons sondes. The Agência Portuguesa do Ambiente (APA) also supplies the NO₂ and O₃ measurements but only at the surface (available at <http://qualar.apambiente.pt/>).
- the fact that Portugal is one of the regions of the European countries with the highest insolation which is a key quantity relevant in the tracers photo-chemistry;
- the fact that the south of Portugal presents clear sky conditions for early spring to autumn which favours the frequent observations using RS instruments.

1.3 Objectives

The main objectives of this work are addressed to the improvements of the algorithms utilized to invert the spectral measurements of the SPATRAM instrument aiming to increase the accuracy and the confidence in the retrieval of:

- total column concentrations of NO₂, O₃ and BrO and comparison with satellite data,
- vertical profiles of stratospheric NO₂ (from 10- 50 km), with a vertical resolution of 2.5 km,
- vertical profiles of tropospheric NO₂ (from the ground till to 2 km of altitude), with a vertical resolution of 250-300 m ,

over Évora - Portugal (38.6°N, 7.9°W, 300 m a.s.l.) for the period comprised between 2007-2011. Furthermore, the synergy between the SPATRAM observations and a dynamical model allowed for the identification of anthropogenic pollution events in the city due to air mass circulation from sites with high pollution loads.

1.4 Thesis structure

This thesis is divided in 6 chapters.

The present composition and structure of the atmosphere is described briefly in chapter 2. In the same section the basic principles of the atmospheric chemistry for ozone, nitrogen dioxide and bromine oxide are presented. Some key aspects of the role of these compounds in the atmospheric processes and some chemical cycles (in particular for ozone) are described.

In chapter 3 a brief description of the absorption and scattering processes in atmosphere is presented giving emphasis to the interactions of the gaseous compounds with the solar radiation in UV-VIS bands.

The overview of the remote sensing techniques is given in the first section of chapter 4, followed by the descriptions of the ground-based spectrometer (SPATRAM) and of the satellite borne equipment's (OMI, SCIAMACHY, GOME, GOME-2) used in this work. The last sections of chapter 4 deal with the spectroscopic technique (DOAS – Differential Optical Absorption Spectroscopy) for the retrieval of the mean content of trace gases along an optical path (SCD – Slant Column Density) from the spectral radiation measurements carried out with the ground based instrument. The DOAS-Master-Equation is derived and the radiative transfer models for the interpretation of the outputs of the DOAS algorithms are presented. Also the inversion methods for the retrieval of the vertical profiles for the studied trace gas using the SCDs values and the output of the radiative transfer models are presented and explained in detail.

The results of this study are presented in chapter 5 in terms of trace gases (O_3 , NO_2 and BrO) variability, air quality monitoring, and vertical distribution of NO_2 . In addition, comparisons of the ground-based results with data obtained with similar satellite borne equipment are shown and discussed. The outlook is presented in chapter 6 as well the future work that can be developed in this field.

2. Chemistry of atmosphere: the role of ozone and nitrogen dioxide

2.1 Introduction

The terrestrial atmosphere is a thin layer of gases that surrounds the planet and separates Earth's surface from space. The atmosphere has several roles in order to support life like the maintenance of temperature, the protection of the earth's surface from radiation, the removal of some oxidant gaseous compounds and the redistribution of heat and water. This chapter presents some aspects of atmospheric dynamics and composition giving emphasis to the role and to the chemistry of ozone and of nitrogen dioxide in the troposphere and stratosphere.

2.2 Atmospheric composition and structure

2.2.1 Atmospheric composition

Presently the Earth's atmosphere is composed by a mixture of gases, water vapour and aerosols. The most abundant species in atmosphere are nitrogen (N₂), and oxygen (O₂). These gases as well as noble gases like Argon (Ar), Néon (Ne), Helium (He), Krypton (Kr) and Xenon (Xe) represent permanent gases which are characterized by their almost constant mixing ratios in time and space over short time scales. Most of these gases are situated in a region under 100 km called homosphere. Table 2.1 presents the permanent constituents of dry "unpolluted" air and their mixing ratios in the atmosphere.

Table 2.1 - Permanent gases in atmosphere and their mixing ration volume in dry unpolluted air (adapted from Brasseur et al., 1999).

Constituent	Symbol	Volume Mixing ratio(VMR)	
		VMR	VMR in ppmv
Nitrogen	N ₂	0.7808	780.0
Oxygen	O ₂	0.2095	209.5
Argon	Ar	9.300 x10 ⁻³	9.300
Neon	Ne	18.18 x10 ⁻⁶	18.18
Helium	He	5.240 x10 ⁻⁶	5.240
Krypton	Kr	1.100 x10 ⁻⁶	1.100
Xenon	Xe	0.9000 x10 ⁻⁶	0.9000

The minor part of the atmosphere is composed by several other substances called trace gases. Despite their low concentration in atmosphere they have a very high impact in atmospheric chemistry and climate. Their mixing ratios vary in time and space, although they constitute only ~0.04 % by volume of the atmosphere. For example, trace gases have significant roles in the transmission of solar and terrestrial radiation and in biogeochemical cycles that restrict the atmospheric lifetime of other gases.

Table 2.2 summarizes the volume mixing ratios of trace gases in atmosphere.

Table 2.2 - Trace gases in atmosphere and their mixing ration volume in dry unpolluted air (adapted from Brasseur et al., 1999).

Constituent	Chemical formula	Volume Mixing ratio
Carbon dioxide	CO ₂	360 ppmv
Methane	CH ₄	1.7 ppmv
Hydrogen	H ₂	0.55 ppmv
Nitrous oxide	N ₂ O	0.31 ppmv
Carbon monoxide	CO	50-200 ppbv
Ozone (troposphere)	O ₃	10-500 ppbv
Ozone (stratosphere)	O ₃	0.5-10 ppm
VOC which include non-methane hydrocarbons (NMHC) and oxygenated NMHC (e.g. alcohols, aldehydes and organic acids)	Isoprene, terpene, C ₂ H ₆ , C ₃ H ₈ , C ₄ H ₁₀ , C ₂ H ₄ , C ₃ H ₆ , C ₂ H ₂ , benzene (C ₆ H ₆), toluene (C ₇ H ₈)	5-20 ppbv
Halocarbons	CFC's	3.8 ppbv
Nitrogen species	NO _y (= NO, NO ₂ ,...)	10 ppt - 1 ppm
Ammonia	NH ₃	10 ppt- 1 ppb
Hydroxyl	OH	0.1 ppt- 10 ppt
Sulphur dioxide	SO ₂	10 ppt- 1 ppb

Figure 2.1 shows a close distribution of the mixing ratio of some atmospheric constituents depending on the altitude. In that figure the N₂ and the noble gases are not represented (with the exception of Argon). The N₂ mixing ratio distribution function should be similar to O₂ profile but starting at sea level with a value of ~0.78.

Other important atmospheric constituents are aerosols which are small particles of liquid or solid matter dispersed and suspended in air as for example, water droplets, dust or soot particles. Their sizes range from 0.001 to 1000 μm. The major aerosol species in the atmosphere are nitrate, sulphate, black carbon, organic carbon, sea salt and mineral dust. Aerosols have many roles in the atmospheric chemistry like interactions with radiation and cloud condensation nuclei.

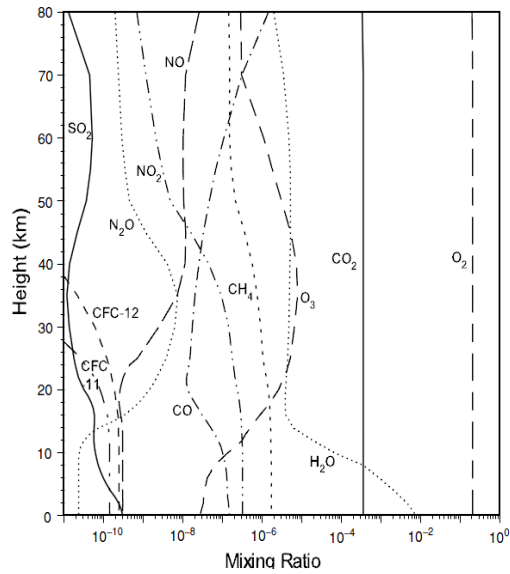


Figure 2.1 - Typical vertical distribution of the concentration of chemical atmospheric constituents under about 120 km (from Liou, 2002.)

2.2.2 Atmospheric vertical structure

The thermal structure of the atmosphere, up to approximately 120 km, can be divided in four layers characterized by different vertical temperature gradients: troposphere, stratosphere, mesosphere and thermosphere (Fig.2.2). The regions are separated by boundaries called pauses: tropopause, stratopause and mesopause, respectively.

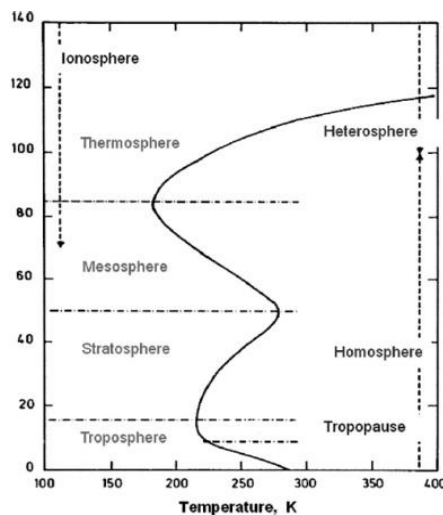


Figure 2.2- Temperature variation in Earth's atmosphere (from Platt & Stutz, 2008).

The troposphere is the first layer which extends from the surface up to about 6-8 km near the poles, 12 km at mid-latitudes and to 18 km at the equator, depending on the water vapour content present in this layer. The troposphere can be sub divided into: i) Planetary Boundary

Layer (PBL) which extends from surface till 1-2 km (depending on the time of the day and meteorological conditions); ii) the free troposphere located between the PBL and the tropopause. The troposphere contains about 85-90% of the atmospheric mass and its temperature profile is mainly explained by the adiabatic expansion and compression of respectively rising and sinking air masses, driven by solar radiation. In this layer occurs all the meteorological phenomena (like rain, snow and wind formation) which are a result of its negative temperature gradient (-5 to -10°C/km) that originates a region of convective and turbulent mixing. The vertical transport of chemical compounds in the troposphere is controlled by strong vertical mixing (including convection) whereas in the stratosphere this vertical mixing is absent.

The stratosphere is located above the tropopause, which is a layer with a fairly uniform temperature (no change of temperature with altitude) of about 40 km depth, and extends up to 50 km. This level contains 90% of the atmospheric ozone located in a stratum generally referred as “ozone layer” and the vertical temperature is constant till ~20 km and then increases till the stratopause. The absorption of UV radiation by ozone causes temperature rising with altitude in this region. The vertical gases transport in the stratosphere is controlled by the Brewer- Dobson circulation. This circulation was first proposed by Brewer (1949) and Dobson (1956) and consists of a global scale air movement in the stratosphere. This movement is composed by three parts: a) air rises in the tropics from the troposphere into stratosphere b) and then moves poleward in the stratosphere and finally c) descends in both the stratospheric middle and polar latitudes (Forster et al., 2010; Butchart et al., 2006; Roscoe, 2006).

The mesosphere is located between the top of the stratopause and extends till 90 km altitude. In this layer the temperature decreases with height due to similar processes as in the troposphere. In the thermosphere, above the mesopause, the temperature increases to maximum values. Like in stratosphere, there are positive temperature gradients in this layer that indicate that there is a heat source inside the thermosphere which is due to the absorption of the short wavelength solar radiation (UV) by atoms and molecules (mainly oxygen) and by the accumulation of energy and matter resulting from interstellar dust and coronal mass ejection. The pressure and density of air decrease with altitude. The pressure of Earth’s atmosphere obeys the barometric equation (Eq.2.1) and falls exponentially as a function of height as shown in Figure 2.3. At higher altitudes (z), the atmospheric pressure ($p(z)$) varies as follows:

$$p(z) = p_0 e^{-\frac{Mgz}{RT}} \quad (2.1)$$

where M is the air mean molar mass (0.02897 kg mol⁻¹), g is the acceleration of gravity (9.8 ms⁻²), and z_s is the ‘scale height’ of the atmosphere ($\sim 7 \pm 1$ km).

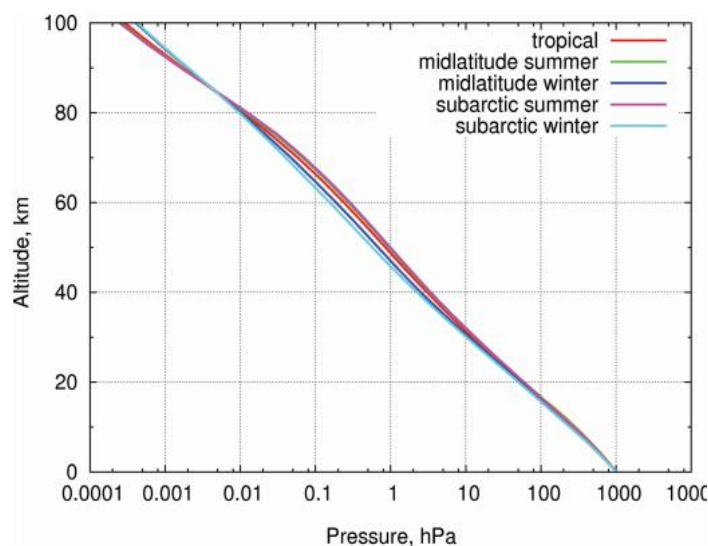


Figure 2.3- Variation of atmospheric pressure in Earth's atmosphere with altitude in the Earth's atmosphere for tropical regions, mid latitudes in summer and winter, and high latitude sub arctic summer and winter (from Burrows et al., 2011).

2.3 Trace gases in the atmosphere

The atmospheric distribution of trace gases is conditioned by atmospheric transport, dispersion, photochemical reactions and physical removal of these gases. As a consequence, the composition of the atmosphere is directly affected by the balance between addition and removal of its components.

Gases are produced by a) chemical processes in the atmosphere, b) biological activity (exchanges with vegetation, biological organisms and ocean), c) volcanic activity, d) radioactive decay, e) human activities. Gases are removed from the atmosphere also by a) chemical processes in the atmosphere and b) biological activity as well as c) physical processes in the atmosphere, d) deposition (wet and dry deposition) and e) uptake by the oceans and land masses.

The lifetime of the species is also an important factor taking into account in the removal of gases from the atmosphere. The lifetime is the time period during which the species stay in atmosphere before their removal. There are species that reside in the atmosphere just a few seconds (e.g. OH) whereas others can last for several years (e.g. CFC's) (Figure 2.4). It is also important to take into account the spatial scales of the atmospheric motions in addition to the removal processes. The atmospheric phenomena can occur in spatial scales varying from 0-100 m (microscale events like urban air pollution), ten to hundreds of kilometres (mesoscale events like land-sea breezes, regional air pollution), hundreds to thousands of kilometres (synoptic scale events like motions of whole weather systems, stratospheric ozone depletion) and large scale events that exceed the 5000 km (global scale/planetary events) (Fig. 2.4).

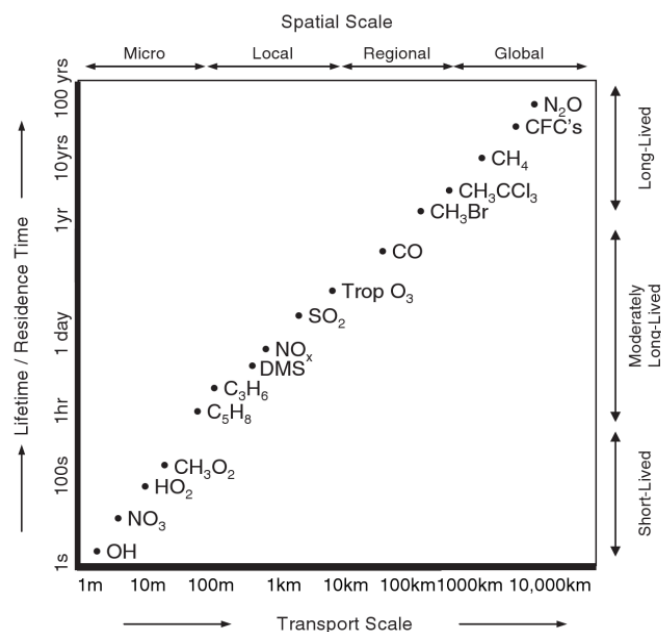


Figure 2.4- Spatial and temporal scales variability of some atmospheric gases (from Platt & Stutz, 2008).

Concerning to air monitoring it is important to acknowledge sources and sinks of the gaseous and particulate components which are emitted to atmosphere. Most of the species considered air pollutants have natural and anthropogenic sources according to the type of sources involved in gaseous emissions. Natural emission of gases includes the following sources: a) volcanic emissions, b) thunderstorms / lightning, c) soil emissions, d) vegetation emissions, e) biomass burning and f) marine emissions. Anthropogenic emissions are directly related to human activity and include: a) industrial processes, b) fossil fuel and biofuel combustion (e.g. traffic related to vehicles exhausts, power plant stations, c) biomass burning (e.g. deforestation, biomass stations VOCs, CO and NO_x), d) agriculture practices (e.g. agricultural land, animals, agricultural waste burning).

The atmospheric traces constituents can be classified according to their chemical composition in small groups: sulphur, nitrogen, carbon and halogen containing compounds. The sources, sinks and lifetimes of the most important trace substances are presented in Table 2.3.

Table 2.3 - Tropospheric major sources, mixing ratios in clean atmosphere, major sinks and atmospheric lifetime of some nitrogen, sulphur, carbon, nitrogen and halogen atmospheric compound species (adapted from Brasseur & Solomon, 2005; Platt & Stutz, 2008).

Gas	Chemical Formula	Mixing Ratios	Major Sources	Major Sinks	Atmospheric lifetime
Nitrogen compounds					
Nitrous oxide	N ₂ O	310 ppb	(Tropical) Soil emission, ocean emission, anthropogenic (mainly from artificial fertilizers and chemical industry)	Loss to stratosphere	110 yr
Nitrogen oxides	NO NO ₂	0.03 - 5 ppb	Fossil fuel combustion, biomass burning, soil emission, microbial production, thunderstorms, aircraft emissions	Oxidation by OH, O ₃ and HNO ₃	~2d
Amonia	NH ₃	~0.1ppb marine ~5 ppb continent	Livestock wastes, emission from vegetation, ocean emission, fertilized soils, modern cars with catalytically converters.	Dry deposition, conversion to NH ₄ ⁺ aerosol.	~5 d
Sulphur compounds					
Sulphur dioxide	SO ₂	0.02-0.09 ppb marine 0.1-5 continent	Fossil fuel burning, volcanoes, sulphide oxidation	Dry deposition, reaction with OH, liquid phase oxidation to SO ₄ ²⁻ =wet deposition	~4 d
Hydrogen sulphide	H ₂ S	0.005-0.09 ppb	Soil emission, vegetation, volcanoes	Reaction with OH	~3 d
Dimethyl sulphide DMS	CH ₃ SCH ₃	0.005-0.1 ppb	Soil and ocean emissions	Reaction with OH, NO ₃ , BrO	~2 d
Carbonyl sulphide	COS	0.5ppb	Soil emission	Uptake by vegetation	7 yr
Carbon containing species					
Carbon dioxide	CO ₂		Combustion, ocean, biosphere		
Methane	CH ₄	1700 ppb	Rice fields, domestic animals, biomass burning, fossil fuel consumptions, swamps	Reaction with OH, export to stratosphere, Soil uptake	~8 yr
Carbon monoxide	CO	200 ppb (N. Hemisphere)	Anthropogenic emission- fossil fuels, biomass burning, CH ₄ and natural VOC oxidation	Reaction with OH, Flux to stratosphere, soil uptake	
VOC alkanes ~40-45%, alkenes ~10%, aromatic hydrocarbons ~20% and oxygenates ~10-15%	Isoprene (C ₅ H ₈) Terpenes (C ₁₀ H ₁₆) etc.	0.6-2.5 ppb 0.03-2 ppb	Emission for deciduous trees Emission for coniferous trees Fossil fuel (emissions from motor vehicles due to either evaporation or incomplete combustion of fuel), biomass burning, foliar and ocean emission	Reaction with OH, ozonolysis	~0.2 d ~0.4 d
Halogens compounds (some examples)					
Chlorofluorocarbons, (CFC) Hydrochlorofluorocarbons(HCFC) Hydrofluorocarbons (HFC)			Anthropogenic (their production is now banned, except for HFC)	-	-
Halons (bromine and fluorine compounds)			Anthropogenic (their production is now banned)	-	-
Methyl chloride	CH ₃ Cl	~550 ppt (Brasseur et al.,1999)	Industrial processes, biomass burning, oceans, wetlands and wood-rot fungi, tropical and subtropical forests (Rhew, 2011)	oxidation by hydroxyl and chlorine radicals as the dominant sink, followed by loss to polar ocean waters and degradation in soils	1 yr (Rhew, 2011)
Methyl bromine	CH ₃ Br	10-15 ppt (Brasseur et al., 1999)	Biological activity in the ocean, emissions from fumigation(soils, quarantine and reshipment), surface oceans, biomass burning, exhaust from automobiles using leaded gasoline combustion, wetlands, brassica crops, and fungus (Cox et al., 2005; Rhew, 2011)	oxidation by hydroxyl radical, followed by chemical and biological degradation in the oceans and biological degradation in soils	0.8yr (Rhew, 2011)
Methyl Iodine	CH ₃ I	~1-10 ppt (Brasseur et al.,1999) ~1-3 ppt and 10-40 ppt (Cox et al., 2005)	Ocean emissions (Voght et al., 1998), biomass burning, rice paddies, soil bacteria (Youcouchi et al., 2008), rice production and peatland/wetland ecosystems (Cox et al.,2005)		3-5 d (Cox et al., 2005)

2.3.1 Ozone and nitrogen oxides chemistry

O₃ and NO_x are key compounds in the chemistry of Earth's Atmosphere since they are involved in several atmospheric phenomena. The next sections present the role of these gases in the atmosphere as well as the chemistry involved in their sources and sinks and in their cycles of formation and destruction.

2.3.1.1 Nitrogen oxides - NO_x

The most important reactive species in the atmosphere composed by nitrogen are: nitrogen atoms (N), nitrous oxide (N₂O), nitrogen oxides (NO_x= NO+NO₂), nitrate radicals (NO₃), dinitrogen pentoxide (N₂O₅), nitric acid (HNO₃), nitrous acid (HONO), peroxyacetic acid (HO₂NO₂), peroxyacyl nitrates (RC(O)O₂NO₂ like for example the peroxyacetyl nitrate (PAN)), organic nitrates (RONO₂), halogen nitrates (XONO₂, X=Cl, Br). These compounds interact, react and interconvert in the atmosphere and therefore affect its chemical composition. The scope of this work is limited to the role of NO_x chemistry that involves some of these compounds.

With respect to nitrogen oxides, often referred as NO_x, they are central compounds in the atmosphere due to their particular characteristics: a) the high reactivity and as consequence a relatively short lifetime and b) the role played in chemical reactions and catalytic cycles involving ozone and hydroxyl radical (OH).

The main motivations for the monitoring and the study of the NO_x compounds are related to their link to ozone and hydroxyl radicals chemistry and the real impacts provoked by the changes in their distribution and concentration, such as (Boersma, 2005; Lammel and Cape, 1996, Lindvall, 1985; WMO, 2003):

- catalytic destruction of ozone by NO_x in the stratosphere,
- photochemical production of ozone by NO_x in the troposphere in polluted or unpolluted atmospheres,
- influence on the photochemical derivative hydroxyl concentrations, therefore NO_x, being a major regulator of the oxidising capacity of the free troposphere by controlling the concentrations of radical species like OH,
- surface acidification and eutrophication by nitrogen deposition,
- effects caused in human health.

The NO_x (in particular NO₂) exposure can cause inflammation on airways, reduce immunity to respiratory infections increasing the susceptibility to respiratory infections. The sensitivity increases for persons with chronic respiratory conditions (e.g. with asthma) and depends on the

time and concentrations to which people are exposed to (WHO, 2011; Ehrlich et al., 1977). NO₂ is also the main source of nitrate aerosols which form an important fraction of PM_{2.5} particulate matter that also have impact on health.

2.3.1.2 Ozone – O₃

Ozone has a dual role in the atmosphere chemistry. While the tropospheric ozone is known as the “bad ozone” for the links to air pollution and for the capacity of unbalance the global climate system, the stratospheric ozone is known for being the “good ozone” for protecting life. The different roles of tropospheric and stratospheric ozone are presented forthwith. The formation mechanisms of tropospheric and stratospheric ozone are different in those atmospheric layers: tropospheric ozone formation is influenced by anthropogenic emissions; stratospheric ozone is formed by natural processes.

Ozone plays an important role in controlling the chemical composition of the atmosphere especially due to the fact that it is a primary source of the hydroxyl radical (OH). Therefore ozone regulates the tropospheric oxidation strength by means of OH formation. The photolysis of ozone near 300 nm followed by reaction with water leads to production of OH. In addition ozone has a negative effect on human health and ecosystems also since it is a strong oxidant. It is a fact that elevated levels of tropospheric ozone are observed in industrialized countries therefore ozone is a well known pollutant, for being a component of smog. This gas is also an important greenhouse gas due to its strong absorption band centered at 9.6 μm (IR) particularly in the upper troposphere (Brasseur et al.1999, Lacis et al., 1990). It is considered one most important greenhouse after water vapour (H₂O) carbon dioxide (CO₂) and methane (CH₄) (Zeng et al., 2008). Because ozone absorbs IR radiation it also plays an important role in the energy budget of the troposphere (Platt & Stutz, 2008; Brasseur et al., 2001) influencing the thermal structure of the atmosphere through long wave absorption. In summary tropospheric ozone is considered poisonous, pollutant to humans, animals and plants and have impact on the thermal structure of the atmosphere.

In the stratosphere ozone has different roles: a) it is responsible for the majority of the absorption of ultraviolet radiation (UVA and UVB) (above 220nm and from 240 to 320 nm, respectively) harmful for animals and plants (Brasseur et al., 1999), b) heating of the middle stratosphere after the absorption of UV-VIS solar radiation playing also a role in the thermal structure of atmosphere by shortwave absorption (Fortuin et Kelder, 1998).

The changes in UV radiation amount reaching Earth surface are not only a result of O₃ depletion, but it is also due to other factors like for e.g. the clouds or forest coverage. Solar UVB radiation

has increased in consequence of stratospheric O₃ depletion. Although UV radiation promotes the syntheses of vitamin D, it can be negative for human health inducing skin cancer (melanoma, non-melanoma skin cancers), eye damages (cataract, pterygium, aged-related macular degeneration, ocular melanoma) and immune system (mechanisms of UV-induced immunosuppression) (Norval et al., 2011). The UV radiation has also effects on materials by accelerating the degradation of plastics, rubber and wood materials (Andrady et al., 2011), and on terrestrial ecosystems. For e.g. UV radiation can also induce changes in leaves that occur at plant level (Ballaré et al., 2011; Aucamp et al. 2011) and in aquatic ecosystems can lead to detrimental of phytoplankton, fish eggs and larvae and zooplankton (Aucamp et al. 2011).

Usually the atmospheric ozone amount is presented as Total Ozone Column (or Vertical Column Density- VCD) and is equal to the amount of ozone contained in a vertical column having a base of 1 cm² at Standard Temperature and Pressure (SPT). Normally this concentration is expressed in Dobson Unit, which is the basic unit used in ozone measurements. One Dobson Unit (DU) is defined to be 0.01 mm thickness at SPT and corresponds to 2.69×10^{16} molecules cm⁻². Other usual units which are used are part per billion (ppb) and $\mu\text{g} / \text{m}^3$.

The global amount of ozone is considered constant. If it would be possible to compress all the ozone present in troposphere and stratosphere all over the world the result would be a layer of ozone approximately with ~3mm. This corresponds to ~300 DU.

The vertical distribution of ozone along the column is not uniform. Although the global amount of ozone is approximately constant, the geographic distribution of this gas depends of several factors. For example the concentration of stratospheric ozone present in the atmosphere depends on the altitude, season, temperature, changes in the stratospheric circulation, eleven year solar cycle, long term climate variability, large volcanic eruptions and Arctic and Antarctic ozone depletion (Harris et al., 2008).

Total ozone varies with latitude, actually the major ozone production occurs in the tropical stratosphere because this region is exposed to a greater intensity of solar radiation (in summer months). However due to the Brewer-Dobson circulation highest values of ozone are found in mid and high-latitudes, since ozone is transported from tropics to poles as a result of the poleward transport of ozone-rich air masses in the stratosphere. So the highest values are found in mid and high-latitudes while the lowest values are found in the tropics, with the exception of the ozone hole phenomenon, as illustrated in Fig. 2.5.

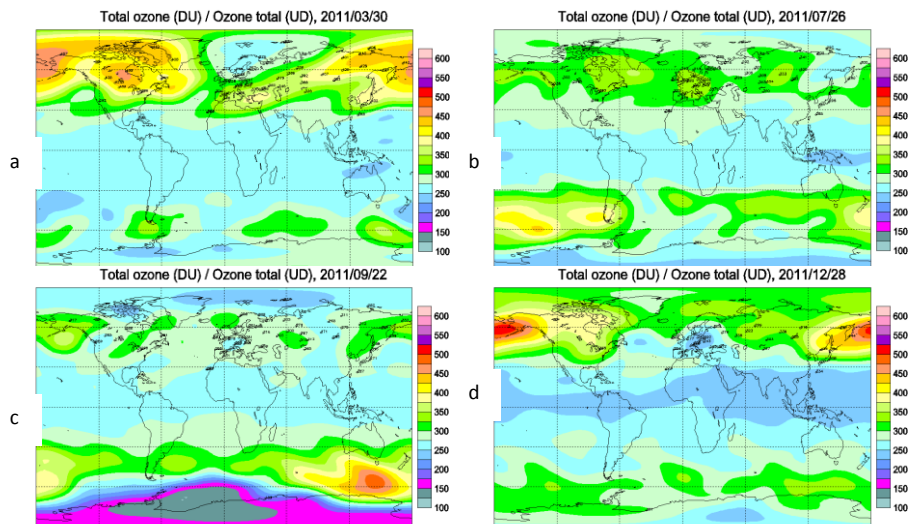


Figure 2.5 - Global distribution of Total Ozone (DU) varying with latitude and time of the year (from http://exp-studies.tor.ec.gc.ca/e/ozone/Curr_map.htm).

Total ozone also varies with season. For mid-latitudes the highest values for ozone are observed during spring and the lowest in the autumn season (Fig. 2.5). During late fall and winter the transport of ozone from tropics toward the polar regions is higher than the same transport made during summer and early fall. As a consequence the maximum values of ozone are found in spring. In the Southern Hemisphere (SH) the values of ozone are overall weaker than the ones registered in the Northern Hemisphere (NH). In the polar regions the situation is different because during the summer (thanks to the period of 24h insolation time) the total ozone column is almost constant; towards the winter months, with the decreasing of the solar radiation the total ozone decreases gradually until its lowest values in late fall.

From the analysis of Fig. 2.6 it is possible to verify that in the Arctic the ozone values increase from the end of the winter till spring, where a maximum is reached, then decreasing again from summer to fall.

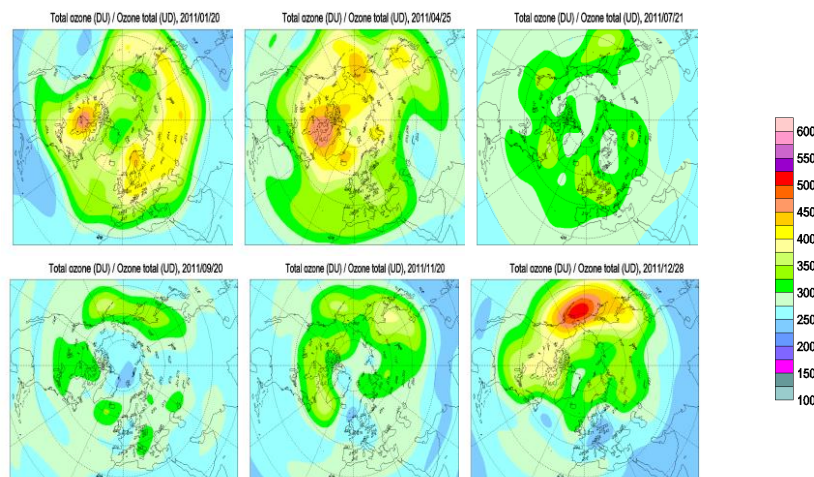


Figure 2.6 - Arctic total ozone (DU) varying with the time of the year from http://exp-studies.tor.ec.gc.ca/e/ozone/Curr_map.htm.

In Antarctica the lowest values are registered in the austral spring as a result of the ozone hole phenomena (Figs. 2.5.c, 2.7). In conclusion ozone has a seasonal behaviour determined by the winter-summer changes in the stratospheric circulation.

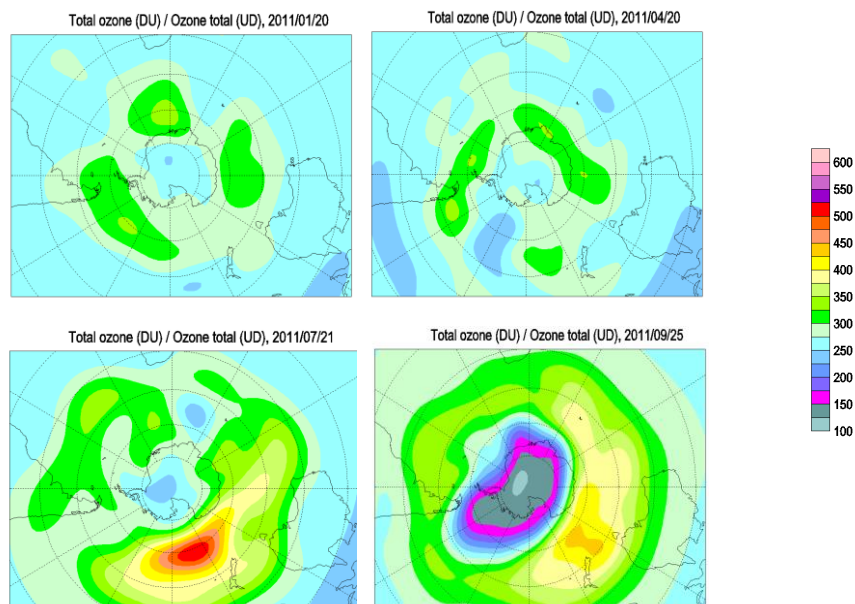


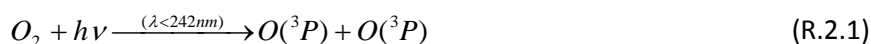
Figure 2.7 - Antarctica total ozone (DU) varying with the time of the year from http://exp-studies.tor.ec.gc.ca/e/ozone/Curr_map.htm.

There is also an inter annual variability in stratospheric ozone amounts since the meteorological conditions and the dynamics in stratosphere and troposphere change each year. These changes can also be linked to the 11-year solar cycle and to the amount of volcanic aerosols reaching the stratosphere (Grainger and Highwood, 2003; Koike et al., 1993; Bien & Zender, 2003; Andreae & Crutzen, 1997; Liao & Seinfeld, 2005). There are also local changes in ozone concentrations originated from the release of anthropogenic pollutants, like for example the ozone depletion in Antarctica (Solomon, 1999) or the occurrence of Ozone Mini-holes (OMs) in mid-latitudes, in both hemispheres on winter and early spring (Antón et al., 2007; Iwao & Hirooka, 2006; Martinez et al., 2011; Krzyscin, 2002). This statement is also valid for tropospheric ozone where its concentration shows a high variability both in space and time due to ozone residence time and the location of sources and sinks of ozone.

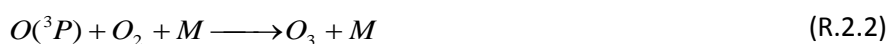
2.3.2 Stratospheric O₃

In the stratosphere, above ~30 km altitude from ground, O₂ molecules are split by short-wave UV radiation (< 242 nm) (R. 2.1) into O atoms which combine with O₂ to form O₃ (R. 2.2) This process is the kernel of the Chapman Cycle proposed by Sydney Chapman in the 1920s He also predicted that the maximum of ozone was situated around ~20 km altitude. The latter

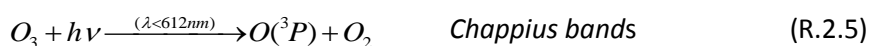
mechanism starts with the photolysis of oxygen molecules (R. 2.1.) for radiation with wavelengths below 242 nm.



After that reaction oxygen atoms (O (³P)) can: a) combine with an oxygen molecule to form ozone with the collision with a third body (M) that can be N₂ or O₂ (R. 2.2); b) can react with an existing ozone molecule (R. 2.3) or c) combine with other oxygen atoms to form O₂ (R. 2.4).



The photolysis of O₃, as described in reaction R. 2.5, also provides the O atoms at a much higher rate than R. 2.1. This molecule absorbs radiation and break down in O and O₂.



Consequently O(¹D) is converted almost instantaneously to ground- state O(³P) by collision with the body M : N₂ or O₂, according to R. 2.7.



In summary reactions R. 2.5 and R.2.6, result in ground-state O atoms production. To complete the Chapman mechanism, O and O₃ react to form O₂ molecules by R. 2.8.



For the above reactions it is necessary to account for their different timescales. More information about this issue can be found in literature (Seinfeld & Pandis, 2006). The set of reactions above presented, explains the steady state of O₃ concentration in the atmosphere in which the production of O atoms is in balance with their destruction.

During the 1960s, studies revealed that some other chemical reactions were taking place in the atmosphere beyond the “Chapman Reactions”. In fact his theory did not considered two processes that occur in atmosphere: a) existence of the Brewer-Dobson circulation that transports ozone from its production location (tropics) to poles and b) other chemical reactions of ozone with gases containing OH_x, NO_x, ClO_x, and halocarbon compounds that contribute to ozone loss process.

These reactions destroy ozone in catalytically reactions that follow the general scheme:

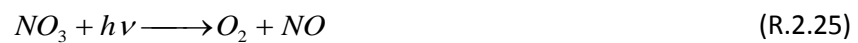


Where X and XO stands for example for NO_2 , HO_2 , ClO , ClO_2 , BrO .

2.3.3 Stratospheric NO_x

It was only in 1970 that Paul Crutzen (Nobel Prize 1995; born 3 December 1933) clarified the role of nitrogen dioxides in the stratospheric ozone chemistry. This was a result of an investigation from possible ozone depletion caused by a supersonic aircraft fleet proposed by Harold Johnston (Raes, 2012). The interest in the stratospheric role of NO_x started with the recognition of its role in the destruction of stratospheric ozone and that human activities could lead to significant increases in the stratospheric abundance of NO (Crutzen, 1979). In fact NO and NO_2 participate in an important set of catalytically reactions, especially effective above ~ 24 km which destroy ozone (cycle A and B).

These cycles involve nitrogen oxides via the following reactions:

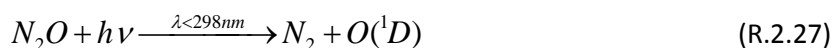


Cycle A is the dominant cycle in the middle stratosphere (~ 30 - 40 km), where the NO_x budget can be altered by increasing the N_2O due to anthropogenic influence. N_2O is crucial to the production of NO in the stratosphere by the oxidation of nitrous oxide (R.2.26)

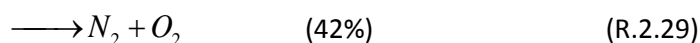


The main source of stratospheric NO_x is nitrous oxide (N_2O). This gas is released at Earth's surface where is inert and have a lifetime of about ~ 120 years, mainly through biological

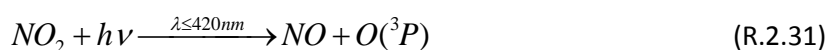
processes although it is also possible some emission during anthropogenic activity. After the release of N₂O it is transported through the troposphere to the stratosphere. Mainly in the middle and upper stratosphere the photolysis or oxidation of N₂O into active nitrogen (N₂) and NO (R. 2.27-2.29) take place. As a consequence about 90% of N₂O is removed from this layer due to R. 2.27.



The remaining N₂O is oxidized to NO (R. 2.28-2.29).



During the day NO and NO₂ are in photochemical equilibrium, rapidly converting into each other.



There are also other reactions which convert NO in NO₂ besides R.2.30-2.31. Some examples of this conversion are:

- a) reaction with peroxy radicals (RO₂=HO₂, CH₃O₂; RO=OH,CH₃O):



- b) reactions with ClO and BrO (X=Cl,Br):



Other phenomena like the actions of galactic cosmic rays at high geomagnetic latitudes especially in lower stratosphere and Solar Proton Events (SPE) can be pointed as natural source of NO_x. Among the NO_x anthropogenic sources are the direct injection of NO from the exhaust gases of aircraft flying in stratosphere, the injection of nitric oxide in the fireballs of nuclear explosions, and man's agricultural manipulation (Crutzen, 1979).

During the night all NO_x is converted to NO₂, NO₃ and N₂O₅ due to lack of sunlight. The production of N₂O₅ takes place entirely at night, due to the reaction between NO₂ and NO₃.



In the presence of sunlight NO₃ is rapidly destroyed because it photolyses very rapidly. In the morning, with the appearance of light, NO₂ and N₂O₅ undergo photolysis (R.2.35 and R.2.36).



N_2O_5 can also be removed during the day, by collision (R.2.37).



Only after approximately 5 years from the discovery of the catalytic destruction of ozone by NO_x it was found that chlorine species (Cl and ClO) are even more effective in the ozone depletion than NO_x (Molina & Rowland, 1974). The role of chlorine compounds in the stratospheric ozone destruction were discovered due to the works of Stolarski and Cicerone (1974), Molina and Rowland (1975). They pointed the similarity of chlorine to the chain reactions of nitrogen oxides and explained also the role of Cl and ClO radicals, derived from anthropogenic CFCs, in ozone depletion. At the same time the role of the bromine compounds was also found. The industrial gases that contained chlorine and bromine compounds included CFCs and HCFCs and halons were used in refrigeration, air conditioning systems and fire retardants. Their use was widespread.

Chlorine has also a big role in the depletion of stratospheric ozone leading to the so called "Ozone Hole" detected over Antarctica in polar spring months. There are several special conditions that trigger the ozone depletion in this area like the presence of certain species like chlorine or bromine, the absence of sunlight, temperatures below 190K and the polar vortex. The major processes leading to ozone depletion in Antarctica includes a) formation of Polar Stratospheric Clouds (PSCs), b) conversion of chlorine reservoirs during the months without light c) formation of ClO_x and d) catalytical ozone depletion triggered by sun light in the polar spring.

2.3.4 Tropospheric ozone and nitrogen dioxide

The tropospheric and stratospheric chemistry of O_3 and NO_x are different due to different factors. One example is the wavelength of radiation needed for R. 2.1. reaction which isn't available in troposphere to trigger the ozone formation. Other example can be the low amount of O_2 present in troposphere which isn't enough to activate NO_x cycles A and B.

2.3.4.1 Tropospheric NO_x

The main role of NO_x in troposphere is its involvement in the tropospheric ozone production. The major tropospheric sources of NO_x are fossil fuel combustion, biomass burning mainly in tropical regions and biogenic emissions from soils, due to the natural cycle of N (microbial nitrification and denitrification). Other sources of NO_x are lightning discharges, emissions of aircraft exhausts, stratospheric injections of NO_x formed from photolysis of N_2O and HNO_3 , and a small contribution from ammonia oxidation emitted by biosphere (Delmas et al., 1997). NO_x

are also produced by non-combustion industrial processes such as manufacture of nitric acid, use of explosives and welding and emitted by indoor sources like tobacco smoking and the use of gas-fired appliances and oil stoves (Lindvall, 1985). Presently more than 50% of the NO_x total emissions are from fossil fuel combustion (originated by power plant, oil refineries, industries, vehicular traffic) and from biomass burning (IPCC, 2007) being the majority of these emissions located in industrialized and big urban areas. The tropospheric levels of NO_x, in the NH, have increased over the last century and exceed the natural background levels (~10 ppt) by several orders of magnitude in polluted urban areas (up to 1 ppm) (Seinfeld & Pandis, 2006).

Almost all NO_x emitted from combustion processes are released as nitrogen monoxide (NO) and converted to nitrogen dioxide in the atmosphere. The mechanism which explains the NO_x formation during a combustion process includes reaction of nitrogen gas (N₂) and organic nitrogen from the fuel. Inside the combustion chamber, high temperatures allow oxygen thermolysis and the produced oxygen (O) reacts with N₂ to produce NO (Delmas et al., 1997).



The same mechanism can be used to explain the NO emissions from lightning (Jacob, 1999).

Another source of tropospheric NO_x is the rapid (~minutes) cycling between NO (primarily emitted by sources) and NO₂ that occurs in this layer. The reactions are the following:



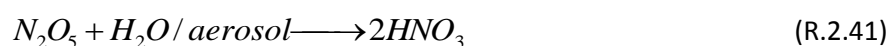
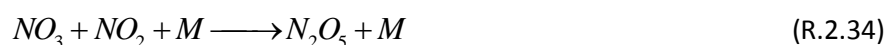
and by the null cycle:



At night there is no light to trigger reaction R.2.27 therefore all NO_x is exclusively NO₂. For that reason NO₂ is a result exclusively of R.2.22. In this period some reactions take place in the presence of O₃. Firstly nitrate radical (NO₃) is formed in presence of NO₂ and O₃ (R. 2.24)

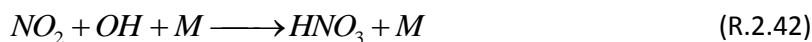


The NO₃ radical have also an important role serving as night time sink of certain VOC species like phenols, terpenes, etc.. Additionally, the NO₃ radical provides a major night time source of nitric acid via the formation and hydrolysis on wet surfaces of dinitrogen pentoxide, N₂O₅:



It is possible to conclude that the last reactions (R.2.34 and R.2.41) act like a sink of NO_x at night period. During daytime occurs the oxidation of NO₂ in HNO₃, which can be considered a sink of NO_x (also consider the R. 2.24, 2.34, 2.41)

It is worth mentioning that nitric acid HNO₃ is a key component of "acid rain," formed in R.2.42 as a co-pollutant of ozone.



HNO₃ and H₂SO₄, present in acid rain, are the products of atmospheric oxidation respectively of NO_x and SO₂, emitted mainly from fossil fuel combustion.

Another removal process (sink) of NO_x is deposition. In the lower troposphere NO, NO₃ and HNO₃ are removed due to dry deposition (taken up by plants over continents) and HNO₃ is scavenged by wet deposition. Since HNO₃ is very soluble in water, this component is removed mainly by precipitation in the troposphere. In the upper troposphere HNO₃ is converted in NO_x by photolysis or reaction with OH (Jacob, 1999). The excess of NO_x deposition stimulate, for example, the growth of surface water algae in excess resulting in the phenomenon known as eutrophication.

The outcome of the removal processes of NO_x in the atmosphere (R. 2.34, 2.41, 2.42 and deposition) is the effect on NO₂ lifetime in the PBL and in the free troposphere. NO_x has a short lifetime (~1 day) in polluted PBL although most of its sources are located at the surface. This is mainly due to reaction with OH (R. 2.42). In free troposphere NO_x can live for 5-10 days due to the fact that the HNO₃ deposition through rainout occurs within days (IPCC, 2001). Therefore the small amount of NO_x present in the free troposphere has more potential in tropospheric ozone formation (see VOC-NO_x-O₃ system in 2.3.4.3 section).

In the troposphere, NO_x can be transported for remote locations through the formation of PAN. PAN is produced in the troposphere, in presence of NO_x, by photochemical oxidation of carbonyl compounds which are produced by photochemical oxidation of hydrocarbons emitted from a variety of natural and anthropogenic sources. This compound is removed by thermal decomposition reaction that recycles back NO₂ by the following reaction:



In the middle and upper troposphere, PAN can be transported over long distances and through R.2.43 releases NO_x far from its source. An illustration of this transport is found in Fig.2.8.

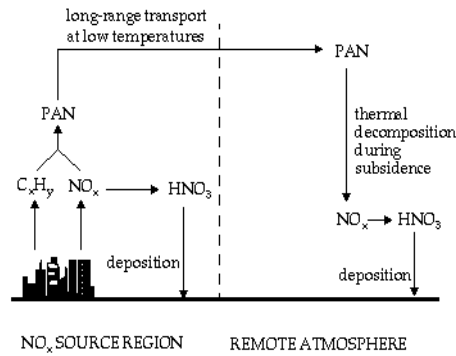
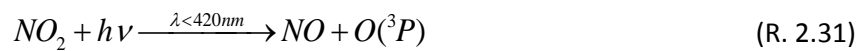


Figure 2.8 - Sinks of NO_x in troposphere (from Jacob, 1999).

2.3.4.2 Tropospheric ozone

In the 1950's Haagen-Smit proposed that the components of photochemical fog, which includes ozone observed in urban sites, could be the result of reactions involving NO_x and VOCs or NonMethane HydroCarbons (NMHC) emitted by vehicular engines (Mathes et al., 2005). From this suggestion it can be concluded that the ozone precursors are NO_x and VOCs in the presence of sunlight. However it was assumed till late 1970s that the major source of tropospheric ozone has its origin in the stratosphere and was transported through the tropopause reaching the troposphere. Today it is believed that only 10% of stratospheric ozone is transported downward to the troposphere, and the major sources of this gas are the products of reactions involving NO_x, CH₄, CO, VOCs. These gases, called “ozone precursors” tend to accumulate in the PBL of urban areas with stable meteorological conditions and, in the presence of sunlight, photochemical transformations can take place. The production of pollutants tends to be higher in summer months due to the intensity of solar radiation. As result of these reactions other harmful products are formed in the atmosphere besides tropospheric ozone like for e.g. aldehydes and PAN. Tropospheric ozone amount reaches its maximum in the early afternoon, after the morning rush hour where its precursors reacted with each others.

NO₂ has a major role in the tropospheric ozone production since the main mechanism of O₃ formation is the photolysis of NO₂ by sunlight (R.2.31 and 2.2).



Where M is an inert molecule needed for the conservation of the momentum.

Reactions R.2.31 and R.2.2 are part of a photo stationary equilibrium cycle and NO and NO₂ are rapidly converted into each other in the daytime atmosphere by R. 2.22.

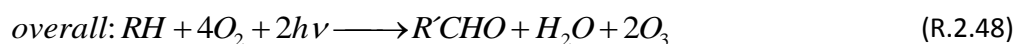
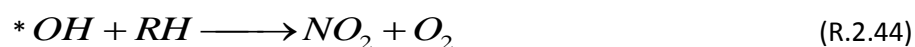


The above set of reactions R.2.31, 2.2, 2.22 determines the ratio of NO₂ to NO and this can be expressed by the Leighton ratio, L:

$$L = \frac{[NO_2]}{[NO]} = \frac{k_{1.3}[O_3]}{j_{1.1}} \quad (2.2)$$

where $k_{1.3}$ is the rate coefficient of reaction R.2.22 and $j_{1.1}$ the photolysis rate in reaction R. 2.31. These reactions may change the ratios of NO/NO₂, NO₂/NO_x and NO₂/O₃.

In polluted BL, ozone production is mainly triggered by the conversion of NO into NO₂ via VOCs. In the presence of OH radicals, VOCs oxidize NO to NO₂ promoting the production of O₃ during daytime, via R.2.30 and R.2.2. The major reactions involving OH radicals, NO and VOCs, in urban sites, are the following (Brasseur et al.,1999):



where RH are NMHC, R'CHO are carbonyl products like aldehydes or ketone (R' denotes an organic fragment having one carbon atom fewer than R).

In sites where the VOC concentrations are small (rural sites and free troposphere), tropospheric ozone production is controlled by CO and CH₄ oxidation (Fig.2.9). These reactions have a big impact in air composition, not only in the city itself but also in the surrounding areas, since the plumes of formed pollutants can be transported downwind affecting the rural areas nearby. The consequences are plant damage, crop productivity and a number of health problems like eye and nose irritation and respiratory problems.

Losses of tropospheric ozone are given by reactions with organic material at the Earth's surface (dry deposition), destruction at earth's surface and due to photochemical reactions with HOX intermediates.

Also in the troposphere, Reactive Halogen Species (RHS = X, X₂, XY, XO, OXO, HO_x, HNO₂, HONO₂ where X,Y denotes an halogen atom) can play a significant role in the catalytic ozone destruction.

Inorganic halogen species (RHS and hydrogen halides HX) are released to the lower troposphere either by (Platt & Honninger, 2003):

- degradation of organic halogen compounds (e.g. methyl bromide CH₃Br) or polyhalogenated species (e.g. CHBr₃, CH₂Br₂, CH₂I₂ or CH₂BrI) emitted by anthropogenic sources, from ocean, or in coastal areas
- oxidation of sea salt halides (X⁻) (e.g. sea salt aerosols or sea salt deposits)

The above inorganic halogen species are rapidly photolysed and as result forms halogen atoms which in turn probably react with ozone by:



In areas where RHS levels are low, like in free troposphere or in mid-latitude coastal areas, ozone destruction includes additionally the following steps that proceed to R.2.49:



This cycle (R.2.49-2.51) includes also the reconversion of OH to HO₂ through for example the reaction R. 2.52:



and the net result R.2.49-2.52 is:



Finally Fig. 2.9 summarizes the reactions involved in the tropospheric NO_x and O₃ chemistry.

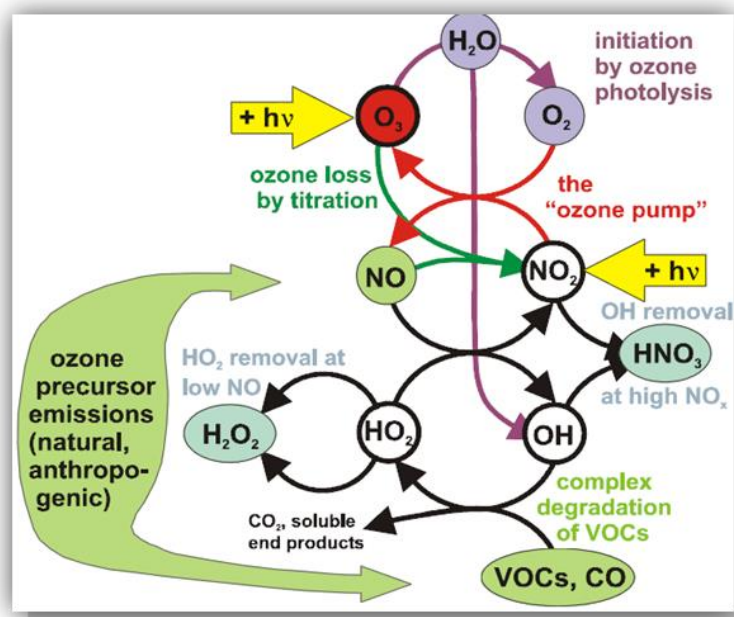


Figure 2.9 - Scheme of the reactions involving tropospheric NO_x and O₃ (from Volz-Thomas et al., 2003).

2.3.4.3 VOC-NO_x –O₃ system

The chemical regime for ozone production is largely determined by the relative magnitudes of the sources of HO_x and NO_x. Depending on the relative supply of NO_x and HO_x an increase in NO_x may cause either an increase or a decrease in ozone abundance (Jaeglé et al., 1998). Tropospheric ozone is more efficiently produced when atmospheric NO_x concentrations are low (Finlayson-Pitts & Pitts, 1993). This is related to the dual role of NO_x in tropospheric chemistry. On the one hand NO_x leads to the ozone formation through R.2.31 and R.2.2. On the other hand NO_x influence the HO_x concentrations by R.2.40.

The first plot of ozone concentrations resulting from initial mixtures of NO_x and VOC appeared in 1954 by Haagen-Smit aiming the development of control strategies for tropospheric ozone reduction. From this graph it is possible to retrieve the maximum ozone concentrations from several initial VOC-NO_x conditions from isopleths (lines of constant value). For that reason, each point on a particular isopleth represents the same ozone concentration. An example of this plot is illustrated in Fig. 2.10.

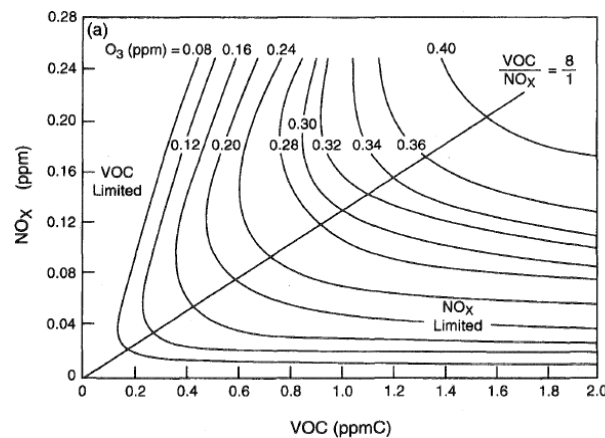


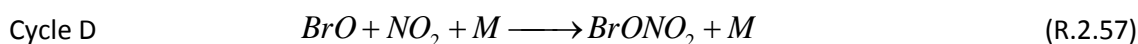
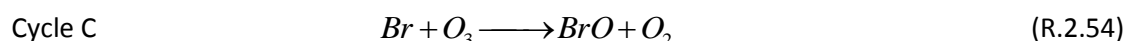
Figure 2.10 - Typical ozone isopleths generated from initial mixtures of VOC and NO_x in air, illustrating the relation between VOC- NO_x –O₃ in troposphere. The VOC-limited region is found in some highly polluted urban centres while the NO_x limited region is typical of downwind suburban and rural areas.

From the analysis of Fig. 2.10 we highlight the diagonal ridge that corresponds to the VOC/NO_x ratio (that can change with several factors) and two areas called VOC limited and NO_x limited. When the system is said to be NO_x limited, the production of O₃ is proportional to abundance of NO_x and independent of VOC abundances and composition. The most important reactions are $NO_2 + h\nu \longrightarrow NO + O(^3P)$ and $O(^3P) + O_2 + M \longrightarrow O_3 + M$. Therefore a decrease in NO_x concentrations results in a directly decrease in ozone. These regimes are characteristic of rural areas and suburbs downwind of cities centres (CGER, 1999). At VOC-limited regime the ozone production is dependent of VOC abundances. Under this regime increasing NO_x emissions could

lead to an increase of ozone production resulting from the complex chemistry involved in ozone formation in the VOC-NO_x mixtures.

2.4 Bromine Oxide - BrO

Among the halogens compounds, chlorine, bromine and iodine play an important role in ozone depletion. As the compounds instability increases, the ozone destruction potential increases as well. Although chlorine represents the major contribution to ozone destruction due to its stratospheric abundances, bromine compounds are much more effective in ozone destruction in stratosphere (probably about a factor of 40-100). The following reactions (Cycles C and D) present the main reactions of O₃ destruction by bromine compounds. Stratospheric bromine sources (BrO_x= Br+ BrO) count with anthropogenic and natural sources like: a) methyl bromide (CH₃Br) released from biomass burning and oceans, agriculture and leaded gasoline, b) halogenated hydrocarbon gases mostly used in fire extinguishers, c) liberation of sea salt, d) volcanic plumes (Bobrowski et al., 2003, 2005). Gases emitted by those sources are destroyed in stratosphere to produce Br and BrO.



When bromine compounds couple with chlorine compounds the ozone destruction process is enhanced and occur a Cycle (E) of reactions that lead to the destruction of ozone.

Cycle E



3. Absorption and scattering of solar radiation in the atmosphere

3.1 Interaction processes between electromagnetic radiation and the Earth's atmosphere components

The electromagnetic spectrum includes the electromagnetic radiation in all forms which are distinguished only by their different wavelength or frequency. When radiation interacts with matter it is absorbed, scattered, or emitted in discrete packets called photons. The energy E of a photon (since electromagnetic radiation can be treated as wave or particle) can be calculated by:

$$E = h\nu = \frac{hc}{\lambda} \tag{3.1}$$

where $h \approx 6.626176 \times 10^{-34} \text{ Js}$ is the Planck's constant, c is the speed of light and λ is the wavelength of the photon. Depending on their energy, photons can interact differently with matter by changing their electric or magnetic properties (e.g. electron distributions, magnetic dipole moment of the molecule). These changes lead to modifications in the electric or magnetic field of the electromagnetic radiation. The energy of the electromagnetic radiation determines the type of the molecular process, as shown in Fig. 3.1. For example UV and Visible radiation leads to electronic excitation, while X-rays can be responsible for ionizing atoms i.e. by ejecting one or more electrons from the atom.

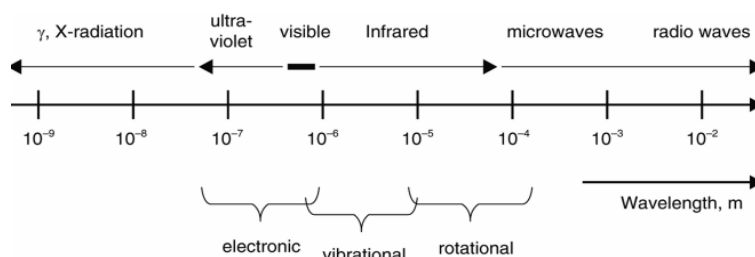


Figure 3.1- The electromagnetic spectrum and the types of transitions in molecules and atoms provoked by the different wavelengths of radiation (from Burrows et al., 2011).

3.2 Basic principles of Molecular absorption (and emission)

Similarly to atoms also molecules have internal energy which is quantised and also discrete energy states. The transitions between those states are the basis of spectroscopy. Also

important is the geometry of the molecules and their ability to interact with the electromagnetic radiation via creation of a permanent dipole moment. In Figure 3.2 are illustrated the geometries of some molecules including O₃. NO₂ geometry (not shown) is angular.

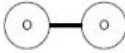
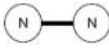

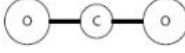
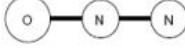

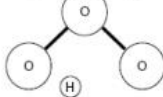
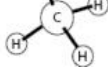
Molecule	Structure	Permanent Electric Dipole Moment?	May acquire dipole moment
Oxygen	 linear	No (magnetic dipole)	No
Nitrogen	 linear	No	No
Carbon Monoxide	 linear	Yes	Yes
Carbon Dioxide	 linear	No	Yes
Nitrous Oxide	 linear	Yes	Yes
Water	 asymmetric top	Yes	Yes
Ozone	 asymmetric top	Yes	Yes
Methane	 spherical top	Yes	Yes

Figure 3.2 - Geometries of important trace gases and dipole moment status (from <http://flux.aos.wisc.edu/~adesai/documents/aos640/AtmosRadCh9-10.pdf>).

The molecular energy states and transitions that we have to take into account are:

- rotational transitions associated to the rotation of the entire molecule about an axis through its center of gravity; it is the angular momentum of the entire molecule that gives rise to the rotational energy states. The corresponding wavelengths are in the microwave and far IR bands.
- vibrational transitions associated to the vibration of the atoms within the molecule relative to each other around their equilibrium positions. The corresponding wavelengths are in the IV spectral range. These transitions can as well be accompanied by a change in the rotational energy therefore vibration-rotation bands are often formed.
- electronic transitions associated to changes in the configuration of the electrons in the molecules. This transition corresponds to wavelengths in the Visible and UV spectrum. These transitions can be accompanied by a change in the vibrational and rotational energy modes.

The results of these transitions between states produce unique molecular spectra. Each atmospheric gas has a specific absorption or emission spectrum – its own radiative signature. These molecular spectra are different from the atomic line spectra because molecules have two additional types of energy (rotational and vibrational) besides the electronic energy. The existence of several forms of molecular internal energy leads to a complex band system that originates a more complicated absorption spectra than in the case of the atoms.

3.2.1 Rotational energy levels and transitions

For pure rotational transitions the molecule must have a permanent electrical or magnetic dipole moment. If there is no permanent dipole moment there is no radiative activity in the far-infrared which is the case of the homonuclear diatomic molecules like N_2 . Although O_2 has no magnetic dipole moment it has a weak permanent magnetic dipole and consequently has a rotational transition in the microwave spectral range. Molecules like CO , N_2O , H_2O and O_3 exhibit pure rotational spectra because they all have permanent dipoles. CH_4 and CO_2 have vibration-rotational bands because they can acquire the oscillating dipole moments in their vibrational modes although they do not have permanent dipole moments.

In Fig. 3.3 are represented molecules behaving as a rotator.

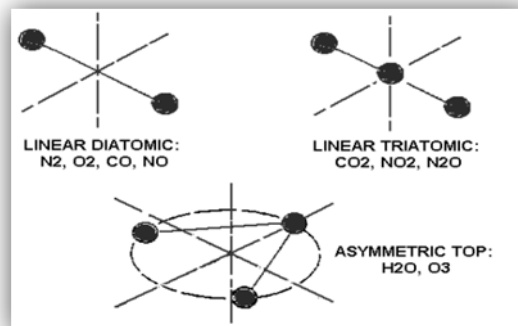


Figure 3.3 - Axes in red of rotational freedom for linear diatomic and triatomic and asymmetric top molecules and some examples (from Socolik, 2009). Diatomic molecules show two degrees of rotational freedom and asymmetric top three and respectively the same number of inertia moments.

The rotational energy levels (E_J) in a molecule are given by Eq. 3.2.

$$E_J = B.J(J + 1) = \frac{J(J + 1)h^2}{8\pi I} \quad (3.2)$$

where J is the rotational quantum number, B is the rotational constant of the particular molecule and rotation mode (rotation axes), I is the moment of inertia with the respect to the axis. The energy of the transitions is given by Eq. 3.3.

$$\Delta E = \frac{h^2}{4\pi^2 I} (J + 1) \quad (3.3)$$

3.2.2 Vibrational energy levels and transitions

Radiative transitions due to vibrational energy require a change in the dipole moment i.e. the molecules must have an oscillating moment. Therefore the vibrations of molecules can be treated approximately as harmonic oscillations and their energy levels can be calculated as follows:

$$E_v = \left(v + \frac{1}{2} \right) \cdot h \nu' \quad (3.4)$$

With $v = 0, 1, 2, \dots$ as vibrational quantum number and ν' is the resonant frequency.

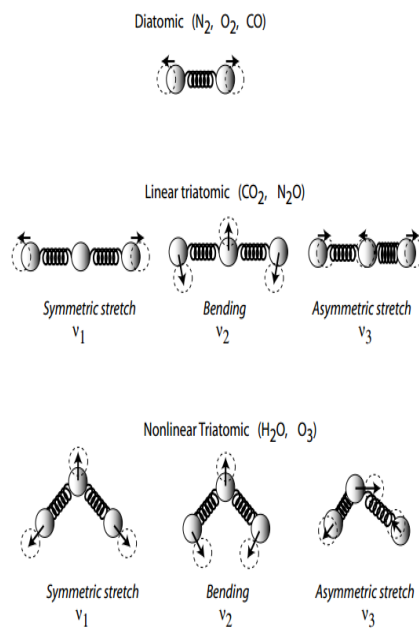


Figure 3.4- Vibrational modes of diatomic and triatomic atmospheric molecules (from <http://flux.aos.wisc.edu/~adesai/documents/aos640/AtmosRadCh9-10.pdf>).

For example O_3 have a structure denoted asymmetric top (Fig.3.3) and have three fundamental vibration modes (ν_1, ν_2, ν_3) as illustrated in Fig. 3.4 and are located at 9066, 14270, and 9597 nm, respectively. Ozone has also another band at 4700 nm. It is also possible to find additional weak vibration-rotation bands in the near-IR regions of the spectrum down to about 2500 μm . Those bands are known as P and R bands (see Fig. 3.5)

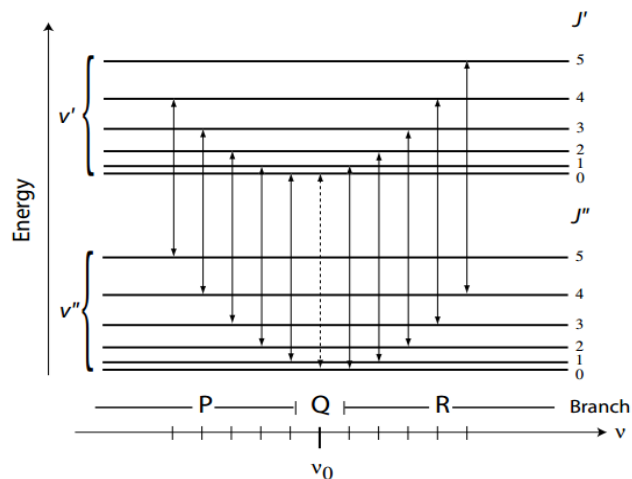


Figure 3.5- Vibrational-rotational transitions for $\Delta v = \pm 1$, $\Delta J = [-1, 0, +1]$ and illustration of the transitions in the spectrum. P and R branches correspond, respectively, to transitions involving $\Delta J = -1$ and $\Delta J = +1$ (from Liou, 2002).

3.2.3 Electronic transitions and energy

The valence electrons are involved in the absorption and emission of UV- visible energies. Electronic transitions in molecules are accompanied by vibrational and rotational transitions and are liable to several selection rules.

Due to these transitions NO_2 and O_3 have an absorption spectrum. Also NO_2 spectrum shows rotational and vibrational structures overlaid on the absorption spectrum. NO_2 absorption spectrum also has narrow spectral features which are temperature and pressure dependent.

In the following figure is possible to have an idea for electronic, vibration and rotation energy levels that are superimposed.

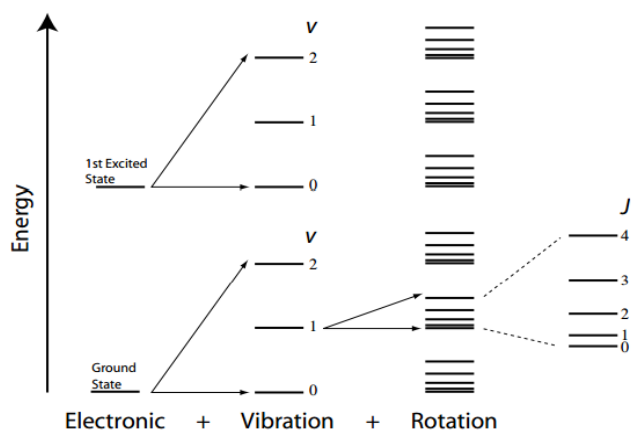


Figure 3.6- Scheme for the electronic, vibration and rotation energy levels (from www.google.com/webhp?nord=1#nord=1&q=http%3F%2Fflux.aos.wisc.edu%2F~adesai%2Fdocuments%2Faos640%2FAtmosRadCh9-10.pdf).

3.2.4 Molecular transitions in the UV-VIS region

It is possible to infer by analysis of Fig. 3.1 that In the UV-visible region several absorption processes are result of electronic and vibrational transitions.

The result of electronic transitions leads to the decomposition of the molecule into its constituents through photo dissociation or photo ionization. Due to vibrational transitions molecules can be excited into a dissociation level or into a specific vibrational level of the upper electronic state like it is illustrated in Fig. 3.7 .The spectrum consists of a smooth continuum at short wavelengths above the dissociation level and of absorption lines at discrete wavelengths (Farahani, 2006; Liou, 2002).

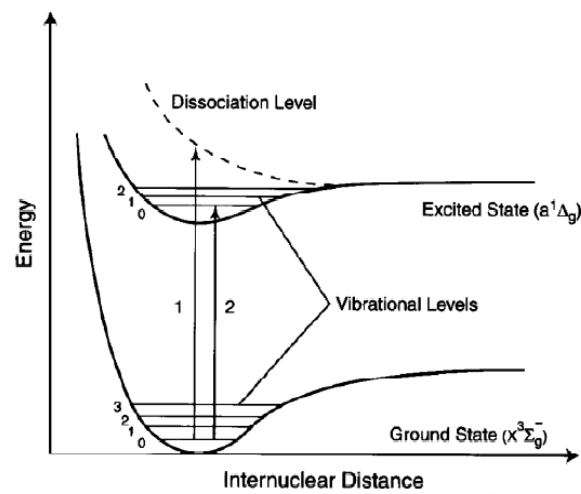


Figure 3.7- Potential energy curves for two electronic states of a diatomic molecule. Molecules can be excited into a dissociation level (e.g. transition 1) or into a specific vibrational level of the upper electronic state (e.g. transition 2) (from Liou, 2002).

3.3 Absorption, emission and scattering of solar radiation

There are several effects derived from the interaction processes between electromagnetic radiation and the gases and particles that constitute the atmosphere. Some effects are visible like the blue sky, red sunsets or white clouds that are a consequence or the different wavelength dependence of light scattering.

Solar radiation (~200 to 800 nm), which passes through the atmosphere, interacts with the air molecules and aerosol particles in a variety of processes such as absorption, emission and scattering. For example the UV-Visible part of solar radiation is mainly absorbed by ozone but also suffers cloud scattering, Rayleigh scattering by air molecules and absorption and scattering by aerosols. It also undergoes reflection and absorption by Earth's surface.

Absorption is a process by which molecules present in atmosphere (e.g. O₃, NO₂, CH₄, CO₂, etc.) or aerosols (e.g. soot) absorb radiation. Due to energy absorption the molecule undergoes an internal change and the energy of the photon promotes the molecule to a higher energy state. In this case the radiation is converted into some other form of energy like for e.g. heat. Therefore absorption of radiation in the atmosphere is a fundamental process in the climate system and for the maintenance of life in Earth (e.g. greenhouse effect, absorption of solar radiation by stratospheric O₃).

Scattering plays an important role in the atmospheric radiative transfer. During this process the photon can change wavelength/energy or direction, or both, according to the type of scattering that occurs: elastic or inelastic scattering. Elastic scattering can occur due to air molecules – Rayleigh scattering- or aerosol particles-Mie scattering. In this process there is a change of the direction of propagation of the photon although its energy is unchangeable and the scattering molecule is unaffected. Inelastic scattering by molecules is called Raman Scattering. This kind of interaction changes both the direction of propagation of the photon and energy. In this process a small quantity of light is scattered by molecules which undergo an internal transition between energy states. The scattered photon thus has a different energy form the exciting photon. Although it is considered a weak interaction of radiation and matter it can provide useful information in passive and active remote sensing and used to identify molecules and determine their molecular concentration. It is important to remind that radiation experience multiple scattering trough the atmosphere. This process is important because reinforce atmospheric and ground absorption since radiation suffers several reflections between Earth's surface and atmospheric layers, especially over highly reflected layers such as snow.

3.3.1 Absorption in the UV- Visible part of the spectrum

The main molecules and atoms that absorb solar radiation are O₃, O₂, CO₂, H₂O, N₂, NH₃, CH₄, O and N. Some of them are more effective in the UV-Visible part of the spectrum ($200 \leq \lambda \leq 850nm$) and others in the near infra-red one ($850 \leq \lambda \leq 5000nm$). The most important absorbers in the IR band (including near-, thermal-, and far-IR), are carbon dioxide (CO₂), water vapour (H₂O), ozone (O₃), methane (CH₄), and nitrous oxide (N₂O). In Table 3.1 are listed the atmospheric minor gases absorbing UV-Vis .

Table 3.1 - Wavelengths of absorption in the UV- Visible range by several atmospheric gases (adapted from Jacobson, 1999).

Gas name	Chemical formula	Absorption wavelengths (nm)
Ozone	O ₃	< 350 ; 450 -750
Nitrate radical	NO ₃	410 – 670
Nitrogen dioxide	NO ₂	<710
Nitrous acid	HONO	<400
Dinitrogen pentoxide	N ₂ O ₅	<380
Formaldehyde	HCHO	250-360
Hydrogen peroxide	H ₂ O ₂	< 350
Acetaldehyde	CH ₃ CHO	< 345
Peroxynitric acid	HO ₂ NO ₂	< 330
Nitric acid	HNO ₃	< 330
Peroxyacetyl nitrogen	CH ₃ CO ₃ NO ₂	< 300
Oxygen	O ₂	< 245
Nitrous oxide	N ₂ O	< 240
CFC-11	CFCl ₃	< 230
CFC-12	CFCl ₂	< 230
Methyl chloride	CH ₃ Cl	< 220
Carbon dioxide	CO ₂	< 210
Water vapour	H ₂ O	< 210
Nitrogen	N ₂	< 100

Due to the role of NO₂ in this work it is necessary to emphasize that this molecule absorbs solar radiation in wavelength between 200 and 700 nm. From the table 3.1, only O₃, NO₂ and NO₃ absorb in the visible part of the spectrum, being the NO₂ the most important compound showing considerable absorption near 430 nm.

Fig. 3.8 illustrates the solar irradiance and the main absorbing molecules in different spectral regions as well as the spectrum of solar radiation at the top of the atmosphere (TOA) and Sea Level (SL). The idea is to highlight the main molecules that absorb those different energies represented by the shaded area. The unshaded area between the TOA and SL curves represents the backscattering by air clouds, aerosols and air molecules and absorption by clouds and aerosols.

Let us focus only in the UV- VIS part of the spectrum (200-800 nm) since it is the range used in this study. In this part of the spectrum radiation is mainly absorbed by O₃ and O₂ (Liou, 2002). This radiation is also absorbed by aerosols and suffers some weak absorption by water vapour. This radiation also undergoes cloud and aerosol scattering.

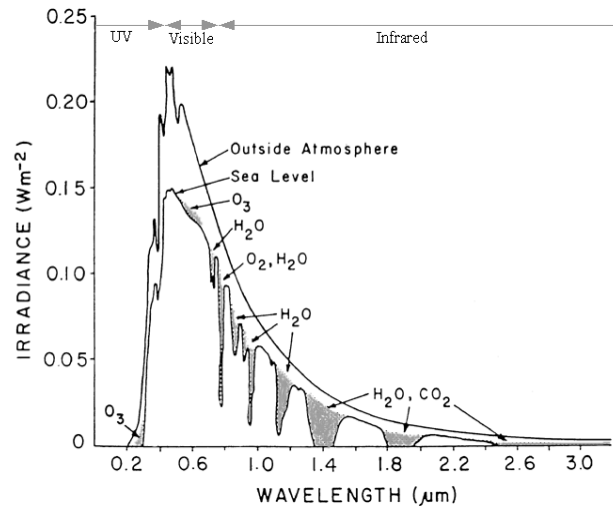


Figure 3.8 - Low resolution solar irradiance at top of atmosphere and at sea level and atmospheric absorption for average atmospheric conditions and an overhead sun (from Palazzi, 2000).

In Fig. 3.9 the O_3 and O_2 absorption bands and their absorption cross sections are displayed. This latter quantity measures the strength of absorption by an air component and it is customarily represented by σ_a in units of cm^2 .

At wavelengths shorter than 100 nm the majority of radiation is absorbed by atomic and molecular oxygen and nitrogen at altitudes between 100 and 200 km (in thermosphere and mesosphere) resulting in ionized products. As consequence ionized layers are formed in the upper atmosphere. As a result of UV solar radiation absorption by molecular oxygen and molecular nitrogen these gases suffer dissociation in both atomic nitrogen (N) and oxygen (O). N and O exhibit an absorption continuum from 0.1-100 nm. N also plays an important role in the absorption of UV radiation in thermosphere even if its quantity in upper atmosphere is not significant as from the other gases. The photo dissociation of molecular nitrogen (N_2) below 100 km plays a small role in the atmospheric chemistry. Nevertheless its absorption spectrum consists of a band system from about 145-112 nm referred as Lyman-Birge-Hopfield bands. Molecular oxygen absorbs between 80 and 120 km (thermosphere) in the Schumann-Runge continuum that corresponds to 130 nm and 175 nm and as consequence it is photo-dissociated in oxygen atoms at 1D state. The Schumann-Runge bands are situated between 200 nm and 175 nm. As shown in Fig. 3.5 these wavelengths present the strongest absorption by O_2 in mesosphere and upper stratosphere. The oxygen Herzberg continuum is found in the range of 200-242 nm. The absorption of UV solar radiation by O_2 occurs in stratosphere and there is also a weak absorption in mesosphere. This band is the weakest one and is of small importance due to the overlap with stronger bands of absorption by O_3 . Nevertheless the absorption in this

wavelength range leads to the O₂ dissociation in two oxygen atoms in the ground state (³P) that are needed for ozone formation.

The O₃ strongest absorption bands are the Hartley bands which are found in the range 200 – ≈ 310 nm .This absorption by ozone occurs primarily in the mesosphere and in the upper stratosphere leading to the formation of O(¹D). Also responsible for the photo dissociation of ozone below 50 km in the stratosphere and troposphere are the Huggins bands in the range ≈ 310- 400 nm that leads to the formation of O(³P). O₃ shows a weaker absorption in the Visible and near infra-red (400 – 850 nm) in Chappius band that occurs in the troposphere leading to photo dissociation even at surface (Brasseur & Solomon, 2005; Liou, 2002).

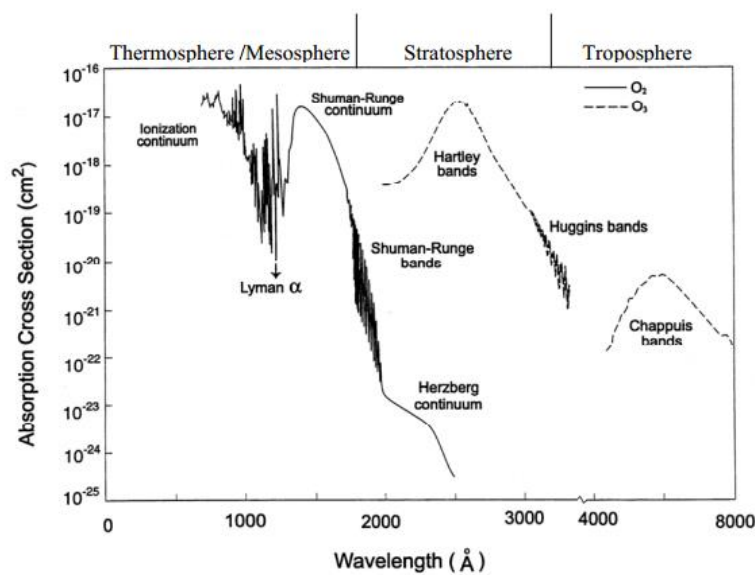


Figure 3.9- Spectral distribution of the absorption cross section of O₂ and O₃ adapted (from Haigh, 2007).

3.4 Atmospheric radiative transfer

In the context of this work the study of the radiation transfer is important since for the retrieval of trace gas parameters by remote sensing technique a precise knowledge of the sources of electromagnetic radiation and its transport through the atmosphere is needed (Burrows et al., 2011). The propagation of radiation in atmosphere is not a straightforward process. Since the atmosphere is an absorbing and simultaneously scattering media the transport of radiation is complex.

In this section the basic equations describing the transfer of radiation in the atmosphere are presented. The exact physical solutions of the radiative transfer equations can only be derived for simple cases. In general accurate Radiative Transfer Models (RTM) are needed to invert trace constituents data products and solve those equations. These numerical models are usually complex. In this work the models used are the Atmospheric Model for Enhancement Factor Computation (AMEFCO) (Petrioli et al.,1998) and the PROcessing of Multi-Scattered Atmospheric Radiation (PROMSAR) (Palazzi et al., 2005a, 2005b, 2005 c) that are briefly described in sections 4.4.2.1 and 4.4.2.2..

3.4.1 Radiative Transfer Equation (Platt & Stutz, 2008; Burrows et al., 2011)

The radiance is defined as the radiant flux (Φ), per unit space angle (Ω) and wavelength, (λ) and therefore its units are $Wsr^{-1}m^{-2}$.

Consider a stream of photons crossing the atmosphere. Their intensity $I(\lambda)$ is attenuated after traversing a layer of infinitesimal thickness ds (along the directions of the propagation) due to absorption and scattering (=extinction) by atmospheric components. If only absorption is considered, $I(\lambda)$ is reduced by the amount $dI_a(\lambda)$ (Eq. 3.5) by crossing an absorbing layer:

$$dI_a(\lambda) = -I(\lambda) \cdot \varepsilon_a(\lambda) \cdot ds = -I(\lambda) \cdot \sigma_a(\lambda) \cdot n \cdot ds \quad (3.5)$$

where $\varepsilon_a(\lambda)$ is the absorption coefficient (m^{-1}), $\sigma_a(\lambda)$ (m^2) is the absorption cross section of the absorbing molecule/atom and n (m^{-3}) is the number of absorbers (atoms) per unit of volume.

The integration of Eq. 3.5. yields to the derivation of Lambert-Beer's Law (or Beer- Bouguer Lambert Law) that will be described in more detail in Chapter 4 section 4.4.1.1.

Similar to absorption, the scatter radiance is given by Eq. 3.6.

$$dI_s(\lambda) = -I(\lambda) \cdot \varepsilon_s(\lambda) \cdot ds = -I(\lambda) \cdot \sigma_s(\lambda) \cdot n \cdot ds = I(\lambda) \cdot \frac{d\sigma_s(\lambda)}{d\Omega} \cdot n \cdot d\Omega \cdot ds \quad (3.6)$$

where $\varepsilon_s(\lambda)$ is the scattering coefficient (m^{-1}), $\sigma_s(\lambda)$ (m^2) is the scattering cross section of the molecule/particles and n (m^{-3}) is the number of scatters (molecules or particles) per unit of volume.

Radiance added by scattering is given by:

$$dI_s^*(\lambda) = \varepsilon_s(\lambda) ds \int_0^\pi \int_0^{2\pi} I(\lambda, \vartheta, \phi) \cdot \frac{S(\vartheta, \phi)}{4\pi} d\phi \cdot \sin\vartheta d\vartheta \quad (3.7)$$

where ϕ is the polar angle, ϑ is the scattering angle and S is a dimensionless scattering function given by:

$$S(\theta, \varphi) = \frac{4\pi}{\sigma_s} \cdot \frac{d\sigma_s(\lambda)}{d\Omega} \quad (3.8)$$

From the sum of Eq. 3.5 and Eq. 3.6 (i.e. absorption and scattering contributions) it is possible to get the total extinction intensity of the incoming radiation traversing the distance ds of an absorbing and scattering layer (Eq. 3.9).

$$dI_\lambda = -dI_a - dI_s = -[\sigma_a(\lambda) + \sigma_s(\lambda)] \cdot n \cdot I_\lambda \cdot ds \quad (3.9)$$

The intensity due to thermal emission (Eq. 3.10.) from a volume element can also be considered but this is negligible when compared to the solar radiation in the near IR, Visible and UV spectra regions.

$$dI_{th}(\lambda, T) = I_p(\lambda, T) \cdot \varepsilon_a(\lambda) \cdot ds \quad (3.10)$$

where $I_p(\lambda, T)$ is the Planck function.

Combining all the described processes we finally get the Radiative Transfer Equation:

$$\frac{dI(\lambda)}{ds} = -[\sigma_a(\lambda) + \sigma_s(\lambda)] \cdot n \cdot I(\lambda) + \varepsilon_s(\lambda) \int_0^\pi \int_0^{2\pi} I(\lambda, \vartheta, \phi) \cdot \frac{S(\vartheta, \phi)}{4\pi} d\phi \cdot \sin\vartheta d\vartheta + I_p(\lambda, T) \cdot \varepsilon_a(\lambda) \quad (3.11)$$

For our purpose in the UV-Visible spectral range some approximations can be made to Eq. 3.11 like the last term of the equation that represents the thermal contribution, can be removed because at short wavelengths (UV and VIS) the Planck term value is very small (due to the low temperature) compared to the other term values.

$$\frac{dI(\lambda)}{ds} = -[\sigma_a(\lambda) + \sigma_s(\lambda)] \cdot n \cdot I_\lambda + \varepsilon_s(\lambda) \int_0^\pi \int_0^{2\pi} I(\lambda, \vartheta, \phi) \cdot \frac{S(\vartheta, \phi)}{4\pi} d\phi \cdot \sin\vartheta d\vartheta \quad (3.12)$$

4. Methods and instruments to monitor atmospheric composition with solar radiation

4.1 Introduction

One of the methods widely used to study the atmospheric composition is the Remote Sensing (RS) technique. RS can be defined as the science and technology by which the features of the analysed objects/compounds can be identified, measured or studied without direct contact of the sensor with the analysed item. RS techniques have several applications in several fields like agriculture, forestry, cartography, meteorology, hydrology, astrophysics, archaeology, geology, oceanography, biology and in atmospheric physics and chemistry more specifically in ozone, climate research field and pollution control. Usually when it comes to terminology remote sounding techniques are commonly used in studies applied to the atmosphere constituents and remote sensing are related more to research dealing with surface parameters.

Remote sensing observations depend on the interaction of electromagnetic radiation with matter (Burrows et al., 2011) therefore this kind of radiation is the usual source of atmospheric remote sensing data (Platt & Stutz, 2008). In the context of this thesis, RS is used for the determination of the total content, vertical distribution and variations of atmospheric trace gases. Therefore after the interpretation of those changes it is possible to disclose information about atmospheric composition. The precision of the derived data products with the RS monitoring techniques depends on our understanding of the interaction of radiation and matter. In our particular case the importance of understanding the relationship between them is crucial for the use of spectroscopy technique which is directly applied to derive the data (trace gases total column amount and vertical profile) presented in this thesis. Spectroscopy is the study of matter (identification of the molecules and their concentration) using electromagnetic radiation. This is possible since different chemical compounds absorb and emit electromagnetic radiation in a different way at particular wavelengths. The result (spectroscopic data) is a spectrum which works as a “fingerprint” for the chemical compound allowing the identification of the gas. It is also possible to determine the amount of the absorber because it is related to the intensity of absorption. In the case of atmospheric studies, spectroscopy may be a passive RS technique that can be used from different platforms. Several ground-based stations, spread all over the world even in most remote regions of the planet, have been providing a large amount of very useful measurements for example the monitoring of environmental pollution,

evaluation of the global warming and its effects on climate. The products resulting from those measurements are long term dataset and high temporal resolution of stratospheric trace gases, aerosol loading, clouds and other important physical parameters like temperature, pressure, precipitation, radiation, winds. Ground- based instruments also allow simultaneous measurements of many trace gases under well-calibrated conditions as well as the comparison and development of different techniques. Also important are the costs associated to these stations that are less expensive than other platforms like balloons, rockets or satellites. In the last years instrumentation on board airborne platforms (Brandtjen et al., 1994; Pfeilsticker et al., 1997; Kostadinov et al., 2006) or satellite (Burrows et al., 1999; Richter et al., 2002; Buchwitz et al.; 2004, Coldewey-Egbers et al., 2005; Boersma et al., 2005) assumed a key role in atmospheric research. The latter instruments are important mainly due to their global coverage. Data obtained with ground- based and satellites instruments are complementary and very useful together, since the ground-based instruments can be used for the comparison/validation of the satellite data once mutually calibrated.

The Differential Optical Absorption Spectroscopy (DOAS) (Plane & Nien 1992; Platt, 1994) is a well spread and established technique used in the monitoring of air quality and also useful for the retrieval of large amount of data and parameters that are important for the study of climate change. DOAS is appropriated for the simultaneous detection of many atmospheric trace gases such as NO₂, O₃, SO₂, BrO, OCIO, IO, HCHO, BTX (Benzene, Toluene and Xylene) (Senne et al., 1996; Hoenninger & Platt, 2002; Kourtidis et al., 2002; Stutz et al., 2004).

This chapter is divided into three parts being the first one dedicated to the basic concepts and physics of atmospheric radiation and its relation with RS techniques (in particular with spectroscopy). In the second part the ground based system and the satellite instruments, sources of the data used in this work, are illustrated. Finally the DOAS theory and the algorithms to retrieve the trace gas concentrations from the spectral data carried out with ground based spectrometer are presented.

4.2 PART I - Remote Sensing/sounding techniques

The RS techniques can be distinguished in two categories based on the type of the source employed:

- 'passive' type if natural sources are used, as the radiation coming from the sun, the moon or the stars,
- 'active' type if it uses artificial sources (usually lamps with a well known and calibrated emission spectrum).

Moreover, the measure can be of the type 'line-integral', supplying the value of the integral of the concentration along the measurement path and these results can be obtained both with "Active" and with "Passive" systems) or 'range-resolved', providing the spatial distribution of the concentration of gases in examination. Since some years ago these information was gathered only with active systems. In the lasts years, with new methodology of analysis, the range resolved measurements can be obtained also with Passive system as it will be shown in section 5 of this thesis.

One more classification of the RS techniques can be done considering different parameters such as:

- type of measurement e.g. imaging, non-imaging and sounding
- spectral region due to the wavelength of measured radiation
- platform e.g. air-born (up to 15 km) , ground-based, sonde / balloon measurements (up to 30 km), rocket measurements (up to 80 km), Space Shuttle / Space Station measurements, satellite measurements
- spectral resolution e.g. low, medium, high
- spatial resolution e.g. low, high
- detection technique eg. absorption, emission or extinction spectroscopy and spectral reflectance.

The possibility to perform measurements in locations that are not easily accessible is one of the main advantages of the RS techniques, in comparison with the 'in situ' measurements. In addition, RS do not introduce alterations in the medium under analysis and by means of satellite platform a global coverage can be achieved. Furthermore, several parameters can be measured at the same time with only one instrument and the operation and maintenance costs are usually smaller than the "in situ" ones.

The main disadvantages can be resumed as:

- remote sensing measurements are always indirect measurements;
- the electromagnetic signal is often affected by more things than just the quantity to be measured;
- interpretation of data can be difficult therefore additional assumptions and models are needed for the interpretation of the measurements;
- usually, the measurement area / volume is relatively large;
- validation of remote sensing measurements is a major task and often not possible in a strict sense;
- estimation of the errors of a remote sensing measurement often is difficult;
- needs solar radiation to perform measurements ;

- limited spatial resolution.

In this study we use a passive-RS technique since the instrument uses natural sources of radiation in particular direct sunlight. In addition to sunlight the attenuated, reflected, scattered, or emitted stellar, lunar light or thermal radiation can also be analysed. In opposition, active RS uses an artificial source of radiation e.g. laser radiation (LIDAR), white light (long path DOAS), radio waves (RADAR) and the reflected or scattered signal is analysed. In this study our system is also a sounding system, since it measures the intensity of radiation to provide information about a property (trace gas concentration) as function of height in atmosphere.

In Fig. 4.1 it is possible to have an idea of the several techniques used in RS. It is not an exhaustive list, but gives a general plan of active and passive RS. More detailed information about each technique can be found in literature (Strong, 2005; Platt & Stutz, 2008).

In the context of this thesis we will focus on spectroscopic remote sounding technique. Measurements gathered with this technique are the result of a two-step process: first the measurement of radiation, and secondly the retrieval of trace gas quantities. In our particular case a spectrometer was used to perform the measurements. This kind of ground-based instrument is able to disperse solar radiation into several wavelengths over a defined spectral range. There are three types of spectrometers:

- grating spectrometers that uses a disperse grating and is commonly used in remote sounding systems on board satellites and in ground-based equipments
- prism spectrometers like for example the Dobson spectrometers where a prism disperses the light in a range of wavelengths
- interferometers that use interference effects e.g. the Michelson and the Fabry-Perot interferometers.

The measurements resulting from these instruments are portions of the electromagnetic spectrum. The signal comes from the absorption or emission of a photon from an atom or molecule and it is accompanied by a change in the state of the atom or molecule.

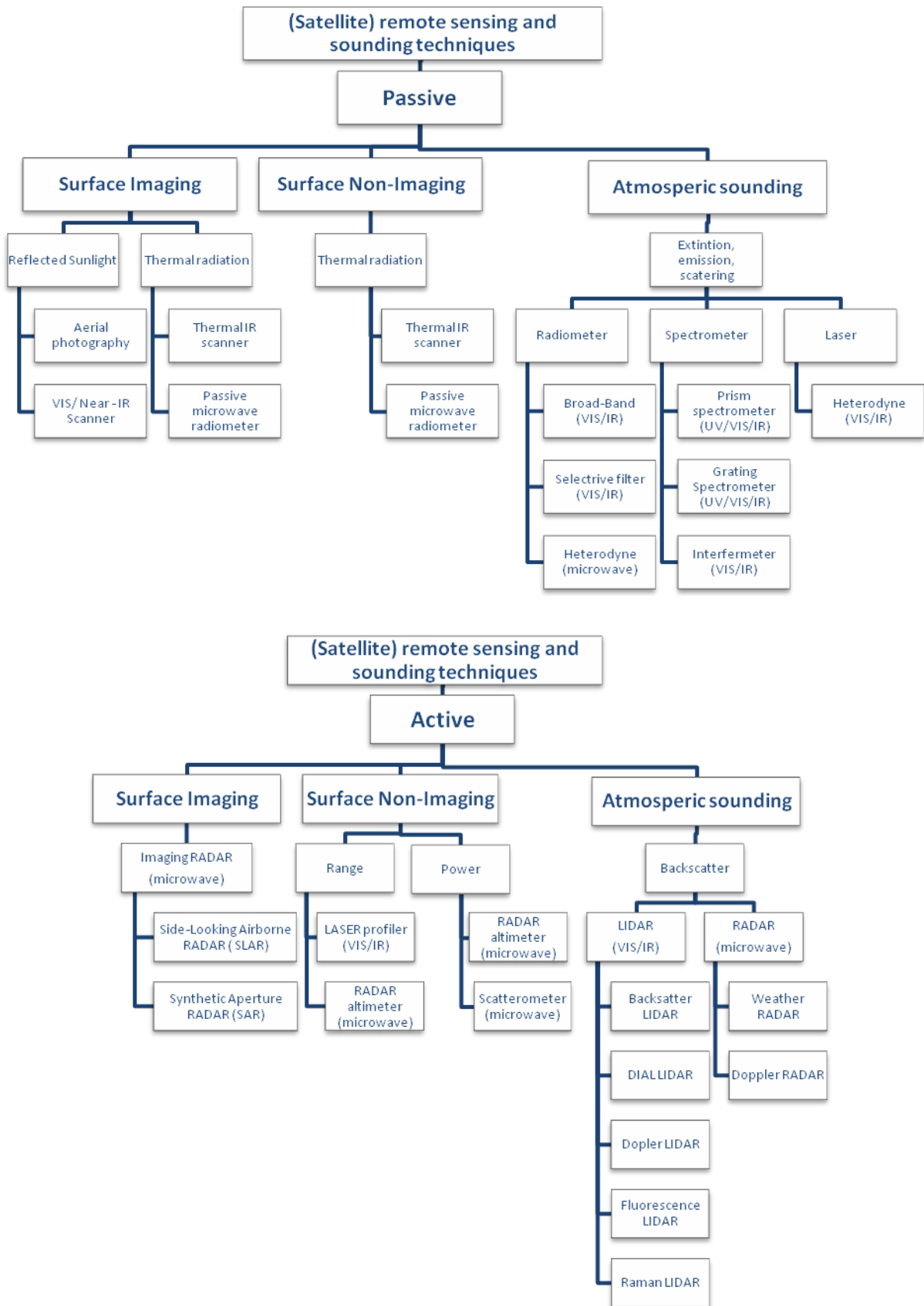


Figure 4.1- General plan of Remote Sensing techniques (from Strong, 2005).

4.3 PART II – Instruments

This section presents the ground based instrument whose data are mainly used in this work: the SPATRAM (SPectrometer for Atmospheric TRacers Monitoring) equipment. The SPATRAM instrument was developed by the Atmospheric Physics and Climate group of CGE-UE in close collaboration with the Institute of Atmospheric Sciences and Climate (ISAC) of the Italian National Research Council (CNR) located in Bologna (Italy) and with Italian National Agency for New Technology, Energy and Environment – (ENEA). The main applications and features of this ground- based instrument are briefly presented as well the description of the Vertical Looking Device (VELOD) and Multiple Input Geometry Equipment (MIGE) devices that are coupled to the spectrometer.

In addition, in this part of the work the descriptions of the satellite instruments utilized for comparison/validation of the SPATRAM results, are presented. Namely the satellite borne equipment's are: the Ozone Monitoring Instrument (OMI), the SCanning Imaging Absorption spectroMeter for Atmospheric CHartography (SCIAMACHY), the Global Ozone Monitoring Experiment (GOME) and the Global Ozone Monitoring Experiment–2 (GOME-2).

4.3.1 The SPATRAM system

The multipurpose UV–Vis. SPATRAM (Bortoli et al., 2010) is a scanning spectrometer and it measures the solar scattered radiation in the 250–900 nm spectral range with typical spectral resolutions varying from 0.3 nm at 250 nm up to 0.9 nm at 900nm.

The main body of the SPATRAM instrument is composed of two distinct units: the Electronic Control Unit (ECU) and the Optical Mechanical Unit (OMU) (Fig. 4.2).

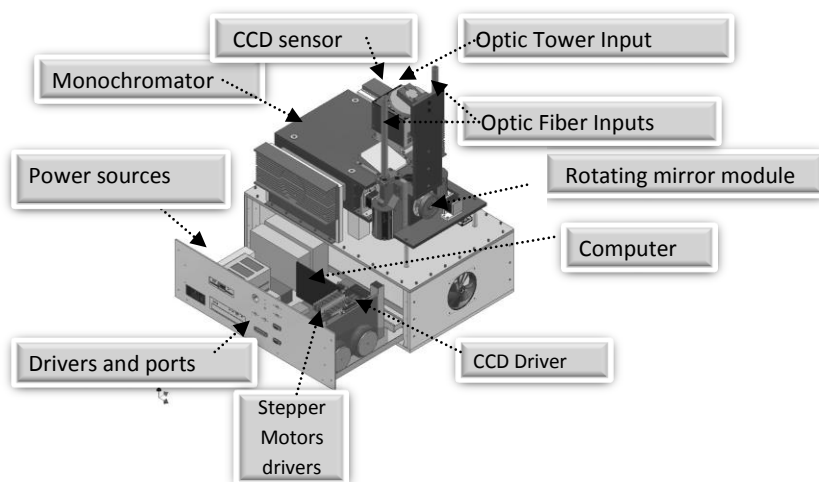


Figure 4.2 - Representation of the main modules of the SPATRAM Instrument.

The OMU includes all optical and mechanical parts of the instrument such as: i) the monochromator; ii) the Charged Coupled Device (CCD) sensor; iii) the thermo-regulators and the filters- the OMU-ECU interface ;iv) the Rotating Mirror Module (RMM), for the selection of the input; v) the two optical fibre inputs – for the input of the radiation from auxiliary optic devices (VELOD or MIGE) and vi) the Optic Tower, which is the primary input of solar radiation. The ECU provides the control and the management of the whole instrument. This unit (rigidly connected to OMU) contains power supplies, an industrial CPU, the CCD driver device, 3 stepper motors controllers, an AD converter for the temperature transducers, present in both units OMU and ECU and other electric and electronic components for the control of the instrument status. The SPATRAM instrument is handled by a software tool named Data Acquisition System (DAS). This software was developed to manage all the spectrometer devices and for automatic scheduled measurements as well as for the unattended mode following the instructions written in a text file read by DAS. The ECU also provides the storage of the measured spectra and their first analysis, with a simplified DOAS approach, in order to obtain the contents of the species presenting absorptions features in the selected spectral range.

Since the 1st of April 2004, the SPATRAM system is installed in Évora (South of Portugal – Fig 4.3 a) at the Observatory of CGE-UE (Fig. 4.3 b, 4.3 c), measuring the solar radiation in the UV- VIS spectral range in subsequent spectral windows of about 60nm each one. This last feature is possible thanks to the precise controlled rotation of the grating normal to its optical axis using a stepper motor and an optimized frequency calibration procedure.

A detailed description of the instrument and working method can be found in the works of Bortoli, 2005; Bortoli et al., 2010; Bortoli et al., 2009.



Figure 4.3- a) The location of Évora city in mainland Portugal. b) The container in the Observatory of the Geophysics Centre of Évora in Évora (38.5°N; 7.9 °W, 300 m a.s.l.). c) The SPATRAM instrument installed inside the container.

In the beginning (2002), the SPATRAM instrument was developed for measurement along the vertical direction using the Optic Tower Input (Fig. 4.2). In order to simplify the installation and setup of the instrument and to increase the measurements capabilities extending the domain of research (detection and monitoring of more atmospheric compounds) two auxiliary optical systems were added to the main body of the SPATRAM spectrometer. Those systems are: i) the VELOD (Vertical Looking Device) for the measurement of the zenith sky scattered radiation using a light guide to carry the signal to the spectrometer; ii) the MIGE (Multiple Input Geometry Equipment) used to collect radiation for directions away from the vertical one.

4.3.1.1 VELOD – VErtical LOoking Device

The VELOD is a small telescope composed of one elliptical flat mirror with a hole in the centre and a spherical mirror placed at the distance necessary to focus the radiation received from the flat mirror in the centre of the flat mirror itself (Fig. 4.4 a). At a distance of 2 mm beyond the mirror an optic fibre is placed (Fig. 4.4b) and the radiation signal is carried out to one of the optic fibre inputs of the SPATRAM main body (Fig. 4.2). The optic system is contained in a small box vacuum proof aiming to avoid events of condensation on the quartz window used for input of the radiation. The window is tilted of 10 degree in order to prevent water accumulation on it.

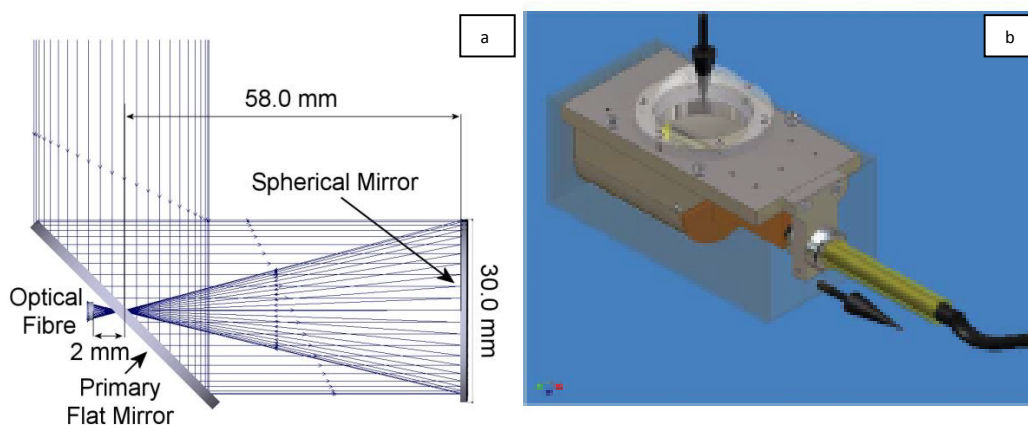


Figure 4.4 – VELOD a) optical layout; b) project design with the vacuum proof box and the optic fibre. The arrows specify the direction of the input and output of the radiation.

4.3.1.2 MIGE -Multiple Input Geometry Equipment

MIGE (Figure 4.5) is an alt-azimuth platform based on the same optical layout of the VELOD, using an optic fibre to transmit the radiation inside the monochromator of the SPATRAM instrument. Thanks to the solutions adopted in the developing phase, the MIGE platform is able

to scan the full azimuth (0-360°) as well as the full zenith plane. The MIGE device can collect both the diffuse and the direct solar radiation in the whole sky.

The equipment is placed under a dome of fused silica to avoid undesired effects of light reflexes and also to allow for measurements in the UV spectral region.



Figure 4.5- The MIGE platform installed on the roof of the container where the SPATRAM instrument is placed. This platform ensure the possibility to carry out measurements in off-axis configuration along many azimuthally directions since the horizon line is almost completely free (from Domingues, 2011).

4.3.1.3 SPATRAM products

The data that can be retrieved from the spectral measurements carried out with the SPATRAM system in zenith sky configuration (that is measuring in the vertical direction) are mainly used for research, case studies and for satellite data validation/comparison. The almost operational products are the total columns for NO₂ and O₃. For NO₂ the vertical distribution from 10 to 50 km of altitude with a spatial resolution of 2.5 km is computed with the application of inversion methods. The output of the DOAS algorithms – the SCD values – thanks to a synergy with a dynamic model, allows also for the identification of events of anthropogenic pollution due to air mass circulation.

The spectral data acquired for direction different from the zenithal one (with the MIGE device) allows for:

- the determination of the profile for NO₂ and O₃ in the lower atmosphere (from the ground till to 2 km of altitude) with a vertical resolution of 250-300 m;
- the measure of the tropospheric column of some optically thin atmospheric compounds such as SO₂, HCHO, CHOCHO and BrO).

These last 2 aspect allows for the assessment of the air quality in urban areas in the PBL.

In addition, the measurements of the spectral sun radiance performed with the MIGE device, after the determination of the radiometric calibration coefficients, can be compared with the AERONET radiance data. At the same time the corrections of the AERONET data for the NO_x signal can be provided.

4.3.2 Satellites data sources

Instruments on board satellites provide a unique global view of the observed phenomena and such comprehensive coverage and sampling are not available from any other measurement platform. In addition, the observations location makes easier the identification of the processes occurring at the highest atmospheric layers.

On the other hand, the spaced based equipment is very expensive in term of setup since complex space-qualified instrumentation is required. Furthermore the launches costs as well as the risks of failure are very high.

4.3.2.1 The Ozone Monitoring Instrument

The OMI, onboard the National Aeronautics and Space Administration's Earth (NASA) Observing System Aura (EOS) Aura satellite, on flight from 15 July 2004, is a nadir viewing imaging spectrograph that measures the solar radiation backscattered by the Earth's atmosphere and surface over the entire wavelength range from 270 to 500 nm with a spectral resolution of about 0.5 nm and with a very high spatial resolution (13 × 24 km in the normal global operation mode and 13 km × 12 km in the zoom mode) and daily global coverage (Levelt et al., 2006). The 114° viewing angle of the telescope corresponds to a 2600 km wide swath on the surface, which enables measurements with a daily global coverage. The light entering the telescope is depolarized using a scrambler and then split into two channels: the UV channel (wavelength range 270 - 380 nm) and the VIS channel (wavelength range 350 - 500 nm).

Trace gases derived from OMI instrument include O₃, NO₂, SO₂, HCHO, BrO, and OCIO. In addition, this satellite instrument estimates aerosol characteristics, cloud top heights, and UV irradiance at the surface. OMI instrument is the successor of the TOMS (Total Ozone Monitoring Spectrometer) equipment that pioneered, since the late seventies, the research on atmospheric composition and its evolution from satellite.

4.3.2.2 The SCanning Imaging Absorption spectroMeter for Atmospheric CHartography

The SCIAMACHY is one of the ten instruments installed on board of ESA's Environmental Satellite (ENVISAT) which was launched on May 2002 and was operational until April 2012. The SCIAMACHY instrument is an imaging spectrometer whose primary mission objective is global measurements of trace gases in the troposphere and in the stratosphere (BrO, OClO, ClO, SO₂, H₂CO, NO₂, CO, CO₂, CH₄, H₂O, N₂O) with the application of the DOAS algorithms, with an improved spatial resolution (typically the ground pixel is 30x240 km.).

This satellite instrument also allows for the monitoring of stratospheric ozone, tropospheric pollution or for other events like volcanic eruptions related to regional or global phenomena. SCIAMACHY also allows for the retrieval of the amounts and distribution of aerosols, radiation, cloud cover and cloud top height. The solar radiation transmitted, backscattered and reflected from the atmosphere is recorded with a resolution of 0.2 nm up to 1.5 nm over the range 240 nm to 1700 nm, and in selected regions between 2000 nm and 2400 nm (Bovensmann et al.,1999). More detailed information about the instrument can be found in literature in Burrows et al.,1995.

4.3.2.3 Global Ozone Monitoring Experiment

ERS-2 was launched in April 1995 into a near-polar sun-synchronous orbit at a mean altitude of 795 km. The descending node crosses the equator every 2800 km at 10:30 local time. GOME is a nadir-scanning double monochromator covering the 237 nm to 794 nm wavelength range with a spectral resolution of 0.17-0.33 nm. The spectrum is split into four spectral channels, each recorded quasi-simultaneously by a 1024-pixel photodiode array. The global spatial coverage is obtained within 3 days at the equator by a 960 km across-track swath (4.5 s forward scan, 1.5 s back scan). The ground pixel size of the measurements is 320 X 40 km². The solar irradiance is measured daily. Details of the overall scientific objectives of GOME, instrument concept, and some first scientific results are reported elsewhere (Burrows et al., 1999).

4.3.2.4 Global Ozone Monitoring Experiment 2

The GOME-2 is a UV-VIS spectrometer scanning spectrometer launched on board the Meteorological Operational Satellite-A (MetOp-A) in October 2006. One of the main goals of GOME-2 is the long-term monitoring of atmospheric ozone started by GOME on ERS-2 and SCIAMACHY on ENVISAT. Apart from the retrieval of total ozone field (ozone total column and

profiles) it allows also for the global monitoring and column densities of other atmospheric trace gases such as NO₂, SO₂, H₂CO, CHOCHO, OClO, H₂O and BrO. This instrument covers the wavelength interval of 240-790 nm with a spectral resolution of 0.2-0.5 nm. Its ground pixel is about 80x40 km².

All the information about this instrument can be found in literature at Callies et al., 2000 and Munro et al, 2006.

4.4 Part III – Methods

In the next subsections the Differential Optical Absorption Spectroscopy (DOAS) algorithms used for the retrieval of the mean trace gas concentrations along the optical path of measure (the Slant Column Densities –SCD) are presented. In addition, the methods to derive the Vertical Column (VC) of the analysed atmospheric compound with different Radiative Transfer Models are shown. Furthermore, the procedures for the assessment of the vertical profiles are described.

4.4.1 DOAS History and background

Since its introduction in 1979 (Perner & Platt, 1979; Platt et al. 1979), DOAS is a technique widely used to obtain the atmospheric trace gases content (Platt, 1994; Solomon et al. 1987) and it is by now a well-established method. Thanks to its high sensitivity, DOAS allows for the detecting of very low tracers concentrations. With this technique the first measurements of atmospheric content of some compounds were obtained starting from the end of the seventies. The first results for OH (Perner et al. 1976), HONO (Perner & Platt, 1979; Platt & Perner, 1980), NO₃ (Platt et al., 1980), BrO (Hausmann & Platt, 1994), IO (Alicke et al.,1999) and glyoxal (Volkamer et al., 2005) were dealing with their tropospheric content, while the studies for OClO and BrO (Sanders et al.,1988) were conducted in the stratosphere (Dix, 2007).

DOAS is the main method used in this work for the processing of the ground-based spectral radiation observations carried out with the SPATRAM instrument. This technique is based on the absorption of the UV-Vis radiation from the minor compounds of the atmosphere along the optical path travelled by the radiation entering the sensor. DOAS identifies and quantifies the trace gas with narrow band absorption structures in the near UV and visible regions. Recent studies also demonstrate its appliance in the IR region for the retrieval of CO₂ and CH₄ concentrations (Frankenberg et al., 2005; Woyde,2007).

As for the others remote sensing techniques (cfr. Section 4.2), DOAS measurements deals with two different configurations: i) active (with an artificial source of radiation - i.e. a halogen lamp)

where the measurements are generally performed along a horizontal path; ii) passive (where the source of radiation is natural – the sun or the moon). Regarding the active configuration, the outputs of the DOAS algorithms (usually called Slant Column Densities - SCDs) are the mean value concentration of the investigated species along the Optical Path of Measurements (OPM). These results are utilized in studies mainly focused on the air quality monitoring and the environmental pollutions problems (Evangelisti et al., 1995; Weibring et al., 2002; Kim et al., 2007; Salerno et al., 2009). Concerning the passive configuration, the measurements are carried out from different directions. The historical one is the zenith sky looking direction. The radiation input of the measuring equipment (usually an UV-VIS Spectrometer) is pointed towards the zenith. Also in this configuration, the outputs of the DOAS processing are the SCDs. In the active mode the OPM is a function of the condition and of the distance of the lamp. In the passive mode the OPM is a function of different parameters such as the Solar Zenith Angle (SZA - i.e. the angle between the position of the sun and zenith), the atmospheric condition and composition. The DOAS methodology is based on the Beer-Bouguer Lambert Law and in the following sections the derivation of this relation is presented and the fundamental equation of the DOAS technique (DOAS Master Equation) is introduced.

4.4.1.1 Beer-Bouguer Lambert Law

The Radiative Transfer equation (Eq. 3.12) can be written as:

$$dI_{\lambda} = -\chi_{\lambda} I_{\lambda} \rho ds + \chi_{\lambda} J_{\lambda} \rho ds \quad (4.1)$$

where χ_{λ} is the mass extinction cross section (m^2 / kg) for radiation of wavelength λ , ρ is the density of the material (kg / m^3), I_{λ} is the intensity of the incident radiation, J_{λ} is the source function and ds is a layer with infinitesimal thickness.

The first term of Eq. 4.1 is the result of extinction (absorption and simple scattering) and corresponds to the attenuation of the intensity of the radiation while the second term comprise the emission and multiple scattering by the particles of the medium into the propagation direction of the incident beam reinforcing the intensity of the beam.

Since absorption is the most relevant process that contributes for the attenuation the last term of Eq. 4.1 can be neglected because $J_{\lambda} = 0$. The term χ_{λ} can be substituted by the absorption cross section of the gas, $\sigma_{\lambda,g}$, in m^2 and ρ by the number of molecules by unit volume, C , in $molecules / m^3$. As a result of these considerations Eq. 4.1 becomes Eq. 4.2

$$dI_{\lambda} = -\sigma_{\lambda,g} I_{\lambda} C ds \quad (4.2)$$

From Eq. 4.2 it is possible to infer that attenuation suffered by radiation depends on the quantity of the optical active gases present in the atmosphere.

The absorption cross sections are unique for each species allowing for the identification of each gas. In Fig. 4.6 the absorption cross sections of some trace gases namely O₃, NO₂ and BrO are presented.

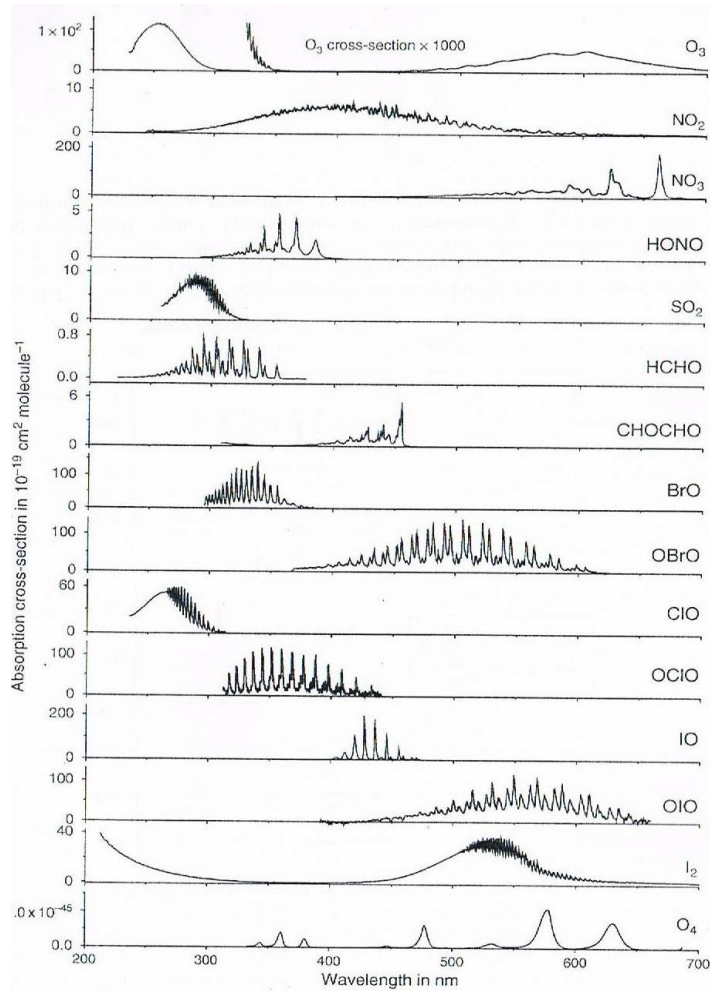


Figure 4.6- Absorption cross sections in cm⁻² of some trace gases from (Platt & Stutz, 2008).

Integrating Eq. 4.2 along an optical path from 0 to S_1 and considering that in the top of the atmosphere the intensity of monochromatic light is equal to $I_{\lambda,0}$ it is possible to obtain Eq. 4.3.

$$I_{\lambda,S_1} = I_{\lambda,0} \exp\left(-\int_0^{S_1} \sigma_{\lambda,g} C ds\right) \quad (4.3)$$

The monochromatic optical thickness (τ_λ) (Eq. 4.4) is dimensionless and measures the quantity of absorbent material that is present along the optical path.

$$\tau_{\lambda} = \int_0^{S_1} \sigma_{\lambda} C ds \quad (4.4)$$

From Eq. 4.4 it is possible to define the Slant Column Density (SCD) in *molecules/m²* as the integrated concentration along the optical path (Eq. 4.5) which depends on the SZA (θ) and on the wavelength of the incident radiation (λ).

$$SCD_g(\theta, \lambda) = \int_{S_{\rho}(\theta, \lambda)} C ds \quad (4.5)$$

Combining Eq.4.3 and 4.4 it is possible to obtain the Beer Bouguer Lambert Law in its classical form (Eq. 4.6) :

$$I_{\lambda, S_1} = I_{\lambda, 0} \exp(-\tau_{\lambda}) \quad (4.6)$$

where I_{λ, S_1} is the intensity of monochromatic light that crosses the atmospheric path S_1 .

From a practical point of view I_{λ, S_1} is the radiance that reaches the instrument after crossing the atmosphere.

4.4.1.2 DOAS master equation

From the linearization of the Lambert-Beer Law in Eq. 4.3, it is possible to deduce the following relation (Eq. 4.7).

$$\ln(I_{\lambda, 0}/I_{\lambda, S_1}) = \sigma_{\lambda, g} \int_{S_{\rho}(\theta, \lambda)} C ds \quad (4.7)$$

Like it was stated in chapter 2 the atmosphere is a mixture of several gases. Having this in mind and combining Eq. 4.7 and 4.5 it is possible to get Eq. 4.8.

$$\ln(I_{\lambda, 0}/I_{\lambda, S_1}) = \sum_g \sigma_{\lambda, g} SCD_g(\theta, \lambda) \quad (4.8)$$

where the symbol \sum stands for all optical active trace gases which have contributed to the attenuation of the radiation in the UV-Vis spectral range.

Since absorption cross sections $\sigma_{\lambda, g}$ are characteristic for each atmospheric compound (as shown in Fig. 4.6.) it is easy to identify the gas that we intend to study. Besides wavelength dependency $\sigma_{\lambda, g}$ also depends on pressure and temperature along the light path. In this work this fact was taking into account by considering that the cross sections were measured at different atmospheric conditions.

The low frequency (the linear or polynomial tendencies) of the various absorption spectra can be removed from the Eq. 4.8 with a high pass filter operator with the goal of separate broad and narrow band features, leading to the DOAS Master equation (Eq. 4.9).

$$\ln\left(\frac{I_0(\lambda, \theta_{\min})}{I_s(\lambda, \theta)}\right) - \overline{\ln\left(\frac{I_0(\lambda, \theta_{\min})}{I_s(\lambda, \theta)}\right)} = \sum_g \left(\sigma_g(\lambda) - \overline{\sigma_g(\lambda)} \right) SCD_g(\theta) \quad (4.9)$$

where $I_0(\lambda, \theta_{\min})$ is the reference spectrum obtained at local noon, $I_s(\lambda, \theta)$ is a spectrum measured for different condition of SZA, $\sigma_g(\lambda)$ are the absorber's cross sections, θ is the solar zenith angle, θ_{\min} is the solar zenith angle reached at the local noon and $SCD_g(\theta)$ are the slant column densities of the g^{th} absorber; the superscript represents the high pass filter operator removing the low frequency features of the spectral series.

Eq. 4.9 is usually solved in a suitable wavelength interval that includes strong differential absorption structures of the trace gases of interest.

4.4.2 DOAS applied to SPATRAM spectral data

The DOAS master equation can be applied, aiming to retrieve the SCD of one or more absorbers, to any spectral series obtained with optical instrumentation obeying to some constrains such as: high spectral resolution, frequency calibrated spectra and constant spectral dispersion parameters. The SPATRAM instrument is one of the equipments whereby the DOAS can be used. Nevertheless, the SPATRAM spectral data have to suffer some pre-processing procedures to be prepared before the application of the DOAS algorithms.

The pre-processing of the data set consists in multiple steps which are applied to the spectral series measured with the SPATRAM instrument, indicated as $I_0(\text{pix}, \theta_{\min})$ and $I_s(\text{pix}, \theta)$ with pix =pixel number of the CCD sensor. The first procedure is called "*linearization*" or "*wavelength to pixel mapping*" and consists in replacing the pixel numbers with the correspondent wavelength value creating a new spectral series where the amplitude of the signal is function of the wavelength values. The new spectral series are denoted with $I_0(\lambda_d, \theta_{\min})$ and $I_s(\lambda_d, \theta)$ where λ_d is a decimal value of wavelength.

The second phase of the pre-processing data is called "*fair-spacing of the spectral data*" (FSSD) and consists in the transformation of the wavelength decimal values to integer values with a fixed spectral step. This algorithms is applied to the new series $I_0(\lambda_d, \theta_{\min})$, $I_s(\lambda_d, \theta)$. In our case a spectral step of 2 Å is chosen and the resulting series are $I_0(\lambda, \theta_{\min})$, $I_s(\lambda, \theta)$. If the absorber's cross section series are measured with SPATRAM, the linearization procedure has to be applied

to $\sigma_g(\text{pix})$ in order to build the series $\sigma_g(\lambda_d)$ and the FSSD algorithms are used to have the $\sigma_g(\lambda)$. On the other hand if the $\sigma_g(\lambda_d)$ are from literature and measured with other equipments, beside the FSSD, a function that is the convolution of the instrument transfer function (generally called 'slit function'), has to be applied to the $\sigma_g(\lambda_d)$ series. The procedure is made by means of polynomial interpolation on 5 points of the original series.

Now, to continue with the creation of the different terms of Eq. 4.9, the log ratio of the reference spectrum - $I_0(\lambda, \theta_{\min})$ - with the analysed one - $I_s(\lambda, \theta)$ - has to be done. The superscript term of the log ratio spectrum (called also the mean function) is obtained with a so called "Smoothing" operation which consists in filtering the high frequency features in the spectral data series. The resulting 'smoothed' series is obtained with a Fast Fourier Transform algorithm (Press et al., 1986). The term on the right side of Eq 4.9 identifying the cross sections series suffers the same treatment of the left terms.

Finally, the last step is the differentiation. This procedure consists in calculating the difference point to point of the log ratio of the reference spectrum and the measured spectrum and its smoothing function. The same for the absolute absorber's cross section and their smoothed functions. Now the solution of the Lambert Beer equation, in its differential form (Eq. 4.9) is obtained by means of the Singular Value Decomposition (SVD). The results for the retrieval of the SCD of O_3 , NO_2 and BrO are presented in chapter 5. In this regards, it has to be noted that SPATRAM measures in consecutive spectral windows of about 60nm each as shown in Table 4.1 together with the spectral resolution and the observable species in each spectral interval.

In the particular case of our study the spectral intervals designated in table 4.1 with ID 3337, 3850 and 4358 are used.

In the following, an example illustrating in a qualitative mode the general procedure leading to the retrieval of O_3 SCD with UV spectral data, is presented. The same method was used for the other gases just varying the wavelength interval and the absorption cross sections series.

In Fig. 4.7 two spectral series measured with the SPATRAM instrument at local noon $I_0(\lambda, \theta_{\min})$ and at twilight (sunset or sunrise periods) $I_s(\lambda, \theta)$ are plotted. It has to be noted the significant difference in the 310-330nm spectral range of the intensity of the measured radiation. This is mainly due to the different atmospheric paths the radiation travelled before reaching the instrument leading to an increased absorption by atmospheric compounds (in this spectral range mainly due to O_3).

Table 4.1 - Observable species detected with SPATRAM and their respective spectral range and ID and optical resolution (from Bortoli et al., 2010).

ID	Spectral range (nm)	Spectral optical resolution (nm)	Observable species
2823	252.3 - 312.3	0.3	O ₃ , SO ₂ , ClO, NO
3337	303.7-363.7	0.3	O ₃ , SO ₂ , H ₂ CO, BrO, OClO, NO ₂ , aerosols
3850	355.0-415.0	0.4	BrO, OClO, NO ₂
4358	405.8-465.8	0.5	NO ₂ , OClO, H ₂ CO
4861	456.1-516.1	0.5	NO ₂
5332	503.2-563.2	0.6	NO ₂ , O ₃ , (O ₂) ₂
5814	551.4-611.4	0.6	NO ₂ , O ₃ , aerosols
6282	598.2-658.2	0.6	O ₃ , O ₂ , (O ₂) ₂ , NO ₃ , H ₂ O, aerosols
673	643.4-703.4	0.6	O ₃ , O ₂ , NO ₃ , H ₂ O, aerosols
7201	690.1-750.1	0.7	O ₂ , H ₂ O
7677	737.7-797.7	0.7	O ₂ H ₂ O, clouds
8195	789.5-849.5	0.7	H ₂ O, aerosols
8622	832.2-892.2	0.8	H ₂ O, aerosols
9023	872.3-932.3	0.8	H ₂ O, aerosols
9405	910.5-970.5	0.9	H ₂ O, aerosols

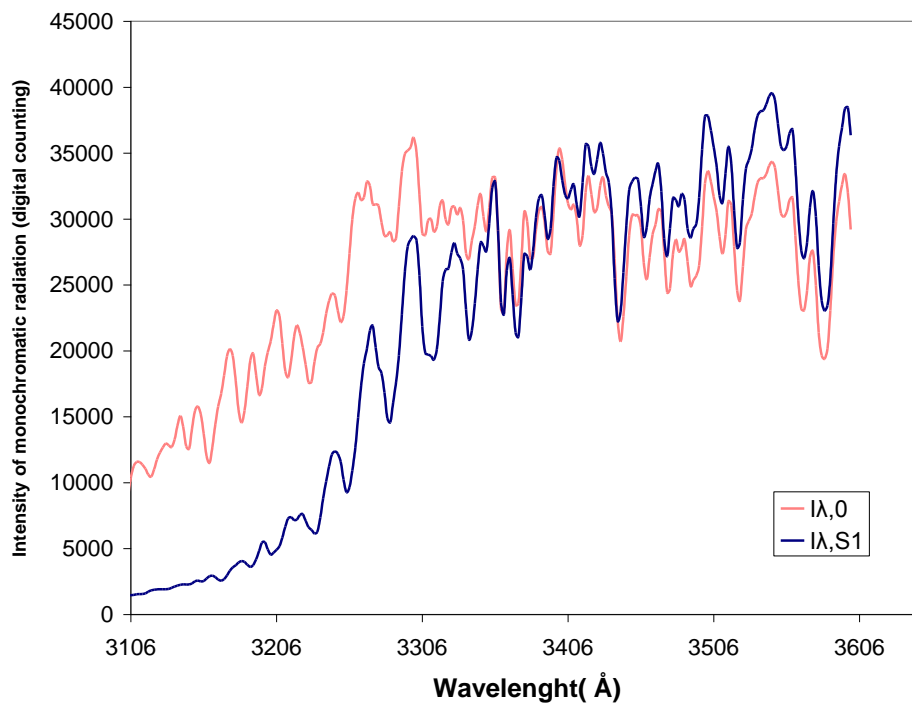


Figure 4.7- Intensity of monochromatic radiation that crosses the atmosphere ($I_{\lambda,S1}$) at twilight (AM or PM) versus the intensity of monochromatic radiation at local noon ($I_{\lambda,0}$) obtained with SPATRAM for Ozone measurements.

The logarithmic term in Eq. 4.9 is plotted in Fig. 4.8 illustrating the variation of $\ln(I_0(\lambda, \theta_{\min})/I_s(\lambda, \theta))$ versus wavelength. The mean function of the log-ratio $\overline{\ln(I_0(\lambda, \theta_{\min})/I_s(\lambda, \theta))}$, obtained applying the high pass filter to the original series, is also shown.

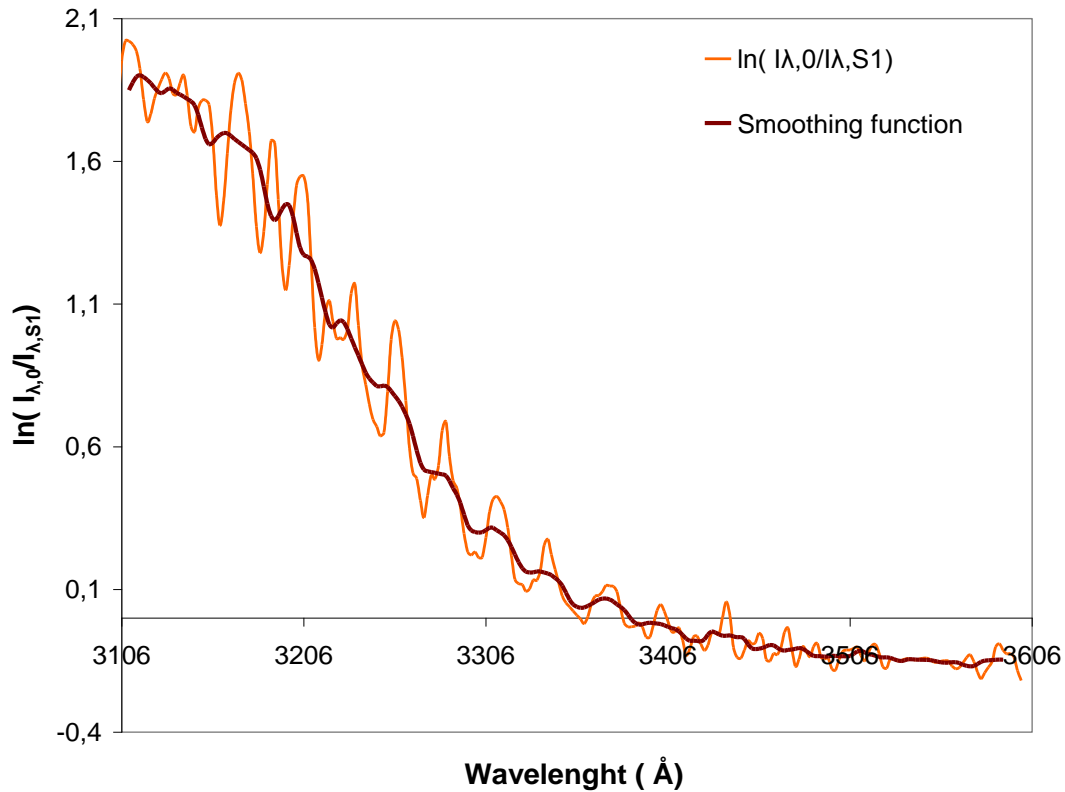


Figure 4.8- Plot of $\ln(I_0(\lambda, \theta_{\min})/I_s(\lambda, \theta))$ versus wavelength for UV spectral range (orange) and the smoothing function (brown).

The same is done for the absorber's cross section series ($\Delta\sigma_g(\lambda) = \sigma_g(\lambda) - \overline{\sigma_g(\lambda)}$) and Fig. 4.9 shows the variation of the difference between $\ln(I_0(\lambda, \theta_{\min})/I_s(\lambda, \theta))$ and $\overline{\ln(I_0(\lambda, \theta_{\min})/I_s(\lambda, \theta))}$ (also called "differential optical density term") and the O₃ differential absorption cross section (red) with the wavelength.

It can be noted how the differentiation procedure amplifies the maxima/minima distances for both series. Furthermore, the shapes of two series are quite similar (with a scaling factor of the order of about 10^{21}), evidencing that in this spectral range the radiance attenuation is almost completely due to the O₃ compound.

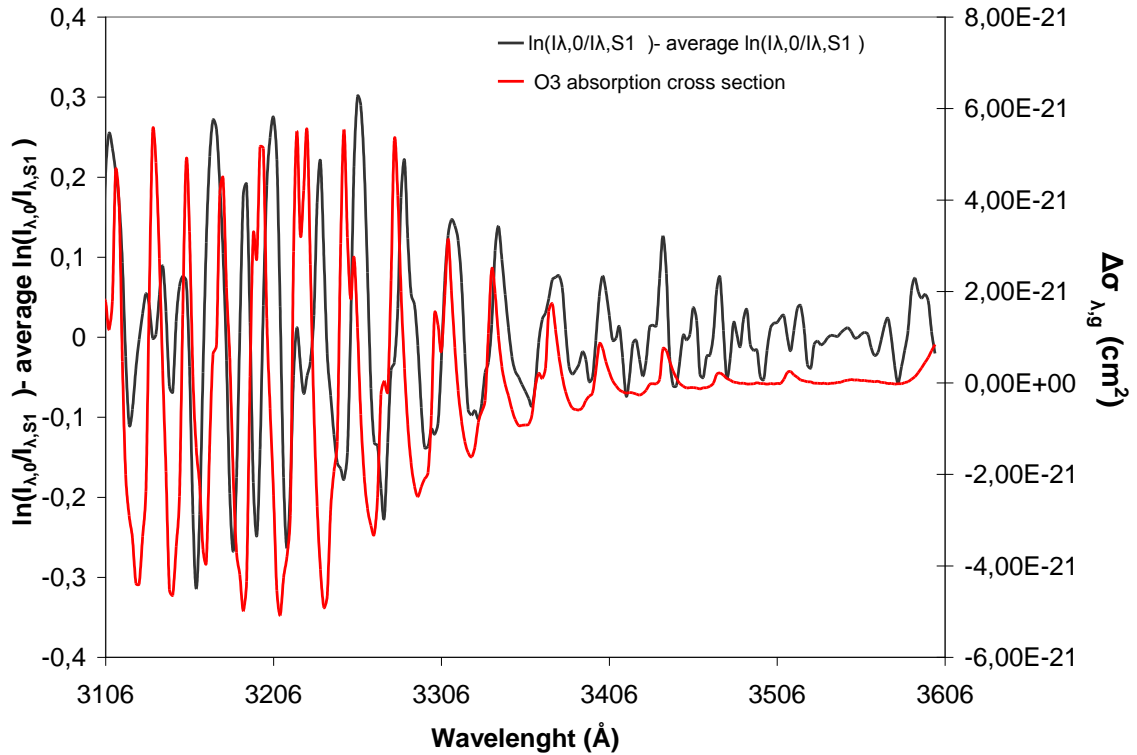


Figure 4.9- “Smoothing” process which consists in filtering the high frequency features in the spectral data series. The presented values are $\ln(I_{\lambda,0}/I_{\lambda,S1}) - \ln(I_{\lambda,0}/I_{\lambda,S1})$ versus wavelength (grey) and ozone differential absorption cross section (red).

After these preliminary operations, a first guess of the O₃ SCD value is obtained solving the DOAS Master Equation with the SVD method (Press et al., 1986).

The true value of the O₃ SCD is the one obtained when a nearly perfect overlap of the differential optical density with the differential cross section is obtained and this can be reached operating an accordion effect on the differential term. This effect is obtained with a procedure called of ‘shift and stretch’ where the modification of some functional parameters leads to the dilatation/compression/shift of the differential optical density. The shift and stretch procedure is an iterative process that is based on the Marquardt’s methods (Press et al., 1986), where the main goal is the minimization of the Sum Of Squares (SOS) of the residual spectrum. The residual spectrum is the difference between the differential optical density and the differential absorption cross section times the solution obtained with the SVD procedure.

Graphically, the iterative process corresponds to the accordion effect previously described.

The absorber’s cross section compounds used in this work are: O₃ (at 221 K and 241 K) (Burrows et al., 1999), NO₂ (at 221 K) (Burrows et al., 1998), and BrO (at 228 K) (Wilmouth et al., 1999). Scattering processes and polarization effects can introduce systematic errors in the retrieved amounts. Therefore, additional ‘non-absorption’ cross sections such as Mie, Rayleigh, Ring and

polarization cross sections are introduced (Chance et al., 1997; Kostadinov et al. 1997) in the data processing procedure.

In summary, the spectral evaluation consists of a least squares fit procedure where differential cross sections of the absorbers are adjusted to the differential log-ratio of the reference spectrum and the measured series obtained in different conditions (read different Sun's elevations).

The solutions of the DOAS master equation are the SCDs of the trace gases that shows absorption features in the investigated spectral range. As remembered in section 2.3.1.2, the atmospheric contents of O₃ and other atmospheric compounds are expressed as vertical column densities (VCD). The factor allowing for the transformation of the SCD to VCD is the Air Mass Factor (AMF). The AMF can be seen as a geometrical factor, function essentially of the Sun's elevation and of the wavelength, and it is defined as follows:

$$AMF_g(\theta, \lambda) = SCD_g(\theta, \lambda) / VCD_g(\theta, \lambda) \quad (4.11)$$

Actually for the computation of the AMF the use of a RTM is required. The main differences between the RTMs developed for this purpose have to be identified in the single or multiple scattering approaches even if for measurements at high SZA, the values obtained for the AMFs are very similar, considering the 2 different scattering conditions. The RTM used in this work are presented in the next sections.

4.4.2.1 Atmospheric Model for Enhancement Factor Computation - AMEFCO

For the retrieval of O₃ and NO₂ total columns and NO₂ vertical profiles it was necessary to use the radiative transfer model AMEFCO. AMEFCO is used basically to calculate the atmospheric Air Mass Factor in the measurement conditions and convert the slant column (SC) into the vertical column (VC) (Petrioli et al., 2002 b). AMEFCO model was developed at ISAC – CNR and it is based on the Intensity Weighted Optical Path (IWOP) approach (Slusser et al. 1996). The AMEFCO is a single-scattering model using ray tracing in a spherical 2-D atmosphere (profile variation with SZA) with optical paths integrated over individual shells. Light refraction is not included. (Petrioli et al., 2002 a).

To understand the mathematical model behind the AMEFCO it is necessary to realize the considered geometric model of the atmosphere (Fig.4.9). For this purpose the atmosphere is structured as spherical shells of 1 km thickness.

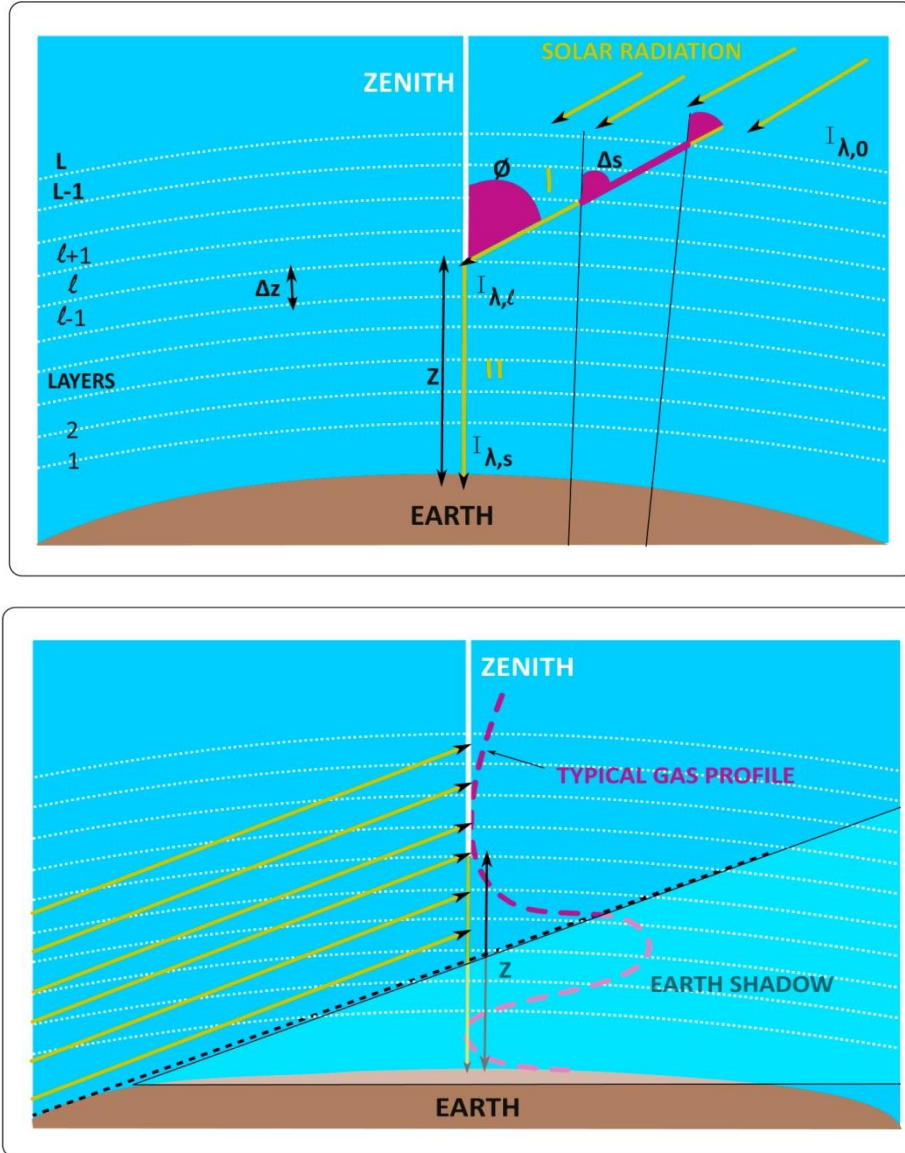


Figure 4.10- Path of radiation (yellow) along the vertical direction for Solar Zenith Angles (SZA) inferior to 90° (upper panel) and superior to 90° (from Bortoli, 2005).

For our study let us consider the radiation that reaches the layer l after crossing obliquely the atmosphere. It is possible to infer that the intensity of the radiation at that altitude is different from the TOA intensity due to scattering of air molecules and to the selective absorption of the atmospheric gases which depend on their absorption cross sections (as in Eq.3.9). Finally the intensity of the radiation that reaches the layer l , $I_l(\lambda)$, is given by equation 4.12.

$$I_\lambda(l) = I_0(\lambda) \exp \left[-\sigma_R(\lambda) \sum_{i=1}^L \rho_a(i) \Delta s_i(\theta) - \sum_{g=1}^n \sum_{i=1}^L \sigma_g(\lambda) \rho_g(i) \Delta s_i(\theta) \right] \quad (4.12)$$

where $I_0(\lambda)$ is the intensity of the radiation at TOA, ρ_a is the density of the air in the i shell in molecules/cm³, $\Delta s_i(\theta)$ is the slant path depending on SZA and altitude, σ_g is the absorption

cross section of the gas, ρ_g are the gas profiles and σ_R is the Rayleigh scattering coefficient given by Eq. 4.13.

$$\sigma_R(\varphi, \lambda) = \frac{\pi^2 \cdot (N^2 - 1)^2}{2 \cdot \rho \cdot \lambda^4} \cdot (1 + \cos^2 \varphi) \quad (4.13)$$

In the last equation ρ is the density of the medium and N it is the respective refractive index calculated by Eq. 4.14.

$$N = 1 + \frac{77.6 \cdot \left(1 + \frac{7.52 \times 10^3}{\lambda^2}\right) \cdot P}{T \cdot 10^{-6}} \quad (4.14)$$

where P and T are the pressure and temperature profiles for the mid- latitudes from the UVSPEC model (Mayer and Kylling, 2005; Mayer et al., 2012). Also the input parameters like air density and gases concentration profile are taken from standard atmosphere UVSPEC database for mid-latitudes (Petrioli et al., 1999).

The intensity of the radiation that reaches the ground-based instrument is given by Eq. 4.15. This radiation suffers a new attenuation along the vertical path l after been scattered at the altitude $z = l\Delta z$.

$$I_{\lambda,s}(l) = G(\lambda, \theta, l\Delta z) \exp \left[-\sigma_R(\lambda) \sum_{i=l}^L \rho_a(i) \Delta z - \sum_{g=1}^n \sum_{i=l}^L \sigma_g(\lambda) \rho_g(i) \Delta z \right] \quad (4.15)$$

where $G(\lambda, \theta, l\Delta z)$ is the part of energy that is scattered along the vertical path direction towards the instrument and is equal to eq. 4.16.

$$G(\lambda, \theta, l\Delta z) = I_i(\lambda) \sigma_R(\lambda) f(\theta) \rho_a(\lambda \Delta z) \Delta z \quad (4.16)$$

In the last equation the fraction of the flux scattered towards the ground as function of the SZA is given by the scattering phase function, $f(\theta)$. For the Rayleigh scattering of unpolarized light $f(\theta)$ is given by eq. 4.17.

$$f(\theta) = \frac{3}{4} \cdot (1 + \cos^2(\theta)) \quad (4.17)$$

The total energy reaching the sensor is given by Eq. 4.18.

$$I_{\lambda,s} = \sum_{l=1}^L I_{\lambda,s}(l) \quad (4.18)$$

In order to calculate the AMF it is essential to reduce the light beam to a single trajectory recalling that the radiation can cover different paths. To choose a single path it is necessary to adopt a criterion that is based on the definition of a function of probability. The scattering

probability, $p_l(\theta, \lambda)$, is the probability that the scattered bundle, at a predefined altitude, reaches the instrument and can be calculated using Eq. 4.19.

$$p_l(\theta, \lambda) = \frac{I_{\lambda,s}(l)}{I_{\lambda,s}} \quad (4.19)$$

After the calculation of $I_{\lambda,s}(l)$ for each layer Eq. 4.19 allows for assigning a weight to any path reaching the layer l of the vertical line. Therefore, Eq. 4.19 allows finding the path that contributes more significantly for the scattering of radiation along the vertical direction. This method is known as IWOP.

The equation that allows for the calculation of the AMF is given by Eq. 4.20 and it is a result of adding the gas profile in the sum (giving the SCD) and dividing by the vertical column.

$$AMF_g(\theta, \lambda) = \frac{\left\{ \sum_{l=MSL}^L \left[\sum_{\gamma(l)} \Delta s_{\gamma(l)}(\theta) \cdot \rho_g(\gamma(l)) \right] \cdot p_l(\theta, \lambda) \right\}}{\Delta z \cdot \sum_{l=1}^L \rho_g(l)} \quad (4.20)$$

where $\gamma(l)$ is the index along the path intersecting the vertical in the l layer, MSL is the Minimum Scattering level which is the minimal layer where the light is scattered and can be calculated with Eq. 4.21 where R_t is terrestrial radius.

$$MSL = R_t \left(\frac{1}{\cos(\theta - 90^\circ)} - 1 \right) \quad (4.21)$$

From the analysis of Eq. 4.20 it is possible to infer that AMF is not a constant value because it varies with some factors such as: a) the gases concentration profile, $\rho_g(\gamma(l))$, b) the SZA, θ , and c) the spectral region where the measurements are obtained due to the influence of wavelength in the light path.

4.4.2.2 PROCESSING OF MULTI-SCATTERED ATMOSPHERIC RADIATION – PROMSAR

PROMSAR is a radiative transfer model that considers the effects of multiple scattering by molecules and aerosols (Palazzi, 2005 a). It has been developed also by the ISAC-CNR Institute and it has been partially validated by comparison with other transfer models (Palazzi, 2005 c). Besides the computation of the effects of multiple scattering by molecules and aerosols, the PROMSAR model also give the possibility to calculate for example transmittances of the atmosphere, irradiances, radiance for a defined atmospheric scenario (Palazzi, 2008). It is

considered a more realistic model of the atmosphere than the AMEFCO model because PROMSAR considers also multiple, Rayleigh and Mie scattering. This is important because it gives a more accurate description of the optical properties of the scattered light leading to a better estimate of the SCD values of the trace gases under investigation.

The PROMSAR model considers that the atmosphere is modelled with a spherical 2D geometry and is divided into several layers. The model calculates the mean path of the radiation for each one of those layers taking into account the processes that solar radiation undergoes in each of them.

The mean path of photons is the main quantity computed by PROMSAR, and it is then employed to calculate the AMF of several trace gases making the ratio of the integral of the gas concentration along the photons-path (the SCD modelled values) with the vertical column of the analysed compound (Eq. 4.24).

The AMF can be estimated for different atmospheric scenarios and different quantities such as the position of the sun (SZA), the telescope Line of sight (LOS – the elevation of the optical device used for the measurements – in our case the MIGE), the aerosol profile in the atmosphere, radiation wavelength, for example. PROMSAR also allows for the calculation of the weighting functions needed for the calculation of trace gas vertical profiles using inversion methods.

This model is based on a backward Monte Carlo technique. This approach consists of using probabilistic methods to simulate the individual trajectories of individual photons in the atmosphere. In order to simulate the trajectories each starting photon is released from an imaginary source (the detector) in the LOS direction and is followed in a direction opposite to its true physical propagation. That is the reason for the name backward Monte Carlo (MC) scheme. After this each original photon is assigned a statistical weight (i.e. the source intensity) and their path in the atmosphere is traced. In general the process behind the generation of a path can be described as the transformation of random numbers generated by computer in probability density functions derived from basic scattering and absorption properties of the medium that lead to the deduction of the Free Optical Path (FOP) from Beer-Lambert Law. These random numbers also determine the type of scattering events that occur. The next procedure is forcing the photons to collide in order to access their new direction. The history of the photon (name given to simulations) continues after a fixed number of collisions and, as a result, a new path length is created. A detailed description of this approach can be found in literature (Palazzi, 2005a, 2005 b; Palazzi et al., 2008; Palazzi, 2008).

In summary: the input data necessary to run the PROMSAR code is the following: a) the features of the MC calculation like the receiver and the source description, batch strategy, etc. and b)

physical data needed to history tracking (simulations) for example absorption and scattering coefficients.

This physical data is available using the MODerate resolution TRANSmittance (MODTRAN) code. This code includes a variety of models of atmosphere including mid-latitude summer and mid-latitude winter models among others and are characterized by temperature, pressure and molecular density vertical profiles and for an accurate description of the scattering and absorption coefficients of molecules and aerosols and the Rayleigh and Mie phase functions.

To run the code some steps must be performed such as (Palazzi, 2008):

- the calculation of the gas slant column, SCD_g , according to equation 4.22.

$$SCD_g(\theta, \lambda) = \sum_{l=1}^L \Delta S_{mul}(l, \theta, \lambda) \cdot \rho_g(l) \quad (4.22)$$

where ΔS_{mul} is the mean photon path into the l^{th} layer computed by PROMSAR in units of centimeters (cm), the subscript mul denotes the multi-scattering process and ρ_g is the gas concentration in molecules/cm³ which is assumed to be constant in each layer, θ is the SZA. ΔS_{mul} varies with SZA and λ and meteorological parameters which characterize the atmospheres taken from MODTRAN code;

- the VCD_g integrating the number density of the considered absorber in the vertical direction over the modelled atmosphere given by equation 4.23:

$$VCD_g = \Delta z \cdot \sum_{l=1}^L \rho_g(l) \quad (4.23)$$

where Δz is the altitude step.

After these steps are fulfilled it is possible to calculate finally the AMF combining Eq. 4.22 and 4.23 according to Eq. 4.24.

$$AMF(\theta, \lambda) = \frac{\sum_{l=1}^L \Delta S_{mul}(l, \theta, \lambda) \cdot \rho_g(l)}{\Delta z \cdot \sum_{l=1}^L \rho_g(l)} \quad (4.24)$$

In spite of the multiple scattering approaches, the differences between the AMEFCO and PROMSAR results in terms of AMFs became noteworthy only for measurements in direction away from the vertical. This new configuration of measurements, called “Off Axis” or “MAX-DOAS” (Multiple AXis DOAS), is briefly presented in the next section.

4.4.2.3 Multiple Axis Differential Optical Absorption Spectroscopy (MAX-DOAS)

The MAX-DOAS configuration represents a significant advance, with respect to the Active and the Zenith sky DOAS, in terms of detectable species and temporal and spatial resolution of the data. This methodology utilizes scattered sunlight received simultaneously or quasi-simultaneously from multiple viewing directions. This method is particularly suitable for the monitoring of tropospheric compounds due to enhanced sensitivity of the off-axis technique (Palazzi, 2008) in the lower troposphere. This increase of sensitivity is due to the enhancement of the length for the tropospheric path that is bigger in the off-axis measurements which leads consequently to the increase in the amount of scattered radiation collected for the low elevation angles of the input device. The dependence of the stratospheric and tropospheric path lengths is function of different quantities: the first one (the stratospheric path length) is a function of SZA while the second one is depending on the variations in the instrument LOS. Therefore in the troposphere the measurements show more sensitivity using this new off axis technique since the atmospheric paths are longer in the viewing directions near the horizon.

Some problems can arise from the use of this technique. For example the AMF, essential for the determination of the vertical column of the analysed compound, have to be calculated accounting for the multiple scattering, since this optical process has an increased weight on the Off-Axis measurements (Fig. 4.11) . Combining the measurements with RTM calculations (that have taken in account the multiple scattering paths) and appropriate inversion techniques it is possible to retrieve the vertical profile information. The vertical resolution of the profiles can reach the 100-200 m in the lower troposphere.

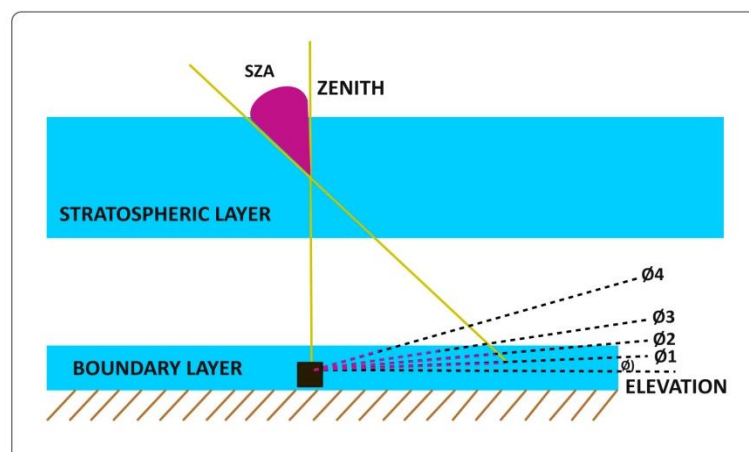


Figure 4.11- Illustration of the zenith sky and off-axis viewing geometry. It is possible to see the enhancement of absorption path length in the troposphere due to several off-axis viewing direction near the horizon (adapted from Heckel et al., 2005).

4.4.2.4 Reference spectrum

Actually, from the definition of the DOAS Master Equation, the SCD are differences between the content of the absorber in the analysed spectrum and the amount of the considered compound in the reference spectrum. Consequently, the SCD are effectively the DSCD (Differential Slant Column Density), therefore the choice of the reference spectrum and the quantification of absorber's content in it, are crucial task that are clarified in the following.

The reference spectrum - $I_0(\lambda, \theta_{\min})$ - used for the DOAS analysis has to be measured in optimal atmospheric conditions (sunny day without clouds) gathered at local noon. Therefore the optical thickness is smaller when compared with the other hours of the day, and due to the shortest optical path the absorption of the atmospheric compounds is minimal.

Depending on the type of study to be carried out, different reference spectrums have to be used for the DOAS processing: in case of assessment of tracer's seasonal/annual variations (climatic studies), only one $I_0(\lambda, \theta_{\min})$ is selected for the whole dataset analysis; to appreciate the diurnal changes in the SCD of the selected compound, the best choice is to use a daily reference spectrum.

The following procedure is mainly used for the selection of $I_0(\lambda, \theta_{\min})$ used for climatic studies. For some days near the summer solstice (highest sun elevation), the ratio between the "exposure" time and mean signal of the spectral series obtained by the spectrometer is calculated. This parameter is called Flux Index (FI) and it provides information on the variation of the incoming radiation quantity and can be used also for the first evaluation of the quality of the measured spectral data.

Fig. 4.12 shows the FI for 2 days under different meteorological conditions at the Évora station: a clear sky day and a cloudy day. For the first case the FI values describe a regular function during the day. In cloudy conditions, the FI can increase and turn irregular, mainly due to the increase in the forward scattering caused by the marked phase function asymmetry of the diffusing particles.

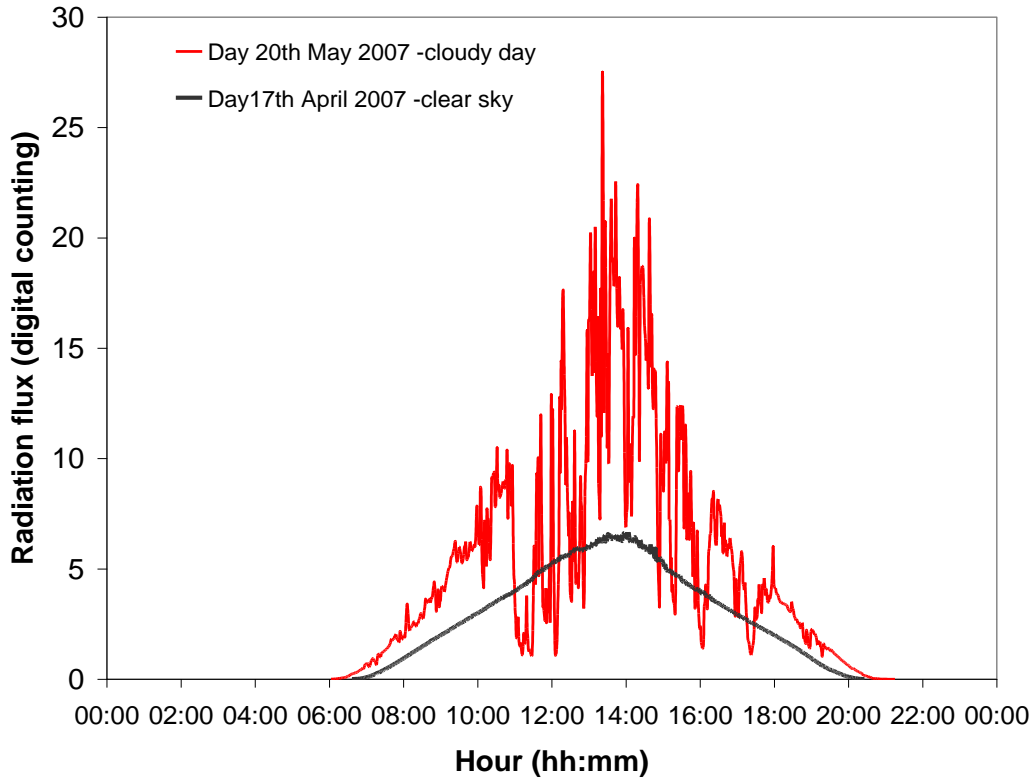


Figure 4.12- Ratio of the signal obtained by the spectrometer and its “exposure” time (Flux Index in ms/ digital counting) calculated at the Évora station for a clear sky day and cloudy day.

The best regular function corresponds to the reference spectrum selected for the DOAS processing.

At mid-latitudes, to estimate the content of the analyzed compound in the reference spectrum ($SCD_{I_0}(\lambda, \theta_{\min})$) the Langley plots of the retrieved values during one day, before the local noon (AM) and after the local noon (PM) versus the series of the calculated AMF values are usually used. The evaluation of the $SCD_{I_0}(\lambda, \theta_{\min})$ cannot be obtained by applying the DOAS algorithms to the reference spectrum itself, since the associated system will be singular. The $SCD_g(\lambda, \theta)$ can finally be calculated as follows:

$$SCD_g(\lambda, \theta) = DSCD_g(\lambda, \theta) + SCD_{I_0}(\lambda, \theta_{\min}) \quad (4.25)$$

4.4.2.5 Error assessment for SCD and VCD calculations

For the calculation of SCD and VCD errors it is necessary to turn to the residual variance definition (Wilks, 1995) given by Eq. 4.26.

$$s_e^2 = \frac{1}{n-2} \sum_{i=2}^n e_i^2 \quad (4.26)$$

where s_e^2 is residual variance, n is the number of data available in the sample and e_i is the residual that can be calculated using Eq. 4.27.

$$e_i = \left(\ln \frac{I_{\lambda,0}}{I_{\lambda,s}} - \overline{\ln \frac{I_{\lambda,0}}{I_{\lambda,s}}} \right) - \left(\sum_g \Delta\sigma_{\lambda,g} SCD_g(\theta) \right) \quad (4.27)$$

The last term of Eq. 4.26 is called Sum of Squared Errors (SSE) and can be calculated using Eq. 4.28.

$$SSE = \sum_{i=2}^n e_i^2 = \sum_{i=2}^n \left[\left(\ln \frac{I_{\lambda,0}}{I_{\lambda,s}} - \overline{\ln \frac{I_{\lambda,0}}{I_{\lambda,s}}} \right) - \left(\sum_g \Delta\sigma_{\lambda,g} SCD_g(\theta) \right) \right]_i^2 \quad (4.28)$$

There are also other errors associated to the results designed as “goodness-fit of measurements” from where it is possible to calculate the Var Slant Absorber (VSA), which is a quality parameter that results from the adjustment between the curves $\ln(I_{\lambda,0}/I_{\lambda,s}) - \overline{\ln(I_{\lambda,0}/I_{\lambda,s})}$ and $\sum_g \Delta\sigma_{\lambda,g} SCD_g(\theta)$. The VSA parameter can be calculated using Eq. 4.29 (Wilks,1995):

$$VSA = \frac{SSR}{SST} \quad (4.29)$$

where SST (Total Sum of Squares) is defined as being the sum, over all observations, of the squared differences of each observation from the overall mean given by Eq. 4.30:

$$SST = \sum_{i=1}^n (y_i - \bar{y})^2 = \sum_{i=1}^n \left[\left(\ln \frac{I_{\lambda,0}}{I_{\lambda,s}} - \overline{\ln \frac{I_{\lambda,0}}{I_{\lambda,s}}} \right) - \left(\overline{\ln \frac{I_{\lambda,0}}{I_{\lambda,s}} - \ln \frac{I_{\lambda,0}}{I_{\lambda,s}}} \right) \right]_i^2 \quad (4.30)$$

where SSR is the Regression Sum of Squares given by Eq. 4.31, defined as the sum of the difference between the parameter related to the regression, $y(x_i)$ and the mean of y , \bar{y} , given by Eq. 4.31:

$$SSR = \sum_{i=1}^n \left(\hat{y}(x_i) - \bar{y} \right)^2 = \sum_{i=1}^n \left[\left(\sum_g \Delta\sigma_{\lambda,g} SCD_g(\theta) \right) - \left(\overline{\ln \frac{I_{\lambda,0}}{I_{\lambda,s}} - \ln \frac{I_{\lambda,0}}{I_{\lambda,s}}} \right) \right]_i^2 \quad (4.31)$$

Note that $\overline{\ln(I_{\lambda,0}/I_{\lambda,s})}$ is a mean function while $\ln \frac{I_{\lambda,0}}{I_{\lambda,s}} - \overline{\ln \frac{I_{\lambda,0}}{I_{\lambda,s}}}$ is an arithmetic mean.

4.4.3 Retrieval of atmospheric trace gases profiles

4.4.3.1 Retrieval process / theory

The retrieval of the vertical distribution of atmospheric constituents from indirect measurements is a used common technique in atmospheric sciences and generalized to several types of instruments like ground-based spectrometers or even instruments onboard satellites. Therefore the solution of the inverse problem is one of the main challenges in the field of remote sensing. The solution to this problem is very useful in order to get information about a physical parameter (e.g. pressure, temperature, trace gas vertical profiles, etc.) that usually cannot be measured directly (using sensors such as radiometers, optical sensors, RADAR, LIDAR, etc.). In this sense we are able to convert observed measurements into information about a system.

The retrieval of an atmospheric trace gas profile using an absorption spectrum recorded by a ground-based instrument relies on the inverse theory. The case studies presented in this work deal with the use of the SPATRAM instrument measuring the UV-VIS (200-900 nm) radiation and with the processing the measured spectral data with DOAS algorithms to obtain the SCD of a trace gas (O₃ and NO₂). After that, the observed SCDs values are used to retrieve the VCD contents and also the vertical profile of those gases in the atmosphere.

In the following the inversion algorithms developed and applied to derive the vertical distribution of NO₂ are presented.

4.4.3.2 Algorithm to retrieve the NO₂ stratospheric vertical profiles

The slant column density of a trace gas for a certain wavelength (λ) and solar zenith angle (SZA) can be related to its concentration (C_g) at a given altitude (z) using equation 4.32 as described in § 4.4.1.

$$SCD_{\lambda}(SZA) = \int_0^z C_g(z) \cdot AMF_{\lambda}(SZA, z) \cdot dz \quad (4.32)$$

With the help of inversion techniques it is possible to determine the vertical profile of the gas (absorber) from Eq. 4.32 using only the variation in SCD with SZA measured by the instrument. If we analyse Eq. 4.32 it is possible to find a similarity between it and a Fredholm first kind integral (Eq. 4.33) which is a typically example of a linear inverse problem:

$$f(t) = \int_a^b k(t, s) \varphi(s) ds \quad (4.33)$$

where the function $k(t, s)$ is the kernel or kernel function where $t, s \in [a, b]$, which represents the relative contribution curve as a function of two variables t and s (can be for example a wavelength or the SZA, and height, respectively); $\varphi(s)$ is the required distribution. In remote sensing problems that involves radiation measurements a measurement made at a certain t_i involves radiation not just from a height (say s_i) but also from the neighbouring region where $k_i(s) = k(t_i, s)$ contribution is considered. If the interval between s and $s + \Delta s$ contributes to the i^{th} measurement the amount of radiation for that height will be $k_i(s)\varphi(s)\Delta s$. The total measured radiation will be $\int k(t, s)\varphi(s)ds$ and the limits for the integral depend on the extension of the observation. Looking to Eq. 4.33, the forward problem is the calculation of the integral when $\varphi(s)$ is given, whereas the inverse problem is the reconstruction of $\varphi(s)$ when $f(t)$ is provided (by observation at various t values) and the kernel is known. The solution of Eq. 4.33 (similar to Eq. 4.32) requires inversion to get the $\varphi(s)$ distribution. In order to solve Eq. 4.33 it is important to use numerical methods for inversion like the Optimal Estimation Method (OEM). The OEM is a generic algorithm formulated by Rodgers (Rodgers, 2000) for solving atmospheric inversion problems like for example solving the underdetermined problem that is deriving a trace gas profile of O_3 and NO_2 from an absorption spectrum. In applied statistics the optimal estimation is a regularized matrix inverse method.

We can rewrite Eq. 4.33 as an operator equation (Eq. 4.34):

$$\vec{f} = K\vec{\varphi} \quad (4.34)$$

with $(K\varphi)(t) = \int_a^b k(t, s)\varphi(s)ds, t \in R$. Comparing Eq. 4.32 with Eq. 4.33 it is possible to identify

the AMF as the kernel of Eq. 4.32. This means that the retrieval of the vertical profiles of the trace gases relies on forward model calculations of the changes in AMF and therefore in SCD as a function of SZA. The sets of AMF are used to generate the square matrix AMF_{ij} in which i represents the SZA and j the number of layers. For this study the vertical column was divided in 20 layers of 2.5 km thickness each from the ground up to 50 km altitude. This square matrix relates the change in apparent SCD of the gas in each layer of the model. This can be expressed by the following linear matrix model (Eq. 4.35) which is important to model the measurements through a RTM.

$$SCD_i^m = AMF_{ij} \cdot VCD_j \quad (4.35)$$

where SCD_i^m is the modelled/corrected slant column amount at a SZA i , AMF_{ij} is the air mass factor matrix at SZA i and at layer j and VCD is the vertical column density (or the concentration of the trace gas) in layer j . The forward model used in this study to calculate the weighting functions is the AMEFCO RTM. A forward model is a physical model that describes the measurement process (with a better accuracy than the measurement itself) and it may be an algebraic or algorithmic description. It is described as a model because there may supports physics which is still uncertain, or the real physics may be so complex that approximations are necessary.

To solve Eq. 4.35 in order to the concentration of the gas in each modelled layer it is necessary to get the inverse of AMF_{ij} (if it is a square and non-singular matrix) which is A_{ji} and solve the matrix equation Eq. 4.36.

$$VCD_j = A_{ji} \cdot SCD_i^o \quad (4.36)$$

where SCD_i^o is the observed SCD at SZA i .

For this study sets of SCDs and AMF were used to retrieve the O₃ and NO₂ vertical profiles using the OEM. Using the OEM it is possible to get a reasonable solution, despite the use of a unconstrained linear method in presence of noise that could lead to a wrong results (negative results) in some atmospheric layers. In order to get the solutions using this method we start to assume an initial guess profile of the trace gas VCD_j^{n-1} for the first iteration. To estimate a new concentration profile VCD_j^{n+1} Eq. 4.37 is used.

$$VCD_j^{n+1} = VCD_j^n \cdot \sum_{l=1}^{NL} \left[W_{jl} \cdot \frac{SCD_{k(j)}^0}{SCD_{k(j)}^m} \right] \quad (4.37)$$

where VCD_j^n is n^{th} iteration solution, NL is the number of layers in the model, W_{jl} are a set of weighting factors used to stabilize the convergence of the solution and $k(j)$ represents the solar zenith angle at which layer j has the largest AMF. For the calculation of the weighting factors we have to apply Eq. 4.38.

$$W_{jl} = \frac{AMF_{k(l)j}}{AMF_{k(l)l}} \quad (4.38)$$

For each layer l , W_{jl} can be normalized using Eq. 4.39.

$$W_{jl} = \frac{W_{jl}}{\sum_{j=1}^{NL} W_{jl}} \quad (4.39)$$

The number of interactions is limited by a maximum value that is imposed at the beginning for that or when the fitting error between the observed and modelled values is approximately the same as the estimated uncertainty in the observations.

4.4.3.3 Algorithm to retrieve the NO₂ tropospheric vertical profiles and tropospheric vertical columns

The main differences between the stratospheric and tropospheric vertical profile retrieval are: i) the different geometry of observation (Zenith-Sky/vertical looking and Multi Axis respectively); ii) the atmospheric model adopted (Fig 4.10); iii) the different forward model utilized (AMEFCO and PROMSAR). As seen in the previous section, for the stratospheric algorithms the SCD observations for different SZA values are related to the correspondent AMF series. For the tropospheric vertical distribution the almost simultaneous SCD observations, for different directions (called LOS - Line of Sight) of the radiation input device, are related to the simulated radiation paths for the correspondent LOS.

Also in this case, the profile retrieval method is based on the OEM described by Rodgers, 2000. The set of measurements, s , can be related to the vertical profile, z , using a forward model, M , as expressed by Eq. 4.40.

$$\bar{s} = M(\bar{z}, \bar{p}) + \delta \quad (4.40)$$

where \bar{p} is the vector of the forward model parameters; δ is the sum of the measurement error and of the model error, \bar{s} is the vector of SCD as a function of the LOS and wavelength obtained from the SPATRAM+MIGE spectral measurements using the DOAS method, and \bar{z} is the vertical profile of the trace gas of interest. The profile z is a continuous function in the real atmosphere, nevertheless the retrieval algorithm has to sample it discretely. Consequently the vertical profile is presented as a vector. The linear form of equation (4.40) is given by Eq. 4.41:

$$\Delta s = K \Delta z \quad (4.41)$$

where Δz is the perturbation in the vertical profile, Δs is the change in the slant columns due to the perturbation in the vertical profile and $K = \frac{ds}{dz}$. The rows of the K matrix are the weighting functions, and each row corresponds to a different measurement taken at a specific LOS and in a specific wavelength region. The weighting function characterizes the sensitivity of the measured slant columns \bar{s} to the variation of the vertical profile \bar{z} . The forward model used in this study to calculate the weighting functions is the PROMSAR Radiative Transfer Model. The PROMSAR provides the light paths that are then converted in the weighting functions of the K matrix. The solutions of the matrix equation 4.41 are the VCD values for each layer of the

atmospheric model of Fig. 4.11. The integration of the VCDs series for the *a priori* fixed altitude limits (typically 2km height with a resolution of 200m) gives the vertical distribution of the considered atmospheric compound.

Focusing the tropospheric part of the atmosphere, the concept of Differential Slant Column Density at the elevation angle ϕ ($DSCD_\phi$) (Fig. 4.11) need to be introduced and it is shown in the following equation:

$$DSCD_\phi = SCD_\phi - SCD_{90^\circ} = \frac{1}{\sigma} \log \left(\frac{I_{90^\circ}}{I_\phi} \right) \quad (4.42)$$

where the SCD_ϕ is the SCD for the trace gas at elevation angle ϕ , SCD_{90° is the SCD of the trace gas obtained for the zenith direction ($\phi=90^\circ$), I_{90° is considered the reference spectrum, i.e. the intensity that reaches the instrument from the zenith direction, I_ϕ is the intensity of solar radiation that enters the instrument at the elevation angle ϕ , and σ is the absorption cross section of the studied gas.

In order to convert the DSCD into a tropospheric trace gas column, a Differential Air Mass Factor ($DAMF_\phi$) given by Eq. 4.43 must be considered:

$$DAMF_\phi = AMF_\phi - AMF_{90^\circ} \quad (4.43)$$

where AMF_ϕ is the AMF related to the elevation angle ϕ and AMF_{90° is the AMF for the zenith direction. The PROMSAR model (instead of the AMEFCO) is used to perform the AMF's calculations since in the troposphere the effects of multiple scattering are more significant than in stratosphere due to the presence of more diffusers of solar radiation.

Combining Eq. 4.42 and 4.43 it is possible to achieve Eq. 4.44 which gives the tropospheric VCD for a given ϕ (VCD_ϕ).

$$VCD_\phi = \frac{DSCD_\phi}{DAMF_\phi} = \frac{SCD_\phi - SCD_{90^\circ}}{AMF_\phi - AMF_{90^\circ}} \quad (4.44)$$

For different elevations it is possible to obtain several values of VCD that will allow for the drawing of the tropospheric vertical profile of the considered trace gas.

In order to calculate the trace gas tropospheric content (VCD_{Trop}) it is necessary to integrate the tropospheric profile (obtained via Eq. 4.44) along the column using Eq. 4.45,

$$VCD_{Trop} = \sum_{j=1}^m VCD_{\phi_j} = \sum_{j=1}^m \Delta h_j \cdot c_j \quad (4.45)$$

where m is the partial vertical columns, j identifies the layers, Δh_j is the thickness of the partial column, c_j is the concentration of the partial column.

5. Results

5.1 Introduction

This chapter is divided in three parts as follows:

- total column variability of trace-gases (O_3 , NO_2 and BrO). All of these data are obtained applying the DOAS methodology to the measurements of diffused spectral sky radiation carried out along the zenith direction performed with the SPATRAM instrument. The forward model AMEFCO is used to retrieve the vertical column for the above mentioned atmospheric compounds ;
- vertical distributions of NO_2 . The profiles are retrieved with inversion methods presented in §4.4.3 applied to the output of the DOAS algorithms (the SCDs);
- air quality monitoring over the CGE-UE observatory in Évora-Portugal, using a synergy between the 'measured' SCDs and the back trajectories computed with the HYSPLIT model .

5.2 Measurement site description

Fig. 5.1 (left panel) shows the location of the Évora station in the South Western part of the Iberian Peninsula. Évora is located at about 130 km eastward from the Lisbon city area and about 100 km westward from Badajoz (Spain). Located in the interior of Portugal, Évora can be considered as a continental rural site having very low pollution levels. The surrounding areas are mainly rural with a small agriculture activity. In Fig. 5.1 (right Panel) the location of the observatory of the CGE is highlighted in the southwest part of the Évora downtown.

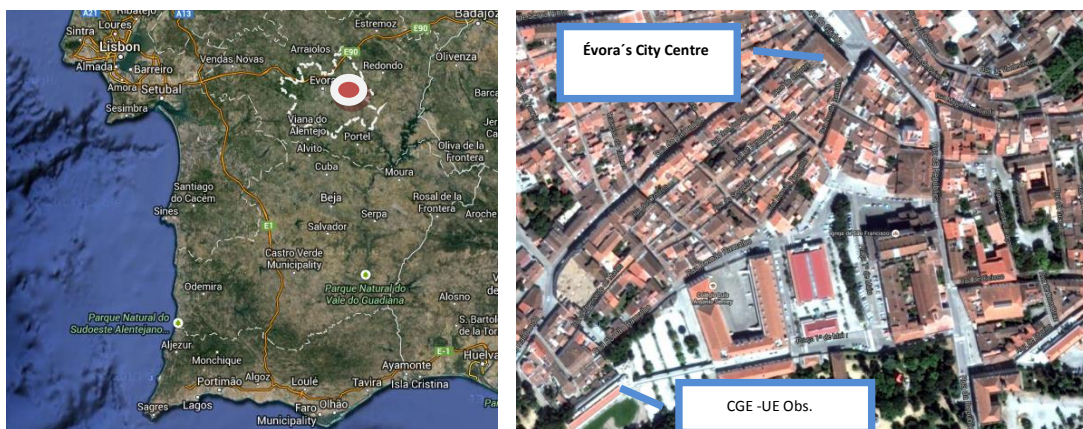


Figure 5.1- (Left Panel) Location of the Évora station in the South Western part of the Iberian Peninsula; (Right Panel) Évora city. SPATRAM + MIGE positioning at the Observatory of the Geophysics Centre of the University of Évora (adapted from Bortoli et al, 2009).

5.3 Total O₃, NO₂ and BrO variability from ground-based and satellite instruments over South of Portugal

This section includes the study of ozone, nitrogen dioxide and bromine oxide variability over Évora station –Portugal with remote sensing measurements. The instruments used for the measurements are the ground based spectrometer SPATRAM (for O₃, NO₂ and BrO) and instruments aboard satellites. The satellite data are obtained from the following sensors: OMI (for O₃, NO₂ and BrO), SCIAMACHY (for O₃ and NO₂), GOME (for O₃) and GOME-2 (METOP-A) (for NO₂) instruments. The SPATRAM measurements were done during the period of 2007-2011 at the Évora CGE-UE Observatory. This section comprises the study of daily and seasonal variability of those gases retrieved from the SPATRAM diffused spectral sky radiation measurements as well the comparison of the gases retrieved from the SPATRAM data with the corresponding data obtained from the above mentioned satellite sensors.

5.3.1 O₃ over Évora station for the period 2007-2011

To retrieve the O₃ Slant Column Density (SCD) values, the DOAS algorithms are applied in the 320-340 nm spectral range. The data obtained with SPATRAM instrument comprises all the solar zenith angles (SZAs) between the highest daily solar elevation (minimum SZA) down to approximately 93° of SZA.

5.3.1.1 O₃ diurnal variation

In order to investigate the O₃ diurnal variation, the values of SCD for this compound are plotted versus the SZA values during one typical day (Fig. 5.2). Aiming to distinguish the SCDs values before and after the local noon, the SCD time series is split in 2 different series: the AM SCD data for the values from the sunrise to the local noon, and the PM SCD time series for the local noon – sunset temporal period.

As expected the O₃ SCDs vary during the day with the SZA. The SCDs values are strongly dependent on the Sun position: actually, referring to figure 4.10 explaining the atmospheric model adopted, and Eq. 4.11 defining the SCD, it can be noted that for the lowest values of SZA (local noon) the optical path of measurement is minimum leading to the minimum value for the SCD value; on the other hand, for values of SZAs towards the sunset or from the sunrise period the optical paths travelled by the radiation entering the instrument increase resulting in the increasing values for the SCDs. In this frame the maximum SCD value should be expected for SZA even greater than 90° due to the increased optical path, but not for SZA of 87° as it can be seen

from Fig. 5.2. This behavior is caused by the attenuation of the UV radiation (320-340nm spectral range) with the increase of the SZA.

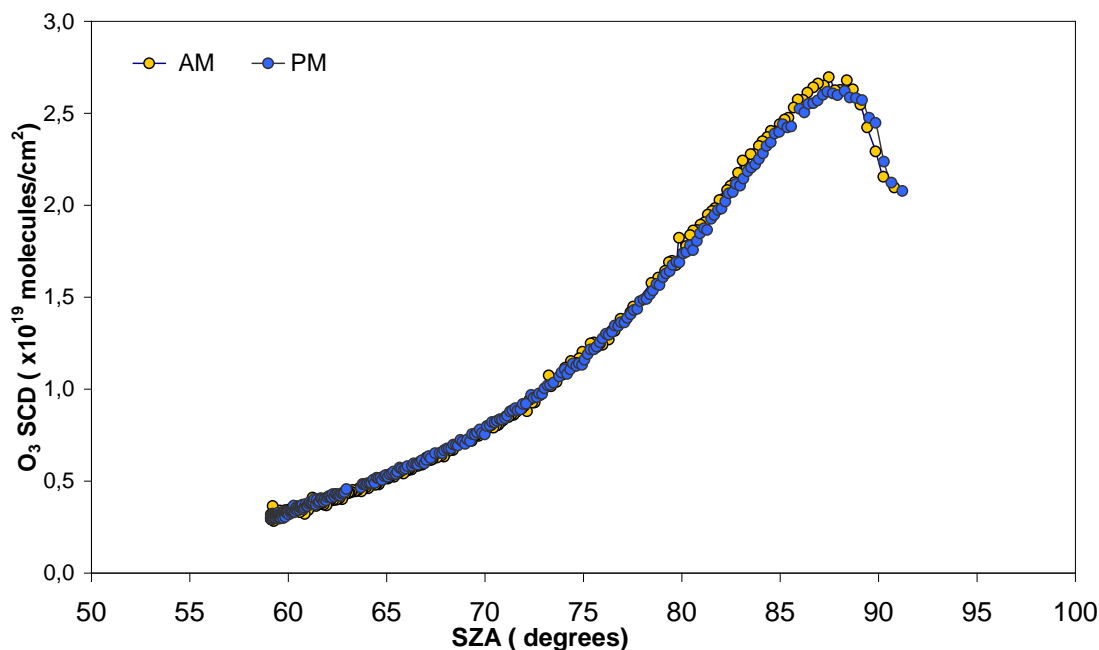


Figure 5.2- Time series of the O₃ Slant Column Density (SCD) in molecules/cm² obtained with the SPATRAM equipment installed at Évora Observatory for the 19th January 2007.

The uncertainties associated to the SCD values are minima since they are originated only by the DOAS algorithms and measurements' systematic errors. Nonetheless, for climatic as well as for air quality studies, the scientific community utilizes the integrated concentration along the vertical direction (VCD - Vertical Column Densities) of the different atmospheric compounds. As detailed presented in section 4.4.2, the VCDs values are the ratio between the SCDs and the Air Mass Factor (AMF). Therefore for the error theory the uncertainty related to the VCD is higher than the ones of the SCD.

Due to the wavelength dependency of the AMF, different run of the forward model utilized for the computation of the AMF (in this case the AMEFCO RTM) were performed, in order to obtain the AMF time series with the best fit to the SCDs values. Fig. 5.3 shows the best AMF function obtained almost perfectly coincident with the SCDs (AM and PM) time series.

The VCD time series correspondent to the SCDs values presented in Fig. 5.3 is shown in Fig. 5.4. The VCD values (or Total Column –TC) are more meaningful than the SCD, even if the inaccuracies increase significantly (§4.4.2.5). The TC are widely used in studies regarding year to year or seasonal variations/fluctuations of the analysed compound.

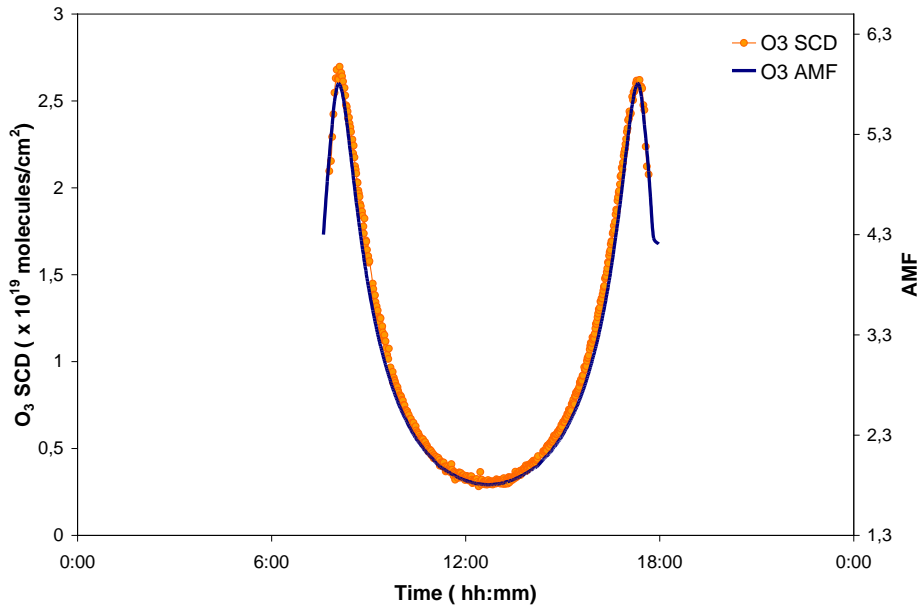


Figure 5.3- O₃ Slant Column Densities (SCD) values and Air Mass Factor (AMF) versus time for the 19th January 2007 over Évora retrieved from SPATRAM measurements.

The daily mean of the data presented in Fig. 5.4 , is of (299 ± 3) DU, and as a first data validation/comparison the TOC (Total Ozone Column) value for the same day measured with the OMI instrument (not shown), is of (302 ± 3) DU. The same diurnal behaviour is observed for the whole considered period (2007-2011), although the O₃ VCD values follow a seasonal pattern as presented in next section.

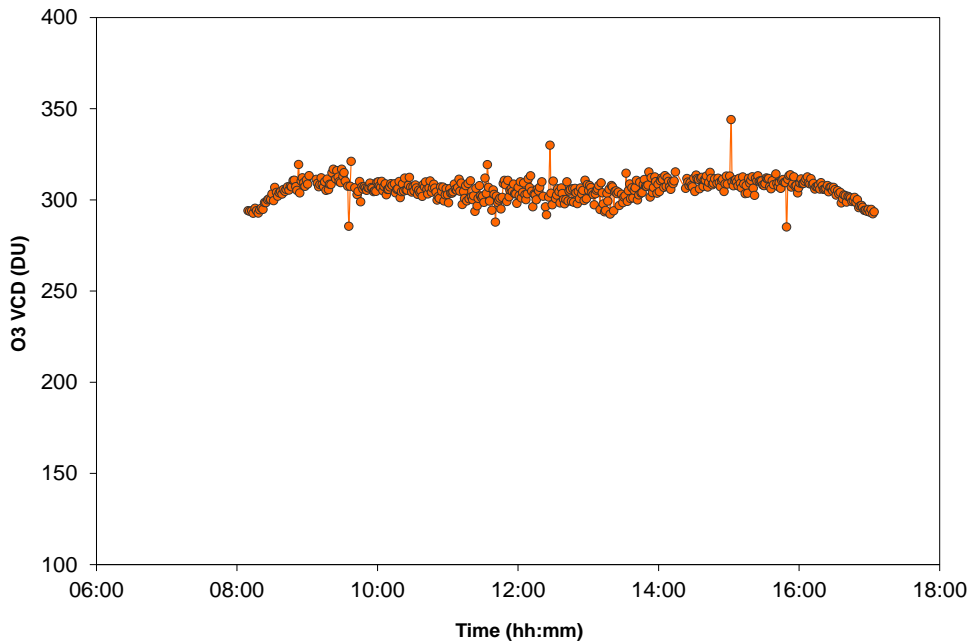


Figure 5.4- O₃ Vertical Column Densities (VCD) for the 19th January 2007 over Évora retrieved from SPATRAM measurements.

5.3.1.2 O₃ seasonal variation

In Fig. 5.5 the time series of the mean daily O₃ VCD retrieved from measurements of the SPATRAM instrument are plotted for the period March 2008 – March 2009. As expected, a clear seasonal trend of the plotted values emerges, following a sinusoidal pattern due to the relation between solar activity and O₃ photochemical behaviour. The seasonal behaviour of O₃ registered at Évora's Observatory using SPATRAM instrument is consistent with the literature for the northern mid-latitudes where the maximum values are found in spring and the minimum values in autumn. At mid-latitudes and specifically over the Iberian Peninsula the strong seasonal variability of the daily O₃ total columns are probably caused by:

- a) dynamical processes such as Dobson-Brewer circulation (Antón et al., 2008, 2009), changes in the position of tropopause, North Atlantic Oscillation (NAO) e.g.,
- b) chemical processes such the polar vortex in the middle latitudes that exports ozone poor vortex air or chemically activated ClO rich air from poles to that latitudes,
- c) injection of aerosols into the atmosphere which induce radiative, chemical and dynamical perturbations.

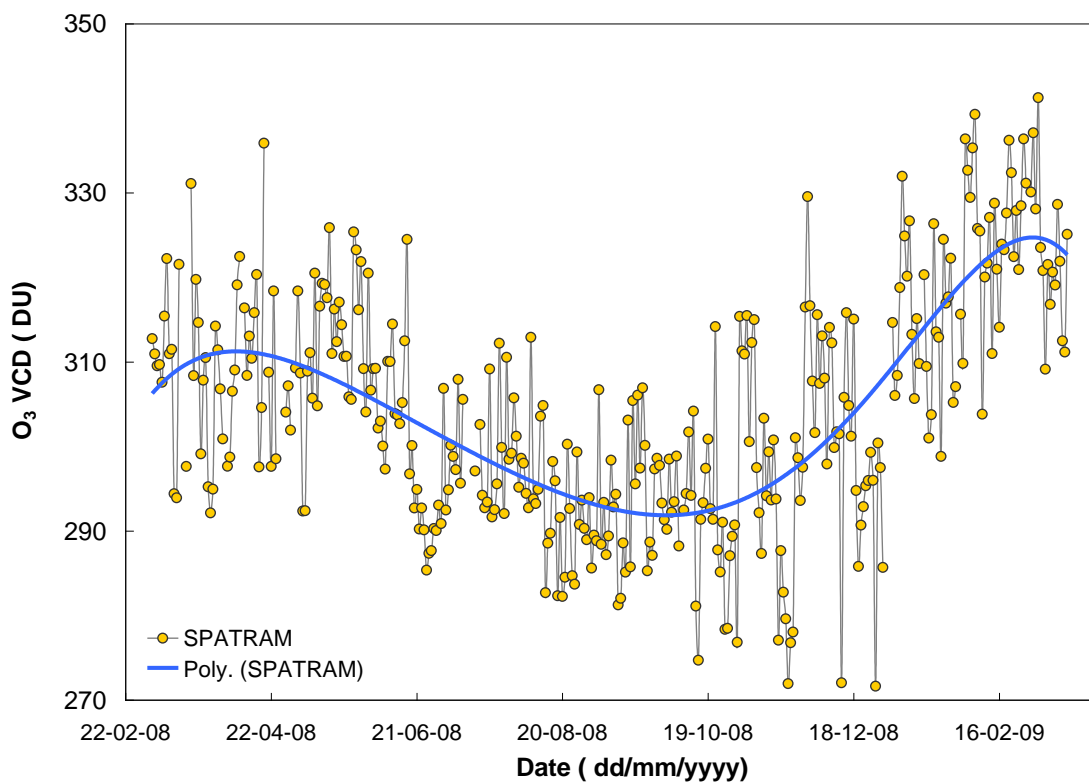


Figure 5.5- Time series of the O₃ VCD obtained with the SPATRAM equipment installed at Évora Observatory during March 2008 - March 2009 period.

The validation of SPATRAM data at Évora station is made using only satellite data. At the Observatory of CGE there is no other instrument measuring O₃ total column. Anyway, a comparison study is presented in the paper by Antón et al., 2010, between SPATRAM (installed at Évora Observatory) and a Brewer Spectrophotometer installed at the Atmospheric Sounding Station of the Spanish Institute for Aerospace Technology (INTA) located at the El Arenosillo station in Spain (37.04° N, 6.44° W, 20 m a.s.l.). The INTA station is part of the Global Atmosphere Watch network (GAW 213) and the Brewer spectrophotometer there installed is a well calibrated instrument measuring Total Ozone Columns (TOC) since the 90's with a good accuracy (Antón et al. 2010). This instrument is used in several validation essays using sensor's data (GOME, GOME-2 and OMI) from satellites and present good agreement between them. Although the two instruments are separated of about 190 km this is considered a small distance in comparison with the homogeneity of the stratospheric ozone. For the period 2006-2008, the two instruments show a good agreement (R² between 0.85 and 0.88) although they have different viewing geometries and use different AMF values.

The SPATRAM instrument has also participated in a field comparison campaign at El Arenosillo station where the data were validated with data from a Brewer spectrophotometer and from several ozone soundings. The results of this inter-comparison exercise are not yet published.

5.3.1.3 Ground based and satellite dataset

5.3.1.3.1 O₃ VCD - SPATRAM vs OMI

Here, the SPATRAM data are compared to OMI dataset. The OMI sensor recorded daily TOC measurements from 1 October 2004 to present. There are two different algorithms that derive total ozone values from OMI: i) the OMI- Total Ozone Mapping Spectrometer (TOMS), ii) the OMI- Differential Optical Absorption Spectroscopy (DOAS).

The first OMI dataset used for this comparison is called **OMTO3** (Level-2 OMI Total Ozone OMI/Aura Ozone Total Column 1-orbit L2 Swath 13x24 km (V003)). The algorithm used is based on the TOMS V8 algorithm method (for the description of the algorithm see http://disc.sci.gsfc.nasa.gov/Aura/data-holdings/OMI/documents/index.shtml/omto3_v003.shtml).

This algorithm performs measurements at the following wavelength centered bands: 313, 318, 331 and 360 nm (Kroon et al., 2008). One of the particularities of this product is that is possible to get the dataset for the overpass of the satellite over several coordinates. For Évora Observatory it is freely available at ftp://toms.gsfc.nasa.gov/pub/omi/data/overpass/aura_omi_l2ovp_omto3_v8.5_evora_999.txt.

The second product used is called **OMDOAO3** (Level-2 OMI DOAS Total Column Ozone-OMDOAO3 (V003)). It is based on the DOAS method as the name suggests. The algorithm allows for the measurements in the 331.1 nm up to 336.6 nm wavelength range. For detailed description of the algorithm see Veeffkind et al., 2006. The product OMDOAO3 data over Évora Observatory is available at http://www.temis.nl/protocols/o3col/data/omi/overpass/Evora_Observatory_omdao3.dat. Fig. 5.6 shows the comparison of the SPATRAM data with OMI (TOMS) – OMTO3 data.

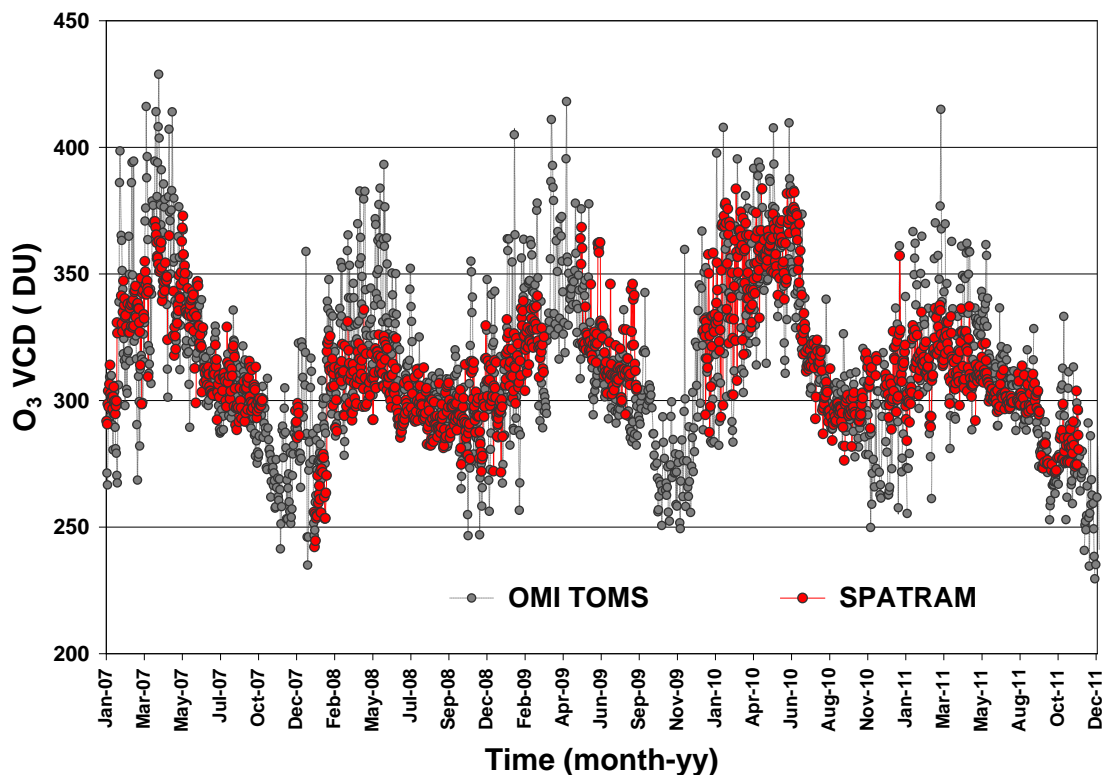


Figure 5.6- Full time series of the O₃ VCD obtained with the SPATRAM equipment installed at Évora Observatory during 2007-2011, and the O₃ data from the OMI (TOMS) - OMTO3 instrument aboard the NASA EOS- Aura Satellite.

The comparison between the SPATRAM and the OMTO3 data presents the same seasonal behaviour. However, the values of O₃ VCD from the SPATRAM instrument are normally lower than the ones derived from the OMI satellite instrument. The mean error of the comparison is of about 4% with higher values during the spring seasons (7- 9%).

It can be seen also an inter-annual variability in both O₃ data set values. In summer periods the O₃ VCD values have tendency to decrease as autumn approaches, but in 2008 this reduction is not so pronounced as in 2007, as it can be seen in Fig. 5.6. In 2010 the decrease is again more pronounced. The possible causes for this behaviour maybe due to the influence of solar cycle,

volcanic aerosols present in atmosphere (eruption of Eyjafjallajökull in April/May 2010) and the release of anthropogenic pollutants from power plants and industries in the big cities nearby. A linear regression analysis on the Total Ozone Columns (TOC) values from SPATRAM and OMI (TOMS) data was also performed and it is presented in Fig.5.7.

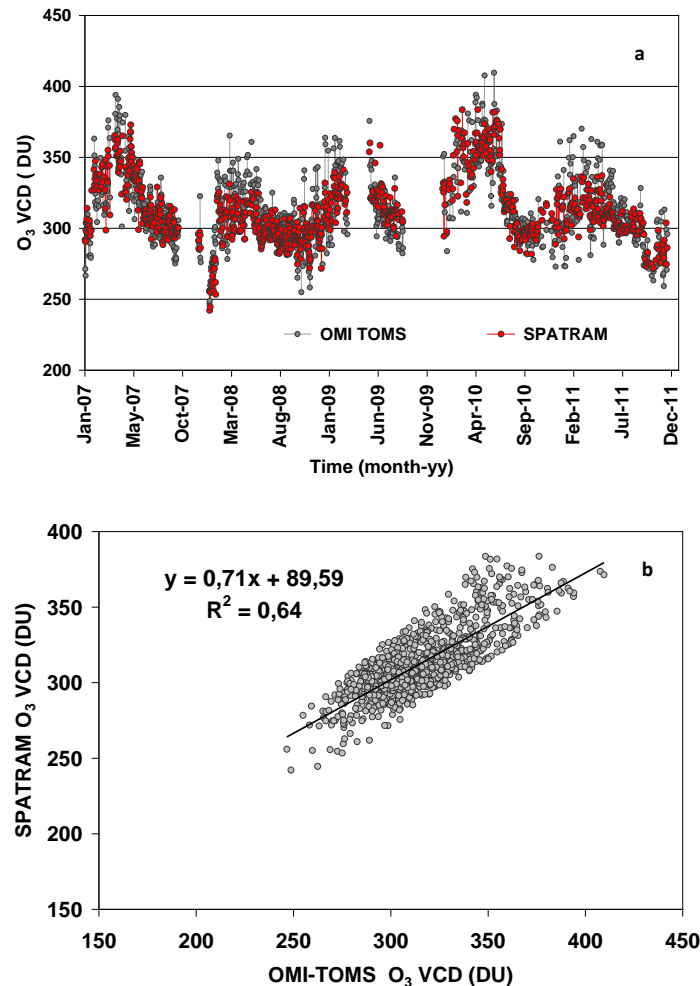


Figure 5.7- a) Filtered time series of the O₃ VCD obtained with the SPATRAM equipment at Évora during 2007-2010, and the O₃ data from the OMI (OMI-TOMS) b) Scatter plot of the O₃ data from the OMI instrument (OMI-TOMS OMTO3 product) aboard the NASA EOS - Aura satellite versus O₃ SPATRAM data retrieved at Évora Observatory during 2007 – 2011 period.

In this plot (Fig.5.7) only the data from the OMI time series obtained for a distance lower than 50 km from the Évora station, are taken into account (number of data N= 986). Also for the other sensors the same distance was taken in account. The SPATRAM data and the “filtered” OMI dataset have a reasonable agreement as evidenced from the correlation coefficient obtained ($R^2 = 0.64$).

Since there are two available products from OMI the comparison with OMDOAO3 dataset is also performed and presented in Fig. 5.8. This figure illustrate the time series of the O₃ VCD obtained with the SPATRAM equipment installed at Évora Observatory and the O₃ data from

the OMI (DOAS) instrument aboard the EOS- Aura Satellite. It is possible to infer that that SPATRAM data also follows the same sinusoidal shape as the OMI (DOAS) data.

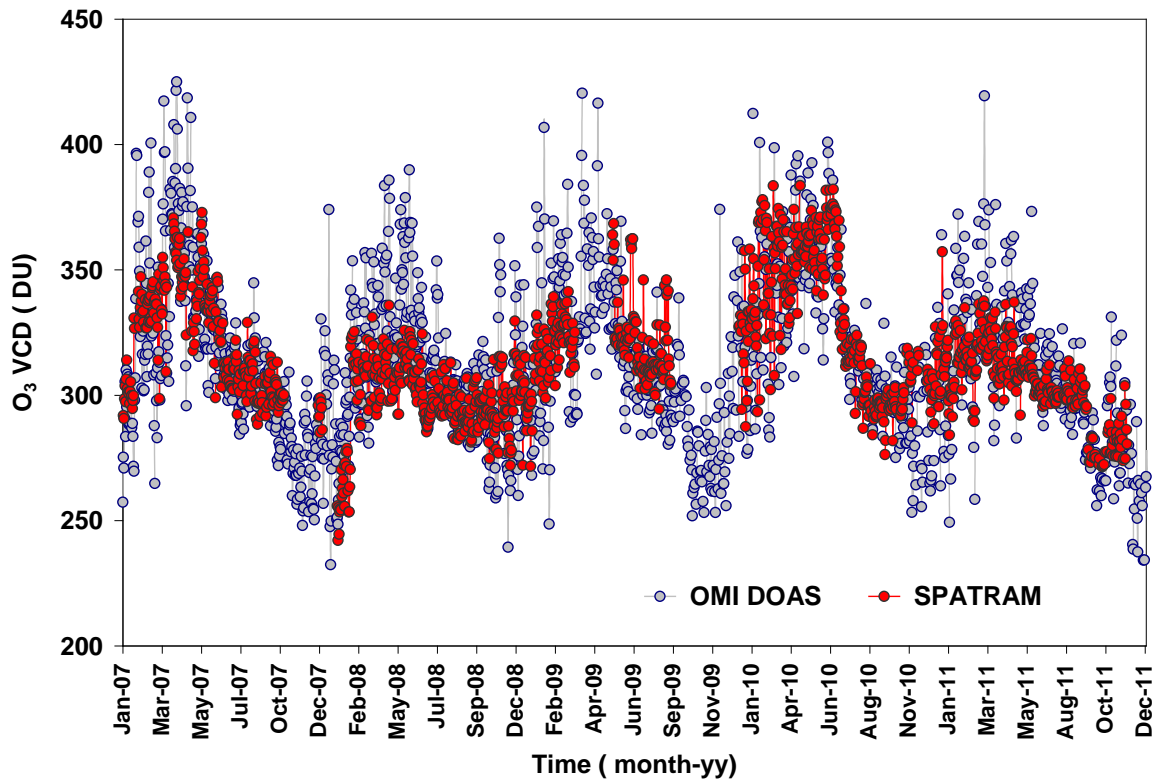
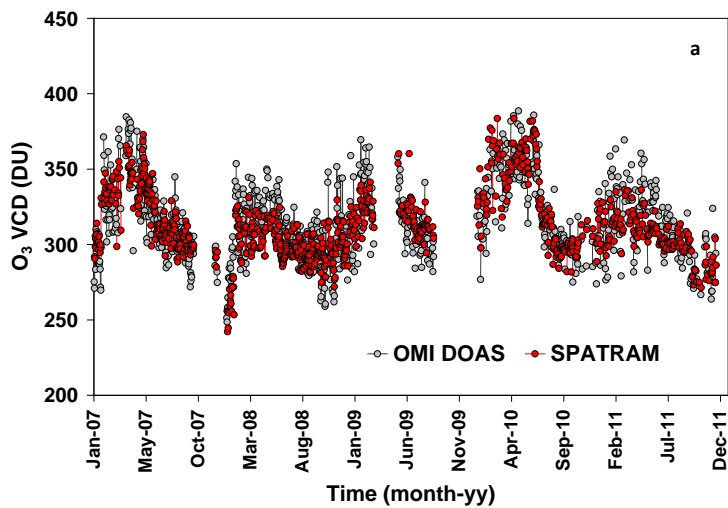


Figure 5.8- Full time series of the O₃ VCD obtained with the SPATRAM equipment installed at Évora Observatory for the SZA of 87°, during 2007-2011, and the O₃ data from the OMI (DOAS) instrument aboard the EOS- Aura Satellite.

The scatter plot derived from the comparison of this two dataset is presented.



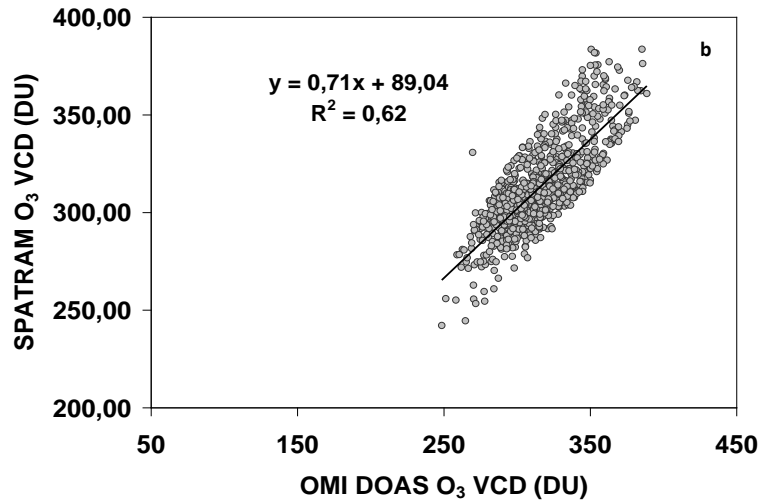


Figure 5.9- a) Filtered time series of the O₃ VCD obtained with the SPATRAM equipment at Évora during 2007-2010, and the O₃ data from the OMI (OMI-DOAS). b) Scatter plot of the O₃ data from the OMI instrument (OMI-DOAS OMDOA3 product) aboard the NASA EOS - Aura satellite versus O₃ SPATRAM data retrieved at Évora Observatory during 2007 - 2011 period.

From the analysis of the latter figures it is possible to infer that there is a fairly agreement between the two instruments ($R^2=0.62$). The mean error of the comparison is of about 4.11 %. Next, in Table 5.1 the maximum and minimum values ± 1 standard deviation from OMI- DOAS are presented. For the other instruments (SCIAMACHY, GOME-2) and also for OMI-TOMS the data is not available for all days. Therefore the comparison is not made with their dataset.

The maximum values of O₃ total columns obtained with SPATRAM vary between 336 and 384 DU. The minimum values change from 242 to 285 DU during 2007-2011.

Table 5.1- O₃ total columns maximums and minimums values obtained with SPATRAM ± 1 standard deviation from OMI- DOAS for the period 2007-2011 over Évora-Portugal.

	Maximum (DU)	Minimum (DU)
2007	(373 \pm 3) 22 nd May 2007	(285 \pm 9) 18 th December 2007
2008	(336 \pm 50) 19 th April 2008	(242 \pm 6) 19 th January 2008
2009	(364 \pm 37) 25 st May 2009	2009 (294 \pm 11) 13 rd August
2010	(384 \pm 2) 21 st April 2010	(276 \pm 31) 19 th September 2010
2011	(338 \pm 39) 14 th March 2011	(271 \pm 5) 11 st October 2011

5.3.1.3.2 O₃ VCD - SPATRAM vs SCIAMACHY

The ESA usable algorithm for SCIAMACHY is called **Total Ozone retrieval scheme for SCIAMACHY based on the OMI DOAS algorithm** or **TOSOMI** (Eskes et al., 2006) and subsequently in GOME algorithm **TOGOMI** (Valks et al., 2004). This algorithm allows for the retrieval of Ozone columns from SCIAMACHY and was developed by the Royal Netherlands Meteorological Institute (KNMI). Although all of the three algorithms are similar TOSOMI presents improvements in comparison with OMI's and GOME's (Eskes et al., 2005) like:

- treatment of the atmospheric temperature sensitivity by using effective ozone cross-sections calculated from ECMWF temperature profiles,
- improvements in the calculation of the air mass factor, using the so-called empirical approach,
- use of the Fast Retrieval Scheme for Clouds from the Oxygen A-band (FRESCO) algorithm for the cloud correction,
- a new treatment of Raman scattering in DOAS that accounts for the smearing of the solar Fraunhofer lines as well as the atmospheric tracer absorption structures,
- use of air-mass factors based on semi-spherical polarization-dependent radiative transfer model (KNMI DAK).

A complete description of the algorithm can be found at Eskes et al., 2006.

TOSOMI product is freely available over several locations including Évora Observatory.

Ozone data can be downloaded at:

http://www.temis.nl/protocols/o3col/data/scia/overpass_v2/Evora_Observatory_tosomi.dat

From the analysis of Fig. 5.10 it is possible to infer that SPATRAM data is also consistent with SCIAMACHY data.

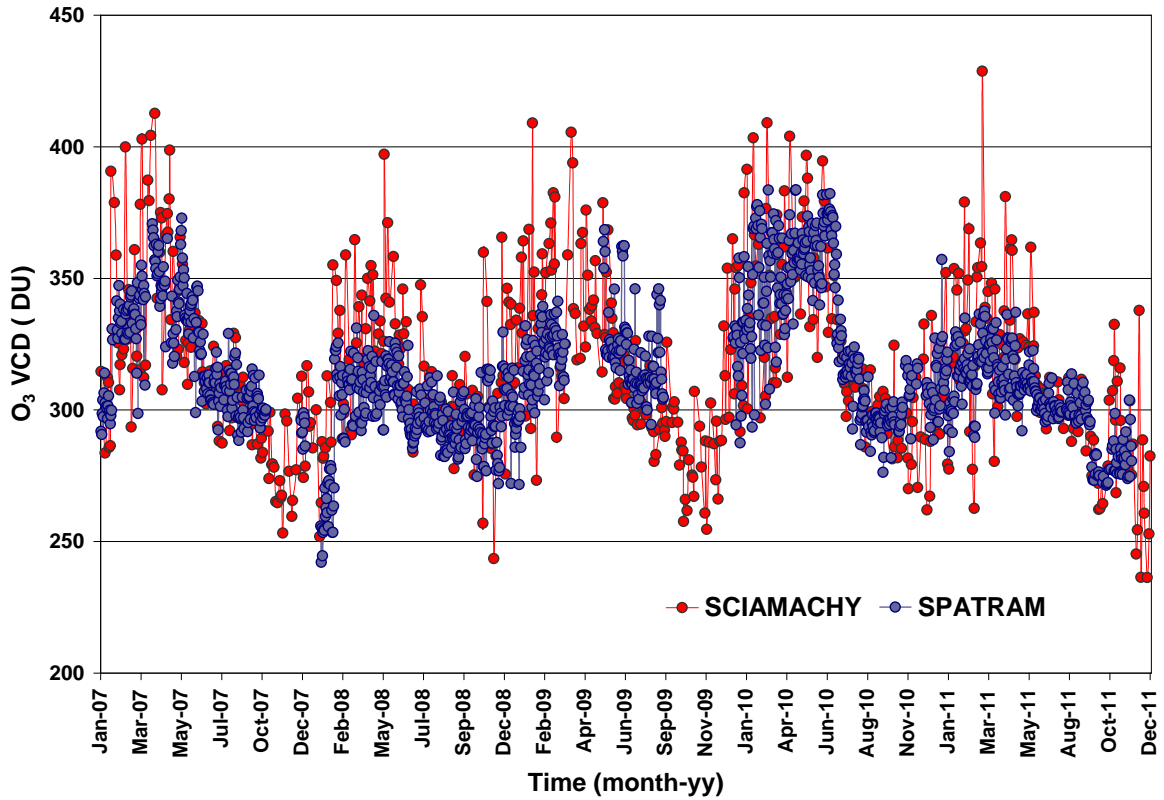
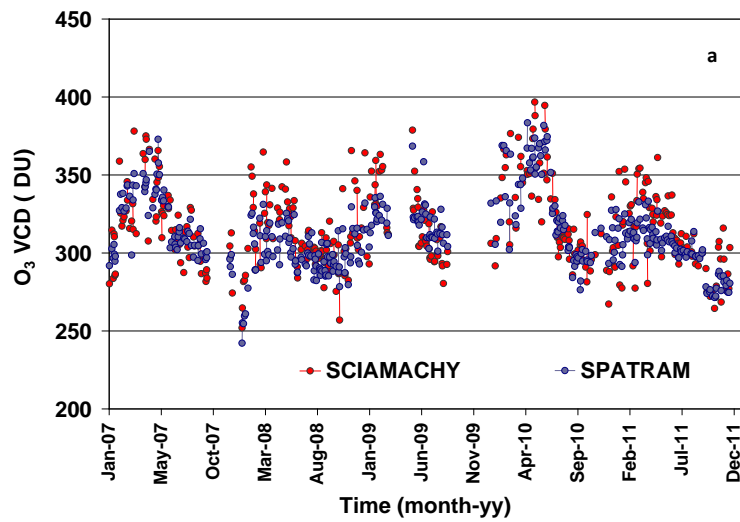


Figure 5.10- Full time series of the O₃ VCD obtained with the SPATRAM equipment installed at Évora Observatory during 2007-2010, and the O₃ data from the SCIAMACHY instrument aboard the ENVISAT satellite.

By the analysis of the scatter plot (Fig. 5.11) it can be noted that the correlation between the two dataset is in agreement with a Pearson's coefficient of $R^2=0.63$. The deviation from the satellite sensor associated is about 4.15%, similar to the previous values obtained with the other satellite data.



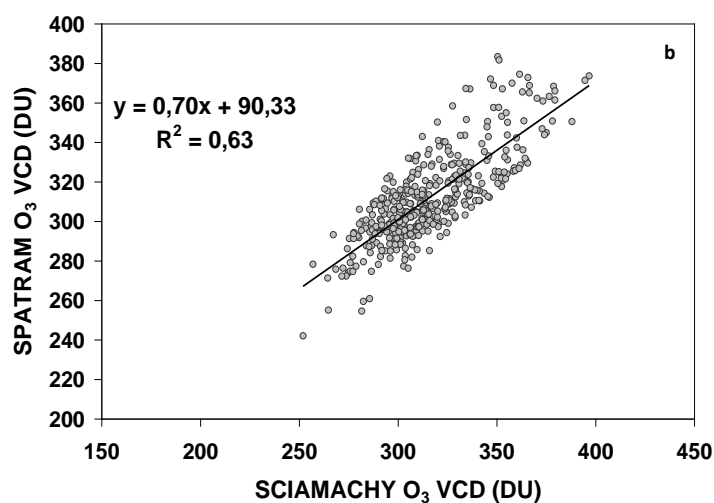


Figure 5.11-a) Filtered time series of the O₃ VCD obtained with the SPATRAM equipment at Évora during 2007-2010, and the O₃ data from the SCIAMACHY. b) Scatter plot of the O₃ data from the SCIAMACHY instrument (TOSOMI product) aboard the ENVISAT satellite versus O₃ SPATRAM data retrieved at Évora Observatory during 2007 - 2011 period.

5.3.1.3.3 O₃ VCD - SPATRAM vs GOME

The GOME dataset is available from 1995 to 2011. For the Évora Observatory the data is freely available at:

http://www.temis.nl/protocols/o3col/data/gome/overpass/Evora_Observatory_togomi.dat
for the considered period (2007-2011).

The algorithm used for measuring trace gases that is current in operation is the GOME total ozone algorithm TOGOMI and was developed under ESA supervision by the German Aerospace Centre (DLR). It is based on the total ozone DOAS algorithm and it is divided in four steps: a) enhancement of the accuracy of the measured Earth radiance and solar irradiance spectrum b) achievement of the SCD using the fitting of reference differential absorption spectrum of ozone and the measured Earth radiance spectrum and solar irradiance spectrum c) conversion of the SCD into the Vertical Column Density using the AMF correction factor d) correction of cloud effects (Valks, 2003).

More information about the algorithm can be found at literature (Valks et al., 2004).

Fig. 5.12 shows the comparison of SPATRAM and GOME datasets.

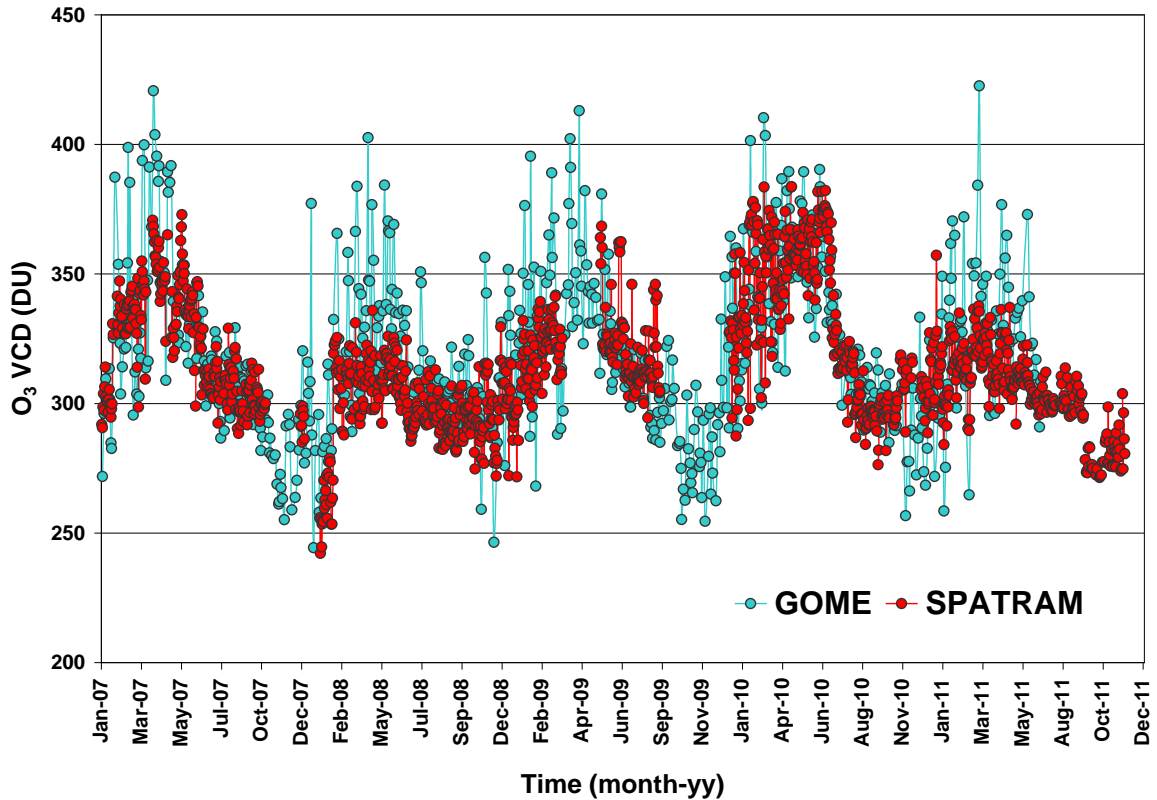


Figure 5.12- Full time series of the O₃ VCD obtained with the SPATRAM equipment installed at Évora Observatory during 2007-2010, and the O₃ data from the GOME instrument aboard the ERS-2 satellite.

The variation of ozone shows the same pattern as the GOME instrument data. The comparison between the SPATRAM and the GOME data describes the same seasonal behavior that was described above. However, the values of O₃ VCD are normally lower than the ones derived from the OMI satellite instrument.

The mean error of the comparison is of about 4.23% with higher values during the spring seasons.

In Fig. 5.13 the scatter plot of the SPATRAM and GOME filtered dataset is plotted. The SPATRAM data and the GOME dataset are in agreement as evidenced from the correlation coefficient obtained ($R^2 = 0.60$). It is important to say that the GOME dataset was also filtered, as equal for all the satellite sensor's dataset, to include only the values that are more approximate from the observatory.

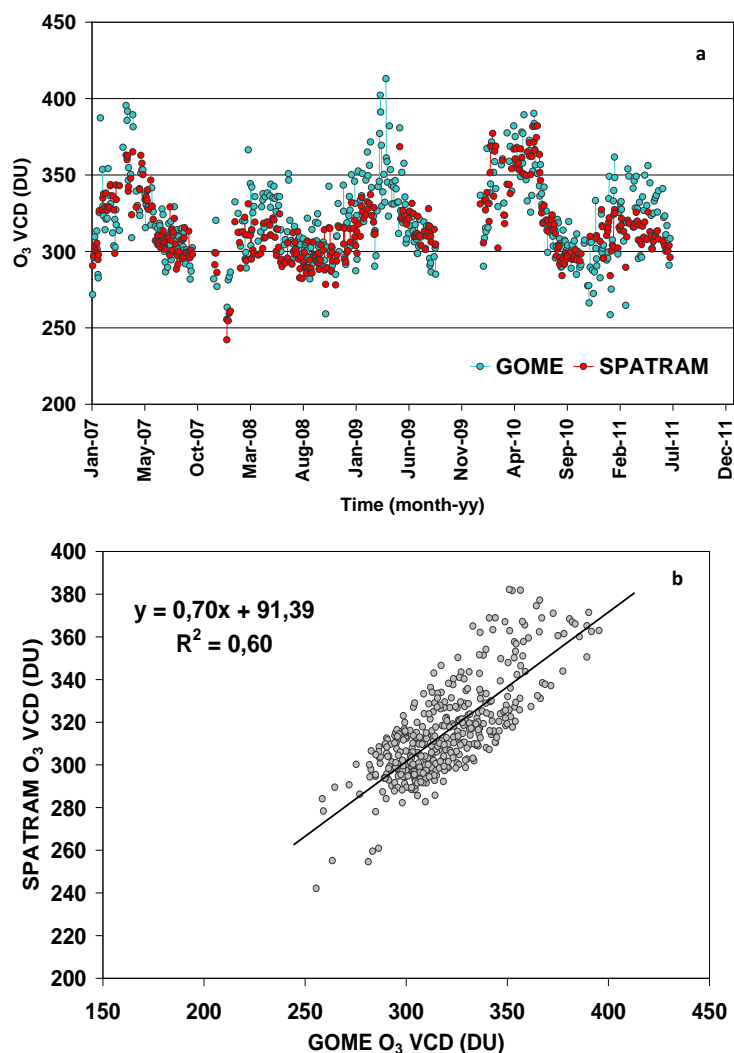


Figure 5.13- a) Filtered time series of the O₃ VCD obtained with the SPATRAM equipment at Évora during 2007-2010, and the O₃ data from the GOME. b) Scatter plot of the O₃ data from the GOME instrument aboard the ERS-2 satellite versus O₃ SPATRAM data retrieved at Évora Observatory during 2007 - 2011 period including the regression line (black line).

5.3.1.3.4 Statistical analysis

The evaluation of some statistical parameters is made in order to validate the SPATRAM data. The presented parameters are related to the comparison of SPATRAM data and each one of the satellite instruments. The values are presented in Table 5.2 and concern to the number of data (N), the slope and the correlation coefficient (R^2) of the scatter plots (Figs. 5.7, 5.9, 5.11, 5.13) and the Root Mean Square Error (RMSE). This latter parameter is frequently used to represent the sample standard deviation of the differences between predicted values (in a model) and observed values (in the real atmosphere). The RMSE is defined as the square root of the mean squared error calculated using Eq. 5.1 and is a measure of the spread of data around the regression line.

$$RMSE(\%) = 100 \sqrt{\frac{1}{N} \sum_{j=1}^N \left(\frac{SPATRAM_{model,j} - SPATRAM_{obs,j}}{SPATRAM_{obs,j}} \right)^2} \quad (5.1)$$

where $SPATRAM_{obs}$ are observed values and $SPATRAM_{model}$ are modelled values calculated using the equation of regression line of the scatter plots (Eq. 5.2)

$$SPATRAM_{model,j} = a + b \cdot Sat.Sensor_j \quad (5.2)$$

where a is the slope, b is the intercept and $Sat.Sensor$ are the values available from the sensors (OMI, SCIAMACHY and GOME) aboard the satellites.

In Table 5.2 the Mean Bias Error (MBE) and the Mean Absolute Bias Error (MABE) are also presented which are two statistical parameters computed using Equations 5.3 and 5.4.

$$MBE(\%) = \frac{100}{N} \sum_{j=1}^N \frac{Sat.Sensor_j - SPATRAM_j}{SPATRAM_j} \quad (5.3)$$

$$MABE(\%) = \frac{100}{N} \sum_{j=1}^N \frac{|Sat.Sensor_j - SPATRAM_j|}{SPATRAM_j} \quad (5.4)$$

Table 5.2 - Correlation analysis of SPATRAM, OMI (TOMS), OMI (DOAS), GOME and SCIAMACHY total ozone data for the period of 2007-2011.

	N	Slope	R ²	RMSE (%)	MBE(%)	MABE(%)
OMI-TOMS	986	0.71	0.64	4.25	0.83 ± 0.15	4.09 ± 0.09
OMI- DOAS	913	0.71	0.62	4.36	1.15 ± 0.23	5.46 ± 0.15
SCIAMACHY	405	0.70	0.63	4.35	1.28 ± 0.25	4.24 ± 0.14
GOME	409	0.70	0.60	4.36	1.04 ± 0.25	4.33 ± 0.14

From the analysis of Table 5.2 it can be inferred that the best correlation found for the SPATRAM data for the period of 2007-2011 is the OMI- TOMS dataset. In all datasets can be seen that in most days the SPATRAM values are lower than the other sensors. Therefore there is an underestimation of the SPATRAM instrument that can be seen by the positive sign in MBE values (see Table 5.2).

The differences found between the SPATRAM and OMI-TOMS, OMI-DOAS, SCIAMACHY and GOME instruments could be due to several facts such as:

- the satellite data presented in Figs. 5.6, 5.8, 5.10 and 5.12, are the O₃ total column values corresponding to the daily overpass of the AURA, ENVISAT and ERS-2 satellites

over a pixel of about 312 km² (13x24 km), 1800 km² (30x60 km) and 1600 km² (40x40 km) containing the Évora station while the SPATRAM Field Of View (FOV), determined by the monochromator f number (f# = 5), is of about 1×10^{-5} sr,

- the differences of methodologies used for the retrieval of O₃ columns,
- the usage of different types of instruments i.e., the comparison between data from ground based spectrometer with instruments aboard satellites and the fact of SPATRAM “looks up” while the other instruments “look down” or, in other words, the SPATRAM measures the zenith sky scattered radiation and the satellite instruments carries out measurements of the radiation back-scattered by the Earth-atmosphere system,
- the employment of different AMF correction factors.

5.3.2 NO₂ over Évora station for the period 2007-2011

Stratospheric NO₂ presents a diurnal and seasonal variation at mid- latitudes due to the joined effect of its photochemistry and atmospheric transport. After the presentation of the typical NO₂ diurnal cycle and the characteristic seasonal pattern retrieved with the application of DOAS methodology to the SPATRAM spectral data, the comparisons between SCHIAMACHY, GOME-2 and OMI NO₂ total content measurements over Évora and the retrieved SPATRAM NO₂ VCD, are discussed for the period 2007-2011. The statistical analyses concerning the comparisons are presented also.

5.3.2.1 NO₂ diurnal variation

The NO₂ SCD values are retrieved from the SPATRAM spectral measurements applying the DOAS algorithms in the 430-450 nm spectral range.

In order to investigate the diurnal variation of NO₂, the retrieved SCDs time series are plotted versus the SZA during one typical day, as shown in Figure 5.14.

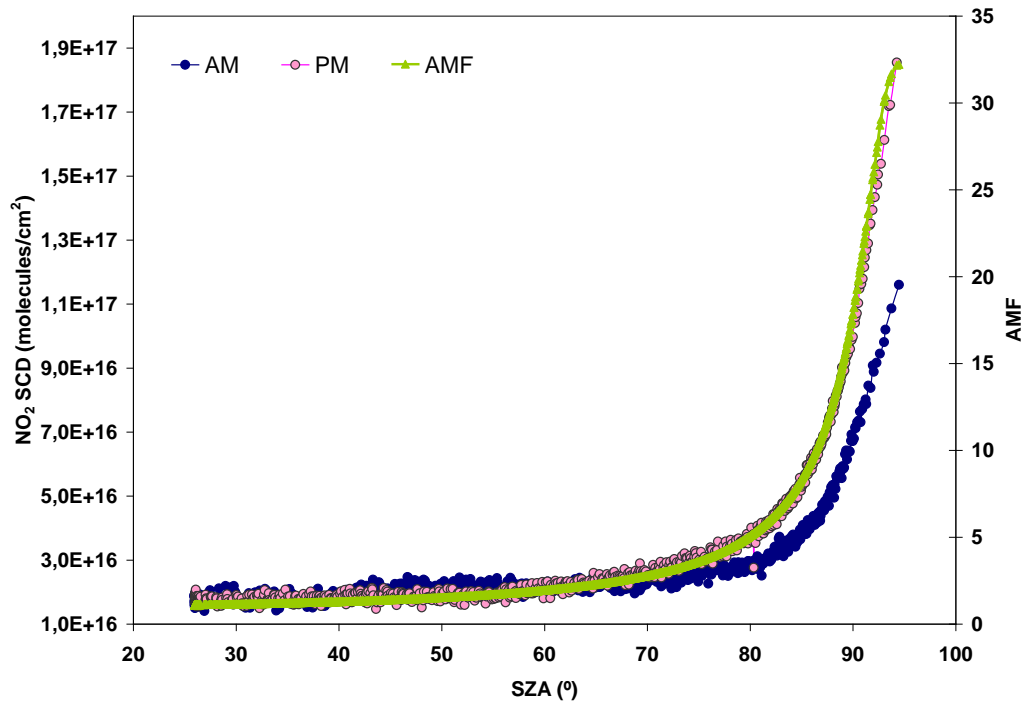


Figure 5.14 - NO₂ Slant Column Densities (SCD) and AMF versus SZA obtained with SPATRAM at Évora-Portugal for 24th April 2010.

As for the O₃ SCD, the NO₂ SCD daily time series is separated into AM and PM subseries, that is: the AM data cover the sunrise – local noon period, while the PM values are for the local noon to the sunset hours.

The main feature emerging from Figure 5.14 is that NO₂ SCD shows a diurnal cycle with value of SCD at sunrise lower than at sunset. For example the first measurement for the NO₂ VCD was taken at 6:25 AM and the registered value was 1.07×10^{17} molecules/cm² while the last value was recorded at 8:34 PM and was 1.77×10^{17} molecules/cm². The reason of this systematic difference between AM and PM SCD values is that NO_x concentration increases due to N₂O₅ photolysis during daytime. From the chemical point of view NO₂ can be oxidized by O₃ to form NO₃ (R: $\text{NO}_2 + \text{O}_3 \rightarrow \text{NO}_3 + \text{O}_2$), a strong atmospheric oxidant and a precursor to the formation N₂O₅. Because NO₃ is rapidly photolyzed at visible wavelengths, both its daytime concentration and chemistry are of relatively minor importance in the lower and middle stratosphere. In contrast N₂O₅ can have morning concentrations in the lower stratosphere comparable to NO_x (NO+ NO₂) even though its production requires the formation of NO₃. During the night, N₂O₅ is formed at the expense of NO₂ (R: $\text{NO}_3 + \text{NO}_2 + \text{M} \rightarrow \text{N}_2\text{O}_5 + \text{M}$). After sunrise, N₂O₅ can be photolyzed essentially into two NO_x molecules (R: $\text{N}_2\text{O}_5 + h\nu \rightarrow \text{NO}_3 + \text{NO}_2$). The photolysis time depends on factors like the solar zenith angle, the altitude, the albedo and the temperature. The minimum NO₂ SCD value is observed during

the local noon; anyway this is an apparent minimum since it is due mainly to the shortest optical path and to the maximum error associated to the measurements for the lower SZA. As for the O_3 , the NO_2 SCD values have to be converted in VCD quantities with the ratio between SCD (SZA) and AMF (SZA). Figure 5.14 shows the AMF values calculated for the different SZA using again the AMEFCO model. The NO_2 VCD time series is plotted in Fig. 5.15. It has to be noted the small uncertainties of the sunrise and sunset observations, and the increasing errors towards the local noon hours. Mainly for this reason, it is common to characterize the daily NO_2 VCD with the values obtained for 90° of SZA at sunrise (AM) and sunset (PM).

In Fig. 5.14 the retrieved NO_2 VCD value at 90° of SZA for sunrise (AM) is 3.11×10^{15} molecules/cm²; the NO_2 VCD PM (sunset) value is (or NO_2 VCD = 5.01×10^{15} molecules/cm²). In the following section dealing with seasonal pattern and comparison with satellite data, the presented results are always referred as NO_2 VCD AM or PM identifying the observations at 90° of SZA at sunrise and sunset respectively.

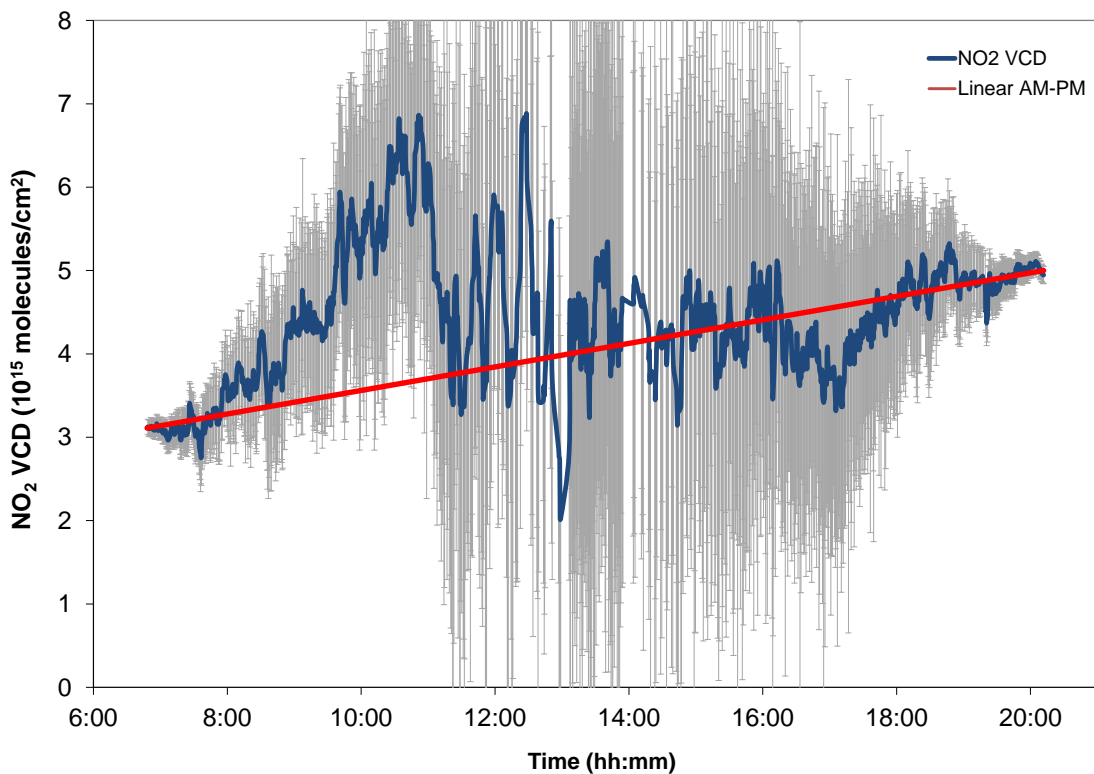


Figure 5.15- Daily variation of NO_2 VCD obtained with SPATRAM at Évora-Portugal for 24th April 2010.

5.3.2.2 NO_2 seasonal variation

In order to examine the seasonal behaviour of NO_2 the time series of NO_2 VCD AM and PM are plotted versus the time in Fig. 5.16. There is no data available in the following periods: 15th October – 15th December 2007; 27th December 2007- 17th January 2008; 3rd April- 31st May 2009 and 18th November- 3rd December 2010 due to the maintenance of the instrument. For 2009

there was not data available for the period comprised 7th September to 10th October due to the participation on a field campaign at El Arenosillo.

From the analysis of the Fig. 5.16 it is possible to mark out a clear seasonal trend of NO₂ VCD values obtained with SPATRAM instrument. The seasonal trend is similar to the one has been pointed out for O₃, but the minima and maxima are presented for different seasons. As expected from the photochemical activities of NO_x family the vertical columns increase till the summer months when the maximum is reached. This fact is directly related with the increasing of the intensity of solar radiation between May and August and increasing of daylight hours. The opposite occurs in the winter months leading to a decrease of the NO₂ concentration. It can be noted the almost constant difference between the NO₂ VCD values for the AM and PM series. The ratio of the AM and PM values range from 0.4 during the winter period to 0.7 for the summer months

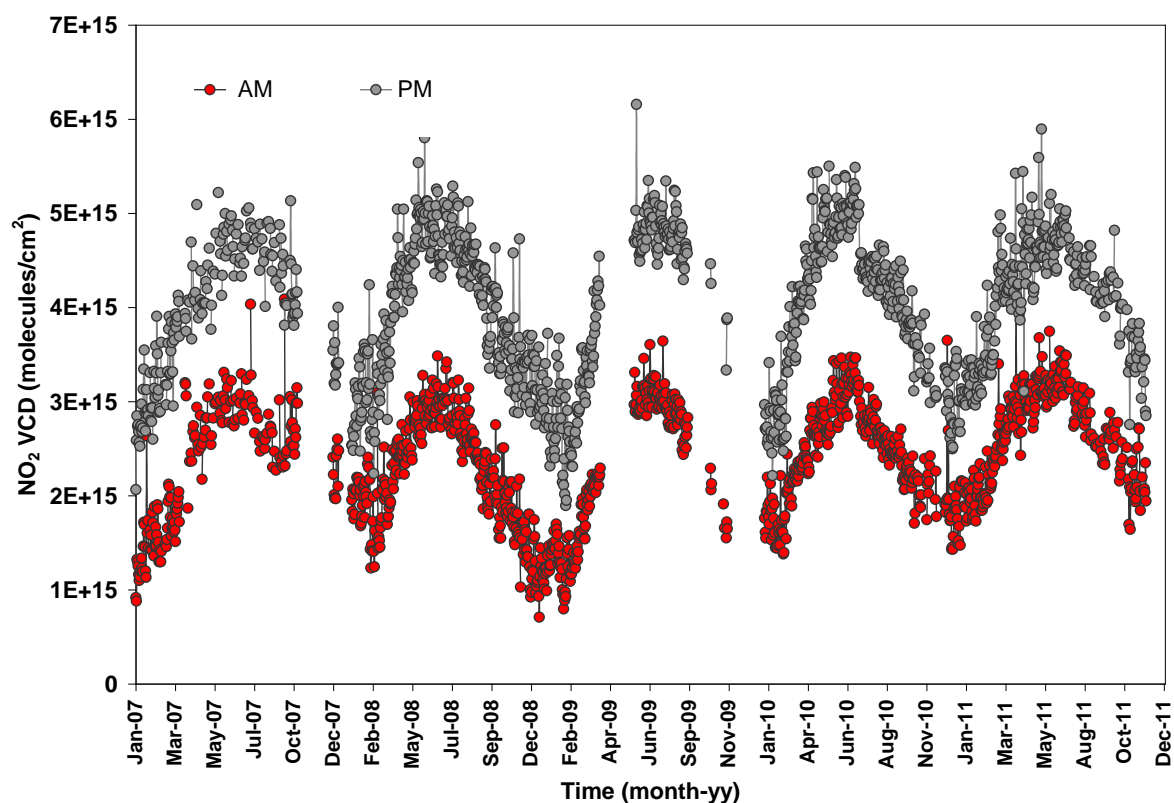


Figure 5.16- Time series of the NO₂ VCD obtained with the SPATRAM equipment installed at Évora Observatory for the SZA of 90°, during 2007-2011.

5.3.2.3 Ground based and satellite dataset

In this section the validation of SPATRAM dataset is done, comparing its results with satellite data from SCIAMACHY, GOME-2 and OMI.

5.3.2.3.1 NO₂ VCD - SPATRAM vs SCIAMACHY

The product that was used to make the validation of SPATRAM dataset is called **SCIAMACHY stratospheric NO₂ columns over stations Version 2.1**. It is available over Évora at http://www.doasbremen.de/data/no2/acve/scia_ubv2-1_no2_evora.day.

The information available about this product can be found at http://www.doasbremen.de/scia_no2_data_acve.htm#Top.

The NO₂ total column provided by SCIAMACHY is plotted versus day of the year jointly with SPATRAM data for SZA of 90° (Fig. 5.17).

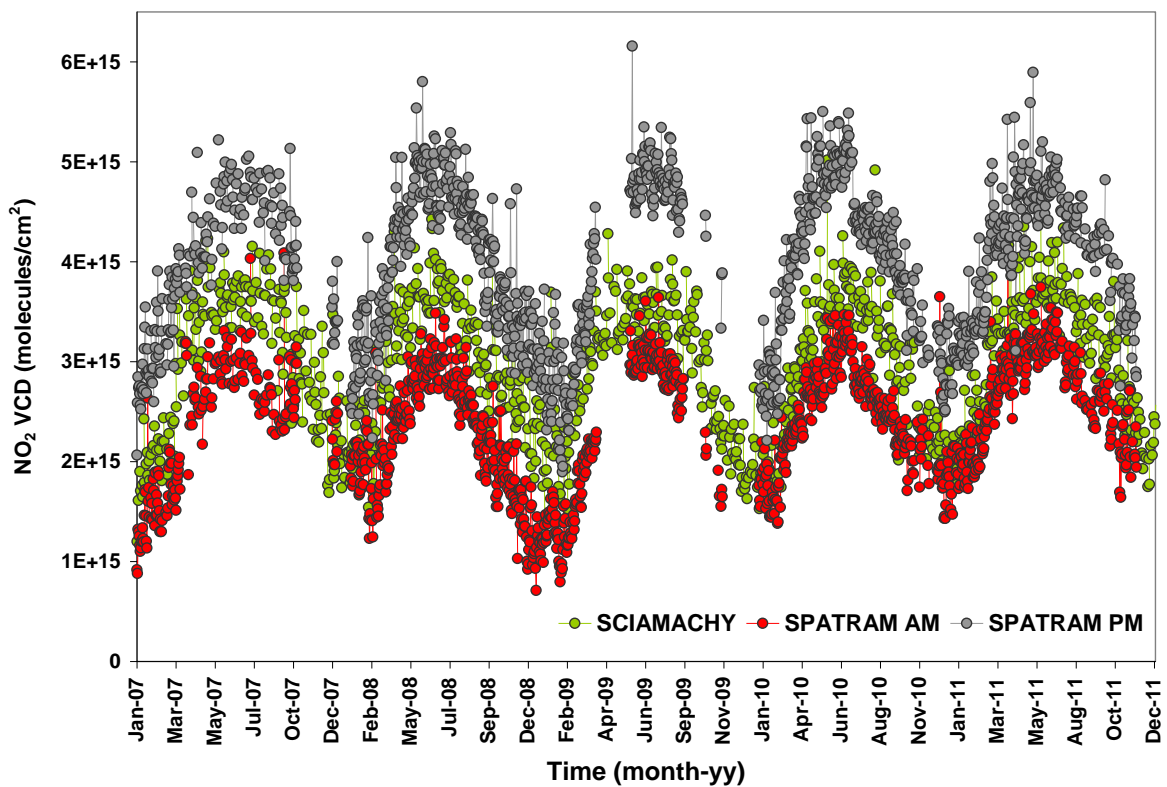


Figure 5.17 - Time series of the NO₂ VCD obtained with the SPATRAM equipment installed at Évora Observatory for the SZA of 90°, during 2007-2011, and the NO₂ total columns acquired from the SCIAMACHY spectrometer aboard ENVISAT.

Fig. 5.17 presents the correlation between the two datasets.

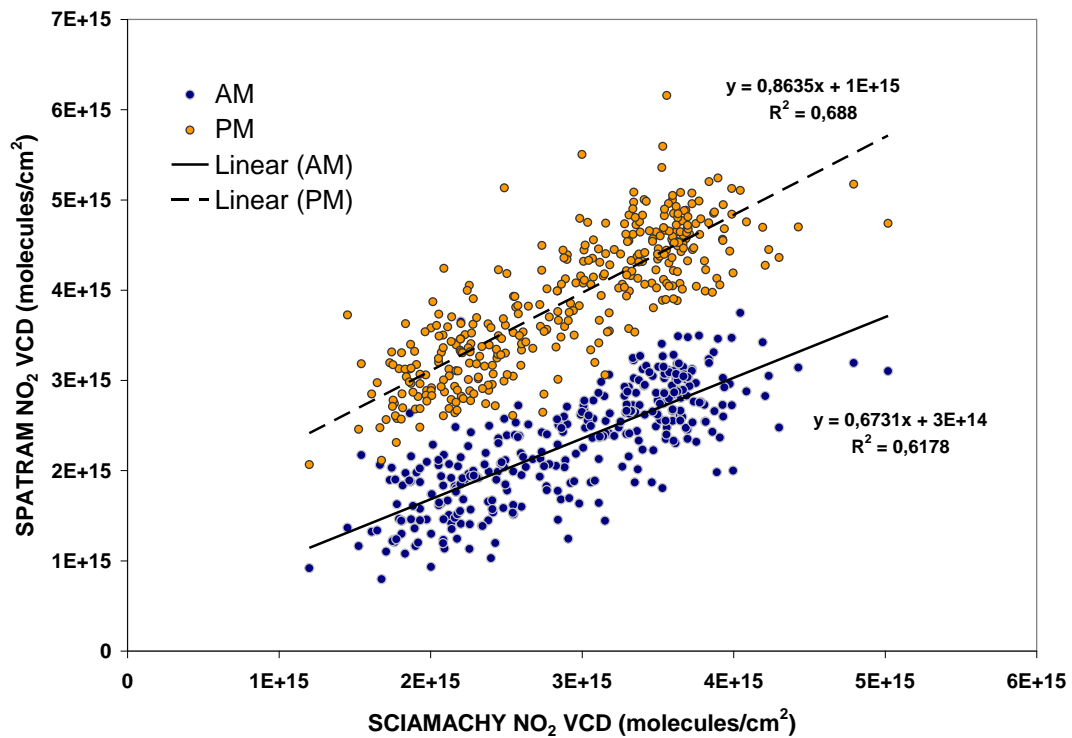


Figure 5.18 - Scatter plot of the NO₂ data from the SCIAMACHY instrument versus NO₂ SPATRAM AM (morning) and PM (afternoon) data retrieved at Évora Observatory for the SZA of 90°, during 2007 - 2011 period including the regression lines for each dataset.

The two datasets are in reasonable agreement.

Due to the overpass of ENVISAT in the morning (~11:00AM UTC), the SCIAMACHY values are located between the AM and PM SPATRAM NO₂ VCD values (respectively at 6:00-8:00 AM and 6:00-8:00 PM UTC depending on the season and for SZA of around 90° where NO₂ SCD reaches its highest values).

In Table 5.3 the maximum and minimum values for the NO₂ VCD AM and PM obtained with SPATRAM and the standard deviation from SCIAMACHY observations are presented.

The SCIAMACHY dataset is the only one that can be fully compared with the SPATRAM data, since the two time series are coincident in time, meaning that to each pair of SPATRAM data (AM and PM), corresponds a SCIAMACHY overpass.

Table 5.3- NO₂ total columns maximums and minimums values obtained with SPATRAM ± 1 standard deviation from SCIAMACHY for the period 2007-2011 over Évora-Portugal.

	Maximum (molecules cm ⁻²)		Minimum (molecules cm ⁻²)	
	AM	PM	AM	PM
2007	$(4.1 \pm 0.4) \times 10^{15}$ 21 st September	$(5.2 \pm 1.5) \times 10^{15}$ 27 th May	8.8×10^{14} 2 nd January	2.1×10^{14} 24 th January
2008	$(3.5 \pm 0.5) \times 10^{15}$ 18 th June	$(5.8) \times 10^{15}$ 26 th May	7.1×10^{14} 15 th December	2.2×10^{15} 26 th February
2009	3.6×10^{15} 22 nd July	6.2×10^{15} 5 th June	$(7.9 \pm 0.9) \times 10^{14}$ 27 th January	2.7×10^{15} 31 st January
2010	$(3.7 \pm 0.3) \times 10^{15}$ 8 th June	$(5.5 \pm 0.3) \times 10^{15}$ 12 th May	$(1.3 \pm 0.5) \times 10^{15}$ 4 th January	$(2.2 \pm 0.1) \times 10^{15}$ 1 st February
2011	$(3.8 \pm 0.3) \times 10^{15}$ 6 th June 2011	$(5.9 \pm 0.3) \times 10^{15}$ 23 rd May	$(2.3 \pm 0.2) \times 10^{15}$ 14 th January	$(2.8 \pm 0.2) \times 10^{15}$ 26 th October

5.3.2.3.2 NO₂ VCD - SPATRAM vs GOME-2

SPATRAM data was also compared with GOME-2 dataset (Fig. 5.19). The product that was used is called http://www.doas-bremen.de/gome2_no2_data_acve.htm and it is available at http://www.doas-bremen.de/data/no2/gome2_strat/gome2_ubv2-0_no2_evora.day. A complete description about this product can be found at Richter, 2011.

Once more the satellite dataset is comprised between the SPATRAM AM and PM measurements. GOME-2 data are obtained between 9:50 AM and 11:16 AM UTC over Évora. From Fig. 5.19 it is possible to highlight the same pattern in both data. Although there is a difference between the NO₂ concentrations because they are taken at different moments of the day, the NO₂ VCD from SPATRAM follows the same pattern as the GOME-2 data.

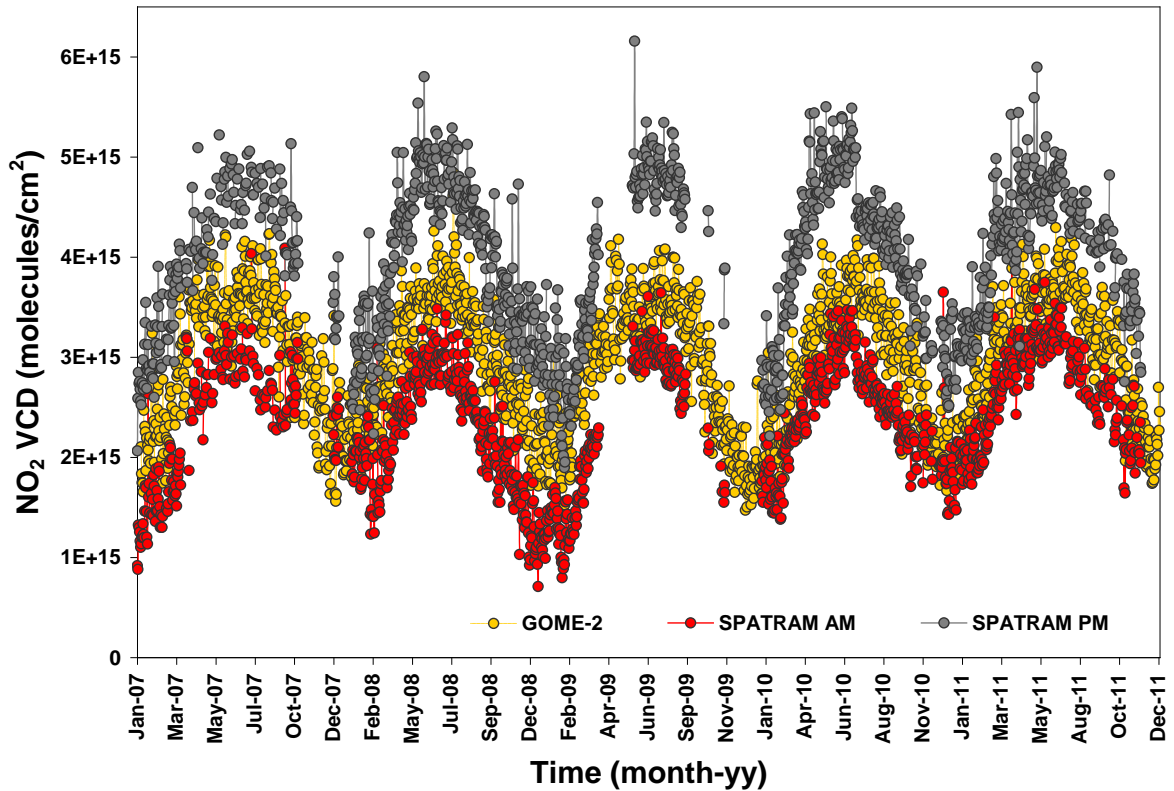


Figure 5.19 - Time series of the NO₂ VCD obtained with the SPATRAM equipment installed at Évora Observatory for the SZA of 90°, during 2007-2011, and the NO₂ total columns acquired from the GOME-2 instrument aboard EUMETSAT.

The correlation plot of the two datasets is presented in next figure.

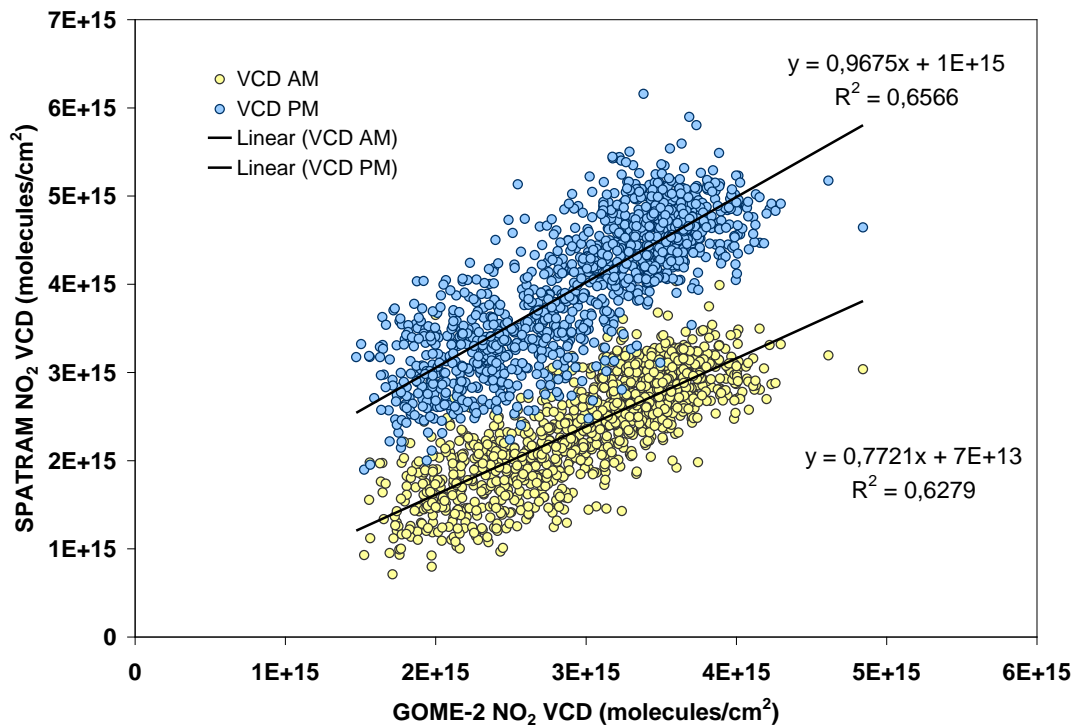


Figure 5.20 - Correlation of SPATRAM data retrieved at Évora Observatory for the SZA of 90°, during 2007-2011, and the NO₂ data from the GOME-2 instrument.

From the analysis of Fig. 5.20 it is possible to infer that the correlation from both data is in accordance with a R^2 of 0.628 for AM values and 0.657 for PM values.

5.3.2.3.3 NO₂ VCD - SPATRAM vs OMI

The OMI product used in the comparison with SPATRAM data is called **OMI Nitrogen Dioxide (NO₂) data product**, or the abbreviated name **OMNO2**. The data is available over several stations at <http://avdc.gsfc.nasa.gov/index.php?site=666843934&id=13>.

The description of the algorithm can be found at Bucsela, 2006 and Boersma, 2001.

The OMI values were filtered using the following quality flags: VCD flag equals to zero, cloud fraction flag < 0.2-0.3 for clear-sky observations and terrain reflectivity flag < 0.3.

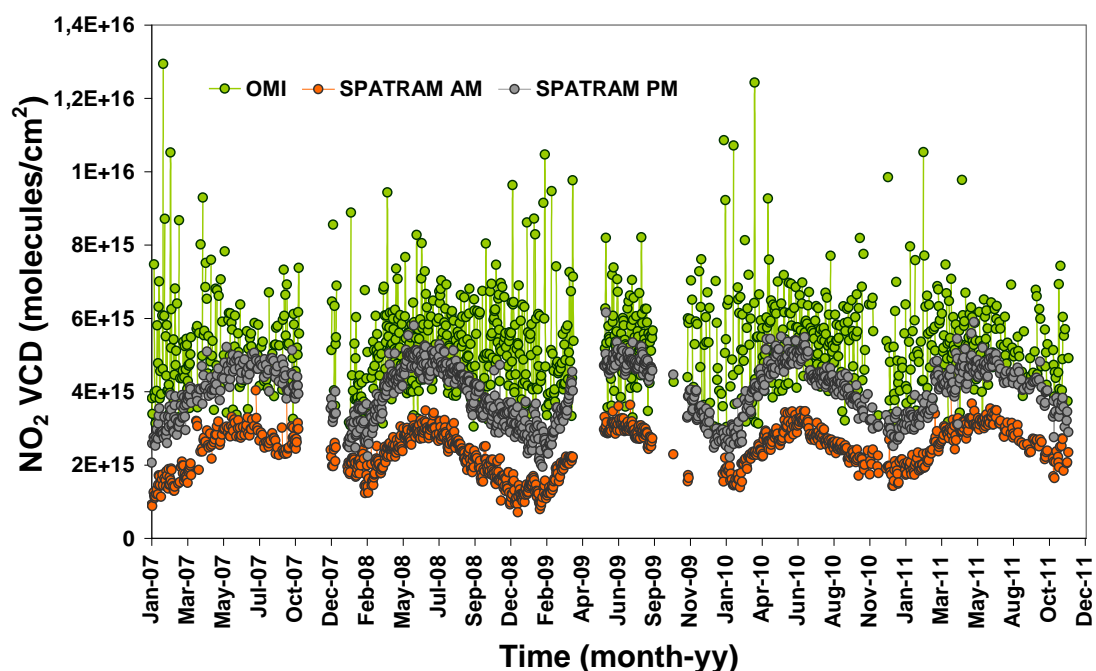
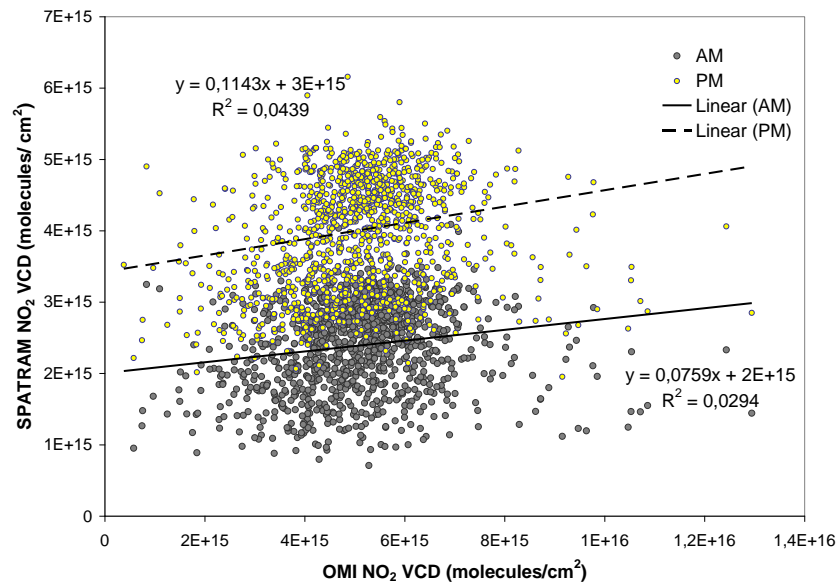


Figure 5.21- Time series of the NO₂ VCD obtained with the SPATRAM equipment installed at Évora Observatory for the SZA of 90°, during 2007-2011, and the filtered NO₂ total columns acquired from the OMI instrument aboard AURA.

The correlation plot (Fig. 5.22) shows no agreement between the two datasets. Although the patterns are similar, the OMI data are more scattered than SCIAMACHY's and GOME's. The sinusoidal pattern is not as visible as the others. Also OMI's overpass over Évora happens between 1:00 PM and 3:00 PM UTC. Therefore the satellite's instrument dataset should appear between the two SPATRAM data series.



Figure

5.22- Correlation of SPATRAM data retrieved at Évora Observatory for the SZA of 90°, during 2007-2011, and the NO₂ data from OMI instrument.

In Table 5.4 it is possible to access to the statistical study of NO₂ dataset. For this study it was considered the value of the mean NO₂ VCD, i.e. the mean between the SPATRAM AM and PM values. The correlation of the mean values of the SPATRAM AM and PM observations with the SCIAMACHY, GOME-2 and OMI data are shown in Figure 5.23, Figure 5.24 Figure 5.25, respectively.

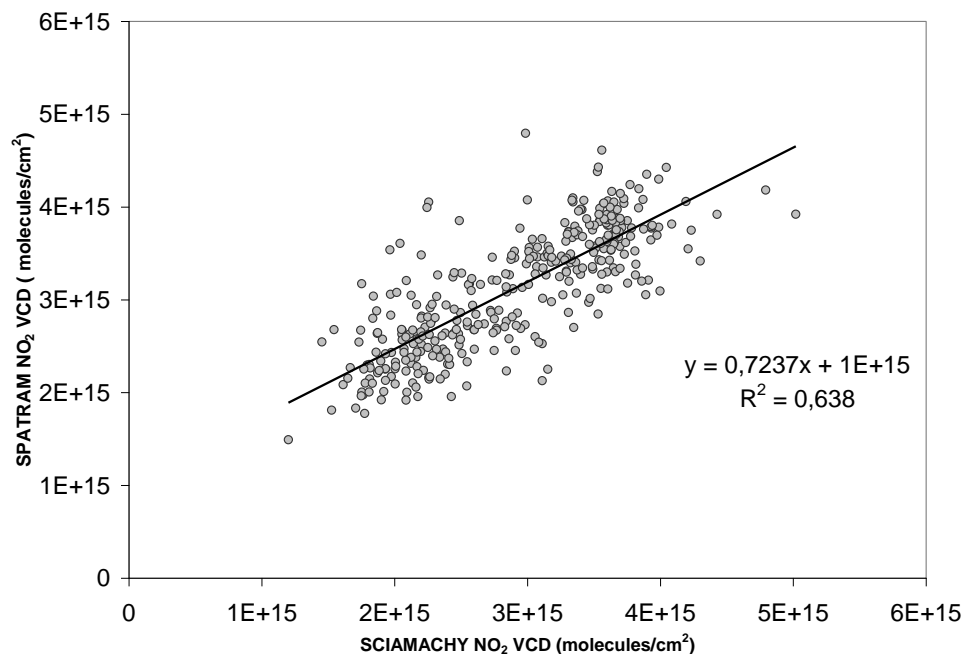


Figure 5.23- Correlation of SPATRAM NO₂ data (average between AM and PM values) retrieved at Évora Observatory for the SZA of 90°, during 2007-2011, and the NO₂ data from the SCIAMACHY instrument.

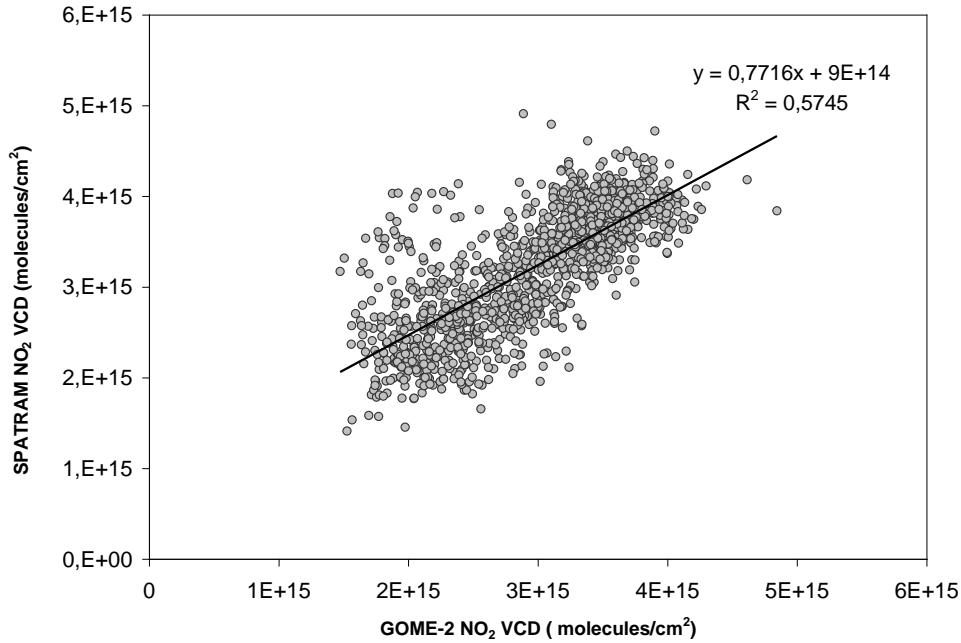


Figure 5.24- Correlation of SPATRAM NO₂ data (average between AM and PM values) retrieved at Évora Observatory for the SZA of 90°, during 2007-2011, and the NO₂ data from the GOME-2 instrument.

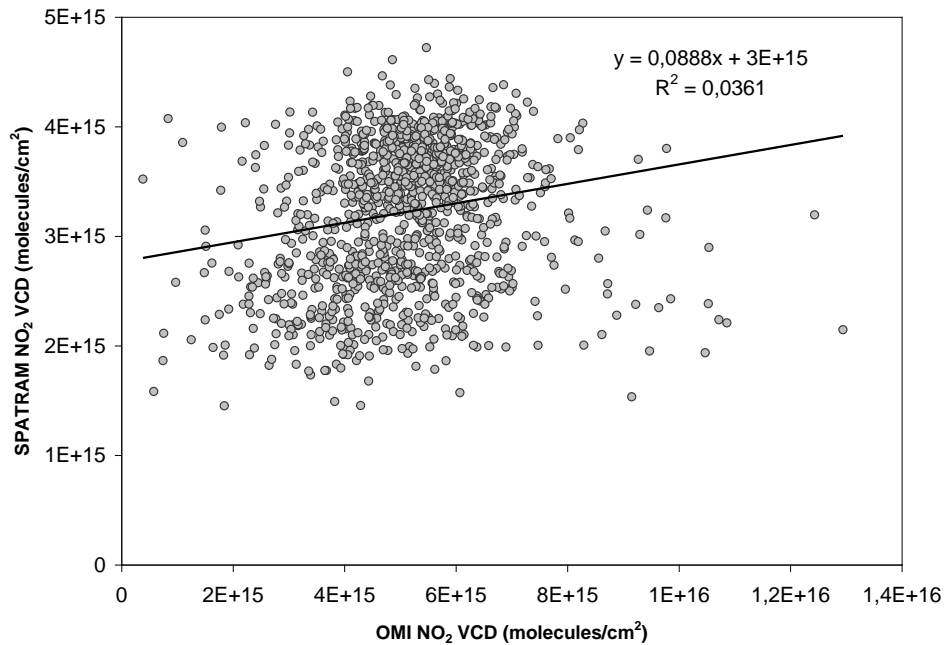


Figure 5.25- Correlation of SPATRAM NO₂ data (average between AM and PM values) retrieved at Évora Observatory for the SZA of 90°, during 2007-2011, and the NO₂ data from the OMI instrument.

For the calculation of RMSE, MBE and MABE parameters, as well the slope and R^2 presented in Table 5.4, it was used the mean value of NO₂ AM and PM from SPATRAM. Those statistical parameters were calculated using Eqs. 5.1 – 5.4.

Table 5.4- Correlation analysis of SPATRAM, OMI, GOME-2 and SCIAMACHY total nitrogen dioxide data for the period of 2007-2011.

	N	Slope	R ²	RMSE (%)	MBE(%)	MABE(%)
SCIAMACHY	717	0.72	0.64	24.33	-6.99 ± 0.53	6.18 ± 0.35
GOME-2	1301	0.77	0.57	11.78	-4.81 ± 0.39	11.10 ± 0.27
OMI	1085	0.09	0.04	22.09	63.31 ± 1.81	70.15 ± 1.84

From the analysis of the latter table it is possible to infer that the best correlations for SPATRAM dataset are the SCIAMACHY and GOME-2 datasets. The values obtained with SPATRAM are higher than the values obtained with SCHIAMACHY and GOME-2 instruments which can be concluded due to the negative sign in MBE values (Table 5.4).

5.3.3 Case study: BrO VCD retrieval

In Figure 5.26 is shown the first results of BrO vertical column obtained from the zenith-sky radiation collected with SPATRAM instrument in the 340-360 nm spectral range and for 90° of SZA for the 6 month period comprised between to 23 January to 2 August 2008. The BrO VCD value is the average between the morning (AM) and the afternoon (PM) observation. The cross sections used for the BrO (243 K) where available from Oliver et al., 2004.

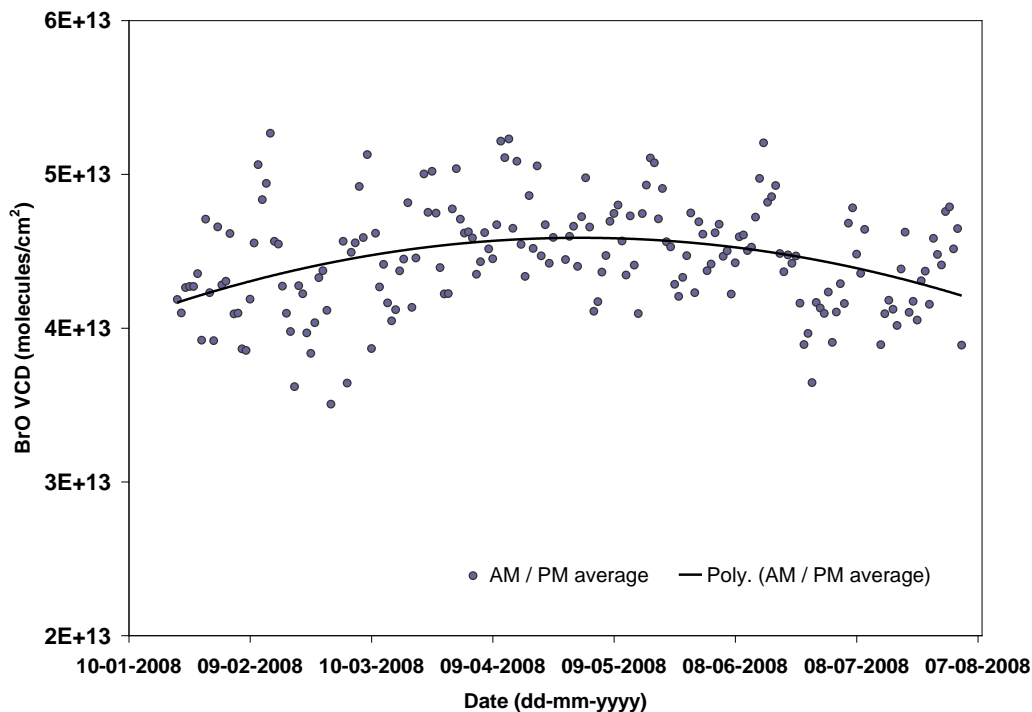


Figure 5.26 -Time series of the BrO VCD obtained with the SPATRAM equipment for the SZA of 90°, a) for morning (AM) and afternoon (PM) and averaged values for the period 23 January – 2 August 2008 at Évora Observatory and the polynomial fit.

Due to the inclusion of the polynomial fit in Fig. 5.26 it is possible to infer that the time series, limited to 6 months shows a slightly seasonal trend reaching the maximum in the spring months.

5.3.3.1 BrO – SPATRAM vs OMI

The values at 90° of SZA for sunset (PM) and sunrise (AM) obtained with SPATRAM are plotted together the BrO data acquired with OMI equipment for the same period in Fig. 5.26.

The dataset used from OMI instrument is called **OMI/Aura Bromine Monoxide Total Column 1-orbit L2 Swath 13x24 km - V003** or abbreviated **OMBRO**. The values of BrO Total columns over Évora station are available from 1st October 2004 until the present and are obtainable at <http://avdc.gsfc.nasa.gov/index.php?site=610245338&id=80>.

The description of the product is available at http://www.cfa.harvard.edu/atmosphere/Instruments/OMI/PGEReleases/READMEs/OMBRO_v300_REA DME.pdf.

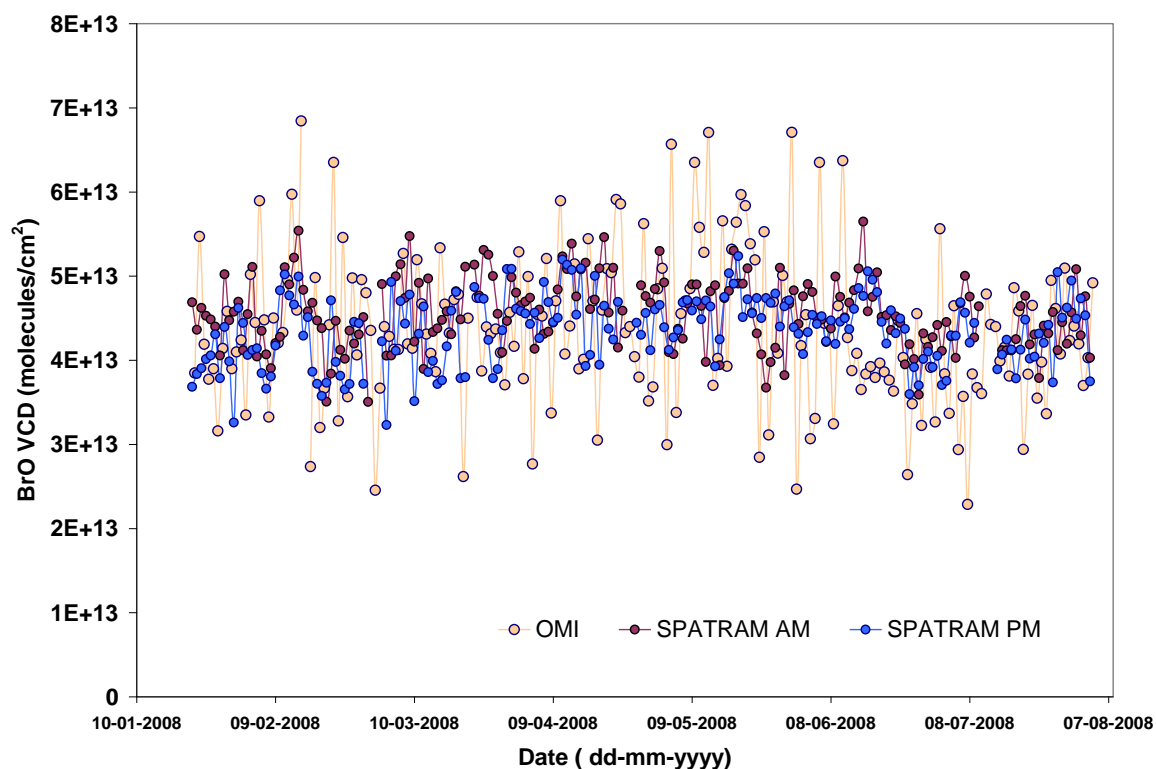


Figure 5.27- Time series of the BrO VCD obtained with the SPATRAM equipment installed at Évora Observatory for the SZA of 90°, for morning (AM) and afternoon (PM), for the period 23 January – 2 August 2008, and the BrO total columns measured with the OMI equipment.

From the analysis of the latter figure it is possible to point the maximums and minimums values found for BrO total columns over Évora. The maximums values for the AM and PM period are found, respectively, for the 15th June 2008 with $(5.64 \pm 0.74) \times 10^{13}$ molecules cm^{-2} and for the 19th May 2008 with $(5.24 \pm 0.65) \times 10^{13}$ molecules cm^{-2} . The minimum values registered with SPATRAM for AM and PM periods are, respectively, $(3.51 \pm 0.48) \times 10^{13}$ molecules cm^{-2} measured in 29th February 2008 and $(3.23 \pm 1.05) \times 10^{13}$ molecules cm^{-2} for the 4th March 2008.

The OMI data are more spread than the SPATRAM results as can be seen by the analysis of Fig. 5.27. This can be confirmed by the correlation plot from Fig. 5.28 in which the values for R^2 are very low ($R^2 = 0.0199$ for AM values and $R^2 = 0.0153$ for PM values). The main conclusion is that considering all the dataset there is no correlation between the two.

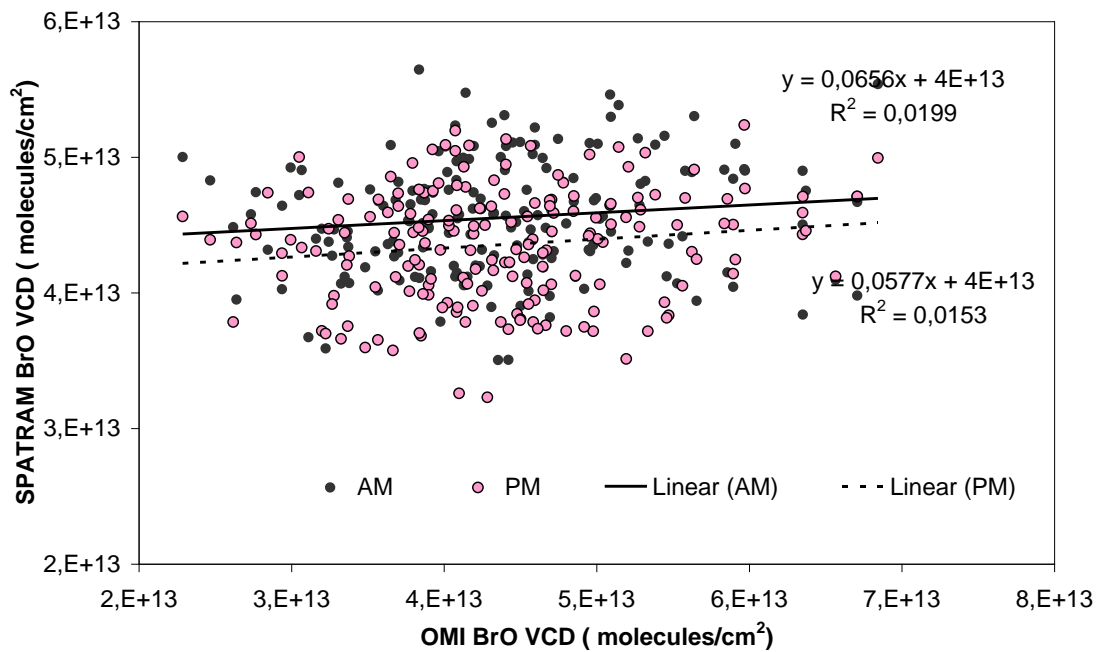


Figure 5.28- Correlation of SPATRAM BrO data retrieved at Évora Observatory for the SZA of 90°, during 2007-2011, and the BrO data from the OMI instrument.

In Fig. 5.29 it is represented all the dataset from OMI and the average between the BrO VCD AM and PM values from SPATRAM. And in Fig. 5.30 the correspondent correlation plot.

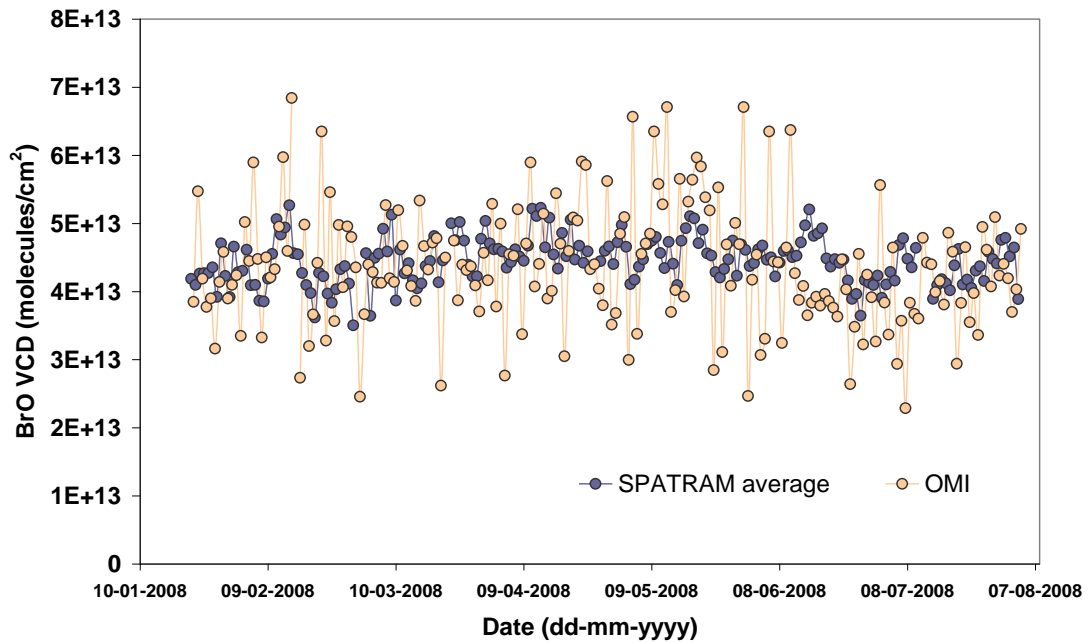


Figure 5.29- Time series (all dataset) of the BrO VCD averaged values from morning (AM) and afternoon (PM) obtained with the SPATRAM equipment installed at Évora Observatory for the SZA of 90° for the period 23 January – 2 August 2008, and the BrO total columns measured with the OMI equipment.

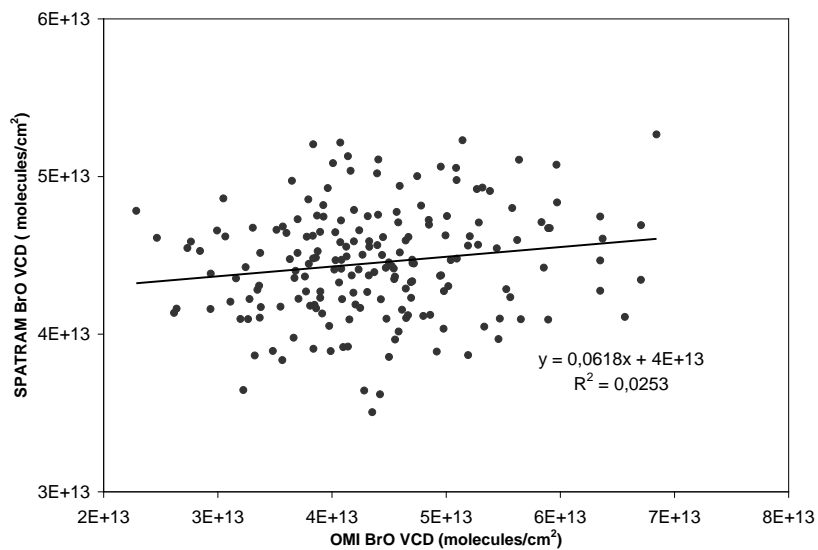


Figure 5.30- Correlation of SPATRAM BrO VCD averaged AM and PM datasets retrieved at Évora Observatory for the SZA of 90°, during 2007-2011, and the BrO data from the OMI instrument.

Once more, using all the dataset from OMI it is possible to conclude that there is no correlation between the two of them.

In conclusion it is necessary to consider the quality flags, from OMI dataset and filter all the data. Therefore using the average of AM and PM data from SPATRAM, and using the filtered OMI data

it is possible to achieve a better correlation between the two instruments, but with errors in the order of 20%. Applying those criteria (VCD flag equals to zero, cloud fraction flag < 0.2-0.3 for clear-sky observations and terrain reflectivity flag < 0.3) it is possible to achieve a better correlation between the two instruments (Fig. 5.32) of approximately $R^2=0.3$. In the Fig. 5.31 it is plotted the BrO VCD averaged values for AM and PM from SPATRAM and OMI BrO VCD filtered versus date.

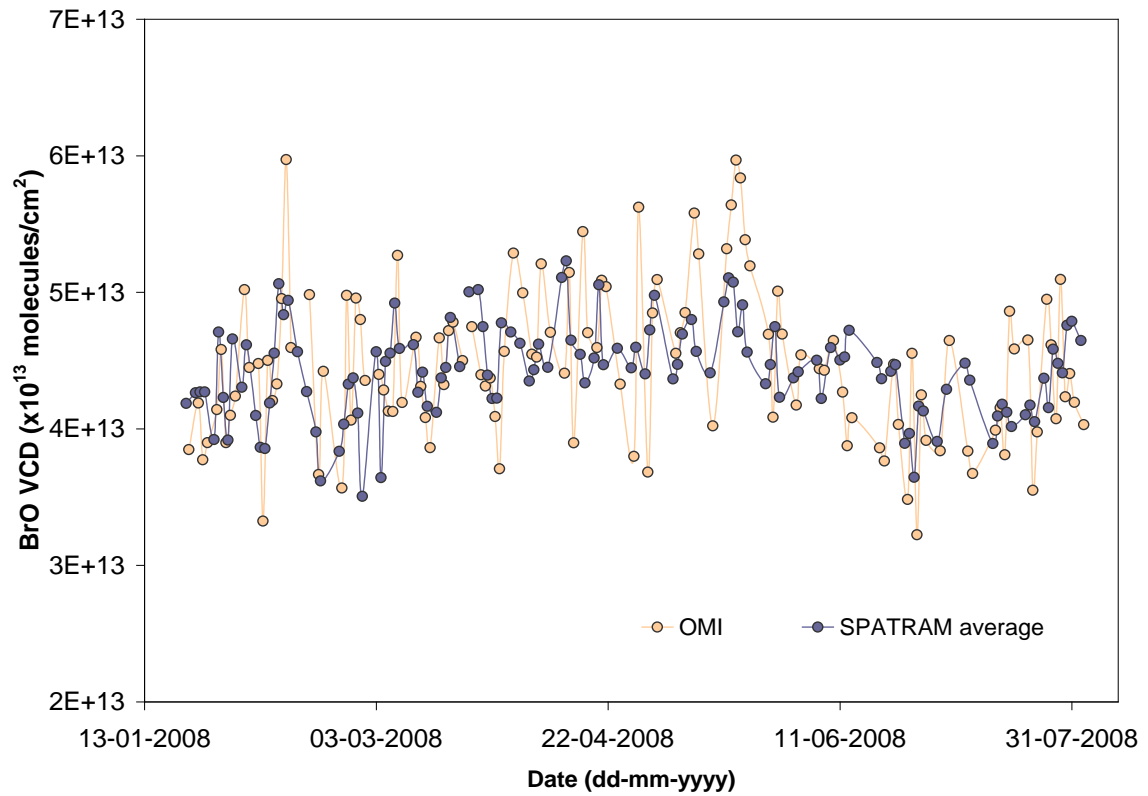


Figure 5.31- Time series (filtered dataset) of the BrO VCD averaged values from morning (AM) and afternoon (PM) obtained with the SPATRAM equipment installed at Évora Observatory for the SZA of 90° for the period 23 January – 2 August 2008, and the BrO total columns measured with the OMI equipment.

It is once more visible that the satellite instrument records higher values from BrO total columns, than the SPATRAM, being the first dataset more spread than the second one.

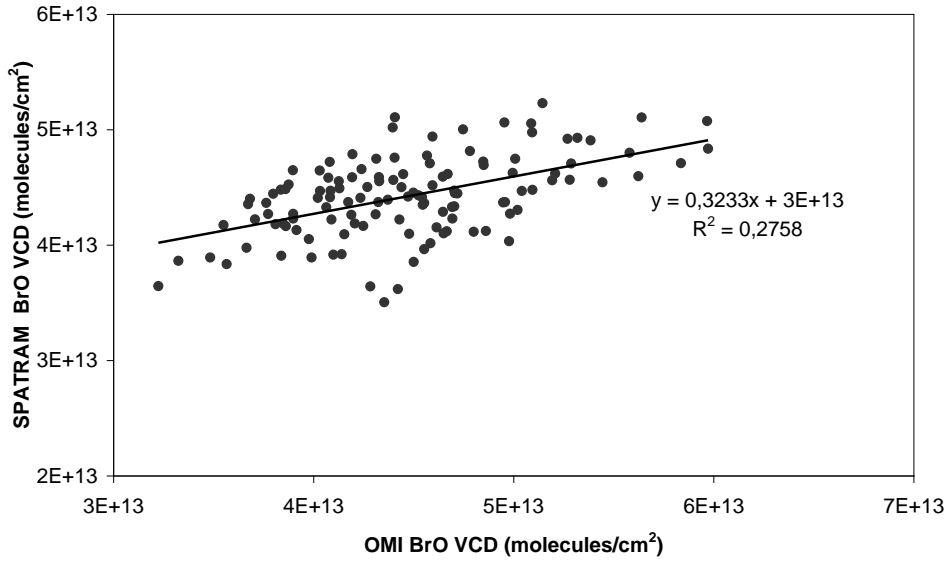


Figure 5.32- Correlation of SPATRAM BrO VCD averaged AM and PM and filtered datasets retrieved at Évora Observatory for the SZA of 90°, during 2007-2011, and the BrO data from the OMI instrument.

Despite the low R^2 achieved in Fig. 5.32 ($R^2 = 0.276$) the comparison with the BrO data obtained from OMI instrument is encouraging for the future work of data comparison/validation.

5.3.3.2 BrO – SPATRAM vs GOME-2

The comparison with GOME-2 BrO total columns was also performed. The data used for this study was provided by Belgian Institute for Space Aeronomy (BIRA-IASB) UV- Visible DOAS group from Belgium. The product used is called BIRA-IASB GOME-2 BrO column product. The approach for the data analysis consists in determination of the BrO SCD from calibrated earth-shine and irradiance spectra using DOAS fit. After that the VCD stratospheric is estimated using simulated stratospheric BrO profiles using the output of the 3-D chemical transport model Belgian Assimilation System of Chemical Observations from ENVISAT (BASCOE) (Theys et al., 2007) Finally VCD tropospheric is calculated using a residual technique according to the Eq. 6.5,

$$VCD_{tropo} = \frac{SCD - VCD_{strato} \cdot AMF_{strato}}{AMF_{tropo}} \quad (6.5)$$

where AMF_{tropo} and AMF_{strato} are, respectively the tropospheric and stratospheric air mass factors. The BrO total column is the sum of the values from VCD stratospheric and VCD tropospheric. Detailed information about the data analysis procedure used for the BrO total columns from BIRA-IASB is found in literature (Theys et al., 2011).

In Fig. 5.33 the BrO Total columns from SPATRAM and GOME-2 instruments are plotted for the considered period in 2008.

From the analysis of Fig. 5.33 it is possible to highlight that from the 2nd June till 3rd August the pattern followed by SPATRAM is the same that for GOME-2, but the values are higher than the satellite's instrument. For 23rd January till 1st June the values are close and the mean deviation is 12%. In the other period the deviation is about 36%, although the pattern is the same.

The maximum values for the AM and PM period are found, respectively, for the 15th June 2008 with $(5.64 \pm 0.89) \times 10^{13}$ molecules cm^{-2} and for the 19th May 2008 with $(5.24 \pm 0.42) \times 10^{13}$ molecules cm^{-2} . The minimum values registered with SPATRAM for AM and PM periods are, respectively, $(3.51 \pm 0.85) \times 10^{13}$ molecules cm^{-2} measured in 29th February 2008 and $(3.23 \pm 0.69) \times 10^{13}$ molecules cm^{-2} for the 4th March 2008.

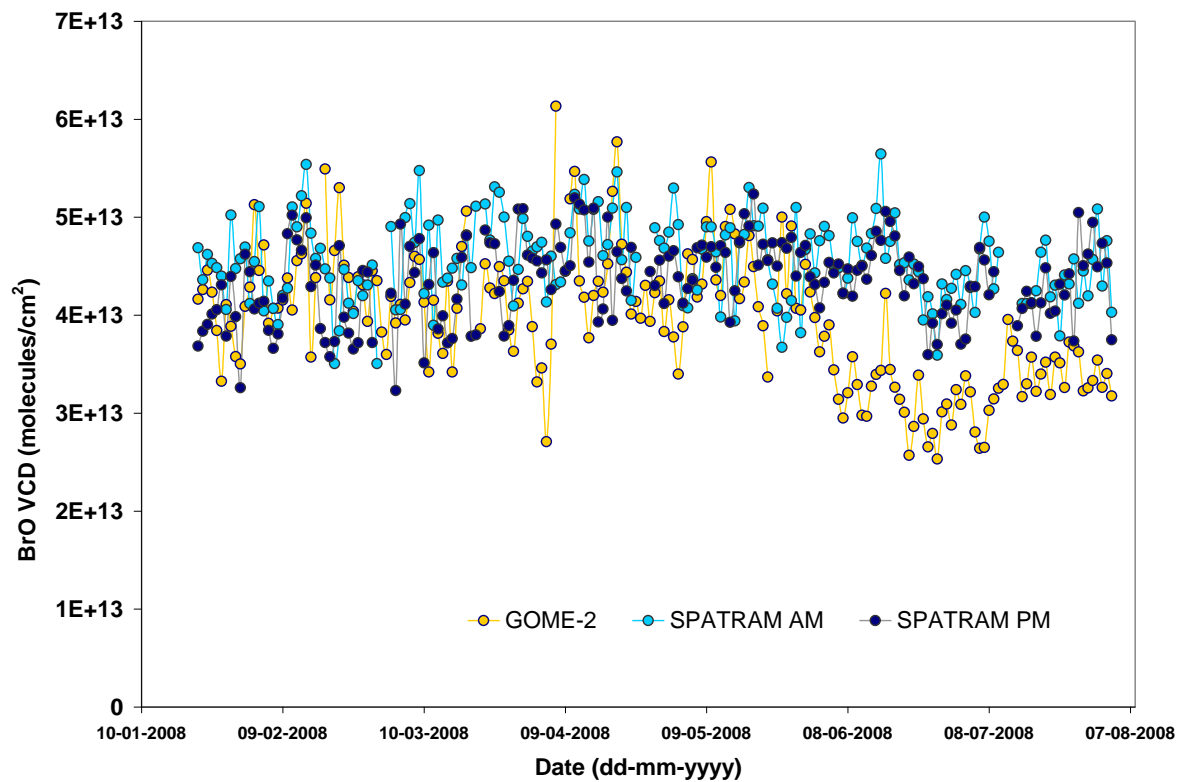


Figure 5.33- Time series of the BrO VCD obtained with the SPATRAM equipment installed at Évora Observatory for the SZA of 90°, for morning (AM) and afternoon (PM), for the period 23 January – 2 August 2008, and the BrO total columns measured with the GOME-2 equipment.

Also the averaged SPATRAM dataset was compared with the GOME-2 dataset. For that the AM and PM values from BrO VCD were taken in account to make the average. The result is the SPATRAM BrO VCD averaged values.

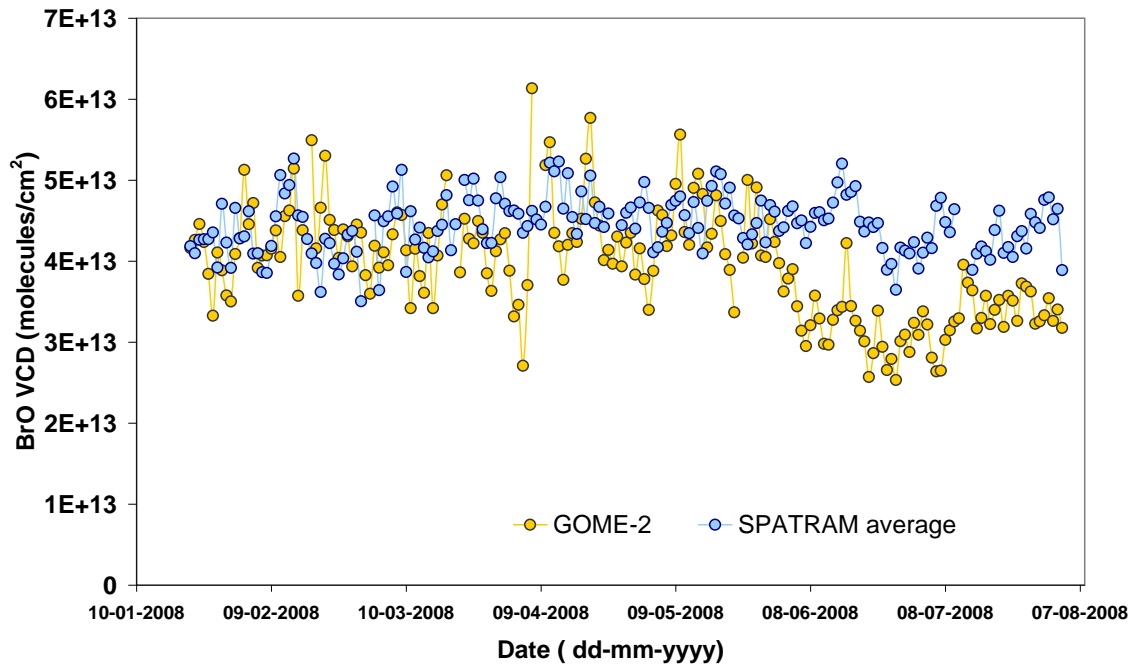


Figure 5.34- Time series (all dataset) of the BrO VCD averaged values from morning (AM) and afternoon (PM) obtained with the SPATRAM equipment installed at Évora Observatory for the SZA of 90° for the period 23 January – 2 August 2008, and the BrO total columns measured with the OMI equipment.

Figures 5.35 and 5.36 shows the scatter plots referring to Fig. 5.33 and 5.34.

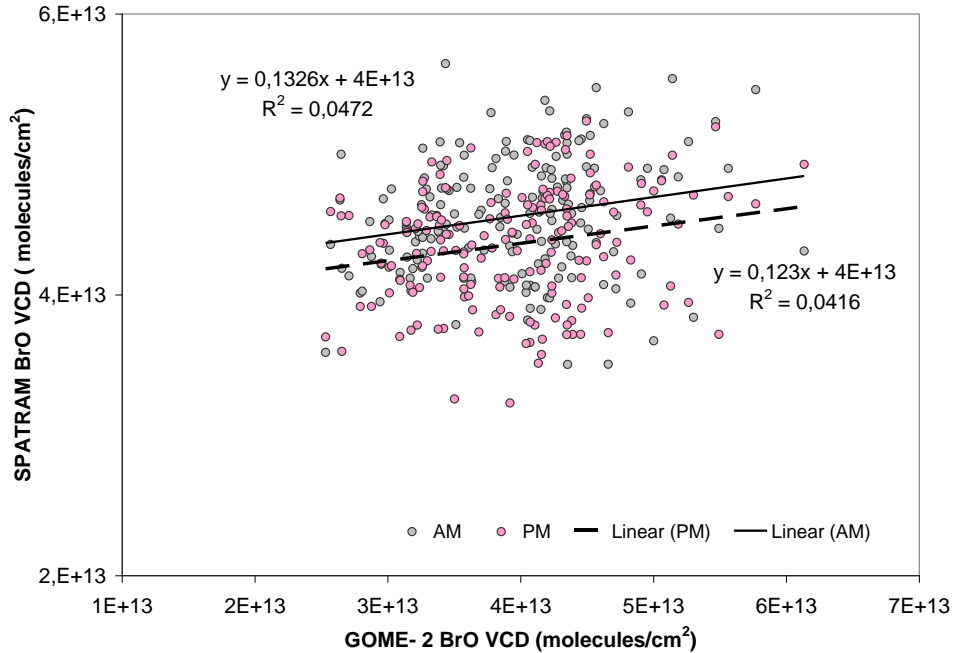


Figure 5.35- Correlation of SPATRAM BrO VCD AM and PM datasets retrieved at Évora Observatory for the SZA of 90°, during 23 January – 2 August 2008, and the BrO data from the GOME-2 instrument.

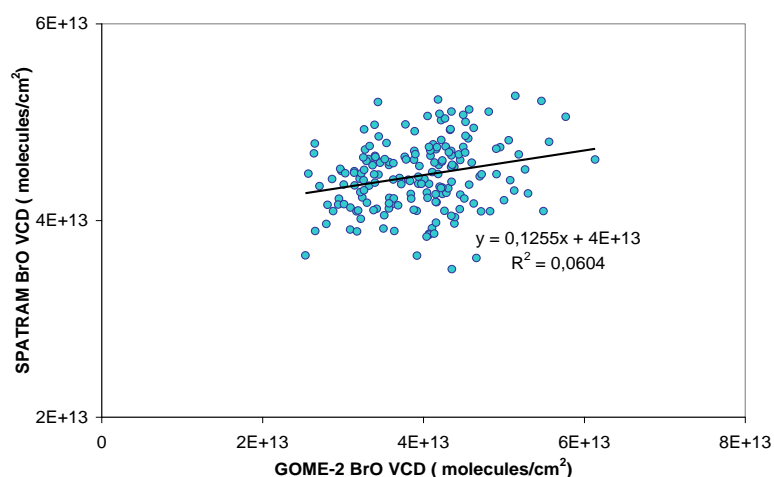


Figure 5.36- Correlation of SPATRAM BrO VCD averaged AM and PM datasets retrieved at Évora Observatory for the SZA of 90°, during 23 January – 2 August 2008, and the BrO data from the GOME-2 instrument.

In Table 5.5 it is possible to access to the statistical study of the dataset 1 (from Fig. 5.29) and dataset 2 (from Fig. 5.31) for OMI and also for dataset 3 (from Fig.5.34). For the calculation of RMSE, MBE and MABE parameters, as well the slope and R^2 presented in Table 5.3, it was used the mean value of BrO VCD AM and PM from SPATRAM. Those statistical parameters were calculated using Eqs. 5.1 – 5.4.

Table 5.5- Correlation analysis of SPATRAM (averages AM and PM values) and OMI total BrO data for the period of 23 January- 2 August 2008 for dataset 1, dataset 2 and dataset 3.

	N	Slope	R^2	RMSE (%)	MBE(%)	MABE(%)
Dataset 1 (SPATRAM BrO VCD AM and PM averaged values, OMI values without filter)	187	0.06	0.03	7.89	-1.86 ± 1.57	15.89 ± 1.08
Dataset 2 (SPATRAM BrO VCD AM and PM averaged values, OMI values filtered)	124	0.32	0.28	7.52	0.33 ± 1.27	9.78 ± 0.91
Dataset 3 (SPATRAM BrO VCD AM and PM averaged values, GOME-2 values filtered)	187	0.13	0.06	7.66	-14.10 ± 1.59	17.97 ± 1.32

From the analysis of Table 5.5 it is possible to conclude that the best correlation is presented for the dataset 2 although the value of R^2 is very low ($R^2=0.28$). In case of OMI values it is possible to infer that they are much dispersed. In case of GOME-2 values, there is accordance for January-May values, but from June to August the BrO values obtained with SPATRAM are higher than the ones from the GOME-2 instrument.

5.4 NO₂ Vertical profiles

The following sections present the retrieval of NO₂ tropospheric profiles and tropospheric NO₂

total columns and NO₂ stratospheric profiles over Évora Observatory using SPATRAM instrument.

5.4.1.1 Retrieval of NO₂ vertical profiles and tropospheric columns at Évora with the SPATRAM and MIGE instruments

The main goal of this study is the retrieval of the NO₂ vertical profiles and the NO₂ tropospheric content in the Planetary Boundary Layer (PBL) at the Évora station using the SPATRAM and MIGE instruments. In this section the results obtained ranging from the ground level to about 1500 m for 30th March and 8th and 9th April 2009, are shown and discussed. In addition an idea about the different behaviour of the NO₂ SCD, depending on the different azimuth angles of measurement, clearly visible in the presented plots, is also given.

5.4.1.2 NO₂ tropospheric total columns

The NO₂ SCDs presented in the following, are retrieved in the 436-460 nm spectral interval for different azimuth and zenith Line of Sight (LOS).

In Fig. 5.37 the time series for the NO₂ SCDs in troposphere measured during 30th March 2009 are shown. The observations are obtained for a solar zenith angle of 88° along the West, East, South and North directions.

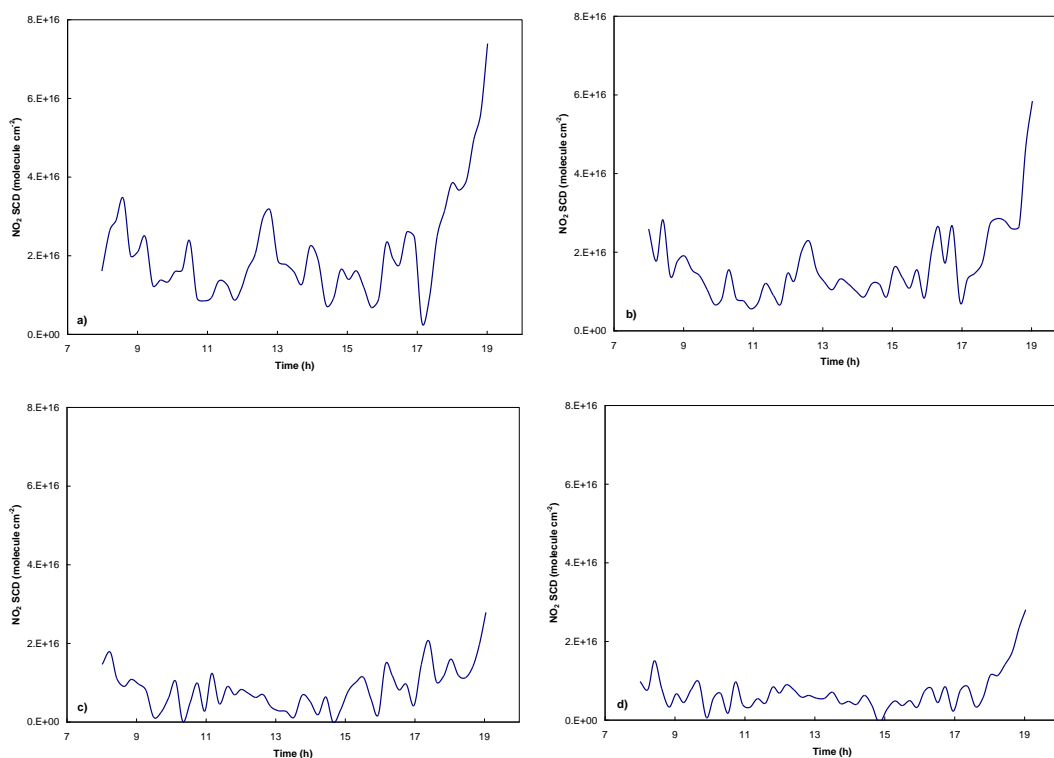


Figure 5.37- NO₂ SCDs during 30th March 2009 for a zenith elevation of 88° along the a) West, b) East, c) North and d) South azimuthal direction.

The analysis of figures 5.37 a) –d) suggests that the observations are largely dependent on the azimuthal direction. Figures 5.37 a) and 5.37 b) correspondent to the West and East directions, respectively, where the values are higher than in Figs. 5.37 c) and 5.37 d) (for the North and South paths). This is mainly due to the presence of very large urban areas as Lisbon (in the West direction of Évora) and Badajoz (at the Portuguese-Spanish border – East direction). The Lisbon urban area is characterized by a very high load of nitrogen compounds caused by the vehicular and industrial emissions. It has to be taken into account also the existence of the international airport of Lisbon, with a very high aerial traffic and consequently high release of nitrogen compounds in the atmosphere. Since Évora is a small city, probably the enhancement of NO₂ SCD value is imputable to measurements including the contribution of the nitrogenised air masses positioned over Lisbon region. In the North and South directions there are not big urban areas like the others, therefore the measured NO₂ SCD values at 88° of zenith elevation can be considered as the background content of stratospheric nitrogen dioxide.

In Fig. 5.37 a) the SCD values present a very clear diurnal cycle with local maximum during the periods of highest vehicular traffic: in the morning between 8:00 and 9:00 and in the afternoon between 12:00 - 14:00 and at 18:00 - 19:00. Also the measurements in the East direction (Fig. 5.37 b) (towards Badajoz) reveal the same diurnal cycle observed in the opposite direction, with the same local maximum during the periods of most probable vehicular traffic in the urban area. In addition Badajoz has also a large industrial area emitting huge quantity of nitrogen compounds. In the North and South directions there are no industrialized as well as big urban areas, therefore the measured NO₂ SCD values at 88° of zenith elevation can be considered as the background content of stratospheric nitrogen dioxide.

The difference between the retrieved values in the West and East directions with the background content obtained for the North and South paths can give an estimation of the emissions in the Lisbon and Badajoz urban areas. As expected, the retrieved vertical profiles are function of the azimuth path.

5.4.2 NO₂ vertical profiles in PBL

In Figures 5.38-5.39, the vertical profiles of NO₂, obtained by the SPATRAM+MIGE and the application of inversion algorithms for the 8-9 May 2009 are presented.

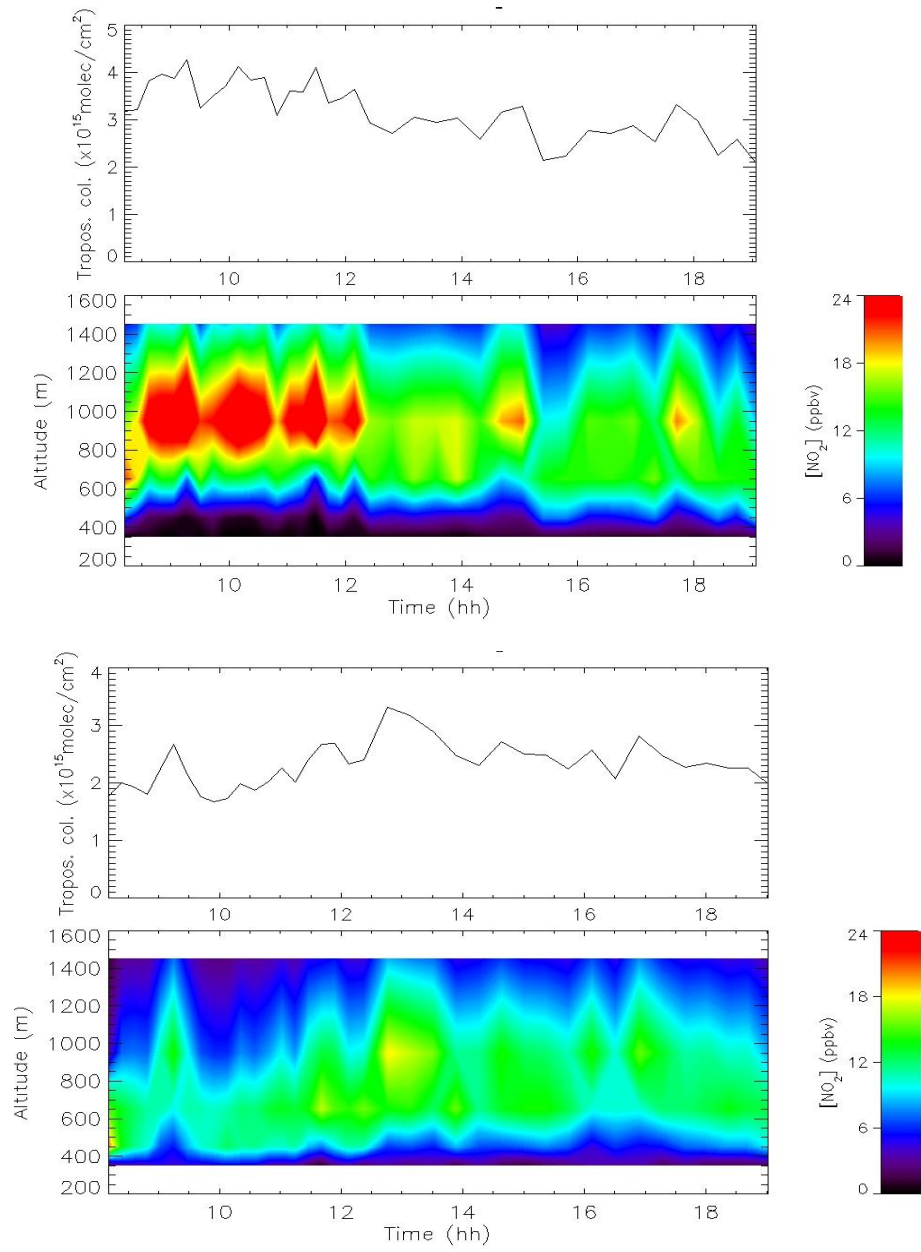


Figure 5.38- NO₂ vertical profiles for 8th April 2009 retrieved a) East b) North azimuthal direction with an horizontal visibility of 30 km.

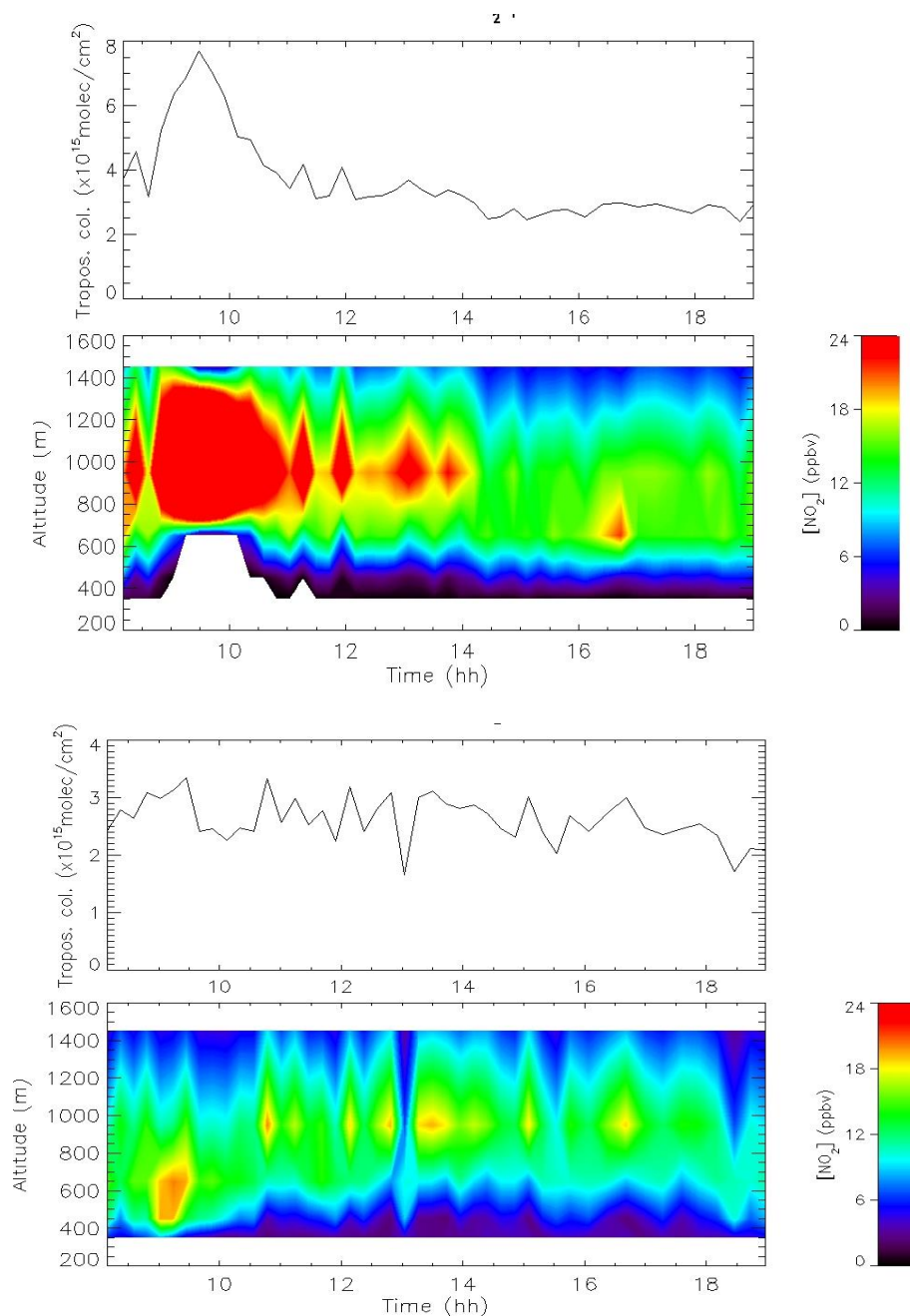


Figure 5.39- NO₂ vertical profiles for 9th April 2009 retrieved a) East b) North azimuthal direction with an horizontal visibility of 30 km.

The analysis of figures 5.38-5.39 suggests that the major concentrations of NO₂ are registered between 9 and 11 AM, at lunch time between 12 and 2 PM, and in the evening in the 5 to 6 PM. These periods correspond to the hours of intense traffic in Évora. Nevertheless the high NO₂ concentration registered in those days cannot be explained only by this reason since that from the analysis of Fig. 5.38b) and 5.39 b) the concentrations are not so high from the north direction. It is possible that the NO₂ enhancement in the atmosphere was provoked by intrusions of NO₂ polluted air masses from distant sites.

5.5 Retrieval of NO₂ stratospheric vertical profiles

In this section the results obtained for the NO₂ profile ranging from the 15 km to about 50 km during May to October of 2010 are shown and discussed. The data was retrieved with SPATRAM instrument over Évora during de period comprised between 5th May and 5th October 2008. The data from SPATRAM is presented for 11.25 to 41.25 km with a step of 2.5 km. For this study it was considered an a priori Gaussian profile that not includes the tropospheric contribution.

The analysis of all the NO₂ stratospheric vertical profiles (Figs.5.40-5.42) suggests that the major concentrations are registered with SPATRAM for the altitude of approximately 28.75 km for the period in analysis. The values at bulk vary between the minimum of $1.31 \times 10^9 \text{ cm}^{-3}$ (at 23rd September 2010) and the maximum $2.29 \times 10^9 \text{ cm}^{-3}$ (at 9th June 2010).

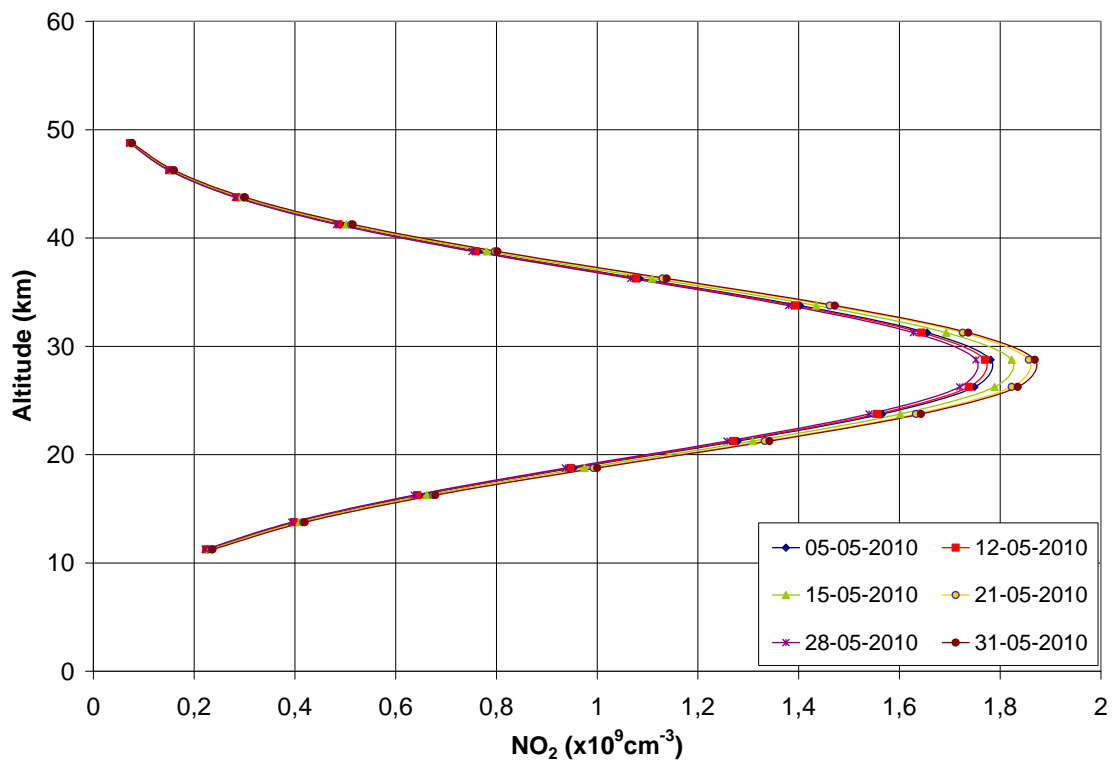


Figure 5.40- NO₂ stratospheric vertical profiles for May of 2010 retrieved with SPATRAM at Évora Observatory.

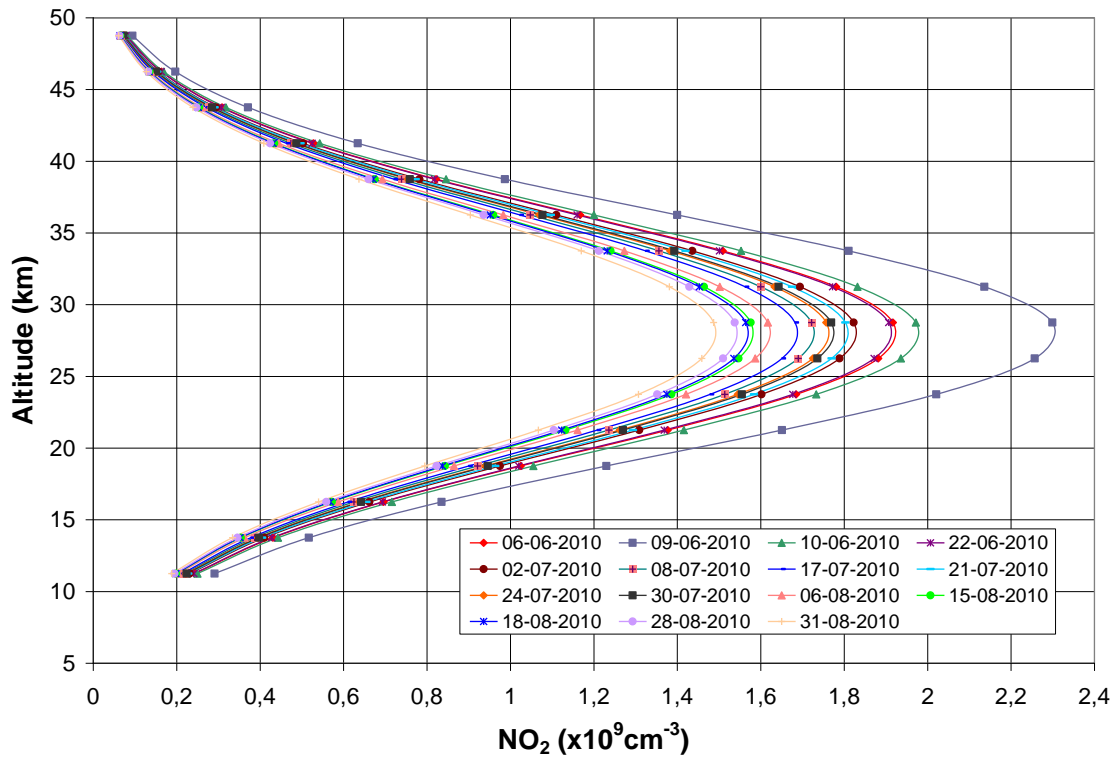


Figure 5.41- NO₂ stratospheric vertical profiles for June- August of 2010 retrieved with SPATRAM at Évora Observatory.

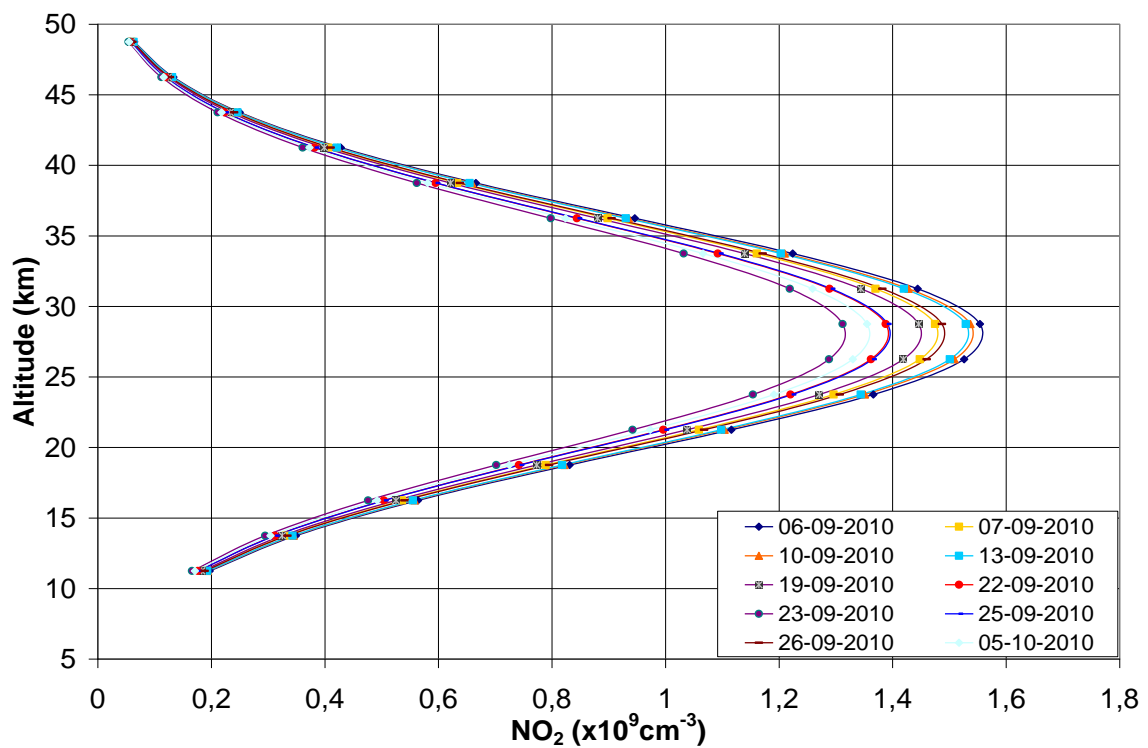


Figure 5.42- NO₂ stratospheric vertical profiles for September and October of 2010 retrieved with SPATRAM at Évora Observatory.

The NO₂ stratospheric vertical profiles retrieved with SPATRAM are compared with two datasets from SCIAMACHY instrument with different algorithms, both retrieved over Évora station. With this latter instrument, using the limb geometry (i.e. tangential view in respect to the Earth surface), it is possible also to retrieve the stratospheric vertical profiles of some gases, including the NO₂ profiles. The first dataset was provided by the team at Max Planck Institute for Chemistry in Mainz, Germany. In this work the dataset is labeled as SCIAMACHY MPI. The profile retrieval algorithm it is a two step process, being the first one the retrieval of SCD by DOAS method. Applying the TRACY-II model, which is a Monte Carlo Radiative Transfer Model, the box air mass factors are calculated and the SCD are converted in vertical concentration profiles in function of altitude. All the details on the profile retrieval algorithms can be found at literature (Kühl et al., 2008; Pukite et al., 2006; Pukite et al., 2008). The second dataset used was also from SCIAMACHY limb data but the algorithms developed at the Institute of Environmental Physics (IUP/IFE) of University of Bremen. The name used in this work for that dataset is SCIAMACHY Bremen. The simulation of the measurements of the scattered solar radiation in limb viewing geometry is done using the SCIATRAN radiative transfer model which considers single and multiple scattering as well the refraction. Only polarization is not taken in account. The solution method is a global fit approach with a pre- processing step aimed to exclude the spectral features not associated to the retrieved parameters. In addition an inversion procedure is applied and the vertical profiles of atmospheric trace gases are retrieved. The values used for absorption cross-section of NO₂ were measured by the SCIAMACHY PFM satellite spectrometer at 293, 273, 243, 223, and 203K (Rosanov, 2007). The a priori information is from a climatological data base provided by C.A. McIlden (Rosanov, 2007). The aerosol settings are also taken in account (Parameterization type: LOWTRAN; aerosol type in the boundary layer are maritime; the boundary layer and tropospheric visibility is 23 km). The product and algorithm description can be found at literature (Rosanov, 2005; Bauer, 2012; Rosanov, 2008).

The data from SCIAMACHY MPI is presented for altitudes ranging from 1.5 to 46.5 km with a step of 3 km, anyway the NO₂ tropospheric part was not considered for this comparison. And for SCIAMACHY Bremen the data is presented from 11- 45 km with a step of 1 km.

In the following plots (Fig. 5.43, 5.44, 5.45) the minimum and maximum profiles are presented, as well as the averaged profile retrieved with SPATRAM, and the two averaged profiles from SCIAMACHY. Those averages are the monthly mean of the data for each altitude.

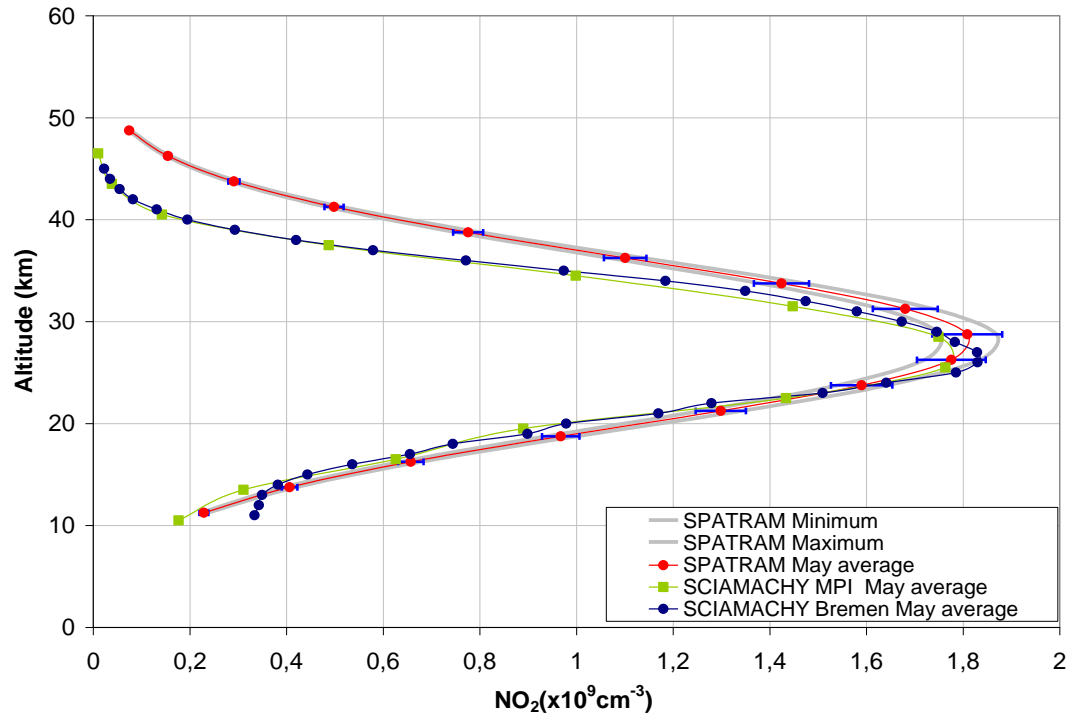


Figure 5.43- NO_2 stratospheric vertical profiles for some days of May 2010, comprising the minimum values, maximum values and the averaged values retrieved with SPATRAM instrument and comparison with SCIAMACHY datasets from Max Plank Institute Mainz (SCIAMACHY MPI) and the Institute of Environmental Physics (IUP/IFE) of University of Bremen (SCIAMACHY Bremen).

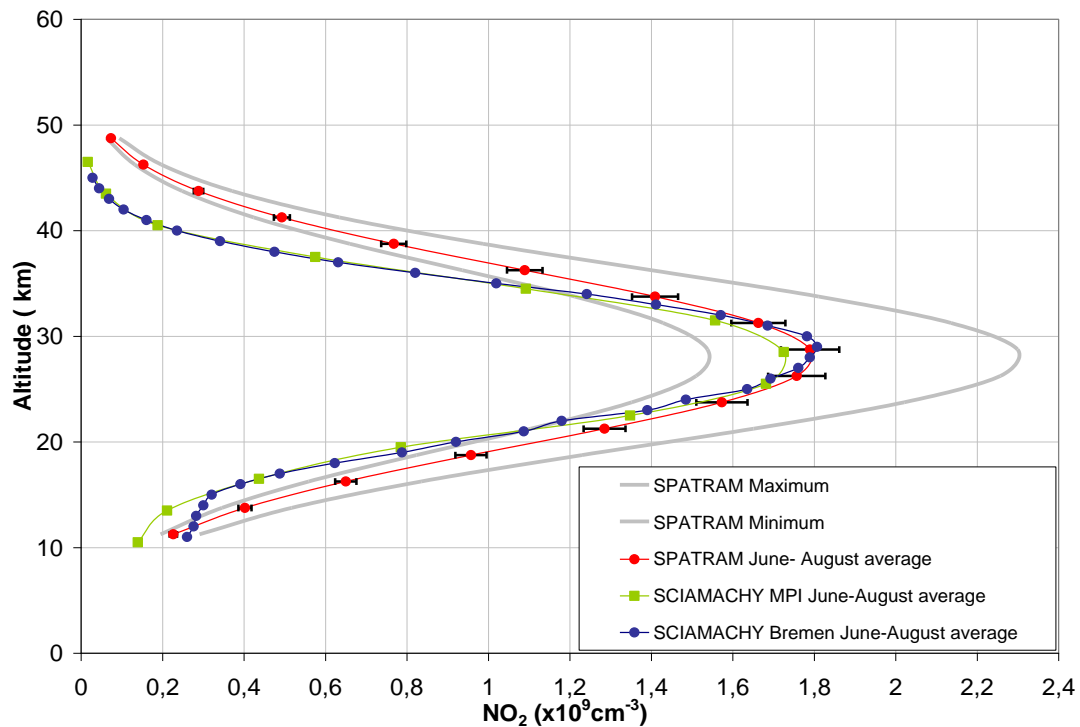


Figure 5.44- NO_2 stratospheric vertical profiles for some days of June, July and August 2010, comprising the minimum values, maximum values and the averaged values retrieved with SPATRAM instrument and comparison with SCIAMACHY datasets from Max Plank Institute Mainz (SCIAMACHY MPI) and the Institute of Environmental Physics (IUP/IFE) of University of Bremen (SCIAMACHY Bremen).

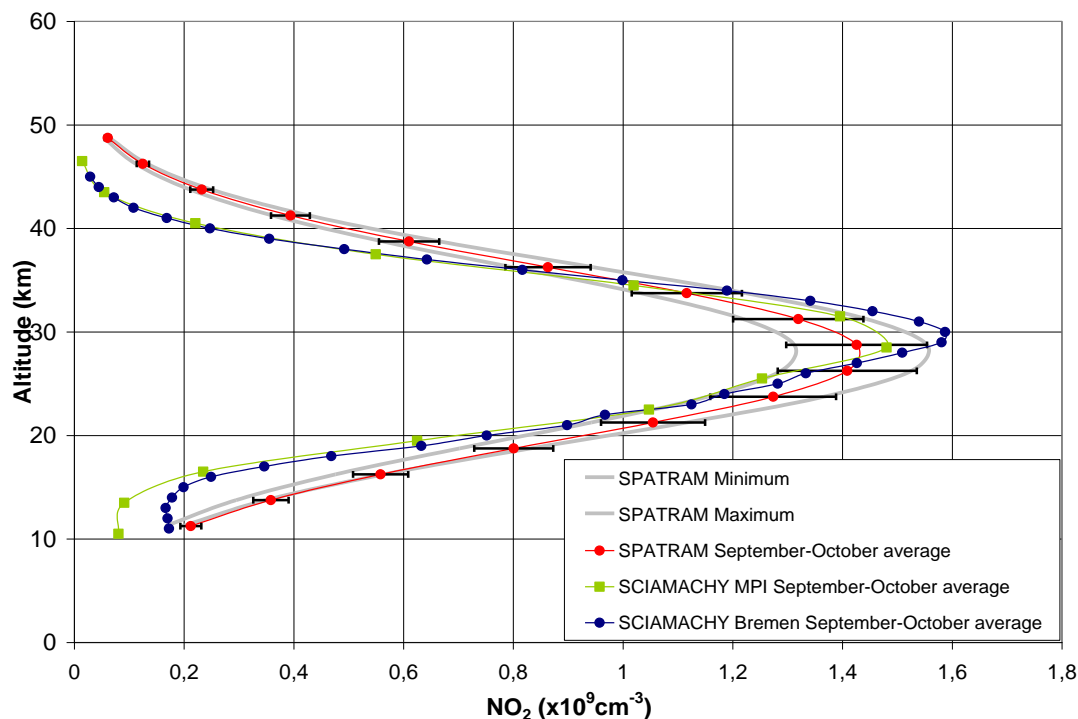


Figure 5.45- NO₂ stratospheric vertical profiles for some days of September and October of 2010, comprising the minimum values, maximum values and the averaged values retrieved with SPATRAM instrument and comparison with SCIAMACHY datasets from Max Plank Institute Mainz (SCIAMACHY MPI) and the Institute of Environmental Physics (IUP/IFE) of University of Bremen (SCIAMACHY Bremen).

From the analysis of the figures it can be inferred that the bulk of NO₂ concentration is different using SCIAMACHY instrument. For example, using MPI algorithms the bulk in the following periods is achieved for: a) May: between 25.5 km and 28.5 km b) June-August: at 28.5 km c) September-October: 28.5 km. Using the IUP/ IFE algorithms the bulk is achieved for the following altitudes a) May: between 26 km and 27 km b) June-August: at 29 km c) September-October: 30 km. The deviation associated between the two instruments is in average between 4%-9% (4% around the bulk and 9% over 33 km).

The differences between the altitudes of the bulk can be explained for the differences in AMF used to make the calculations. The AMF is calculated using different models.

5.6 Air quality evaluation in the south-western regions of the Iberian Peninsula

5.6.1 Introduction

Air quality in cities is the result of a multipart interaction between natural and anthropogenic environmental conditions (Fenger, 1999).

A major likely reason for the air quality problems is urban population growth combined with change in land use due to increasing urban areas (Fenger, 1999). The urban population growth

has many consequences like the higher emissions of air pollutants. These emissions can be categorised as a) motor traffic, b) industry, c) power plants, d) trade and e) domestic fuel (Mayer, 1999). Nevertheless the motor vehicle traffic seems to be the most important source group for air pollution especially in cities. As cities expand the number of motor vehicles increase and more people buy a car and travel in it much longer than before and over greater distances. Therefore air pollution has become one of the major environmental issues and has become a very important factor to the maintenance the urban air quality. The process of air pollution works as follows: gases and particulate pollutants emitted into the atmosphere are diluted or dispersed by air movements that carry them away from the initial source and diffuse them into larger volumes of air by turbulent eddies (Mayer, 1999). Those gases and particles in the atmosphere can affect the populations locally as well as at distant places from the sources and in a more or less permanent way causing health problems.

The aim of this study is the use of the ground-based spectrometer SPATRAM installed at Évora to identify and characterize some sources of the episodes of air pollution (in terms of high loads of NO_2) reaching the city. This study provides information about nitrogenous (polluted) air masses transported over Évora, in 2010, detected with SPATRAM. The joint action of the SPATRAM data and HYSPLIT (HYbrid Single-Particle Lagrangian Integrated Trajectory) maps, allows for the identification of the sources responsible for the pollution events recorded at the Évora Observatory.

The abundance of NO_2 in the troposphere is highly variable and influenced by both anthropogenic and natural emissions (Palmgren et al., 1996). Recalling chapter 2, on a global scale the major sources of NO_2 and NO (NO_x = nitrogen oxides) are fossil fuel combustion, biomass burning, lightening and soil microbial production, the oceans, the input for stratosphere and the oxidation of ammonia in the atmosphere (Logan, 1983).

Tropospheric NO_x has a relatively short lifetime on order of hours in the boundary layer and a few days in the upper troposphere and is usually considered to be confined to polluted areas (Ordóñez et al., 2006).

Nitrogen dioxide is a major problem in urban areas representing an important urban pollutant in most of European cities. The nitrogen compounds especially the NO_x compounds play a very important role in atmospheric chemistry and for formation of photochemical oxidants (O_3 , NO_2 , nitrates and PAN) many of these compounds act as irritants on the respiratory tract of humans and may also lead to chronic diseases. The exposure to NO_2 has been associated with an increase in respiratory infection and wheezing (Bernstein et al., 2004).

Road traffic is the main source of nitrogen oxides in urban areas in most of large cities all over the world (Palmgren et al., 1996). Nitrogen oxides are formed under combustion at high

temperatures in petrol as well as diesel engines. The emission of nitrogen oxides from road traffic is typically less than 50 % of the total emission, but because the emission from vehicles occurs near the ground, in contrast to the emission from power plants and industries the road traffic contributes up to 90% of the concentration in urban air (Palmgren et al., 1996).

Most of the nitrogen oxides are emitted to atmosphere as NO, which is believed to be harmless in the usual concentrations even in heavily polluted cities (Palmgren et al., 1996) and the remaining part is mainly NO₂. Concerns over the health impacts, lead to the EU First Daughter Directive (2008/50/CE) (and in Portugal the DL 102/2010) which sets an annual mean limit of 32 µg/m³, and a hourly limit of 140 µg/m³ that must not be exceeded on more than 18 occasions each year for human protection, and 24 µg/m³ for vegetation and ecosystem protection (WHO,2000; Carslaw, 2005, DL 102/2010).

5.6.2 Methodology

The used methodology combines the SPATRAM data (NO₂ SCDs) to the HYbrid Single-Particle Lagrangian Integrated Trajectory (HYSPLIT) - at [http://www.arl.noaa.gov/ready/HYSPLIT- 24](http://www.arl.noaa.gov/ready/HYSPLIT-24) hours back-trajectory's at different altitudes (1000m, 3000m, 5000m, 10000m, 15000m and 25000m). The period under investigation is 1st January 31st December of 2010. This association allows for the recognition and identification of the potential sources responsible for the pollution events recorded at the site Évora.

Reminding that Évora surrounding areas are mainly rural like the city itself. In the West direction, very large urban and industrial areas are located (e.g. Lisbon, Setúbal, Barreiro, Seixal), and in the East direction Badajoz is situated which is an important Spanish city known for its large urban and industrial development. Due to the fact that Évora is considered an unpolluted city allows for the detection of unexpected variations in the diurnal NO₂ cycle derived from the NO₂ SCDs obtained with SPATRAM. The identification of potential pollution sources is related to the high possibility of an intrusion of a polluted air mass rich in NO₂ into another with low concentration in this particularly gas on urban and industrial sites that travels from the pollution site to the Évora site.

Whenever a variation in the normal behavior of the NO₂ SCD tendencies was detected (a demarked peak), that peak was pointed as one 'pollution event', meaning that an event of tropospheric pollution occurred during the day, at a distant site. The event is marked as 'tropospheric', although SPATRAM, measuring in the zenith sky configuration (pointing to the vertical direction), is most sensitive to the stratospheric content of NO₂ since the bulk of NO₂ is located at 25-27 km of altitude. However, high loads of tropospheric NO₂ content can be detected by the SPATRAM instrument.

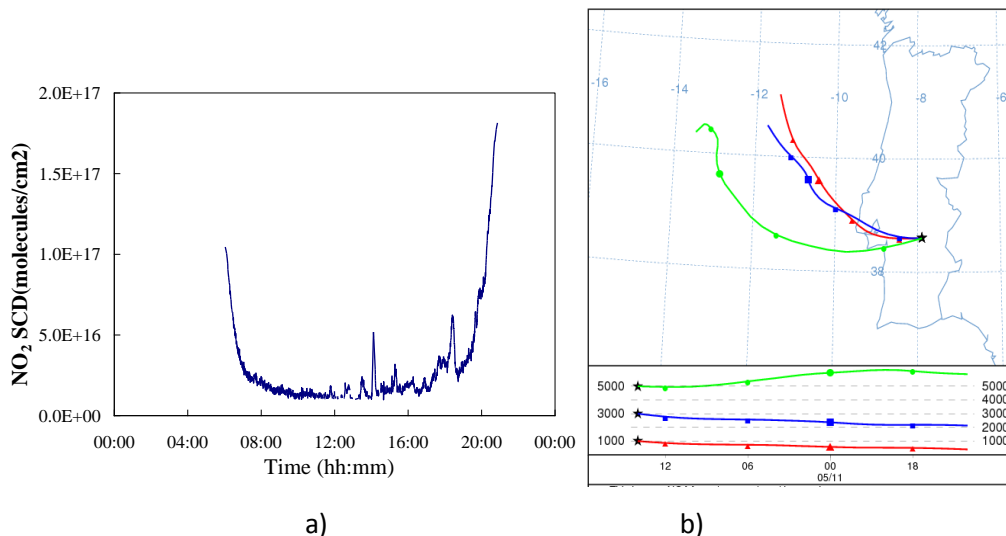
5.6.3 Results

Using the above methodology were identified 71 days in 2010 with pollution events. In thirty of those days two or three demarked peaks were registered that were considered as 2 or 3 pollution events. In the other 41 days there was registered only one demarked peak correspondent to only one pollution event.

The potential air pollution sources registered were from sites mainly in Portugal. It was also identified possible pollution sources from Spain and North of Africa.

The next examples illustrate some of the results obtained with the SPATRAM instrument with the application of the above mentioned methodology.

The following example illustrates the pollution event detected in Évora with potential sources in Lisbon and Tagus Valley area. Fig. 5.46 shows that near 01:30 PM, 02:00 PM, 03:00 PM and 06:30 PM there are demarked peaks on the NO₂ SCD daily concentration obtained with SPATRAM measurements. Analyzing the 24 hours HYSPLIT back-trajectories (Fig. 5.46 b) for the same day, for example for the 02:00 PM it can be seen that, at different altitudes, the air mass is passing over high polluted industrial and urban areas like Setúbal (5000 m), Barreiro, Montijo, Seixal (1000 m), Lisboa area (1000 and 5000 m) (Fig. 5.46) towards Évora. Apart from being a high populated and industrial region there are also power plants (Alto do Mira- near Amadora, Setúbal and Barreiro) that release also NO₂ to atmosphere.



The NO₂ quantity measured at Évora site for the 02:00 PM event was 0.1901 µg/m³ (approximately 3.78×10¹⁶ molecules/cm²).

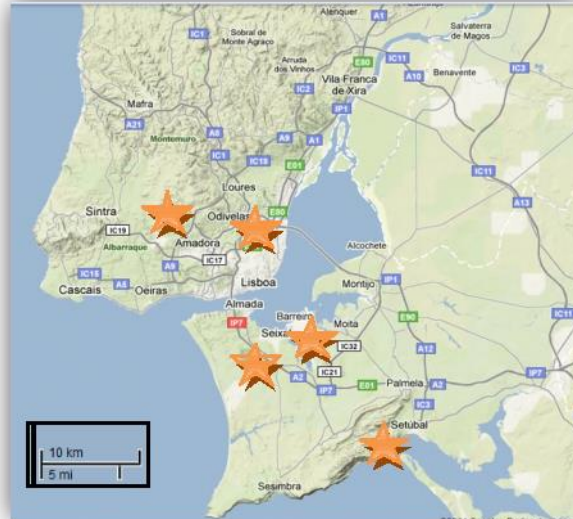


Figure 5.47- Location of the potential pollution sources (Setúbal, Barreiro, Seixal, Lisboa, Amadora) detected by the combination of SPATRAM data and HYSPLIT back-trajectories for the 11th May of 2010 at the heights of 1000, 3000 and 5000 m- at www.maps.google.com.

The frequency of pollution events occurrence with potential sources in Portugal, during 2010, is summarized in Fig. 5.48.

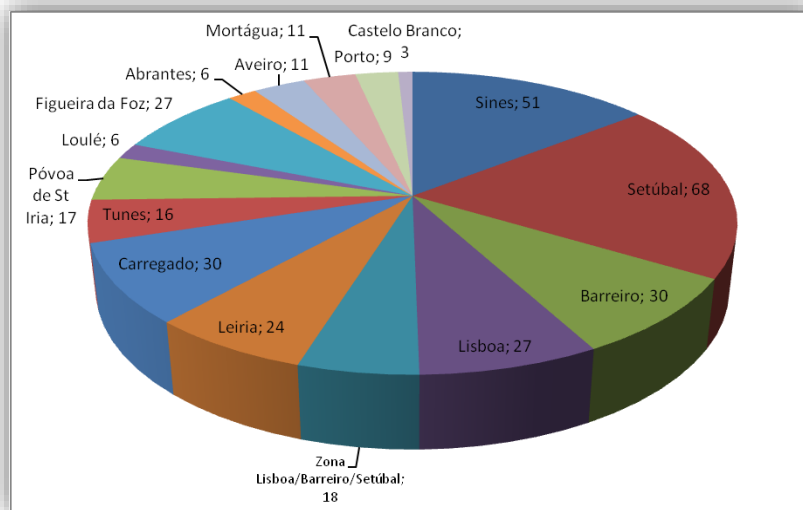


Figure 5.48 - Number of pollution events registered at Évora's Observatory in 2010 with the potential sources located in Portugal.

The above identified sites are the locations of power plants (Barreiro, Setúbal, Carregado, Póvoa de Santa Iria, Abrantes, Tapada do Outeiro near Porto, e.g.), biomass stations (Vila Velha de Rodão near Castelo Branco e.g.), industrial units (Leiria surroundings, Lisboa, Porto, e.g.) and concrete factories (Setúbal, Loulé, e.g.).

Other cases of atmospheric pollution originated in Spain and Morocco were also identified. The next example shown in Fig. 5.49 is related to a pollution event occurred in the north of Spain and Portugal.

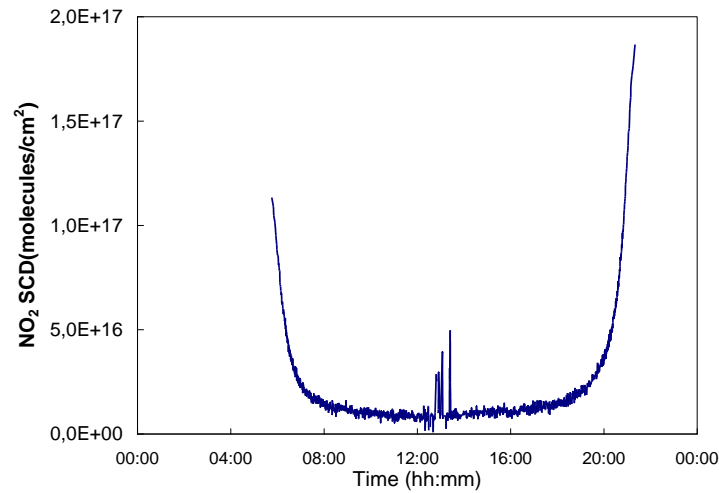


Figure 5.49- The NO₂ Slant column densities (SCD) daily variation during 12th June of 2010 retrieved by SPATRAM at Évora.

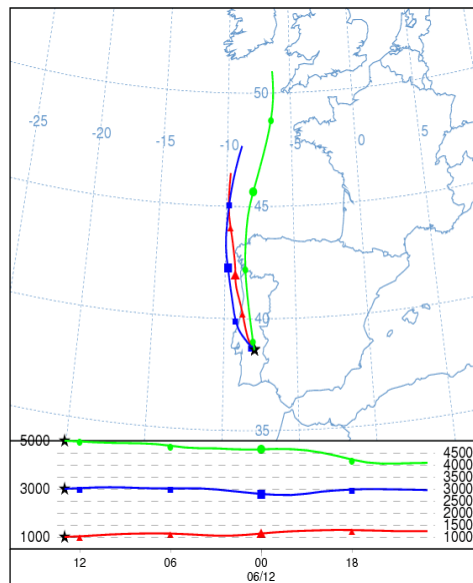


Figure 5.50 - The HYSPLIT back-trajectories for the 12th June of 2010 (ending at 13 UTC) at the heights of 1000, 3000 and 5000 m (at <http://ready.arl.noaa.gov/hysplit-bin/trajtype.pl?runtype=archive>)

The load of NO₂ was identified at Évora Station at 01:04 and 01:24 PM. The most probable NO₂ sources are identified in Leiria (3000m), Figueira da Foz (3000 m), Aveiro (1000, 1500m) and Porto (1000, 1500m) all in Portugal and in Vigo (5000 m) and Coruña (5000m) in Spain with the help of HYSPLIT maps (Fig.5.50).

The NO₂ loads derived from the SPATRAM scattered radiation measurements were, at 01:04 and 01:24 PM respectively, 0.158 µg/m³ (approximately 2.973×10¹⁶ molecules/cm²), 0.216 µg/m³ (approximately 4.241×10¹⁶ molecules/cm²).

There are also records of air pollution event from Oviedo and San Sebastian, Salamanca and Madrid in the North of Spain that correspond to urban centers, industrial sites and location of oil refineries and power plants. Cities like Badajoz, Sevilha, Huelva, Cadiz and others like Portullano, Alicante, Córdoba, Cáceres, Gibraltar, Almendralejo, Murcia, Valência, and Cartagena were also identified as potential NO₂ sources.

The following situation (Fig. 5.51 and Fig.5.52) illustrates one case where it is possible to observe an air mass motion reaching Évora originated in South of Spain and in North of Africa, namely in Rabat and Casablanca known by the intense road traffic.

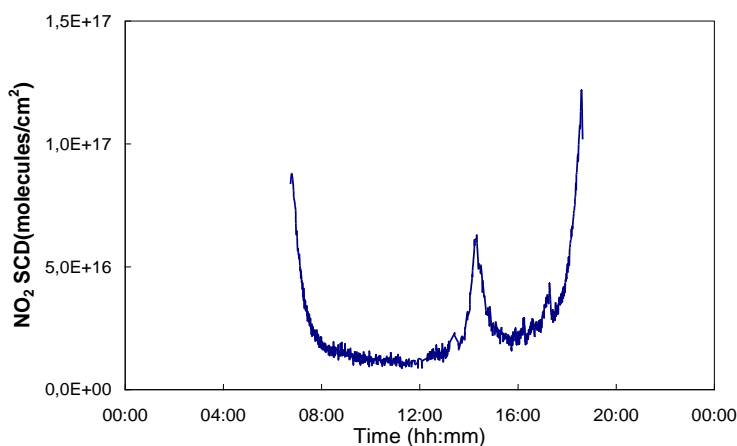


Figure 5.51- The NO₂ Slant column densities (SCD) daily variation during the 2nd of March 2010 retrieved by SPATRAM at Évora.

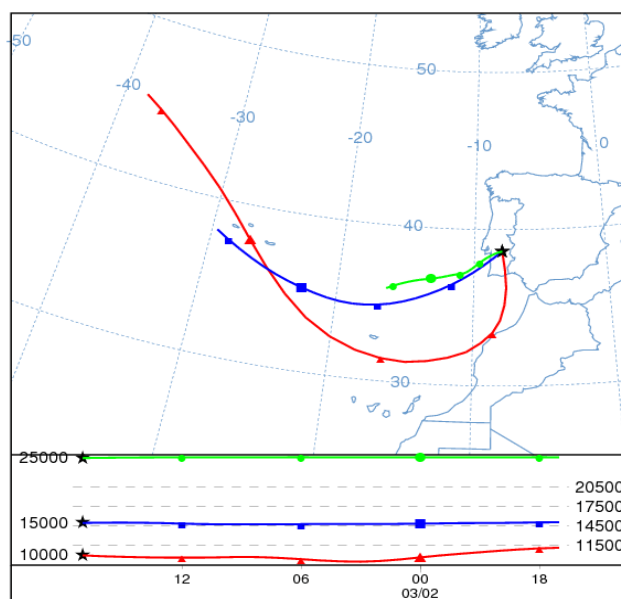


Figure 5.52- The HYSPLIT back-trajectories for the 2nd March of 2010 (ending at 17 UTC) at the heights of 10000, 15000 and 25000 m (at <http://ready.arl.noaa.gov/hysplit-bin/trajtype.pl?runtype=archive>).

For the same day it is also possible to identify intrusion of NO₂ air masses from Tunes (5000 and 3000 m) Portimão and from Huelva and Cadiz (1000m). Fig. 5.53 exhibits the air mass back-trajectories ending at Évora and originated in the above industrial areas (power plant, urban traffic and refineries stations).

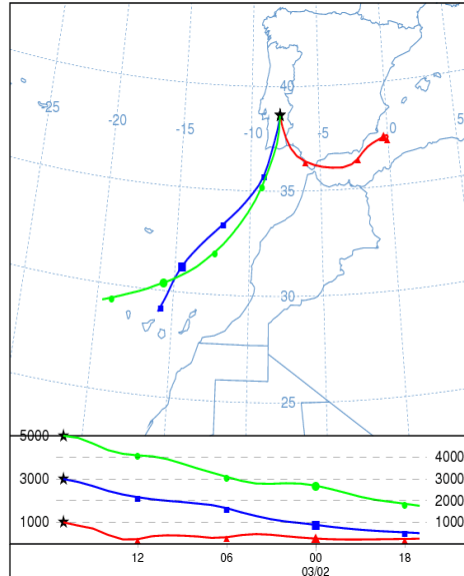


Figure 5.53- The HYSPLIT back-trajectories for the 2nd March of 2010 at the heights of 1000, 3000 and 5000 m (at <http://ready.arl.noaa.gov/hysplit-bin/trajtype.pl?runtype=archive>).

The total contribution of the above sites that was detected by the SPATRAM was 0.159 µg/m³ (approximately 3.89 × 10¹⁶ molecules/cm²).

In the North of Africa there were also identified other sources of NO₂, like El Jadida (1 event), Tanger (2 events) and Algecira (1 event).

Fig. 5.54 summarizes the number of occurrences and the potential sources of NO₂ located in Spain.

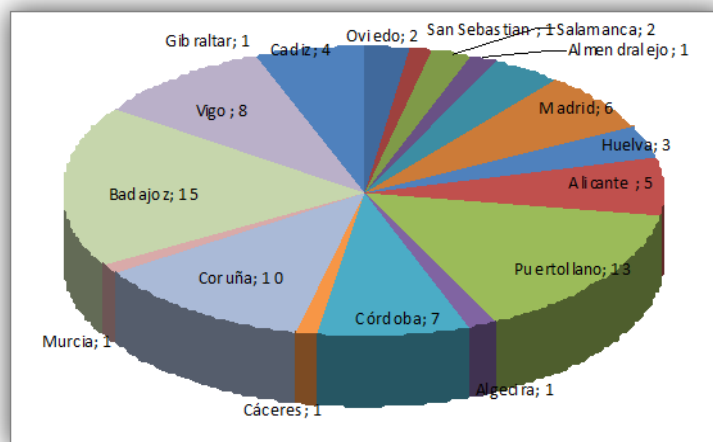


Figure 5.54- Number of pollution events registered at Évora's Observatory in 2010 with the potential sources located in Spain.

The nitrogen pollution loads were simply calculated as the differences between the maximum value for each registered event and the background values extrapolated by the regular function described by the daily SCDs. In Fig. 5.55 is shown the number of events with NO₂ concentration between 0.03 and 0.28 µg/m³ (9 bins of 0.03 µg/m³ each) that were retrieved by the SPATRAM.

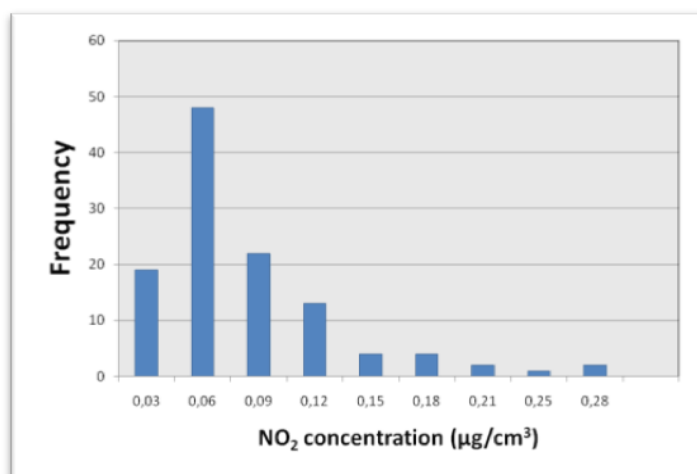


Figure 5.55- Histogram that illustrated the quantity of NO₂ detected in Évora in µg/m³ with the SPATRAM instrument for each pollution event, for the 115 events recorded at Évora Station.

For the analysis of Fig. 5.55 one can conclude that 48 events were registered where the NO₂ concentrations are between 0.03 and 0.06 µg/m³, 22 events where the NO₂ concentrations are between 0.06 and 0.09 µg/m³, 19 events where the NO₂ concentrations are between 0 and 0.03 µg/m³ and 13 events with NO₂ values between 0.09 and 0.12 µg/m³. On the other 13 events the NO₂ concentrations lay between 0.12 and 0.28 µg/m³. The maximum value obtained in a 'pollution' event occurred in 9th May 2010 from the SPATRAM scattered radiation measurements reached 0.251 µg/m³ (approximately 5.133×10^{16} molecules/cm²) and the minimum value of 0.011 µg/m³ (approximately 0.94×10^{16} molecules/cm²) was registered in the 2nd February 2010.

6. Conclusion and outlook

6.1 Conclusion

This PhD work aims to be a contribution in the framework of the atmospheric sciences since we presented a review of the atmospheric composition and structure together with a presentation of the main physical and chemical processes suffered by the atmospheric compounds and by the solar radiation. Furthermore, after the presentation of the equipment utilized in this study, the algorithms applied to the spectral data carried out with the SPATRAM spectrometer for the assessment of atmospheric tracers content along the optical path of measurements (Slant Column Density – SCD) are explained. The demonstration of how the DOAS master equation is obtained starting from the Lambert-Beer extinction Law is furnished. The DOAS technique is applied to a spectral series in a UV spectral range (300-360nm) for the identification of the O₃ absorption features in a qualitative mode aiming to highlight the strength of this spectroscopic method. Furthermore, the forward models (AMEFCO and PROMSAR) for the computation of the AMF used to convert the SCD into Vertical Column Density (VCD), are presented. Moreover, the inversion methods for the retrieval of the vertical distribution of some tracers in the stratosphere as well as in the troposphere are described. After these most theoretical sections, the presented algorithms are applied to the ground based spectral data for the retrieval of the VCD of the studied tracers, namely O₃, NO₂ and BrO. The analysis of the obtained results highlighted that the O₃ total columns values are approximately constant during the day and NO₂ total columns values at sunset (PM series) are systematically higher than the sunrise (AM) ones. This is the expected results considering the photo-chemistry activities of both species. With respect to the seasonal behavior of the studied gases (O₃, NO₂ and BrO) it was possible to point out that:

- O₃, NO₂ and BrO shows a sinusoidal variation through the years;
- the O₃ seasonal trend shows a maximum in spring months and a minimum in autumn;
- a inter-annual variability in O₃ values, being that in the years 2008 and 2010 the decrease in the autumn is lower than in the other years in the same period;
- the NO₂ seasonal trend registers higher concentrations in summer months (May, June, July, August) and lower values in winter months (October, November, December, January).

- the first preliminary results for the BrO VCD measured with SPATRAM are presented. The time series, limited to 6 months show a slightly seasonal trend reaching the maximum in the spring season.

The results for the seasonal variation of O₃, NO₂ and BrO were compared with the satellite data from OMI, SCIAMACHY, GOME and GOME-2 instruments. In general the comparison/validation revealed a fair agreement between the datasets proving that SPATRAM instrument (in zenith sky configuration) and the employed DOAS algorithms are a good tools for the monitoring of these compounds.

The coupling of the MIGE equipment with SPATRAM and the consequent improvement in the algorithms allowed for the retrieval of NO₂ tropospheric total columns in east, west, south and north azimuth LOS. The results obtained suggested that the observations are dependent on the azimuthal direction. For the studied period (30th March, 8th and 9th April) it was conclusive that the registered NO₂ concentrations were higher from the West and East directions which correspond to the directions of large urban centres (Lisbon (Portugal) and Badajoz (Spain), respectively). Therefore from the analysis of the vertical profiles in PBL it was also possible to infer that the higher values of NO₂ are correspondent to the rush hours in the city (9 and 11 AM, 12 an 2 PM, 5 to 6 PM) although NO₂ polluted air masses from remote sites have also a role in the enhancement of NO₂ concentrations during the day.

The vertical profiles achieved for the period comprised between 5th May to 5th October 2010 present a NO₂ concentration bulk at altitude of approximately 28.75 km. The comparison with the SCIAMACHY data from MPI and University of Bremen are in fairly agreement showing a deviation of 4%-9% in data.

The combination of the NO₂ column content measured with the SPATRAM with the 24 hours back-trajectories ending at Évora for different altitudes, obtained with the HYSPLIT model, allowed for the identification, several long range as well as short range pollution sources from a wide variety of sites. The main sources of NO₂ pollution that were identified at Évora's Observatory are located in Lisboa and Tagus Valley and Sines – Portugal – that correspond to urban and industrial sites where Power Plants are placed. There are other sources of pollution related to the NO₂ emissions like the Cogeneration Power Plants located at Leiria, Póvoa de Santa Iria, Lavos-Leiria, the Biomass Centers placed at Vila Velha de Ródão and Mortágua), oil refineries located at Porto, Sines e.g.), industrial units at Sines, Barreiro, Setúbal, Carregado, among other, and the multi sources produced by the heavy traffic existing in the major cities like Lisbon and Porto and in the Great Lisbon and Porto surrounding areas. The above method has also identified long distant NO₂

sources from Spain and Morocco. This is the first study performed in Portugal on pollution transport using a spectrometer.

6.2 Future work

The present study can be extended to the monitoring of other trace gases, such as sulphur dioxide (SO₂), formaldehyde (HCHO) and glyoxal (CHOCHO), etc.. Therefore will be possible the assessment of diurnal cycles, seasonal and inter-annual variations for the total columns and atmospheric profiles of other trace gases. With the improvement of the algorithms for the retrieval of the vertical distributions using the SPATRAM it is open a path also to extend the research to ozone profiles. It is also important continue this work in order to maintain the measurements of total columns of the presented compounds for future climatologically studies. The monitoring of the PBL in terms of total columns and profiles of NO₂ also can be developed. It is important to make more measurements and also other measurement campaigns in other cities in order to evaluate the air quality.

7. References

A

Alvim-Ferraz M. C. M., S. I. V. Sousa, M. C. Pereira and F. G. Martins (2006), Contribution of anthropogenic pollutants to the increase of tropospheric ozone levels in the Oporto Metropolitan Area, Portugal since the 19th century, *Environ. Pollut.*, 140(3), 516-524.

Andrady, A. L., H. Hamid and A. Torikai (2011), Effects of solar UV and climate change on materials, *Photochem. Photobiol. Sci.*, 10, 292-300. doi: 10.1039/C0PP90038A

Andreae, M. O. and Paul J. Crutzen (1997), Atmospheric Aerosols: Biogeochemical Sources and Role in Atmospheric Chemistry, *Science*, 276, 1052-1057.

Anton, M., A. Serrano, M.L. Cancillo and J.A. Garcia (2008), Total ozone and solar erythemal irradiance in the Southwestern Spain: Day-to-day variability and extreme episodes, *Geophys. Res. Letters*, 35(20), L20804. doi:10.1029/2008GL035290

Anton, M., D. Bortoli, J.M. Vilaplana, A.M. Silva, A. Serrano, M.J. Costa, B. de la Morena and M. Kroon (2010), Total Ozone Column From Direct And Diffuse Spectral Solar Irradiance In The Southwest Of The Iberian Peninsula, *J. Geophys. Res.*, 115, 5305. doi:10.1029/2009JD012514

Antón, M., M. López, J. M. Vilaplana, M. Kronn, M. Bañon, and A. Serrano, (2009), Validation of OMI-TOMS and OMI-DOAS total ozone column using five Brewer spectroradiometers at the Iberian Peninsula, *J. Geophys. Res.*, 114, 14302. doi:10.1029/2009JD012003

Antón, M., M. L. Cancillo, A. Serrano, M. Vaquero and J. A. Garcia (2007), Ozone mini-hole over southwestern Spain during January 2004: Influence over ultraviolet radiation, *Geophys. Res. Lett.*, 34, L10808, doi:10.1029/2007GL029689.

Arsene, C., A. Bougiatioti and N. Mihalopoulos (2009), Sources and variability of non-methane hydrocarbons in the Eastern Mediterranean, *Global Nest J.*, 11(3), 33-340.

Aucamp, P. J., L. Olof Bjorn and R. Lucas (2011), Questions and answers about the environmental effects of ozone depletion and its interactions with climate change: 2010 assessment, *Photochem. Photobiol. Sci.*, 10, 301-316. doi: 10.1039/C0PP90045A

B

Ballaré, C. L., M. M. Caldwell, S. D. Flint, S. A. Robinson and J. F. Bornman (2011), Effects of solar ultraviolet radiation on terrestrial ecosystems. Patterns, mechanisms, and interactions with climate change, *Photochem. Photobiol. Sci.*, 10, 226-241. doi: 10.1039/c0pp90035d

Bauer R., A. Rozanov, C. A. McLinden, L. L. Gordley, W. Lotz, J. M. Russell III, K. A. Walker, J. M. Zawodny, A. Ladstätter-Weißenmayer, H. Bovensmann, and J. P. Burrows (2012), Validation of SCIAMACHY limb NO₂ profiles using solar occultation measurements, *Atmos. Meas. Tech.*, 5, 1059-1084.

Bell, N., L. Hsu, D. J. Jacob, M. G. Schultz, D. R. Blake, J. H. Butler, D. B. King, J. M. Lobert, and E. Maier-Reimer (2002), Methyl iodide: Atmospheric budget and use as a tracer of marine convection in global models, *J. Geophys. Res.*, 107(D17), 4340. doi:10.1029/2001JD001151

Bernstein, J., N. Alexis, C. Barnes, I.L. Bernstein, A. Nel, D. Peden, D. Diaz-Sanchez, S. Tarlo and P.B. Williams (2004), Health effects of air pollution, *J. Allergy Clin. Immun.*, 114(5), 1116-1123.

Bian, H. S., and C. S. Zender (2003), Mineral dust and global tropospheric chemistry: Relative roles of photolysis and heterogeneous uptake, *J. Geophys. Res.*, 108(D21), 4672, doi:10.1029/2002JD003143.

Boersma, K. (2005). *Satellite observations of tropospheric nitrogen dioxide: retrieval, interpretation, and modelling* (doctoral dissertation), available at <http://alexandria.tue.nl/extra2/200511514.pdf>. ISBN 90-386-2211-2

Boersma, K. F., E. J. Bucsela, E. J. Brinksma, J. F. Gleason (2002), OMI-EOS Algorithm Theoretical Basis Document: Trace Gas Algorithms: NO₂, 4, 12-35.

Bortoli, D. (2005), *SPATRAM- Spectrometer for Atmospheric Tracers Measurements- A prototype Equipment for the monitoring of minor compounds of the atmosphere* (Unpublished doctoral dissertation). University of Évora, Évora, Portugal.

Bortoli, D., A. M. Silva, and G. Giovanelli (2010), A new multipurpose UV-Vis spectrometer for air quality monitoring and climatic studies, *Int. J. Remote Sens.*, 31(3), 705-725. doi: 10.1080/01431160902896231

Bortoli, D., A. M. Silva, M. J. Costa, A. F. Domingues, and G. Giovanelli (2009), Measurements of stratospheric ozone and nitrogen dioxide at Évora, Portugal, *Int. J. Remote Sens.*, 30(15-16), 4209-4226.

Bortoli, D., A.M. Silva, M. J. Costa, A. F. Domingues, and G. Giovanelli (2009), Monitoring of atmospheric ozone and nitrogen dioxide over the south of Portugal by groundbased and satellite observations, *Opt. Express*, 17(15), 12944- 12959.

Bortoli, D., G. Giovanelli, F. Ravegnani, I. Kostadinov and A. Petritoli (2005), Stratospheric nitrogen dioxide in the Antarctic, *Int. J. Remote Sens.*, 26(16), 3395-3412. doi 10.1080/01431160500076418

Bortoli, D., S. Masieri, A. F. Domingues, M. J. Costa, A. M. Silva, M. Anton and E. Palazzi (2009), Observations of tropospheric compounds at Évora station with multi-axis hyper spectral measurements, in *Remote Sensing of Clouds and the Atmosphere XIV*, edited by Richard H. Picard, Klaus Schäfer, Adolfo Comeron, Evgueni I. Kassianov, Christopher J. Mertens, Proceedings of SPIE Vol. 7475 (SPIE, Bellingham, WA 2009) 74751K.

Bovensmann, H., J.P. Burrows, M. Buchwitz, J. Frerick, S. Noel, and V.V. Rozanov (1999), SCIAMACHY: Mission Objectives and Measurement Modes, *J. Atmos. Sci.*, 56, 127-150. doi: [http://dx.doi.org/10.1175/1520-0469\(1999\)056<0127:SMOAMM>2.0.CO;2](http://dx.doi.org/10.1175/1520-0469(1999)056<0127:SMOAMM>2.0.CO;2)

Brandtjen, R., T. Klupfel, D. Perner and B.M. Knudsen (1994). Airborne measurements during the European Arctic Stratospheric Ozone experiment: observations of OClO, *Geophys. Res. Lett.*, 21, 1363-1366.

Brasseur, G. P., J. J. Orlando and G. S. Tyndall (1999). *Atmospheric Chemistry and Global Change*, New York: Oxford University Press. ISBN: 9780195105216

Brasseur, G. P., Müller, J.-F., Tie, X.-X. & Horowitz, L. (2000). Tropospheric Ozone and Climate: Past, Present and Future. In T. Matsuno and H. Kida (Eds.), 14th Toyota Conference (pp.63-76). Mikkabi. ISBN 4-88704-127-6. Acedido de <http://www.terrapub.co.jp/e-library/toyota/pdf/063.pdf>

Brasseur, G. and S. Solomon (2005). *Aeronomy of the middle atmosphere: Chemistry and Physics of the Stratosphere* (pp. 151-156), Netherlands: Springer Netherlands. ISBN 978-1-4020-3824-2

Bobrowski, N. (2005). *Volcanic gas studies by multi axis differential optical absorption spectroscopy* (Unpublished doctoral dissertation). Institut für Umweltphysik, Universität Heidelberg, Heidelberg, Germany.

Bobrowski, N., G. Hönniger, B. Galle, and U. Platt (2003), Detection of bromine monoxide in a volcanic plume, *Nature*, 423, 273–276.

Bucseles, E., E. Celarier, M. Wenig, J. Gleason, P. Veefkind, K.F. Boersma and E. Brinksma (2006), Algorithm for NO₂ vertical column retrieval from the Ozone Monitoring Instrument, *IEEE T. Geosci. Remote*, 44, 1245-1258.

Buchwitz, M. and J.P. Burrows (2004), Retrieval of CH₄, CO, and CO₂ total column amounts from SCIAMACHY near-infrared nadir spectra: retrieval algorithm and first results, K. P., Schaefer, A., Comeron, M. R., Carleer & R. H. Picard (Eds.) *Proceedings of SPIE 5235: Remote Sensing of Clouds and the Atmosphere VIII-375* (pp. 375-388) . Barcelona: SPIE. doi:10.1117/12.514219.

Burrows, J. P., A. Dehn, B. Deters, S. Himmelmann, A. Richter, S. Voigt and J. Orphal (1998), Atmospheric remote-sensing reference data from GOME: 1. Temperature-dependent absorption cross sections of NO₂ in the 231–794 nm range, *J. Quant. Spectrosc. Radiat. Transfer*, 60, 1025–1031.

Burrows, J. P., A. Dehn, B. Deters, S. Himmelmann, A. Richter, S. Voigt, and J. Orphal (1999), Atmospheric remote-sensing reference data from GOME: 2. Temperature dependent absorption cross sections of O₃ in the 231–794 nm range, *J. Quant. Spectrosc. Radiat. Transfer*, 61, 509–517.

Burrows, J. P., E. Holzle, A.P.H. Goede, H. Visser, W. Fricke (1995), SCIAMACHY-Scanning Imaging Absorption Spectrometer for Atmospheric Cartography, *Acta Astronaut.*, 35(1), 445-451.

Burrows, J., U. Platt and P. Borrell (2011), *Tropospheric Remote Sensing from Space*, Berlin: Springer-Verlag Berlin Heidelberg. ISBN: 978-3-642-14790-6. Available at <http://www.iup.uni-bremen.de/materials/remensingbook/>

Butchart, N., A. A. Scaife, M. Bourqui, J. de Grandpre, S. H. E. Hare, J. Kettleborough, U. Langematz, E. Manzini, F. Sassi, K. Shibata, D. Shindell and M. Sigmond (2006), Simulations of anthropogenic change in the strength of the Brewer–Dobson circulation, *Clim. Dyn.*, 27, 727–741.

C

Callies, J., E. Corpaccioli, M. Eisinger, A. Hahne and A. Lefebvre (2000), GOME-2 – Metop’s Second-Generation Sensor for Operational Ozone Monitoring, *ESA bulletin*, 102, 28-36.

Carslaw, D. (2005), Evidence of an increasing NO₂/NO_x emissions ratio from road traffic emissions, *Atmos. Environ.*, 39, 4793-4802.

Chance, K. V., and R. J. D. Spurr (1997), Ring effect studies: Rayleigh scattering, including molecular parameters for rotational Raman scattering and the Fraunhofer spectrum, *Appl. Opt.*, 36(21), 5224–5230.

Committee on Tropospheric Ozone, National Research Council (1991), Atmospheric Chemistry of Ozone and Its Precursors. Rethinking the Ozone Problem in Urban and Regional Air Pollution. Washington, DC: The National Academies Press.

Cordero, M.P. Free, A. I. Jonsson, J. Logan, D. Stevenson (2010), Report of the 2010 Assessment of the Scientific Assessment Panel- chapter 4, UNEP. Available at http://ozone.unep.org/Assessment_Panels/SAP/Scientific_Assessment_2010/06-Chapter_4.pdf

Coldewey-Egbers, M., M. Weber, L. N. Lamsal, R. de Beek, M. Buchwitz, J. P. Burrows (2005), Total ozone retrieval from GOME UV spectral data using the weighting function DOAS approach, *Atmos. Chem. Phys.*, 5, 5015-5025.

Cox, M. L., G. A. Sturrock, P. J. Fraser, S. T. Siems and P. B. Krummel (2005), Identification of Regional Sources of Methyl Bromide and Methyl Iodide from AGAGE Observations at Cape Grim, Tasmania, *J. Atmos. Chem.*, 50, 59–77.

Crutzen, P. (1979), The role of NO and NO₂ in the chemistry of troposphere and stratosphere, *Ann. Rev. Earth Planet Sci.*, 7, 443-72.

Crutzen, P., P. H. Zimmermann (1991), The changing photochemistry of the troposphere, *Tellus*, 43, 136-151.

D

Decreto-Lei nº 102/2010 de 23 Setembro. *Diário da República nº 186 – 1ª Série*. Ministério do Ambiente. Lisboa.

Deepak, A. (1977), *Inversion methods in atmospheric remote sounding*, New York: Academic Press.

Delmas, R., D. Serca and C. Jambert (1997), Global inventory of NO_x sources, *Nutrien Cycling in Agroecosystems*, 48, 51-60.

Dix, B. (2007). *Spectroscopic Measurements of Atmospheric Trace Gases on Long-Distance Flights* (Unpublished doctoral dissertation). University of Heidelberg, Heidelberg, Germany.

Domingues, A. F., D. Bortoli, A. M. Silva (2011), Determination of NO₂ amount in polluted air masses over Évora- Portugal, during 2010 with remote sensing measurements, Proceedings of GCGW – Global Conference on Global Warming – 11-14 July 2011 Lisbon Portugal.

Domingues, A. F., D. Bortoli, A. M. Silva, M. Antón and S. Masieri (2009), NO₂ seasonal variations and tropospheric vertical profiles retrieval with ground based and satellite equipments at Évora Station-Portugal, in Proceedings of Atmospheric Science Conference, Barcelona, Spain, pp.6 (ESA SP-676, November 2009).

Domingues, A. F., D. Bortoli, M. Antón, and A. M. Silva (2009), Ozone, nitrogen dioxide and BrO total columns over Évora-Portugal during 2007-2008, in Remote Sensing of Clouds and the Atmosphere XIV, edited by Richard H. Picard, Klaus Schäfer, Adolfo Comeron, Evgueni I. Kassianov, Christopher J. Mertens, Proceedings of SPIE Vol. 7475 (SPIE, Bellingham, WA 2009) 74751L.

Domingues A.F., D. Bortoli, M. Antón, and A.M. Silva (2011), Ozone Seasonal Variation with Ground-Based and Satellite Equipments at Évora Observatory: Portugal During 2007-2010, in Lecture Notes in Geoinformation and Cartography, edited by Jukka M. Krisp, Liqiu Meng, Roland Pail, Uwe Stilla, Proceedings of Earth Observation of Global Changes (EOGC)(Springer-Verlag Berlin Heidelberg 2013), 137-146, DOI: 10.1007/978-3-642-32714-8_9.

E

Ehrlich, R., J.C. Findlay, J.D. Fenters, D.E. Gardner (1977), Health effects of short-term inhalation of nitrogen dioxide and ozone mixtures, *Environ. Res.*, 14, 2, 223–231.

Elokhov A. S. and A. N. Gruzdev (2000), Nitrogen Dioxide Column Content and Vertical Profile Measurements at the Zvenigorod Research Station, *Atmos. Ocean. Phys.*, 46, 763-777.

Eskes H. J., R. J. van der A, E. Brinksma (2006), Algorithm Document TOSOMI. Available at http://www.temis.nl/docs/AD_TOSOMI.pdf.

Eskes, H. J., R. J. van der A, E. J. Brinksma, J. P. Veefkind, J. F. de Haan, and P. J. M. Valks (2005), Retrieval and validation of ozone columns derived from measurements of SCIAMACHY on Envisat, *Atmos. Chem. Phys. Discuss.*, 5, 4429-4475.

Evangelisti F., A. Baroncelli, P. Bonasoni, G. Giovanelli and F. Ravegnani (1995), Differential optical absorption spectrometer for measurement of tropospheric pollutants, *Appl. Optics*, 34, 2737–2744.

Evyugina, M., T. Nunes, C. Pio, C. S. Costa (2006), Photochemical pollution under sea breeze conditions, during summer, at the Portuguese West Coast, *Atmos. Environ.*, 40, 6277-6293.

F

Fahey, D.W., Michaela I. Hegglin (2010), Twenty Questions and answers about the ozone Layer: 2010, Available at http://ozone.unep.org/Assessment_Panels/SAP/Scientific_Assessment_2010/SAP-2010-FAQs-update.pdf

Farahani, E. (2006), *Stratospheric Composition Measurements in the Arctic and at Mid-latitudes and Comparison with Chemical Fields from Atmospheric Models* (Unpublished doctoral thesis). University of Toronto, Toronto, Canadá.

Ferral, A. (2011), Atmospheric gas detection with remote sensing technologies, seminary document from Instituto de Altos Estudios Espaciales Mario Gulich, Centro Espacial Teo_lo Tabanera, CONAE, Cordoba – Argentina. Available at http://aulavirtual.ig.conae.gov.ar/moodle/pluginfile.php/513/mod_page/content/71/AnabellaFerral__seminario.pdf

Fenger, J. (1999), Urban Air quality, *Atmos. Environ.*, 33, 4877-4900.

Finlayson-Pitts, B.J. and J.N. Pitts, Jr. (1993), Atmospheric Chemistry of Tropospheric Ozone Formation: Scientific and Regulatory Implications, *Air & Waste*, 43 (8), 1091-1100. doi: 10.1080/1073161X.1993.10467187

Fleischmann, O. C., M. Hartmann, J. P. Burrows, , J. Orphal (2007), New ultraviolet absorption cross-sections of BrO at atmospheric temperatures measured by time-windowing Fourier transform spectroscopy, *J. of Photochemistry and Photobiology A: Chemistry*, 168, 117–132, doi: 10.1016/j.jphotochem.2004.03.026

Fortuin, J. and H. Kelder (1998), An ozone climatology based on ozonesonde and satellite measurements, *J. Geophys. Res.*, 103, 31,709-31,734.

Forster, P.M., and D.W.J. Thompson (Coordinating Lead Authors), M.P. Baldwin, M.P. Chipperfield, M. Dameris, J.D. Haigh, D.J. Karoly, P.J. Kushner, W.J. Randel, K.H. Rosenlof, D.J. Seidel, S. Solomon, G. Beig, P. Braesicke, N. Butchart, N.P. Gillett, K.M. Grise, D.R. Marsh, C. McLandress, T.N. Rao, S.-W. Son, G.L. Stenchikov, and S. Yoden, Stratospheric ozone and surface ultraviolet radiation, Chapter 2 in Scientific Assessment of Ozone Depletion: 2010, Global Ozone Research and Monitoring Project–Report No. 52, 516 pp., World Meteorological Organization, Geneva, Switzerland, 2011.

Frins, E., N. Bobrowski, U. Platt and T. Wagner (2006), Tomographic multi-axis-differential optical absorption spectroscopy observations of Sun-illuminated targets: a technique providing well-defined absorption paths in the boundary layer, *Appl. Opt.*, 45, 6227-6240.

G

Grainger, R. G. and E. J. Highwood (2003), Changes in stratospheric composition, chemistry, radiation and climate caused by volcanic eruptions, Geological Society, London, Special Publications, 213, 329-347.

H

Haigh, J. (2007), Lecture 6- Absorption by atmospheric gases in the IR, visible and UV spectral regions. Available at <http://solarphysics.livingreviews.org/open?pubNo=lrsp-2007-2&page=articlesu8.html>

Harris, N. R. P., E. Kyro, J. Staehelin, D. Brunner, S.-B. Andersen, S. Godin-Beekmann, S. Dhomse, P. Hadjinicolaou, G. Hansen, I. Isaksen, A. Jrrar, A. Karpetchko, R. Kivi, B. Knudsen, P. Krizan, J. Lastovicka, J. Maeder, Y. Orsolini, J. A. Pyle, M. Rex, K. Vanicek, M. Weber, I. Wohltmann, P. Zanis, and C. Zerefos (2008), Ozone trends at northern mid- and high latitudes – a European perspective, *Ann. Geophys.*, 26, 1207–1220.

Hausmann, M. and U. Platt (1994), Spectroscopic measurement of bromine oxide and ozone in the high Arctic during Polar Sunrise Experiment 1992, *J. Geophys. Res.*, 99 (D12), 25399-25413. doi: 10.1029/94JD01314.

Heckel, A., A. Richter, T. Tarsu, F. Wittrock, C. Hak, I. Pundt, W. Junkermann, and J. P. Burrows (2005), MAX-DOAS measurements of formaldehyde in the Po-Valley, *Atmos. Chem. Phys.*, 5, 909–918.

Hendrick F., M. Van Roozendaal, A. Kylling, A. Petritoli, A. Rozanov, S. Sanghavi, R. Schofield, C. Von Friedeburg, T. Wagner, F. Wittrock, D. Fonteyn, and M. De Maziere (2006), Intercomparison exercise between different radiative transfer models used for the interpretation of ground-based zenith-sky and multi-axis DOAS observations, *Atmos. Chem. Phys.*, 6, 93–108.

Hönninger, G., C. von Friedeburg, and U. Platt (2004), Multi axis differential Optical absorption spectroscopy (MAX-DOAS), *Atmos. Chem. Phys.*, 4, 231-254.

I

IPCC 2001: Climate Change 2001: Impacts, Adaptation, and Vulnerability, Contribution of Working Group II to the Third Assessment Report of the Intergovernmental Panel on Climate Change [McCarthy, J., O. Canziani, N. A. Leary, D-J. Dokken, K. S. White (eds.)], Cambridge University Press, Cambridge, United Kingdom and New York, NY, USA.

IPCC, 2007: Climate Change 2007: The Physical Science Basis. Contribution of Working Group I to the Fourth Assessment Report of the Intergovernmental Panel on Climate Change [Solomon, S., D. Qin, M. Manning, Z. Chen, M. Marquis, K.B. Averyt, M. Tignor and H.L. Miller (eds.)]. Cambridge University Press, Cambridge, United Kingdom and New York, NY, USA.

IPCC, 2013: Climate Change 2013: The Physical Science Basis. Contribution of Working Group I to the Fifth Assessment Report of the Intergovernmental Panel on Climate Change [Stocker, T.F., D. Qin, G.-K. Plattner, M. Tignor, S.K. Allen, J. Boschung, A. Nauels, Y. Xia, V. Bex and P.M. Midgley (eds.)]. Cambridge University Press, Cambridge, United Kingdom and New York, NY, USA, 1535 pp, doi:10.1017/CBO9781107415324.

Iwao, K., and T. Hirooka (2006), Dynamical quantifications of ozone mini-hole formation on both hemispheres, *J. Geophys. Res.*, 111, D02104, doi: 10.1029/2005JD006333.

J

Jacob, D. (1999). *Introduction to Atmospheric Chemistry*, Cambridge: Princeton University press.

Jacobson, M. (1999), *Fundamentals of Atmospheric Modeling*, Second edition, New York: Cambridge University Press. ISBN (e-book): 978-0-511-11115-0

Jacobson, Mark (2002), *Atmospheric pollution: History, Science and regulation*, New York: Cambridge University Press.

Jacobson, M. (2012), *Air pollution and global warming: history, science and solutions*, New York: Cambridge university press.

Jaeglé, L., D. J. Jacob, W. H. Brune, D. Tan, I. C. Faloona, A. J. Weinheimer, B. A. Ridley, T. L. Campos, G. W. Sachse (1998), Sources of HO_x and production of ozone in the upper troposphere over the United States, *Geophys. Res. Lett.*, 25, 1705-1708.

K

Kampa, M., E. Castanas (2008), Human health effects of air pollution, *Environ. Pollut.*, 151, 362 -367.

Kerr, A. Elokhov, G. Giovanelli, F. Ravegnani, M. Premuda, I. Kostadinov, F. Erle, T. Wagner, K. Pfeilsticker, M. Kenntner, L. C. Marquard, M. Gil, O. Puentedura, M. Yela, D. W. Arlander, B. A. K. Hoiskar, C. W. Tellefsen, K. K. Tornkvist, B. Heesel, R. L. Jones, S. R. Aliwell, and R. A. Freshwater (1999), Slant columns measurements of O₃ and NO₂ during the NDSC intercomparison of zenith-sky UV-visible spectrometers in June 1996, *J. Atmos. Chem.*, 32, 281-314.

Kim, S.W., S.C. Yoon, J.G. Won, and S.C. Choi (2007), Ground-based remote sensing measurements of aerosol and ozone in an urban area: A case study of mixing height evolution and its effect on ground-level ozone concentrations, *Atmos. Environ.*, 41(33), 7069-7081.

Kostadinov, I., G. Giovanelli, F. Ravegnani, F. Evangelisti, P. Bonasoni, R. Werner, and U. Bonafè (1997), Polarization and Ring Effect Influences upon Stratospheric DOAS Measurements, *Proceedings SPIE 3106: Spectroscopic Atmospheric Monitoring Techniques (pp.74–83)*.Munich: SPIE.

Kostadinov, I., G. Giovanelli, D. Bortoli, A. Petrioli, F. Ravegnani, G. Pace and E. Palazzi (2006), A multi-input UV-VIS airborne GASCOD/A4r spectroradiometer for the validation of satellite remote sensing measurements, *Annals of Geophysics*, 49,71–81.

Kronn, M., J. P. Veefkind, M. Sneep, R. D. Mcpeters, P. K. Bhartia and P.F. Levelt (2008), Comparing OMI-TOMS and OMI-DOAS total ozone columns data, *J. Geophys. Res.*, 113, D16S28.doi: 10.1029/2007JD008798

Krzyscin, J. W. (2002), Long-term changes in ozone Mini-Hole event frequency over the northern Hemisphere derived from ground-bases measurements, *Int. J. Climatol.*, 22, 1425-1439.

Koik, M., Y. Kond, W. A. Matthew, P. V. Johnsto and K. Yamazak (1993), Decrease of stratospheric NO₂ at 44°N caused by Pinatubo Volcanic aerosols, *Geophys. Res. Lett.*, 20, 18, 1975-1978.

Kourtidis, K.A., I. Ziomias, C. Zerefos, E. Kosmidis, P. Symeonidis, E. Christophilopoulos, S. Karathanassis, A. Mploutsos (2002), Benzene, toluene, ozone, NO₂ and SO₂ measurements in an urban street canyon in Thessaloniki, Greece, *Atmos. Environ.*, 36(34), 5355-5364.

Kühl, S., Puķite, J., Deutschmann, T., Platt, U., and Wagner, T. (2008), SCIAMACHY Limb Measurements of NO₂, BrO and OClO, Retrieval of vertical profiles: Algorithm, first results, sensitivity and comparison studies, *Adv. Space Res.*, 42, 1747-1764.

L

Lacan, A. (2009), Potentialités d'une mesure télédéetectée du dioxyde de carbone atmosphérique par spectrométrie par transformation de Fourier statique (Unpublished doctoral thesis), Université de Versailles Saint-Quentin-En-Yvelines, Versailles France.

Lacl A. A., D. J. Wuebbles, J. A. Logan (1990), Radiative Forcing of Climate by Changes in the vertical distribution of Ozone, *J. Geophys. Res.*, 95, D7, 9971-9981.

Laj, P., J. Klausen, M. Bilde, C. Plaß-Duelmer, G. Pappalardo, C. Clerbaux, U. Baltensperger, J. Hjorth, D. Simpson, S. Reimann, P.-F. Coheur, A. Richter, M. De Mazière, Y. Rudich, G. McFiggans, K. Tørseth, A. Wiedensohler, S. Morin, M. Schulz, J. Allan, J.-L. Attié, I. Barnes, W. Birmilli, P. Cammas, J. Dommen, H.-P.

Dorn, D. Fowler, J.-S. Fuzzi, M. Glasius, C. Granier, M. Hermann, I. Isaksen, S. Kinne, I. Koren, F. Madonna, M. Maione, A. Massling, O. Moehler, L. Mona, P. Monks, D. Müller, T. Müller, J. Orphal, V.-H. Peuch, F. Stratmann, D. Tanré, G. Tyndall, A.A. Riziq, M. Van Roozendaal, P. Villani, B. Wehner, H. Wex and A. A. Zardini (2009), Measuring atmospheric composition change, *Atmos. Environ.*, 43(33), 5135-5442. doi: 10.1016/j.atmosenv.2009.08.020

Lammel, G., and J. N. Cape (1996), Nitrous acid and nitrate in the atmosphere, *Chem. Soc. Rev.*, 25, 361–368.

Levelt, P. F., G. van den Oord, M. R. Dobber, A. Mälkki, H. Visser, J. Vries, J. P. Stammes, J.O.V. Lundell, H. Saari, H. (2006), The Ozone Monitoring Instrument, *IEEE Transactions on Geoscience and Remote Sensing*, 44(5), 1093-1101.

Levelt, P. F., R. Noordhoek (2002), OMI Algorithm Theoretical Basis Document Volume 1. Available at <http://eosps0.gsfc.nasa.gov/sites/default/files/atbd/ATBD-OMI-01.pdf>

Liao, H. and J. H. Seinfeld (2005), Global impacts of gas-phase chemistry-aerosol interactions on direct radiative forcing by anthropogenic aerosols and ozone, *J. Geophys. Res.*, 110, D18208. doi:10.1029/2005JD005907

Liou, K. (2002), *An introduction to atmospheric radiation*, Second edition, USA: Academic press.

Lindvall, T. (1985), Recommendations for air quality standards for nitrogen dioxide and ozone, *Scand. J. Work. Environ. Health*, 11(3), 3-9.

Logan, J. (1983), Nitrogen Oxides in the Troposphere: Global and Regional Budgets, *J. Geophys. Res.*, 88(15), 10785-10807.

Loyola, D., P. Valks (2007), A stratospheric BrO climatology based on the BASCOE 3D chemical transport model, In H. Lacoste & L. Ouwehand (Eds.). *Proceedings 'Envisat Symposium 2007': Envisat symposium*, Montreux: ESA Communication Production Office.

M

Martinez-Lozano, J. A., M. P. Utrillas, J. A. Nunez, J. Tamayo, M. J. Marin, A. R. Esteve, J. Canada and J. C. Moreno (2011), Ozone mini-holes over Valencia (Spain) and their influence on the UV erythemal radiation, *Int. J. Climatol.* , 31, 1554–1566.

Mateer, C. (1964). A study of the information content of Umkehr observations (Unpublished doctoral thesis). University of Michigan, Michigan, USA.

Matthes, S., V. Grewe, R. Sausen and G.-J. Roelofs (2005), Global impact of road traffic emissions on tropospheric ozone, *Atmos. Chem. Phys. Discuss.*, 5, 10339–10367.

Mayer, H. (1999), Air pollution in cities, *Atmos. Environ.*, 33, 4029- 4037.

Mayer, A. and A. Kylling (2005), Technical note: The libRadtran software package for radiative transfer calculations – description and examples of use, *Atmos. Chem. Phys.*, 5, 1855–1877.

Mayer, B., A. Kylling, C. Emde, U. Hamann, and R. Buras (2012). libRadtran user's guide. Available at <http://www.libradtran.org/doc/libRadtran.pdf>

McElroy, M. B (2002), *The Atmospheric Environment: Effects of Human Activity*, New Jersey: Princeton University press.

Meena, G. S., A. L. Londhe, C. S. Bhosale, D. B. Jadhav, D.B. (2009), Remote sensing ground based automatic UV/visible spectrometer for the study of atmospheric gases, *Int. J. of Remote Sens.*, 30(21), 5633-5653.

Mendes, J. F. G., L. M. M. L. Ramos, R. A. R. Ramos (2008), Air quality in the North of Portugal, *Proceedings of 2nd International Conference on Waste Management, Water pollution, air pollution, indoor climate (WWAI'08): 2nd International Conference on Waste Management, Water pollution, air pollution, indoor climate* (pp. 26-28), Corfu: ESEAS Press.

Molina, M. J. and F. S. Rowland (1974), Stratospheric sink for chlorofluoromethanes: chlorine atom-catalysed destruction of ozone, *Nature* 249, 810 – 812. doi:10.1038/249810a0

Monteiro, A., A. I. Miranda, C. Borrego, R. Vautard (2007), Air quality assessment for Portugal, *Sci. of Total Environ.*, 373, 22-31.

Munro, R., C. Anderson, J. Callies, E. Corpaccioli, M. Eisinger, R. Lang, A. Lefebvre, Y. Livschitz, A. P. Albiñana, (2006), GOME-2 on METOP, *Proceedings of the 2006 EUMETSAT Meteorological Satellite Conference: EUMETSAT* (pp.48). Helsinki: EUMETSAT.

N

Norval, M., R. M. Lucas, A. P. Cullen, F. R. de Gruijl, J. Longstreth, Y. Takizawa and J. C. van der Leun (2011), The human health effects of ozone depletion and interactions with climate Change, *Photochem. Photobiol. Sci.*, 10, 199.

O

Fleischmann, O. C., M. Hartmann, J. P. Burrows and J. Orphal (2004), New ultraviolet absorption cross-sections of BrO at atmospheric temperatures measured by time-windowing Fourier transform spectroscopy, *J. Photoch. Photobio. A: Chemistry*, 168, 117–132.

OMI SIPS (2008) , OMI/Aura Bromine Monoxide (BrO) Total Column 1-orbit L2 Swath 13x24 km V003 (OMBRO) at GES DISC , version 003 , Greenbelt, MD, USA , Goddard Space Flight Center Distributed Active Archive Center (GSFC DAAC). Available at http://disc.sci.gsfc.nasa.gov/Aura/data-holdings/OMI/ombro_v003.shtml

Ordóñez, C., A. Richter, M. Steinbacher, C. Zellwager, H. Nuß, J.P. Burrows and A. S. H. Prévôt (2006), Comparison of 7 years of satellite-borne and ground-based tropospheric NO₂ measurements around Milan, Italy, *J. Geophys. Res.*, 111, D05310.

P

Palazzi, E. (2003), *Sviluppo di modelli a supporto della metodologia DOAS per la determinazione degli inquinanti in troposfera* (Unpublished graduation thesis). Università degli Studi di Bologna, Bologna, Italy.

Palazzi, E. (2008), *Retrieval of trace gases vertical profile in the lower atmosphere combining Differential Optical Absorption Spectroscopy with radiative transfer models* (Unpublished doctoral thesis), Università degli Studi di Bologna, Bologna, Italy.

Palazzi, E., A. Petritoli, F. Ravegnani, I. Kostadinov, D. Bortoli, S. Masieri, M. Premuda, and G. Giovanelli (2008), Retrieval of Gas Pollutants Vertical Profile in the Boundary Layer by Means of Multiple Axis DOAS, *Special Issue IEEE Transactions on Geoscience and Remote Sensing*, 46(10), 2796 – 2802.

Palazzi, E., A. Petritoli, G. Giovanelli, F. Ravegnani, I. Kostadinov and D. Bortoli (2005), The Monte Carlo radiative transfer model "PROMSAR" for the interpretation of DOAS remote sensing measurements, *Geophysical Research Abstracts*, 7, 02584. a)

Palazzi, E., A. Petritoli, G. Giovanelli, I. Kostadinov, D. Bortoli, F. Ravegnan, and S.S. Sackey (2005), PROMSAR: A backward Monte Carlo spherical RTM for the analysis of DOAS remote sensing measurements, *Adv. Space Res.*, 36(5), 1007-1014. b)

Palazzi, E., M. Premuda, A. Petritoli, G. Giovanelli, F. Ravegnani, I. Kostadinov, D. Bortoli and F. Margelli (2005), PROMSAR: a multiple scattering atmospheric model for the interpretation of DOAS measurements, *Atti della fondazione Giorgio Ronchi, Selected papers of GOLD IEEE Remote Sensing conference*, M. Migliaccio, and A. Iodice (Eds.), ANNO LX, 2005, N. 4, pp.689-695. c)

Palmgren, F., R. Berkowicz, O. Hertel, E. Vignati (1996), Effects of reduction of NO_x on the NO₂ levels in urban streets, *The Science of the Total Environment*, 189/190, 409-415.

Paul J., F. Fortuin and H. Kelder (1998), An ozone climatology based on ozonesonde and satellite measurements, *J. Geophys. Res.*, 103 (D24), 31,709-31,734.

Payan, S. (2003), Retrieval algorithm. Available at http://www.lisa.u-pec.fr/FREJUS-HIRESMIR/down_files/cours/PAYAN-Inversion_Cours.pdf

Perner, D., D. H. Ehhalt, H. W. Paetz, U. Platt, E. P. Roeth, and A. Volz (1976), OH Radicals in the lower Troposphere, *Geophys. Res. Lett.*, 3, 466- 468.

Perner, D. and U. Platt (1979). Detection of Nitrous Acid in the Atmosphere by Differential Optical Absorption, *Geophys. Res. Lett.*, 6, 917-920.

Petritoli, A. (1998). Distribuzioni verticali di gas in traccia in atmosfera ottenute con metodi di inversione applicati a misure di quantità colonnari (Unpublished graduation thesis), Università degli Studi di Bologna, Bologna, Italy.

Petritoli, A., F. Ravegnani, G. Giovanelli, D. Bortoli, U. Bonafè, I. Kostadinov, and A. Oulanovsky (2002), Off-axis measurements of atmospheric trace gases by use of an airborne ultraviolet-visible spectrometer, *Appl. Opt.*, 41(27), 5593–5599. a)

Petritoli, A., G. Giovanelli, I. Kostadinov, F. Ravegnani, D. Bortoli, P. Bonasoni, F. Evangelisti, U. Bonafè, F. and Calzolari (2002), Tropospheric and stratospheric NO₂ amount deduced by slant column measurements at Mt. Cimone station, *Adv. Space Res.*, 29(11), 1691–1695. b)

Petritoli, A., G. Giovanelli, P. Bonasoni, T. Colombo, F. Evangelisti, U. Bonafè, D. Bortoli, I. Kostadinov and F. Ravegnani (1999) , Ground-based NO₂ and O₃ analysis at Monte Cimone station during 1995-1996: A

case study for spring 1995 NO₂ concentration profiles. *Proc. SPIE 3867, Satellite Remote Sensing of Clouds and the Atmosphere IV*, 280 (December 8, 1999). doi:10.1117/12.373060. Available at <http://dx.doi.org/10.1117/12.373060>

Petritoli, A., P. Bonasoni, G. Giovanelli, F. Ravegnani, I. Kostadinov, D. Bortoli, A. Weiss, D. Schaub, A. Richter and F. Fortezza (2004), First comparison between ground-based and satellite-borne measurements of tropospheric nitrogen dioxide in the Po basin, *J. Geophys. Res.*, 109, D15307. doi:10.1029/2004JD004547.

Pfeilsticker, K., C.E. Blom, R. Brandtjen, H. Fischer, N. Glatthor, A. Grendel, T. Gulde, M. Höpfner, D. Perner, Ch. Piesch, U. Platt, W. Renger, J. Sessler and M. Wirth (1997), Aircraft-borne Detection of the Stratospheric Column Amounts of O₃, NO₂, OClO, ClNO₃, HNO₃ and Aerosols around the Arctic Vortex (79°N to 39°N) during Spring 1993, 1. Observational data, *J. Geophys. Res.*, 102, 10801-10814.

Pieter Valks (2003). *Retrieval of total and tropospheric ozone from observations by the Global Ozone Monitoring Experiment* (PhD thesis). ISBN 90-386-1825-5

Plane, J. M. C., C. F. Nien (1992), Differential optical absorption spectrometer for measuring atmospheric trace gases, *Rev. Sci. Instr.*, 63, 1867-1876.

Platt, U. (1994), *Differential Optical Absorption Spectroscopy (DOAS)*. In M. W. Sigrist (Ed.), *Monitoring by Spectroscopic Techniques*. New York: John Wiley & Sons, Inc.

Platt, U. (1994), *Differential Optical Absorption Spectroscopy (DOAS) in Air Monitoring by Spectroscopic Techniques*, New York: John Wiley and Sons Inc.

Platt, U. and G. Honninger (2003), The role of halogen species in the troposphere, *Chemosphere*, 52, 325-338.

Platt, U. and D. Perner (1980), Direct Measurements of Atmospheric CH₂O, HNO₂, O₃, NO₂ and SO₂ by Differential Optical Absorption in the Near UV, *J. Geophys. Res.*, 85, 7453-7458.

Platt, U., D. Perner, G. W. Harris, A. M. Winer, and J. N. Pitts Jr. (1980). Detection of NO₃ in the Polluted Troposphere by Differential Optical Absorption. *Geophys. Res. Lett.*, 7, 89-92.

Platt, U. and J. Stutz (2008). *Differential Optical Absorption Spectroscopy*. Berlin: Springer. ISBN: 978-3-540-21193-8

Premuda, M. (2011), Monte Carlo Simulation of Radiative Transfer in Atmospheric Environments for Problems Arising from Remote Sensing Measurements, Applications of Monte Carlo Method in Science and Engineering, Prof. Shaul Mordechai (Ed.), ISBN: 978-953-307-691-1, InTech, doi: 10.5772/15556.

Press, W., B. Flannery, S. Teukolsky, and W. Vetterling (1986), *Numerical Recipes - The Art of Scientific Computing*, Cambridge Cambridge: University Press.

Puķite, J., S. Kühn, T. Deutschmann, U. Platt, and T. Wagner (2008), Accounting for the effect of horizontal gradients in limb measurements of scattered sunlight, *Atmos. Chem. Phys.*, 8, 3045-3060. doi:10.5194/acp-8-3045-2008

Puķīte, J., S. Kühl, W. Wilms-Grabe, C. Friedeburg, U. Platt, and T. Wagner (2006), Retrieval of stratospheric trace gases from SCIAMACHY limb measurements. In H. Lacoste (Eds.). Proceedings of the First Atmospheric Science Conference: Atmospheric Science Conference. Frascati: ESA publications division.

R

Raes, F. (2012), *About Molecules and Planets with Humans in between*, Luxembourg: Publications Office of the European Union. Available at http://ec.europa.eu/dgs/jrc/downloads/jrc_air_climate_conversations_en.pdf. ISBN 978-92-79-25195-5.

Rhew, R. C. (2011), Sources and sinks of methyl bromide and methyl chloride in the tallgrass prairie: Applying a stable isotope tracer technique over highly variable gross fluxes, *J. Geophys. Res.*, 116, G03026. doi:10.1029/2011JG001704

Richter, A. (2004), *Optical Remote Sensing Methods, Instruments, and Applications Lecture Environmental Physics*, University of Bremen, WS 2004/2005. Available at http://www.doas-bremen.de/lecture_material.htm

Richter, A., Begoin, M., Hilboll, A., and Burrows, J. P. (2011), An improved NO₂ retrieval for the GOME-2 satellite instrument, *Atmos. Meas. Tech.*, 4, 1147-1159. doi:10.5194/amt-4-1147-2011

Rodgers C.D. (1990), Characterization and Error Analysis of Profiles Retrieved from remote sounding measurements, *J. Geophys. Res.*, 95, 5587-5595.

Rodgers, C. D. (2000), *Inverse methods for atmospheric sounding: Theory and Practice*, Singapore: World Scientific.

Rodgers C. D. and B. J. Connor (2003), Intercomparison of remote sounding instruments, *J. Geophys. Res.*, 10 (D3), 4116. doi:10.1029/2002JD002299

Rosanov, A. (2007), Algorithm document: retrieval of NO₂ and BrO vertical profiles from SCIAMACHY limb measurements at university of Bremen. Available at http://www.iup.uni-bremen.de/~sciapro/CDI/DOCU/Algorithm_Document.pdf

Rosanov, A. (2008), Retrieval of NO₂ vertical profiles from SCIAMACHY limb measurements at university of Bremen processing version >=3.1. Available at http://www.iup.uni-bremen.de/~sciapro/CDI/DOCU/PSD_NO2_v3_1.pdf

Roscoe, H. K. (2006), The Brewer–Dobson circulation in the stratosphere and mesosphere – Is there a trend?, *Adv. Space Res.*, 38, 2446–2451.

Roscoe, H. K., P. V. Johnston, M. van Roozendaal, A. Richter, A. Sarkissian, J. Roscoe, K. E. Preston, J. C. Lambert, C. Hermans, W. DeCuyper, S. Dzienus, T. Winterrath, J. Burrows, F. Goutail, J. P. Pommereau, E. D'Almeida, J. Hottier, C. Coureul, R. Didier, I. Pundt, L. M. Bartlett, C. T. McElroy, J. E. (1999), Slant columns measurements of O₃ and NO₂ during the NDSC intercomparison of zenith-sky UV-visible spectrometers in June 1996, *J. Atmosph. Chem.*, 32, 281–314.

Rozanov A., H. Bovensmann, A. Bracher, S. Hrechanyy, V. Rozanov, M. Sinnhuber, F. Stroh and J.P. Burrows (2005), NO₂ and BrO vertical profile retrieval from

SCIAMACHY limb measurements: Sensitivity studies, *Adv. Space Res.*, 36(5), 846-854. doi:10.1016/j.asr.2005.03.013

S

Salerno, G.G., M. R. Burton, C. Oppenheimer, T. Caltabiano, D. Randazzo, N. Bruno, and V. Longo (2009), Three-years of SO₂ flux measurements of Mt. Etna using an automated UV scanner array: Comparison with conventional traverses and uncertainties in flux retrieval, *J. Volcanol. Geoth. Res.*, 183(1-2), 76-83.

Sanders, R. W., S. Solomon, M. A. Carroll, and A. L. Schmeltekopf (1988), Ground based Measurements of O₃, NO₂, OClO and BrO during the Antarctic Ozone Depletion Event. In R. D. Bjokov and P. Fabian (Eds.), *Ozone in the Atmosphere: Quadrennial Ozone Symposium 1988* (pp. 65-70). Hampton, Va.: Deepak Publishing.

Seinfeld, J. H., S. N. Pandis (2006), *Atmospheric Chemistry and Physics: From air pollution to climate change*, Second edition, New Jersey: Wiley.

Senne, T., J. Stutz, U. Platt (1996). Measurements of the latitudinal distribution of NO₂ column density and layer height in Oct./Nov. 1993, *Geophys. Res. Lett.*, 23, 805-808.

Slusser, J., K. Hammond, A. Kylling, K. Stamnes, L. Perliski, A. Dahlback, D. Anderson and R. Demajistre (1996). Comparison of air mass computations, *J. Geophys. Res.*, 101, 9315-9321.

Socolik, I. (2009), Lecture 6- Absorption by atmospheric gases in the IR, visible and UV spectral regions. Available at http://irina.eas.gatech.edu/EAS8803_Fall2009/Lec6.pdf

Solomon, S. (1999). Stratospheric ozone depletion: a review of concepts and history, *Rev. Geophys.*, 37, 275-316.

Solomon, S., A. L. Schmeltekopf, and R. W. Sanders (1987), On the interpretation of zenith sky absorption measurements, *J. Geophys. Res.*, 92, 8311-8319.

Solomon, S., D. Qin, M. Manning, Z. Chen, M. Marquis, K. Averyt, M. Tignor, and H. Miller (2007), IPCC, 2007: *Climate Change 2007: The Physical Science Basis*. Contribution of Working Group I to the Fourth Assessment Report of the Intergovernmental Panel on Climate Change, Cambridge, United Kingdom and New York, NY, USA.: Cambridge University Press.

Sousa S. I. V., M. C. M. Alvim-Ferraz, F. G. Martins, M. C. Pereira (2009), Ozone exposure and its influence on the worsening of childhood asthma, *Allergy*, 64, 1046-1055.

Sousa S. I. V. , M. M. C. Pereira , F. G. Martins , C. M. Alvim-Ferraz (2008), Identification of regions with high ozone concentrations aiming the impact assessment on childhood asthma , *Journal of Human and Ecological Risk Assessment*, 14, 3, 610-622.

Strong, K. (2005), *Earth Observations from Space*, Spring Term 2005. Available at http://www.atmosph.physics.utoronto.ca/people/strong/phy499/section4_05.pdf

T

Theys, N., M. Van Roozendael, F. Hendrick, X. Yang, I. De Smedt, A. Richter, M. Begoin, Q. Errera, P. V. Johnston, K. Kreher, and M. De Maziere (2011), Global observations of tropospheric BrO columns using GOME-2 satellite data, *Atmos. Chem. Phys.*, 11, 1791–1811.

Theys, N. M. Van Roozendael, Q. Errera, S. Chabrillat, F. Daerden, F. Hendrick, D. Loyola, P. Valks (2007), A stratospheric BrO climatology based on the BASCOE 3 D chemical transport model, Proc. 'Envisat Symposium 2007', Montreux, Switzerland, 23–27 April 2007 (ESA SP-636, July 2007).

Twomey, S. (1996), *Introduction to the mathematics of inversion in remote sensing and indirect measurements*, New York: Dover publications.

V

Valks, P. J. M. (2003), TOGOMI Algorithm Theoretical Basis Document. Available at http://www.gse-promote.org/services/ozone_nrt/togomi_ATBD_v1.21.pdf

Valks, P.J.M., J.F. de Haan, J.P. Veefkind, R.F. van Oss and D.S. Balis (2004), TOGOMI: An improved total ozone retrieval algorithm for GOME, XX Quadrennial Ozone Symposium, 1/6/2004-8/6/2004, C.S. Zerefos (Ed), Athens, University of Athens, 129-130.

Vaughan, G., K.K. Roscoe, L.M. Bartlett, F.M. O'Connor, A. Sarkissian, M. van Roozendael, J.C. Lambert, P.C. Simon, K. Karlsen, B.A.K. Hoiskar, D.J. Fish, R.L. Jones, R.A. Freshwater, J.P. Pommereau, F. Goutail, S.B. Andersen, D.G. Drew, P.A. Hughes, D. Moore, J. Mellqvist, E. Hegels, T. Klupfel, F. Erle, K. Pfeilsticker, and U. Platt (1997), An intercomparison of ground-based UV-visible sensors of ozone and NO₂, *J. Geophys. Res.* 102(D1), 1411–1422.

Veefkind, J. P., J. F. de Haan, E. J. Brinksma, M. Kroon, and P. F. Levelt (2006), Total ozone from the Ozone Monitoring Instrument (OMI) using the OMI-DOAS technique, *IEEE Trans. Geosci. Remote Sens.*, 44(5), 1239 – 1244.

Vogt, R., R. Sander, R. Von Glasow, and P.J. Crutzen (1999), Iodine Chemistry and its Role in Halogen Activation and Ozone Loss in the Marine Boundary Layer: A Model Study, *J. Atmos. Chem.*, 32, 375–395.

Volkamer, R., L. T. Molina, M. J. Molina, T. Shirley, and W. H. Brune (2005), DOAS measurement of glyoxal as an indicator for fast VOC chemistry in urban air, *Geophys. Res. Lett.*, 32, L08806.

Volz-Thomas, A., M. Beekmann, D. Derwent, K. Law, A. Lindskog, A. Prévôt, M. Roemer, M. Schultz, U. Schurath, S. Solberg and A. Stohl (2003), Synthesis and Integration Report: Towards Cleaner Air for Europe - Science, Tools and Applications Part 1, Results from the EUROTRAC-2 Synthesis and Integration (S&I) Project available at http://www.helmholtz-muenchen.de/eurotrac/SI_report/ 10/10/2012.

W

Wagner, T., B. Dix, C. von Friedeburg, U. Frieß, S. Sanghavi, R. Sinreich, and U. Platt, (2004), MAXDOAS O₄ measurements: A new technique to derive information on atmospheric aerosols-Principles and information content, *J. Geophys. Res.* 109, D22205. doi: 10.1029/2004JD004904

Weibring, P., J. Swartling, H. Edner, S. Svanberg, T. Caltabiano, D. Condarelli, G. Cecchi, and L. Pantani, L. (2002), Optical monitoring of volcanic sulphur dioxide emissions - comparison between four different remote-sensing spectroscopic techniques, *Opt. Lasers Eng.*, 37(2-3), 267-284.

World Health Organization Regional Office for Europe (2000), Air quality guidelines for Europe, 2nd Edition, WHO Regional Publications, *European Series*, 91, 175- 179.

Wilks, D. (1995), *Statistical Methods in Atmospheric Sciences*. San Diego: Academic Press. ISBN: 978-0-12-385022-5.

Wilmouth, D. M., T. F. Hanisco, N. M. Donahue, and J. G. Anderson (1999), Fourier transform ultraviolet spectroscopy of the $A(2\Pi(3/2) < -X(113/2)-1-2$ transition of BrO, *J. Phys. Chem. A*, 103(45), 8935–8945.

WHO Regional Office for Europe (2000), Nitrogen dioxide- Chapter 7.1. Available at http://www.euro.who.int/__data/assets/pdf_file/0017/123083/AQG2ndEd_7_1nitrogendioxide.pdf 22 outubro de 2012.

WHO (2011), Air quality and health. Available at <http://www.who.int/mediacentre/factsheets/fs313/en/index.html> in 22 october 2012.

Y

Yilmaz, S. (2012), Retrieval of Atmospheric Aerosol and Trace Gas Vertical Profiles using Multi-Axis Differential Optical Absorption Spectroscopy (Unpublished doctoral thesis). Combined Faculties for the Natural Sciences and for Mathematics of the Ruperto-Carola University of Heidelberg, Heidelberg Germany.

Yokouchi, Y., K. Osada, M. Wada, F. Hasebe, M. Agama, R. Murakami, H. Mukai, Y. Nojiri, Y. Inuzuka, D. Toom-Saunry and P. Fraser (2008), Global distribution and seasonal concentration change of methyl iodide in the atmosphere, *J. Geophys. Res.*, 113, D18311. doi:10.1029/2008JD009861

Z

Zabalza, J. , D. Ogulei, D. Elustondo, J. M. Santamaria, A. Alastuey, X. Querol and P. K. Hopke (2007), Study of urban atmospheric pollution in Navarre (Northern Spain), *Environ. Monit. Assess.*, 134, 137-151.

Zeng, G., J. A. Pyle, and P. J. Young (2008), Atmospheric Chemistry and Physics Impact of climate change on tropospheric ozone and its global budgets , *Atmos. Chem. Phys.*, 8, 369–387.

Zujic, A., B. Radak, A. Filipovic and D. Markovic (2009), Extending the use of air quality indices to reflect effective population exposure, *Environ. Monit. Assess.*, 156, 539-549.

